Spatio-Temporal Stability Analysis in Two-Phase Mixing Layers

Effect of a Velocity Deficit near the Interface

Dissertation zur Erlangung des akademischen Grades
Doktor-Ingenieur (Dr.-Ing.)

vorgelegt der Fakultät für Maschinenbau
der Technischen Universität Ilmenau

von Dipl.-Math. Thomas Otto

1. Gutachter: PD Dr. rer. nat. habil. Thomas Boeck
2. Gutachter: Univ.-Prof. Dr. rer. nat. habil. Jörg Schumacher
3. Gutachter: Univ.-Prof. Dr. Ing. habil. Günter Brenn

Tag der Einreichung: 01.02.2012
Tag der wissenschaftlichen Aussprache: 25.06.2012

urn:nbn:de:gbv:ilm1-2012000259

Zusammenfassung

Die vorliegende Arbeit befasst sich mit dem Wachstum wellenförmiger Störungen an der Fluidgrenze in Zwei-Phasen-Mischungsschichten. Dieses Phänomen tritt z.B. beim primären Zerstäubungsprozess von Flüssigkeiten durch ein angrenzendes oder die Flüssigkeit umschließendes Gas auf. Im Rahmen der linearen Stabilitätstheorie wird sowohl der Einfluss der verschiedenen Stoffgrößen als auch jener der Beschaffenheit der Grundströmung betrachtet. Die gegebene Grundströmung, auf der sich die Störungen ausbreiten, ist dabei durch ein ebenes Geschwindigkeitsfeld mit parallelen Stromlinien gegeben. Ferner wird die charakteristische Struktur des Geschwindigkeitsfeldes am Düsenausgang berücksichtigt: Zunächst werden im Inneren der Düse Flüssigkeit und Gas getrennt voneinander auf unterschiedliche Geschwindigkeiten beschleunigt. Infolge der trennenden Wand im Inneren der Düse kommt es zur Bildung von Geschwindigkeitsgrenzschichten in beiden Medien mit verschwindender Geschwindigkeit an der festen Wand. Nach anschließendem Kontakt beider Ströme bildet sich somit ein Geschwindigkeitsfeld mit Nachlaufströmung in der Umgebung der Grenzfläche heraus. Für das Studium des Stabilitätsproblems unter Berücksichtigung viskoser Reibung wird die Grundströmung mit einem Profil aus Errorfunktionen modelliert, welches nicht nur die Geschwindigkeitsgrenzschichten sondern auch den Geschwindigkeitsdefekt infolge der Nachlaufströmung berücksichtigt. Für anwachsende wellenförmige Störungen in unmittelbarer Nähe der Grenzfläche zwischen beiden Fluiden werden die Wellenlängen und Wachstumsraten untersucht, wobei sowohl die zeitliche als auch die räumliche Ausbreitung der Störungen von Interesse ist. Die Abängigkeit der Größen von den Stoffparametern, Fluidgeschwindigkeiten, sowie dem Geschwindigkeitsdefekt relativ zu den mittleren Geschwindigkeiten der flüssigen und gasförmigen Phase werden dokumentiert. Dabei wird die Oberflächenspannung berücksichtigt, jedoch Einflüsse des Schwerefeldes vernachlässigt. Zusätzlich wird eine Studie unter Vernachlässigung der Viskosität durchgeführt. Dafür wird das Geschwindigkeitsfeld durch ein stückweise lineares Grundprofil angenähert. Das hat zur Folge, dass die Dispersionsrelation $D(\alpha, \omega) = 0$ für die Störungen in analytischer Form geschrieben werden kann. Man erhält dabei eine transzendente Funktion für die Wellenzahl α und – je nach Komplexität des Problemes – ein Polynom dritten oder vierten Grades für die Frequenz ω. Im Gegensatz dazu müssen im viskosen Fall die linearen Stabilitätsgleichungen für die Störungen vollständig numerisch behandelt werden. Entwickelt man die Störungen in eine Reihe aus Chebyshev-Polynomen, so erhält man für das Stabilitätsproblems beider gekoppelte Phasen sowohl für sich zeitlich als auch räumlich entwickelnde Störungen je ein algebraisches, verallgemeinertes Eigenwertproblem des Orr-Sommerfeld-Typs. Die Lösung eines solchen Eigenwertproblems liefert üblicherweise mehrere instabile Moden für einen gegebenen Parametersatz, deren physikalischer Instabilitätsmechanismus sich anhand der Abhängigkeit von der Reynoldszahl, der Struktur der Eigenfunktion und einer Analyse ihrer Energiebilanz identifizieren lässt. Auf diese Weise kann man Beiträge des nicht-viskosen Kelvin-Helmholtz-Mechanismus finden, der sowohl in nur einer von beiden Phasen auftreten kann als auch kombiniert in beiden. Weiterhin lassen sich Beiträge des Tollmien-Schlichting-Mechanismus und des Instabilitätsmechanismus infolge einer Viskositätsänderung identifizieren.

Neben dem Einfluss der Stoffgrößen und des Geschwindigkeitsdefekts im Grundprofil auf die zeitlichen und räumlichen Wachstumsraten und Wellenlängen, wird sowohl für den viskosen als auch den nicht-viskosen Fall der Übergang von konvektiver zu absoluter Instabilität betrachtet. Dafür ist die Berechnung verallgemeinerter räulicher Stabilitätskurven notwendig. Bei Vernachlässigung viskoser Reibung werden für das stückweise lineare Geschwindigkeitsprofil Bedingungen für konvektive Instabilität angegeben. Unter Berücksichtigung der Viskosität erhält man das für das Errorfunktion-Grundprofil, dass ein stärkerer Geschwindigkeitsdefekt den Übergang zu absoluter Instabilität hin zu geringeren Unterschieden der Geschwindigkeiten in der flüssigen und gasförmigen Phase verlagert. In ähnlicher Weise begünstigen sowohl die Viskosität als auch die Oberflächenspannung für gewöhnlich das Auftreten von absoluter Instabilitat.

Abschließend werden die numerischen Ergebnisse sowohl der nicht-viskosen als auch der viskosen Theorie mit experimentellen Daten aus der Literatur verglichen.

Abstract

Motivated by the atomization of liquids by fast gas streams, the present work is focussed on the growth of wavy perturbations on the liquid-gas interface in two-phase mixing layers. In the framework of linear stability theory it is analyzed how the parallel basic flow is affected by various fluid properties, flow parameters, and also the velocity field itself. The planar basic velocity distribution is modeled by taking into account the particular flow structure near the tip of the splitter plate: separated streams form boundary layers on the splitter plate, where the liquid and gas have zero velocity, causing a wake-like distribution once the streams come into contact. In the viscous study this basic velocity profile is parametrized by a combination of error functions with different length scales reflecting the boundary layer sizes and the velocity deficit near the interface associated with the wake. It leads to an additional parameter describing the velocity deficit at the interface relative to the free stream velocities in the liquid and gas phases. In terms of both temporal and spatial modes the main interest is in the wavelengths and growth rates of the growing interfacial waves that appear near the nozzle or splitter plate. Surface tension is taken into account, but gravity effects are neglected.

In additon, the viscous results are compared with inviscid computations for a piecewise linear velocity distribution with sloped segments corresponding to the boundary layers associated to the viscous profile. As a result, the dispersion relation for the streamfunction perturbations can be given analytically. Depending on the details of the problem it is a polynomial of third or fourth degree in the frequency ω, but transcendental in the wave number α. In the viscous case the traditional Orr-Sommerfeld problem for the streamfunction perturbations is solved numerically for two coupled layers in both temporal and spatial setting using expansions in Chebyshev polynomials. From the solution of the Orr-Sommerfeld eigenvalue problem typically several unstable modes are found for a given set of parameters, and their driving instability mechanism is identified based on their Reynolds number dependence, structure and an energy budget. By that, contributions from the inviscid Kelvin-Helmholtz mechanism are identified, which can either involve both phases or act predominantly within a single phase. In addition, the Tollmien-Schlichting mechanism, and the viscosity-contrast or H mechanism to the unstable modes can be identified.

For both the viscous and the inviscid case it is shown, how the structure of the basic velocity distribution modifies the temporal and spatial stability properties. In addition, transition from convective to absolute instability is determined by computing generalized spatial branches. In inviscid theory, conditions for convective instability are identified for the piecewise linear basic flow. In the viscous case, transition from convective to absolute instability occurs at lower velocity contrast between gas and liquid free streams when a defect is present. Furthermore, both viscosity and surface tension usually promote absolute instability.

Finally, the numerical results for both viscous and inviscid theory are compared with experimental data available in the literature.

Contents

Chapter 1

Introduction

1.1 Motivation

Liquid atomization is of great practical importance in both nature and industry. In the atomization process bulk liquid is converted into small drops until a spray is formed. A spray is considered as a system of drops immersed in a gaseous continuous phase. Examples of natural sprays include rain, drizzle, ocean sprays and waterfall mists. As an example, a mist of very small drops produced by the Iguazu Falls in Argentina is shown in Figure 1.1.
In industry, liquid atomization and spray systems are used in mechanical, chemical, aerospace, and civil engineering. Important applications are spray combustion processes in gas turbines, furnaces, rockets and engines. In agriculture atomization finds implementation in crop spraying and food preservation. In addition, spray systems are used in medical inhalation therapy, spray drying and cooling, air conditioning, industrial cleaning, powdered metallurgy, spray painting and coating, fire protection, and many other areas [2, 37, 58].

Figure 1.1: *Natural spray: The Garganta del Diablo (Devil Throat) Iguazu Falls in Argentina. Photograph taken by L. Galuzzi (http://www.galuzzi.it).*

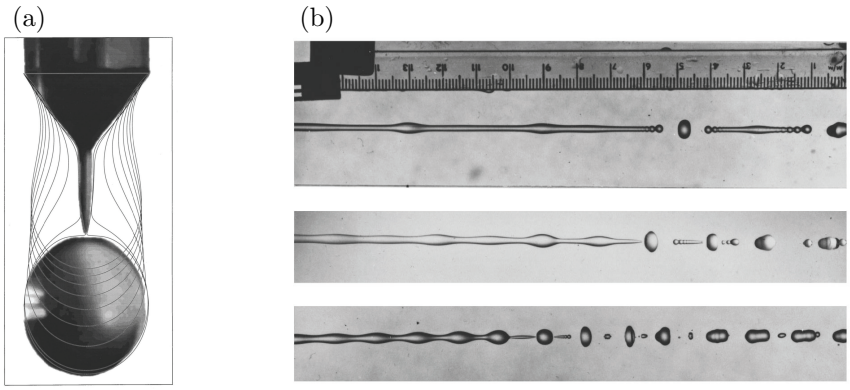

Figure 1.2: *Simple drop formation: (a) The shape of a water drop falling from a nozzle. The lines represent the shape of the water at earlier times. (b) Photographs of a decaying jet for three different frequencies of excitation. From Eggers [19].*

Atomization occurs not only in rather complicated industrial spray devices, but can also be observed at home: a dripping faucet is one of the most basic examples of drop formation. In this case flow is released very slowly from a nozzle. At first, surface tension forces are in balance with gravitational forces. With increasing time the drop becomes heavier and gravity finally overcomes surface tension. As a result, the fluid begins to fall and eventually a drop separates. Figure 1.2(a) shows the shape of a drop of water falling from a nozzle at pinch-off. A theoretical study of the detachment process is given by Eggers [19]. His equations characterize the shape of the water at times $t < t_0$, where pinch-off occurs at $t = t_0$. Such earlier stages of the detachment process are shown by the lines in Figure 1.2(a).
When the water emerges at higher velocity in quiescent air, it forms a cylindrical jet that suffers a capillary instability due to the action of surface tension. The instability is named after Plateau [47], who identified and observed the instability experimentally, and Rayleigh [48], who first solved the full inviscid stability problem of the breakup of a long cylindrical laminar liquid jet. The Plateau-Rayleigh instability is driven by modulations of the jet radius along the axis, where perturbations with wavelengths greater than the circumference of the jet cause its surface to decrease at a constant volume. As a result its surface energy is decreased, thus favouring the disintegration of the jet, see Figure 1.2(b). The disintegrated liquid forms spheroidal drops, since a sphere has minimum surface energy. The wavelength of maximum amplification was shown to be $\lambda_{\max} = 4.51d$, with d denoting the mean diameter of the jet [48]. Consequently, the corresponding drop diameter is 1.89 times larger than the initial diameter of the jet [58].

Compared to a simple faucet, the spray systems used in industry are much more complex. However, essentially all that is needed to produce sprays of reasonable drop sizes, is a high relative velocity between the liquid to be dispersered and the surrounding air or gas. In addition, disintegration proceeds more easily if the liquid is present in thin jets or sheets of liquid. This is due to the fact, that these geometries provide the highest surface energy and thus the greatest instability. Therefore, the bulk liquid is first transformed into thin jets or sheets of liquid by nozzles and atomizers, where the detailed design of the spray devices depends strongly on the application. Atomizers can, for example, be classified taking into account the type of energy used for atomization. Such a classification is given by Bayvel and Orzechowski [2]:

- The energy most commonly used in atomization is that of the liquid itself. In order to accomplish the high relative velocity between the phases necessary for disintegration, the liquid to be atomized is discharged at high pressure into stagnant surrounding air or gas. At the orifice the pressure drop within the liquid is converted into kinetic energy, resulting in the high velocity of the liquid. This is the principle of operation of pressure atomizers, which are applied in Diesel engines, for example [2, 58].

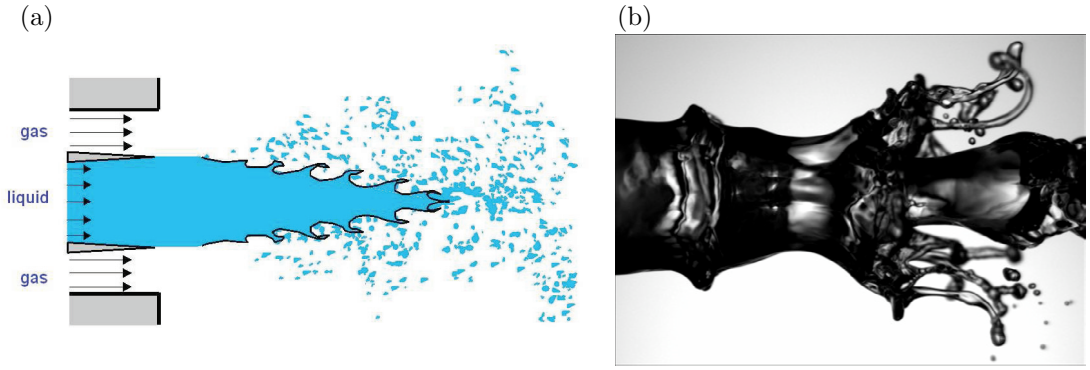

Figure 1.3: *Gas-assisted atomization: (a) Schematic representation of atomization from a concentric nozzle by a fast gas stream; from Boeck [5]. (b) Destabilization of a slow water jet by a fast coaxial air stream and formation of ligaments; from Marmottant and Villermaux [39].*

- Gas-assisted atomizers use the energy of a gas, and are characterized by an interaction between a relatively slow moving liquid and a fast gas stream. The interaction between the phases can have a parallel, crossing, or swirled direction [2]. In general, finest atomization is obtained when the liquid is present as a jet or sheet of minimum uniform thickness, and is exposed to the gas at the highest possible velocity. For both liquid jets and sheets, the atomization process occurs at increasingly smaller length scales, where the axisymmetric geometry is practically relevant in aerospace engineering: In liquid-gas propellant rocket engines a slow, dense stream of liquid oxygen is surrounded by a light, gaseous hydrogen annular stream of high velocity [56]. The atomization process in such a flow configuration is shown schematically in Figure 1.3(a).

- Liquid can also be disintegrated as a result of energy applied externally. For example, in rotary atomizers the mechanical energy of a rotating cup or disk is converted into kinetic energy. As a result the liquid is ejected at high velocity from the periphery of the rotating device [2, 37]. Rotary atomizers are used to disperse suspensions in spray drying applications [58].

1.2 Atomization Process and Parameters

In parallel gas-assist flow atomizers a liquid is disintegrated by a fast gas stream, where both phases are initially segragated; see the schematic in Figure 1.3(a). The liquid jet is discharged with a relatively low velocity and surrounded by the gas stream propagating in the same direction. In consequence of strong shear forces infinitesimal disturbances develop a wavy deformation of the interface, which increases with the distance from the nozzle exit. Farther downstream transverse modulations form on the crests of the propagating waves, which are drawn into liquid ligaments. The development of ligaments of water under the action of a fast coaxial air stream is shown by the photograph in Figure 1.3(b). The liquid ligaments are further accelerated and stretched in the gas stream, their diameters decrease, and they finally disintegrate into drops under the Plateau-Rayleigh instability [39]. The breakup process described for a jet is similar for a liquid sheet, and is refered to as primary drop disintegration [2, 37, 58].
Many of the larger drops produced in the initial disintegration process undergo a secondary destabilization in the fast gas stream. Due to the strong aerodynamic forces waves form on the surfaces of the drops moving in the gaseous medium. Amplification of the waves destabilize the drops and they further disintegrate into smaller droplets. In addition, secondary breakup can also occur after collisions of drops with each other or with a solid or liquid surface [36, 37].

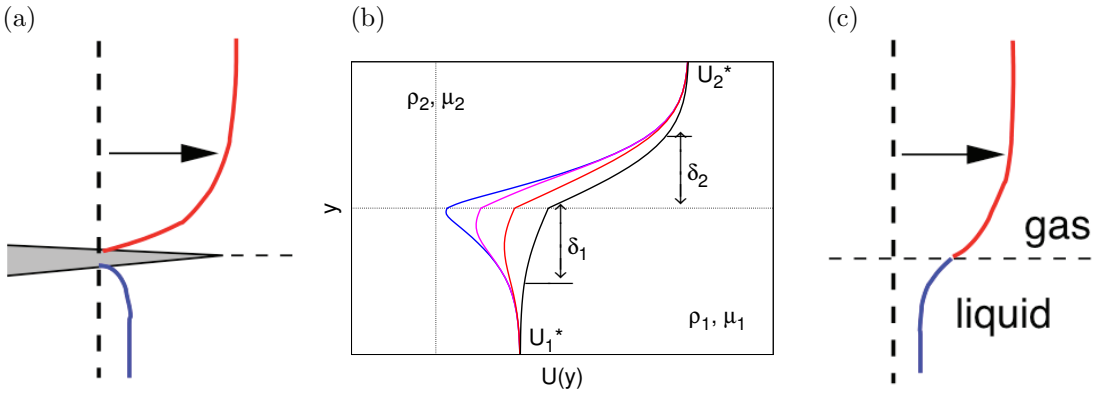

Figure 1.4: *Evolution of the basic velocity profile close to the interface with increasing downstream distance: (a) initial shape of the mean velocity profile; (b) compensation of the velocity defect; (c) final shape of the relaxed mean velocity profile. Figures (a) and (c) from Boeck [5].*

In the atomization process just described, the liquid disintegrates into a more or less uniform spray, whose quality can be characterized by its averaged drop size and its drop size distribution. These statistical quantites depend both on the type, size and internal geometry of the atomizer, and on the physical properties of the dispersed and continuous phases [36, 37].

As already mentioned, the primary disintegration process in gas-assisted atomization is based on strong shear forces between the two phases involved. The shear is produced by accelerating the two nearly parallel streams of gas and liquid in distinct channels and merge them downstream. The velocities at large distance from the interface are assumed to be constant. Thus, the effect of outer boundaries is neglected. In Figure 1.4(a) the velocity profile is shown some distance before the streams come into contact. Since the phases are separated, e.g. by a splitter plate, boundary layers form at the rigid boundary [18]. In addition, at the edge of the splitter plate the velocity profile is continuous across the interface separating the two streams [56]. However, in the vicinity of the initial contact point the exact flow between both phases close to the interface is not precisely known from either theory or experiment (but see Woodley and Peake [57]). Nevertheless, due to the no-slip condition upstream of the splitter lip, as the streams come into contact the velocity distribution has a structure somewhat similar to a wake with a certain velocity defect. The defect decreases with increasing distance from the splitter lip since the slower liquid phase is accelerated by the fast gas stream. This is shown in Figure 1.4(b). Eventually, the velocity distribution approaches the defect-free *relaxed* shape illustrated in Figure 1.4(c).

In principle almost all liquids with very diverse properties are atomized. However, the most atomized liquids are fuels and water. Water is generally used in cooling and cleaning processes, whereas liquid fuels are still the main sources of energy worldwide. In addition, water solutions, oil solutions, and water-oil solutions are used in agriculture as crop protections (fungicides, herbicides, and others) [2, 37]. The properties of the liquid most relevant to atomization are density ρ_1, viscosity μ_1, and surface tension s. The liquid flow variables of importance are the velocity of the liquid jet or sheet U_1^*, and the boundary layer thickness in the liquid stream δ_1. The gas properties to be considered are density ρ_2, and viscosity μ_2. In addition, the following gas flow variables are important: the absolute gas velocity U_2^*, the relative gas-to-liquid velocity $\Delta U = U_2^* - U_1^*$, and the boundary layer thickness in the gas stream δ_2. The most important quantities are shown in Figure 1.4(b), which sketches the mean flow under consideration. Since the fluid properties and flow variables of both phases significantly influence the atomization process, the parameter range to be considered is quite large. However, it is possible to reduce the number of independent variables up to the following set of dimensionless quantities:

- For given flow conditions the Reynolds number R quantifies the relative importance of the inertial forces to viscous drag forces.
- The dimensionless surface tension parameter S (inverse Weber number) is the ratio of the surface tension of the liquid to inertial forces.
- A dimensionless relative velocity is defined by the ratio $M \equiv \Delta U/(2\bar{U})$, where ΔU is the velocity difference between the two streams, and $\bar{U} = (U_1^* + U_2^*)/2$ is their average velocity.
- Other dimensionless numbers are the ratios of densities $r = \rho_2/\rho_1$, dynamic viscosities $m = \mu_2/\mu_1$, and boundary layer thicknesses $n = \delta_2/\delta_1$ of the gas and liquid phases.

Strictly, gravity has to be taken into account as well, but both theoretical and experimental studies have demonstrated, that gravitational forces become negligibly small in gas-assisted atomization processes of practical interest [2, 37].

1.3 Previous Results for Linear Theory

In experiments a number of mean features of the flow in the atomization process are observed: Before the liquid is completely disintegrated into drops, the length of the liquid core and the opening angle of the spray can easily be measured [36]. In addition, the average drop size and the drop size distribution of the ultimate spray are of main interest [36, 39]. These features are related to the above dimensionless properties by a number of models. However, most of these involve significant simplifications and assumptions of uncertain validity, and are therefore limited. Although the complete process of atomization is highly nonlinear, linear stability analysis is frequently used to characterize the initial stage in the primary destabilization phase. In this context, a considerable number of works have addressed certain idealized configurations including most or all of the following assumptions [5]:

1. time-independent basic flow with parallel streamlines,
2. axisymmetric or two-dimensional perturbations,
3. inviscid flow,
4. temporal stability analysis.

The first assumption is almost universally adopted, since it reduces the stability problem to one inhomogeneous direction in space. In simple models the remaining constraints are assumed as well [36, 39, 56]. However, the relaxation of one of the above modelling assumptions has progressed incrementally: Studies including viscosity have been performed [6, 23, 61], in addition to considerations of spatially growing disturbances [1, 29, 33, 64]. Finally, transient growth of three-dimensional temporal perturbations was investigated as well [60].

Since only relaxed velocity profiles satisfy the assumption of an essentially time-independent mean flow in linear stability theory, in previous studies the basic velocity distribution was assumed to be monotonous in the cross-stream coordinate with the velocity increasing from the liquid to the gas side. In addition, parallel two-phase mixing layers have been frequently considered in the framework of two-dimensional temporal instability with real wave number. Moreover, since in the applications the Reynolds numbers are high, inviscid flow is frequently assumed, and piecewise-linear velocity profiles are often used for the explanation of the instability of parallel two-phase flow in atomization [39, 56]. The simplest example of a flow using all the assumptions 1.-4. is clearly that of a step-like basic profile with different uniform velocities U_1^* and U_2^* in the liquid and gas phases, and a jump in both density and velocity entirely located at the interface. This leads to the classical *Kelvin-Helmholtz instability* between different fluids, which can be treated analytically in the framework of hydrodynamic stability theory [18].

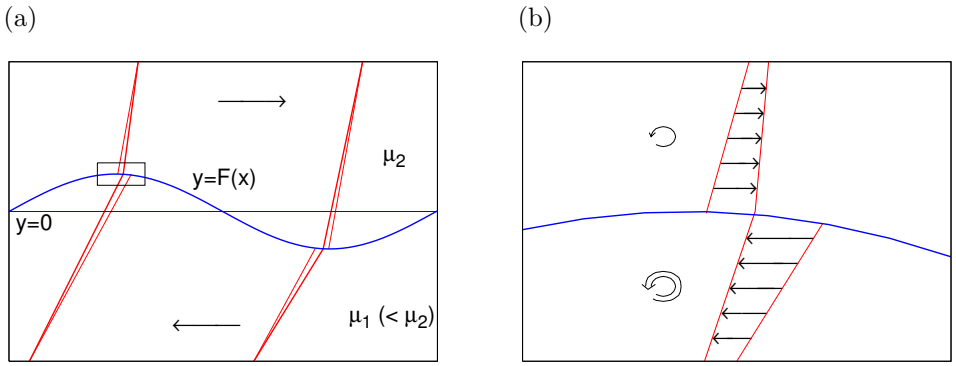

Figure 1.5: *(a) The horizontal velocity profiles. The thin curves represent the undisturbed shear, while the bold curves are the disturbed (i.e. undisturbed + disturbance) profiles; (b) blow up of region indicated in (a).*

The step-like basic flow can be extended by introducing a shear layer of finite thickness in which the velocity decreases linearly from U_2^* to U_1^*. This modification of the velocity profile accounts for the continuity of the mean flow. The presence of the shear layer, which is essentially located in the gaseous medium [49], modifies the Kelvin-Helmholtz instability at the liquid-gas interface, see References [39] and [56]. The wavelength of the interface deformation produced by the shear instability is $\lambda \sim \delta\sqrt{\rho_1/\rho_2}$ [39], and decreases with increasing gas velocity proportionally to the thickness of the shear layer, which is defined by the vorticity thickness [39]

$$\delta = \frac{U_{\max} - U_{\min}}{\frac{\partial U}{\partial y}|_{\max}}.$$

Various further modifications of the Kelvin-Helmholtz configuration have been studied. To name a few, one can introduce surface tension at the gas-liquid interface [50], one can consider several interfaces [12, 23], or confinement through parallel bounding walls [24, 25, 32, 33]. Most studies, however, are only performed in the inviscid context and depend on the broken-line velocity profile or on a smooth standard profile such as the hyperbolic tangent profile. If one wishes to take viscous effects into consideration in the stability analysis, i.e. to relax assumption 3., realistic viscous basic velocity profiles should include viscous boundary layers adjacent to the interface to satisfy both continuity of velocity and shear stress on the interface. These assumptions have been employed in previous temporal stability investigations for parallel steady unconfined flow [6, 61].

For the two-phase mixing layer flow inviscid models already predict instability. Such models therefore seem to be adequate when the Reynolds number is large. However, in addition to the inviscid Kelvin-Helmholtz instability mechanism due to shear, for moderate Reynolds numbers the *Tollmien-Schlichting mechanism* is significant. Tollmien-Schlichting waves are instabilities occuring in parallel shear flows, which are stable according to Rayleigh's inviscid criterion, but may become unstable in the presence of viscosity [52]. In addition, a third kind of instability can occur, which is neither inviscid nor of the Tollmien-Schlichting type and is addressed to the viscosity contrast at the interface separating the different fluid phases. This instability was first observed by Yih [63] and Hooper and Boyd [27] between two immiscible fluids in an unbounded shearing motion of plane Couette type,

$$U(y) = \begin{cases} U_1(y) = A_1 y, & y \le 0, \\ U_2(y) = A_2 y, & y \ge 0, \end{cases}$$

with respective viscosities μ_1 and μ_2. It was later explained by Hinch [26], and is therefore refered to as *H mode instability* by Boeck and Zaleski [6].

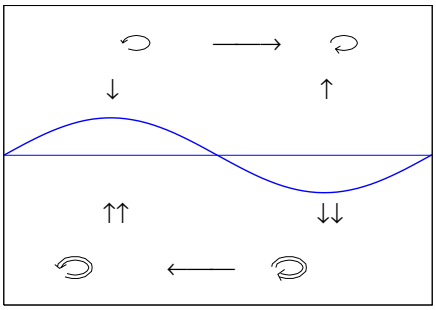

Figure 1.6: *Enhanced vertical motion of the interface due to the action of disturbance vorticity.*

In the basic flow the interface is flat, and, for example, the upper fluid is more viscous, i.e. $\mu_2 > \mu_1$. In addition, $U(y)$ satisfies the conditions of continuity of velocity and stress across the unperturbed interface $y = 0$, i.e.,

$$U_1(0) = U_2(0) \quad \text{and} \quad \mu_1 \frac{\partial U_1}{\partial y}(0) = \mu_2 \frac{\partial U_2}{\partial y}(0). \tag{1.1}$$

Therefore, $\mu_1 A_1 = \mu_2 A_2$ at $y = 0$. Now the interface is displaced by means of a small-amplitude wavelike perturbation of the form $y = F(x) = f\cos(\alpha x)$, see Figure 1.5(a). Consider a peak position of the perturbed interface. Here the undisturbed velocity of the upper fluid is slower than that of the lower fluid. Then, continuity of velocity at the interface requires an acceleration of the upper fluid on the perturbed interface while the lower fluid must slow down. Thus, horizontal disturbance velocities are induced, which are positive in the upper fluid and negative in the lower fluid. Since the disturbance velocities are maximum on the interface and decay away into the interior of the fluids, they can be converted into disturbance vorticities which are anticlockwise in both phases. This is shown in Figure 1.5(b). By an analogous consideration, the disturbance velocities at the troughs can be shown to be of opposite signs resulting into clockwise disturbance vorticities [26].
Differential advection of this vorticity distribution by the basic flow then creates small out-of-phase components of vorticity midway between the peaks and troughs. The vorticity component in the lower fluid induce an upward motion of the peaks and a downward motion of the troughs. On the other hand, in the upper fluid this vorticity induces the opposite motion. Because the viscous stresses match at the interface, the vorticity will be larger in the less viscous lower fluid. As a result the peaks will move up and the troughs down. Consequently the disturbance on the interface grows [26]. This is illustrated in Figure 1.6.

It is finally remarked, that the H mode instability mechanism described above is relevant to any situation in which a shear flow acts in the vicinity of a viscosity jump, since for sufficiently short waves any parallel shear flow having velocity components $(U_j(y), 0, 0)$, $\frac{\partial}{\partial y}U_j(0) \neq 0$, locally resembles plane Couette flow near the interface between the fluids [27].

1.4 Scope of Thesis

As already mentioned, the characteristics of liquid atomization by a fast gas stream at all stages, even the ultimate formation of a spray, depend strongly on the nature and properties of the initial stage of the atomization process, which is usually regarded as a shear-driven instability of a planar liquid-gas interface. In the framework of hydrodynamic stability theory, the characteristic features (length scales, growth rates and wave speeds) of such a process correspond to

those of the most amplified linear perturbations. However, none of the previous studies is fully capable in predicting all the characteristic features present in the initial state of the atomization process observed in experiments. For example, the measured growth rates are underpredicted by inviscid theory, but overpredicted by applying a viscous study of temporally growing disturbances [6]. The claim of the present work is to overcome the discrepancy between experiment and theory by adopting a viscous instability analysis of spatially growing disturbances, i.e. both assumptions 3. and 4. are relaxed.

In linear stability theory, whose basic equations and concepts are summarized in Chapter 2, the mean flow with known basic velocity profile is superimposed with small wavelike perturbations. On account of this assumption, in the governing equations all terms involving the square of the perturbation amplitude are neglected. In this context it is analyzed, how the growth of the perturbations on the liquid-gas interface in two-phase mixing layers is affected by various fluid properties, flow parameters, and also the basic velocity field itself, assuming that the interface is flat, i.e., not too far from the splitter lip. It should be noted again, that in a fully rigorous treatment a spatially developing, two-dimensional basic flow $U(x, y)$ should be studied, which depends on the downstream distance from the edge of the splitter plate. In the present work, however, the consequences of a given defect size is considered, and the problem is reduced using the standard parallel flow hypothesis. Then, for both viscous and inviscid theory the instability equations constitute a generalized eigenvalue problem. For given real values of flow parameters, only certain combinations of the dimensionless streamwise wave number α and the frequency ω will satisfy the boundary conditions and thus define an eigensolution [17, 52]. In general α and ω are complex. However, two special cases are of interest:

- For temporally growing waves, α is fixed and real. In this case the problem becomes linear in the complex eigenvalue $\omega = \omega_r + i\omega_i$, and the disturbances grow or decay with time depending on the sign of ω_i.

- In spatial instability calculations, the modes are given in terms of the complex wave number $\alpha = \alpha_r + i\alpha_i$, and the eigenvalue α appears nonlinearly in the governing equations up to the fourth power. This higher-order eigenvalue problem can subsequently be reduced to a linear one as shown in Section 3.4.

The eigenvalues resulting from either the temporal or spatial instability formulation are determined as the eigenvalues of linear algebraic equations. In inviscid theory these equations often take simple analytical forms for piecewise linear velocity distributions. Depending on the details of the problem, in the present work the dispersion relation for the streamfunction perturbations is a polynomial of third or fourth degree in the frequency ω, but transcendental in the wave number α. For temporal modes the dispersion relation is solved using MAPLE, whereas the eigenvalues for the spatial problem are obtained numerically for suitable initial values using Mathematica's *FindRoot* procedure, that is a variant of the secant method.
For viscous flows generally the dispersion relation cannot be given analytically, and the eigenvalues must be determined by means of appropriate numerical methods. In the present work, the linearized stability equations are solved numerically for two coupled layers in both temporal and spatial setting using expansions in Chebyshev polynomials. Finite Chebyshev expansions for the eigenfunctions are significantly more accurate than either finite-difference approximations, or expansions in other orthogonal polynomials. More precisely, when the solutions are infinitely differentiable, the order of accuracy of the Chebyshev polynomial solutions is $f(N) = O(N^{-p})$, as $N \to \infty$ [9, 11, 45]. Thus, the convergence is faster than any finite power of p. Therefore, Chebyshev series approximations are referred to as infinite order accurate.
The resulting generalized linear algebraic eigenvalue problem for the viscous stability problem is coded in FORTRAN and solved numerically using the LAPACK routine *ZGGEV* based on the QZ algorithm [21]. Chapter 3 summarizes the numerical methods used to solve the viscous eigenvalue problem. The codes for both temporally growing and spatially growing waves are

verified by recalculating results of previous studies. Some of these results are included in this chapter as well.

In previous works [6, 61], the basic velocity distribution was usually assumed to be monotonous in the cross-stream coordinate with the velocity progressively increasing from the liquid to the gas side. Consequently, the interface velocity is larger than the velocity of the slow liquid phase. From an experimental perspective, this is questionable because liquid and gas are separated by a splitter plate before coming into contact as free streams. Hence, in the present work the planar basic velocity distribution is modeled by taking into account the particular flow structure near the tip of the splitter plate: separated streams form boundary layers on the splitter plate, where the liquid and gas have zero velocity, causing a wake-like distribution once the streams come into contact. The mean velocity profile under consideration is sketched in Figure 1.4(b) for different distances downstream the splitter lip. A similar basic flow was used in an inviscid study by Koochesfahani and Frieler [34]. Their infinitely smooth basic velocity profile is composed of the hyperbolic tangent profile plus a wake component represented by a Gaussian distribution.

In order to compare with previous inviscid results, in Chapter 4 the instability of piecewise linear basic flow is considered for two broken-line velocity profiles, chosen to match increasingly more characteristic features of the velocity distribution sketched in Figure 1.4(b). The free stream velocities U_1^* and U_2^* have the same values in both cases, where generally $U_1^* < U_2^*$. However, the two families of broken-line profiles differ in the vicinity of the interface:

- In the piecewise linear basic flow of Section 4.2 the velocity at the interface is assumed to equal that in the liquid, i.e. $U_0^* = U_1^*$. Hence, the basic flow effectively includes only a boundary layer in the gas phase.
- Contrary, in the piecewise linear basic flow of Section 4.3 the interface velocity U_0^* can be chosen independently from the values in the free stream. As a result, boundary layers next to the interface are included in each fluid.

In terms of both temporal and spatial modes, for both velocity distributions the main interest is in the wave numbers, frequencies, and growth rates. Compared to instability results available in the literature a number of extensions is made, especially in the context of spatially growing disturbances. In addition, conditions for convective instability are identified.

However, since inviscid stability theory does neither describe unstable long-wave Tollmien-Schlichting modes due to the action of viscous Reynolds stresses, nor the short-wave H mode instability present in fully viscous studies, the inviscid piecewise approach is a generally inadequate model to apply to two-phase mixing layers [6, 61]. Therefore, viscous linear instability analysis is considered in Chapter 5.
For viscous problems the choices of basic velocity distributions are much more constrained as discussed at length in Section 5.1. In this work, the parallel viscous basic velocity profile is parametrized by a combination of error functions in each layer, where each of them is characterized by its boundary layer thickness and asymptotic velocity far away from the liquid-gas interface. In addition, a vorticity layer is introduced near both sides of the interface in order to mimick the finite thickness of the splitter plate, and also to maintain the shear balance. It leads to an additional parameter describing the velocity deficit at the interface relative to the free stream velocities in the liquid and gas phases; see Section 5.1.
From the solution of the linearized stability equations typically several unstable modes are found for a given set of parameters, and their driving instability mechanism is identified based on their Reynolds number dependence, structure and an energy budget. By that, contributions from the inviscid Kelvin-Helmholtz mechanism are identified, which can either involve both phases or act predominantly within a single phase. In addition, the Tollmien-Schlichting mechanism, and the viscosity-contrast or H mechanism to the unstable modes can be identified.

The temporal study in Section 5.3 is an extension of those by Boeck and Zaleski [6] for a basic flow without velocity defect, which is appropriate only after some distance from the splitter plate. It is shown how both the dimensionless parameters introduced in Section 1.2 and the structure of the basic velocity distribution modify the temporal stability properties. The spatial analysis is performed in Section 5.4. In addition, transition from convective to absolute instability is determined by computing generalized spatial branches; see Section 5.5.

In Chapter 6 the numerical results for both viscous and inviscid spatial theory are compared with experimental data available in the literature [39, 41]. It is shown that the growth rates and wavelengths observed in experiments can be predicted much better when applying a viscous study of spatially growing disturbances.

Finally, Chapter 7 summarizes the results of this work. In addition, conclusions are drawn and a brief outlook is given.

Chapter 2

Basic Equations and Concepts

The basic concepts of the linear theory of hydrodynamic stability were formulated in the 19th century by Kelvin, Rayleigh, Reynolds, Taylor and others. In the past this theory was widely applied to single-phase parallel shear flows, and a significant amount of results is summarized in several textbooks [13, 18, 31, 52]. On the other hand, for the stability of two-phase flow much less results are available, and increasingly more attention is shifted to this situation.

In Section 2.1 the linearized equations governing the growth or decay of wavelike perturbations in a flow of two superimposed layers of different immiscible, incompressible, Newtonian fluids are derived in the framework of both viscous and inviscid theory. Thereafter, by neglecting one of the layers, the instability problem for two-fluid flow is reduced to result into those for a single fluid only. In comparison with the case of a homogeneous fluid the existence of Squire's theorem for two-fluid flow is discussed in Section 2.3. Next, temporally and spatially growing perturbations are considered in Section 2.4. In both cases, for two-dimensional disturbances the linear energy rate equation is given in Section 2.5. Based on this equation the driving instability mechanism of the several unstable modes found in two-fluid flows can be identified. Finally, Section 2.6 summarizes the local instabiliy concepts including those of convective and absolute instability, and their detection by means of generalized spatial branches.

2.1 Linear Equations of Two-Fluid Instability

2.1.1 The Linearized Problem for Viscous Parallel Two-Fluid Flow

A flow of two superimposed layers of different immiscible, incompressible, Newtonian fluids, labeled $j = 1, 2$, with densities ρ_1, ρ_2, kinematic viscosities ν_1, ν_2, and surface tension s at the interface is considered in a given domain. At a given point $\hat{\vec{x}} = (\hat{x}, \hat{y}, \hat{z})$ and time $\hat{t}$ the velocity and pressure are

- $\hat{\vec{u}}_1 = (\hat{u}_1, \hat{v}_1, \hat{w}_1)$ and $\hat{p}_1$ in fluid 1,
- $\hat{\vec{u}}_2 = (\hat{u}_2, \hat{v}_2, \hat{w}_2)$ and $\hat{p}_2$ in fluid 2.

Then the flow in each layer is governed by the incompressible Navier-Stokes equations,

$$\frac{\partial \hat{\vec{u}}_j}{\partial \hat{t}} + \hat{\vec{u}}_j \cdot \hat{\nabla} \hat{\vec{u}}_j = -\frac{1}{\rho_j} \hat{\nabla} \hat{p}_j + \nu_j \hat{\Delta} \hat{\vec{u}}_j, \tag{2.1}$$

the equation of continuity,

$$\hat{\nabla} \cdot \hat{\vec{u}}_j = 0, \tag{2.2}$$

$j = 1, 2$, and certain boundary conditions. On the left-hand side of the dynamical equation (2.1) the first expression characterizes the acceleration of a fluid particle due to an explicit temporal change of its velocity, while the second term describes the change in velocity due to the motion of the fluid particle itself relative to the velocity field. In addition, the right-hand side terms characterize pressure forces of normal stresses and viscosity forces due to the deformation of fluid elements.
Suppose that the above equations have a certain solution (or approximate solution) for given boundary conditions. This solution describes a steady basic flow whose stability is of interest. The basic flow is specified by the velocity field $\hat{\vec{U}} = \left(\hat{\vec{U}}_1, \hat{\vec{U}}_2\right)$, where $\hat{\vec{U}}_j = \left(\hat{U}_j, \hat{V}_j, \hat{W}_j\right)$, $j = 1, 2$, and the pressure field $\hat{P} = \left(\hat{P}_1, \hat{P}_2\right)$ of an incompressible viscous fluid. It is convenient to choose dimensionless variables. Let L and U^* be some characteristic length and velocity scale of the basic flow. Then dimensionless variables such as

$$\vec{x} = \frac{\hat{\vec{x}}}{L}, \qquad \vec{u}_j = \frac{\hat{\vec{u}}_j}{U^*}, \qquad p_j = \frac{\hat{p}_j}{\rho_2 U^{*2}}, \qquad t = \frac{U^*}{L}\hat{t}$$

are defined, and the Reynolds number,

$$R = \frac{U^* L}{\nu_2} = \frac{\rho_2 U^* L}{\mu_2}, \tag{2.3}$$

characterizes the ratio of nonlinear to viscous terms. R is based on the properties of fluid 2. However, there is also an analogous Reynolds number $R_1 = U^* L/\nu_1$ based on fluid 1. It is related to R by the relation $R_1 = (m/r)R$, where

$$r = \frac{\rho_2}{\rho_1} \quad \text{and} \quad m = \frac{\mu_2}{\mu_1} = \frac{\rho_2 \nu_2}{\rho_1 \nu_1} \tag{2.4}$$

denote the ratios of densities and dynamic viscosities, respectively. In equations (2.1), (2.2), the velocity and pressure fields are written as the time-independent primary flow plus time-dependent perturbation quantities $\vec{u}'_j = \left(u'_j, v'_j, w'_j\right)$ and p'_j, i.e.,

$$\vec{u}_j = \vec{U}_j + \vec{u}'_j \quad \text{and} \quad p_j = P_j + p'_j, \qquad j = 1, 2. \tag{2.5}$$

Since the definition of stability concerns the evolution of small perturbations, stability is investigated by neglecting products of the perturbed quantities and their derivatives in the equations of motion. This gives the linearized problem,

$$\frac{\partial \vec{u}'_1}{\partial t} + \vec{U}_1 \cdot \nabla \vec{u}'_1 + \vec{u}'_1 \cdot \nabla \vec{U}_1 = -\nabla p'_1 + \frac{r}{mR} \Delta \vec{u}'_1, \tag{2.6}$$

$$\nabla \cdot \vec{u}'_1 = 0 \tag{2.7}$$

for fluid 1. Analogous, for fluid 2 one obtains

$$\frac{\partial \vec{u}'_2}{\partial t} + \vec{U}_2 \cdot \nabla \vec{u}'_2 + \vec{u}'_2 \cdot \nabla \vec{U}_2 = -\nabla p'_2 + \frac{1}{R} \Delta \vec{u}'_2, \tag{2.8}$$

$$\nabla \cdot \vec{u}'_2 = 0. \tag{2.9}$$

The $'$, denoting the perturbation quantities in equations (2.6)-(2.9), are neglected from now on. In addition, parallel flow is assumed, i.e., a flow in the x-direction that varies with y only. Thus the basic velocity profile is independent of x and z,

$$\frac{\partial U_j}{\partial x} = \frac{\partial U_j}{\partial z} = 0, \qquad j = 1, 2. \tag{2.10}$$

In the case of laminar flow, the velocity profiles $U_1(y)$, $y \leq 0$, and $U_2(y)$, $y \geq 0$, can be calculated exactly. However, when the flow in one of the two phases is turbulent, a 'quasi-steady' description of the flow in that phase may be used, i.e., the velocity profile is assumed to be given by its time-averaged value. Further, in the primary flow the interface separating the two immiscible layers is flat. In addition, the basic flow satisfies the continuity of velocity and stress across the unperturbed interface $y = 0$, i.e. relations (1.1) hold:

$$U_1(0) = U_2(0) \quad \text{and} \quad \mu_1 \frac{\partial U_1}{\partial y}(0) = \mu_2 \frac{\partial U_2}{\partial y}(0).$$

Since $\vec{U}_j = (U_j(y), 0, 0)$, $j = 1, 2$, equations (2.6), (2.7) for the lower layer read

$$\frac{\partial u_1}{\partial t} + U_1 \frac{\partial u_1}{\partial x} + v_1 \frac{\partial U_1}{\partial y} = -\frac{\partial p_1}{\partial x} + \frac{r}{mR}\left(\frac{\partial^2}{\partial x^2} + \frac{\partial^2}{\partial y^2} + \frac{\partial^2}{\partial z^2}\right) u_1, \tag{2.11}$$

$$\frac{\partial v_1}{\partial t} + U_1 \frac{\partial v_1}{\partial x} = -\frac{\partial p_1}{\partial y} + \frac{r}{mR}\left(\frac{\partial^2}{\partial x^2} + \frac{\partial^2}{\partial y^2} + \frac{\partial^2}{\partial z^2}\right) v_1, \tag{2.12}$$

$$\frac{\partial w_1}{\partial t} + U_1 \frac{\partial w_1}{\partial x} = -\frac{\partial p_1}{\partial z} + \frac{r}{mR}\left(\frac{\partial^2}{\partial x^2} + \frac{\partial^2}{\partial y^2} + \frac{\partial^2}{\partial z^2}\right) w_1, \tag{2.13}$$

$$\frac{\partial u_1}{\partial x} + \frac{\partial v_1}{\partial y} + \frac{\partial w_1}{\partial z} = 0. \tag{2.14}$$

Next, consider relation $\frac{\partial^2}{\partial y \partial z}(2.13) - \frac{\partial^2}{\partial z^2}(2.12) - \frac{\partial^2}{\partial x^2}(2.12) + \frac{\partial^2}{\partial x \partial y}(2.11)$. Then the sum of all pressure terms is zero. Using the equation of continuity (2.14), and assuming that the basic velocity profile is parallel yields an equation for the normal velocity v_1,

$$\left(\frac{\partial}{\partial t} + U_1 \frac{\partial}{\partial x}\right) \Delta v_1 - U_1'' \frac{\partial v_1}{\partial x} = \frac{r}{mR} \Delta \left(\Delta v_1\right), \qquad y \leq 0, \tag{2.15}$$

where $' \equiv \partial/\partial y$ is used from now on. An analogous equation can be obtained for v_2:

$$\left(\frac{\partial}{\partial t} + U_2 \frac{\partial}{\partial x}\right) \Delta v_2 - U_2'' \frac{\partial v_2}{\partial x} = \frac{1}{R} \Delta \left(\Delta v_2\right), \qquad y \geq 0. \tag{2.16}$$

To describe the complete three-dimensional flow field, additionally the equations for the normal vorticities

$$\eta_j = \frac{\partial u_j}{\partial z} - \frac{\partial w_j}{\partial x}, \qquad j = 1, 2,$$

are required. Consider relation $\frac{\partial}{\partial z}(2.11) - \frac{\partial}{\partial x}(2.13)$. Again the pressure terms vanish, and one obtains

$$\left(\frac{\partial}{\partial t} + U_1 \frac{\partial}{\partial x}\right) \eta_1 + U_1' \frac{\partial v_1}{\partial z} = \frac{r}{mR} \Delta \eta_1, \qquad y \leq 0. \tag{2.17}$$

Similarly, for η_2 one has

$$\left(\frac{\partial}{\partial t} + U_2 \frac{\partial}{\partial x}\right) \eta_2 + U_2' \frac{\partial v_2}{\partial z} = \frac{1}{R} \Delta \eta_2, \qquad y \geq 0. \tag{2.18}$$

Equations (2.15)-(2.18) together with the initial conditions

$$v_j(x, y, z, t = 0) = v_0^{(j)}(x, y, z), \tag{2.19}$$

$$\eta_j(x, y, z, t = 0) = \eta_0^{(j)}(x, y, z), \qquad j = 1, 2, \tag{2.20}$$

and appropriate boundary conditions form a complete description of the evolution of an arbitrary infinitesimal disturbance in the viscous flow in both space and time. Since $\vec{U} = \left(\vec{U}_1, \vec{U}_2\right)$ is

independent of all x, z and t for a parallel, steady basic flow, all coefficients of the linearized partial differential system are constants. It follows plausibly that the variables may be separated, so that the general solution of an initial-value problem can be written as a linear superposition of normal modes. Thus wavelike solutions of the form

$$v_j(x,y,z,t) = \phi_j(y)\exp[i(\alpha x + \beta z - \omega t)], \tag{2.21}$$

$$\eta_j(x,y,z,t) = \tilde{\eta_j}(y)\exp[i(\alpha x + \beta z - \omega t)], \qquad j = 1,2, \tag{2.22}$$

are introduced, where ω is the frequency, α and β denote the streamwise and spanwise wave numbers, respectively, and $k^2 = \alpha^2 + \beta^2$. Substituting (2.21) and (2.22) into (2.15)-(2.18), and neglecting all symbols $\tilde{}$, one obtains

$$\left[(-i\omega + i\alpha U_1)\left(\frac{\partial^2}{\partial y^2} - k^2\right) - \frac{r}{mR}\left(\frac{\partial^2}{\partial y^2} - k^2\right)^2 - i\alpha U_1''\right]\phi_1 = 0, \tag{2.23}$$

$$\left[(-i\omega + i\alpha U_1) - \frac{r}{mR}\left(\frac{\partial^2}{\partial y^2} - k^2\right)\right]\eta_1 = -i\beta U_1'\phi_1, \qquad y \le 0, \tag{2.24}$$

$$\left[(-i\omega + i\alpha U_2)\left(\frac{\partial^2}{\partial y^2} - k^2\right) - \frac{1}{R}\left(\frac{\partial^2}{\partial y^2} - k^2\right)^2 - i\alpha U_2''\right]\phi_2 = 0, \tag{2.25}$$

$$\left[(-i\omega + i\alpha U_2) - \frac{1}{R}\left(\frac{\partial^2}{\partial y^2} - k^2\right)\right]\eta_2 = -i\beta U_2'\phi_2, \qquad y \ge 0. \tag{2.26}$$

Relations (2.23) and (2.25) are the Orr-Sommerfeld equations in fluid 1 and 2, respectively, whereas (2.24) and (2.26) are the Squire equations in the respective layers. Together relations (2.23)-(2.26) are two systems of fourth- and second-order differential equations each. Therefore twelve boundary conditions are required.

First, the boundary conditions imposing a perturbation decay at the rigid channel walls or in the far field at infinity are

$$\phi_1 = \frac{\partial\phi_1}{\partial y} = \eta_1 = 0 \quad \text{at the lower boundary} \quad y = -L_1, \tag{2.27}$$

$$\phi_2 = \frac{\partial\phi_2}{\partial y} = \eta_2 = 0 \quad \text{at the upper boundary} \quad y = L_2. \tag{2.28}$$

Thus, unbounded flow is described by considering it as a limiting case of bounded flow, i.e., the layer thicknesses L_1 and L_2 are chosen to take very large values.

In addition, the interface conditions coupling the two phases need to be imposed. Formally, they must be evaluated at the location of the interface in the disturbed flow $y = \hat{f}(x,z,t)$. However, instead the interface conditions can be given at the originally flat interface by means of a Taylor expansion in $\hat{f}$ around $y = 0$. When the interface is perturbed by a small-amplitude wave from $y = 0$ to $y = f_{3D}\exp[i(\alpha x + \beta z - \omega t)]$, the kinematic condition for the interface gives

$$f_{3D} = if \quad \text{with} \quad f = \frac{\phi_1(0)}{\omega - \alpha U_0}, \tag{2.29}$$

where $U_0 = U_1(0) = U_2(0)$. The continuity of cross-stream, streamwise, and spanwise velocities at the interface reads as

$$\phi_1 = \phi_2, \tag{2.30}$$

$$\phi_1' - \phi_2' = \alpha(U_2' - U_1')f, \tag{2.31}$$

and

$$\eta_1 - \eta_2 = \beta(U_1' - U_2')f. \tag{2.32}$$

The continuity of tangential stresses gives

$$\left(\frac{\partial^2}{\partial y^2}+k^2\right)\phi_1+\alpha U_1''f=m\left[\left(\frac{\partial^2}{\partial y^2}+k^2\right)\phi_2+\alpha U_2''f\right], \tag{2.33}$$

$$\eta_1'-\beta U_1''f=m\left[\eta_2'-\beta U_2''f\right]. \tag{2.34}$$

Finally, continuity of normal stresses imposes

$$\begin{aligned}&\frac{1}{imR}(\phi_1'''-3k^2\phi_1')+\frac{1}{r}[\alpha U_1'\phi_1+(\omega-\alpha U_0)\phi_1']\\&\quad-\frac{1}{iR}(\phi_2'''-3k^2\phi_2')-\alpha U_2'\phi_2-(\omega-\alpha U_0)\phi_2'\;=\;k^2[F+k^2S]f.\end{aligned} \tag{2.35}$$

The dimensionless expressions

$$S=\frac{s}{\rho_2 U^{*2}L}\quad\text{ and }\quad F=\frac{(\rho_1-\rho_2)}{\rho_2}\frac{gL}{U^{*2}} \tag{2.36}$$

represent the physical effects of interfacial tension s, and gravity g, respectively. A detailed derivation of conditions (2.29)-(2.35) is given below.

Derivation of the Interface Conditions

First, the three-dimensional stress tensors for incompressible Newtonian fluids in terms of dimensionless quantities are defined as

$$\sigma_k=\begin{bmatrix}\sigma_{11}^{(k)}&\sigma_{12}^{(k)}&\sigma_{13}^{(k)}\\ \sigma_{21}^{(k)}&\sigma_{22}^{(k)}&\sigma_{23}^{(k)}\\ \sigma_{31}^{(k)}&\sigma_{32}^{(k)}&\sigma_{33}^{(k)}\end{bmatrix},\qquad k=1,2,$$

where

$$\begin{aligned}\sigma_{ij}^{(1)}&=-\frac{1}{r}(P_1+p_1)\delta_{ij}+\frac{1}{mR}\left(\frac{\partial(U_{1i}+u_{1i})}{\partial x_j}+\frac{\partial(U_{1j}+u_{1j})}{\partial x_i}\right),\\ \sigma_{ij}^{(2)}&=-(P_2+p_2)\delta_{ij}+\frac{1}{R}\left(\frac{\partial(U_{2i}+u_{2i})}{\partial x_j}+\frac{\partial(U_{2j}+u_{2j})}{\partial x_i}\right),\qquad i,j=1,2,3.\end{aligned}$$

Here $(x_1,x_2,x_3)=(x,y,z)$, $(u_{k1},u_{k2},u_{k3})=(u_k,v_k,w_k)$, $(U_{k1},U_{k2},U_{k3})=(U_k,V_k,W_k)$ with $V_k=W_k=0$, where the subscript $k=1,2$ refers to the phase. At the interface the velocity components are continuous,

$$U_1+u_1=U_2+u_2, \tag{2.37}$$

$$v_1=v_2, \tag{2.38}$$

$$w_1=w_2. \tag{2.39}$$

Further, the shear stresses in both phases are equal at the interface, and the normal stresses balance the surface tension. There is also a kinematic condition which states that the fluid elements on the interface remain there, i.e., the velocity of the fluid particles normal to the interface equals those of the interface. Beginning with the kinematic equation, define $\hat{f}(x,z,t)$ as the normal displacement of the interface from the equilibrium position. Then

$$\frac{D\hat{f}}{Dt}=v\quad\text{ at }\quad y=\hat{f}(x,z,t),$$

where D/Dt is the substantial derivative. Linearizing the above for small displacements, and using (2.38), one obtains

$$\left(\frac{\partial}{\partial t}+U_0\frac{\partial}{\partial x}\right)\hat{f}=v_1(0)=v_2(0). \tag{2.40}$$

Assuming the interface displacement to be of the form

$$\hat{f}(x,z,t) = f_{3D}\exp[i(\alpha x + \beta z - \omega t)], \tag{2.41}$$

the kinematic condition (2.40) reads as (2.29). In addition, (2.38) readily yields (2.30). Next, the unit surface normal $\vec{n}$ is given by

$$\vec{n} = [n_1, n_2, n_3]^T = \frac{\nabla\hat{F}}{|\nabla\hat{F}|} = \frac{\left[-\hat{f}_x, 1, -\hat{f}_z\right]^T}{\sqrt{\hat{f}_x^2 + 1 + \hat{f}_z^2}}, \tag{2.42}$$

because $\vec{n} \sim \nabla\hat{F}$, and the surface is described by $\hat{F}(x,y,z,t) = y - \hat{f}(x,z,t) = 0$. In the above equation the subscripts represent the partial derivatives of the surface displacement. Linearizing for small surface displacements, (2.42) becomes

$$\vec{n} = [n_1, n_2, n_3]^T = \left[-\frac{\partial\hat{f}}{\partial x}, 1, -\frac{\partial\hat{f}}{\partial z}\right]^T.$$

The stress vectors are given by

$$\vec{t_k} = \begin{bmatrix} \sigma_{11}^{(k)}n_1 + \sigma_{12}^{(k)}n_2 + \sigma_{13}^{(k)}n_3 \\ \sigma_{21}^{(k)}n_1 + \sigma_{22}^{(k)}n_2 + \sigma_{23}^{(k)}n_3 \\ \sigma_{31}^{(k)}n_1 + \sigma_{32}^{(k)}n_2 + \sigma_{33}^{(k)}n_3 \end{bmatrix}, \qquad k = 1, 2.$$

Then, the interface conditions of shear stresses are

$$\vec{t_1} - (\vec{n}^T\sigma_1\vec{n})\vec{n} = \vec{t_2} - (\vec{n}^T\sigma_2\vec{n})\vec{n}.$$

Thus, in linearized form the components read

$$\frac{1}{mR}\left(\frac{\partial v_1}{\partial x} + \frac{\partial U_1}{\partial y} + \frac{\partial u_1}{\partial y}\right) = \frac{1}{R}\left(\frac{\partial v_2}{\partial x} + \frac{\partial U_2}{\partial y} + \frac{\partial u_2}{\partial y}\right), \tag{2.43}$$

$$\frac{1}{mR}\frac{\partial U_1}{\partial y}\frac{\partial\hat{f}}{\partial x} = \frac{1}{R}\frac{\partial U_2}{\partial y}\frac{\partial\hat{f}}{\partial x}, \tag{2.44}$$

$$\frac{1}{mR}\left(\frac{\partial v_1}{\partial z} + \frac{\partial w_1}{\partial y}\right) = \frac{1}{R}\left(\frac{\partial v_2}{\partial z} + \frac{\partial w_2}{\partial y}\right). \tag{2.45}$$

Note that (2.44) reduces to the shear stress condition on the basic velocity profile at the interface,

$$\frac{\partial U_1}{\partial y}(0) = m\frac{\partial U_2}{\partial y}(0), \tag{2.46}$$

that was already given in (1.1). Finally, the balance between the normal stresses and the surface tension S is given by

$$\vec{n}^T\sigma_2\vec{n} - \vec{n}^T\sigma_1\vec{n} = S(\nabla\cdot\vec{n}).$$

The term $\nabla\cdot\vec{n}$ is equal to the sum of the inverse of each of the two principal radii of curvature, $\nabla\cdot\vec{n} = -\hat{f}_{xx}^2 - \hat{f}_{zz}^2$. Using (2.46), the above relation in linearized form reads

$$-(P_2 + p_2) + \frac{2}{R}\frac{\partial v_2}{\partial y} + \frac{1}{r}(P_1 + p_1) - \frac{2}{mR}\frac{\partial v_1}{\partial y} = -S\left(\frac{\partial^2}{\partial x^2} + \frac{\partial^2}{\partial z^2}\right)\hat{f}. \tag{2.47}$$

Formally, the interface conditions must be evaluated at the location of the interface in the disturbed flow $y = \hat{f}(x,z,t)$ instead at $y = 0$, because the gradients of both shear stress and

pressure of the primary flow are not zero at the originally flat interface $y = 0$. However, the interfacial conditions can be transferred to $y = 0$ by means of Taylor series expansions in $\hat{f}$ around $y = 0$. Taking only terms up to the first derivative into account,

$$U_k(\hat{f}) = U_k(0) + \hat{f}\ \frac{\partial U_k}{\partial y}(0), \qquad k = 1, 2. \tag{2.48}$$

Using the equations of continuity in each fluid, u_k and w_k can be written in terms of the normal velocities v_k and the normal vorticites $\eta_k = \partial u_k/\partial z - \partial w_k/\partial x$ via

$$\left(\frac{\partial^2}{\partial x^2} + \frac{\partial^2}{\partial z^2}\right) u_k = -\frac{\partial^2 v_k}{\partial x \partial y} + \frac{\partial \eta_k}{\partial z},$$
$$\left(\frac{\partial^2}{\partial x^2} + \frac{\partial^2}{\partial z^2}\right) w_k = -\frac{\partial^2 v_k}{\partial y \partial z} - \frac{\partial \eta_k}{\partial x}, \qquad k = 1, 2.$$

When applying the Taylor expansion (2.48) of the basic flow in $\hat{f}$ around $y = 0$ in addition to the normal modes (2.21), (2.22), (2.41), using $U_1(0) = U_2(0)$, and multiplying with $k^2 = \alpha^2 + \beta^2$, the interface condition (2.37) of continuity of the streamwise velocity u in terms of v_k and η_k correct to the leading order in f takes the form

$$\alpha(\phi_1' - \phi_2') - \beta(\eta_1 - \eta_2) = k^2(U_2' - U_1')f. \tag{2.49}$$

Analogous, the interface condition (2.39) of continuity of the the cross-stream velocity w after some manipulations gives

$$\beta(\phi_1' - \phi_2') = \alpha(\eta_2 - \eta_1). \tag{2.50}$$

Instead of conditions (2.49), (2.50) it is possible to impose (2.31) and (2.32). These sets of equations are equivalent, because the conditions (2.49) and (2.50) can be easily derived from $\alpha(2.31) - \beta(2.32)$ and $\beta(2.31) + \alpha(2.32)$, respectively.

When applying the Taylor expansion (2.48) of the basic flow in $\hat{f}$ around $y = 0$ in addition to the normal modes (2.21), (2.22) and (2.41), using the shear stress condition on the basic velocity profile at the interface (2.46), and multiplying with k^2, the condition (2.43) of continuity of stress at the interface in the x direction in terms of v_k and η_k correct to the leading order in f reads

$$\alpha\left(\frac{\partial^2}{\partial y^2} + k^2\right)\phi_1 - \beta\eta_1' - k^2 U_1'' f = m\left[\alpha\left(\frac{\partial^2}{\partial y^2} + k^2\right)\phi_2 - \beta\eta_2' - k^2 U_2'' f\right]. \tag{2.51}$$

Analogous, the interface condition (2.45) of continuity of stress at the interface in the z direction finally reads

$$\beta\left(\frac{\partial^2}{\partial y^2} + k^2\right)\phi_1 + \alpha\eta_1' = m\left[\beta\left(\frac{\partial^2}{\partial y^2} + k^2\right)\phi_2 + \alpha\eta_2'\right]. \tag{2.52}$$

Instead of relations (2.51), (2.52), it is possible to impose the conditions (2.33) and (2.34). These sets of equations are equivalent, because (2.51) and (2.52) can be easily derived from equations $\alpha(2.33) - \beta(2.34)$ and $\beta(2.33) + \alpha(2.34)$, respectively.

Finally the condition for continuity of normal stress (2.47) is considered. When expanding the basic pressure in $\hat{f}$ around $y = 0$ in terms of a Taylor series and using the relations

$$\frac{1}{r}P_1(0) = P_2(0) \quad \text{and} \quad \frac{\partial P_2}{\partial y}(0) - \frac{1}{r}\frac{\partial P_1}{\partial y}(0) = \frac{g d_2}{U^{*2}}\left(1 - \frac{1}{r}\right) \equiv -F,$$

the normal stress interface condition takes the form

$$-p_2 + \frac{1}{r}\ p_1 - F\hat{f} + \frac{2}{R}\frac{\partial v_2}{\partial y} - \frac{2}{mR}\frac{\partial v_1}{\partial y} = -S\left(\frac{\partial^2}{\partial x^2} + \frac{\partial^2}{\partial z^2}\right)\hat{f}. \tag{2.53}$$

Consider the Navier-Stokes equation in the lower fluid in components. Then $\frac{\partial}{\partial x}(2.11)+\frac{\partial}{\partial z}(2.13)$ together with the equation of continuity (2.14) yields

$$-\left(\frac{\partial}{\partial t}+U_1\frac{\partial}{\partial x}\right)\frac{\partial v_1}{\partial y}+\frac{\partial U_1}{\partial y}\frac{\partial v_1}{\partial x}=-\left(\frac{\partial^2}{\partial x^2}+\frac{\partial^2}{\partial z^2}\right)p_1-\frac{r}{mR}\frac{\partial}{\partial y}\Delta v_1. \tag{2.54}$$

An analogous expression is obtained for the upper layer:

$$-\left(\frac{\partial}{\partial t}+U_2\frac{\partial}{\partial x}\right)\frac{\partial v_2}{\partial y}+\frac{\partial U_2}{\partial y}\frac{\partial v_2}{\partial x}=-\left(\frac{\partial^2}{\partial x^2}+\frac{\partial^2}{\partial z^2}\right)p_2-\frac{1}{R}\frac{\partial}{\partial y}\Delta v_2. \tag{2.55}$$

Using these relations in equation $\left(\frac{\partial^2}{\partial x^2}+\frac{\partial^2}{\partial z^2}\right)(2.53)$, the pressure is eliminated. The result is

$$\begin{aligned}&\left[\frac{1}{R}\Delta v_2'-\left(\frac{\partial}{\partial t}+U_2\frac{\partial}{\partial x}\right)v_2'+U_2'\,\frac{\partial v_2}{\partial x}\right]-\frac{1}{r}\left[\frac{r}{mR}\Delta v_1'-\left(\frac{\partial}{\partial t}+U_1\frac{\partial}{\partial x}\right)v_1'+U_1'\,\frac{\partial v_1}{\partial x}\right]\\&\quad+\frac{2}{R}\left(\frac{\partial^2}{\partial x^2}+\frac{\partial^2}{\partial z^2}\right)\left[v_2'-\frac{1}{m}\,v_1'\right]=\left[F-S\left(\frac{\partial^2}{\partial x^2}+\frac{\partial^2}{\partial z^2}\right)\right]\left(\frac{\partial^2}{\partial x^2}+\frac{\partial^2}{\partial z^2}\right)\hat{f}.\end{aligned}$$

By applying normal modes in v_1, v_2, and $\hat{f}$ given by (2.21) and (2.41), the final form of the normal stress interface condition (2.35) is obtained.

Note finally, that when non-dimensionalization is performed with respect to fluid 1, in the governing ordinary differential equations and boundary conditions (2.23)-(2.35) the indices are interchanged and $1/r$, $1/m$ are replaced by r, m.

2.1.2 Two-dimensional Perturbations

For describing the flow field in two dimensions the z direction is neglected, and perturbations about the given basic flow are assumed in the form of streamfunctions ψ_j, $j=1,2$. The streamwise and cross-stream velocity components u_j and v_j in the Navier-Stokes equations are defined by

$$u_j=\frac{\partial\psi_j}{\partial y}\quad\text{and}\quad v_j=-\frac{\partial\psi_j}{\partial x},\qquad j=1,2. \tag{2.56}$$

Thus, in both layers the equation of continuity is automatically fullfilled. Because the primary flow only depends on the y-coordinate, the streamfunctions are assumed to take the form of normal modes:

$$\psi_j(x,y,t)=\phi_j(y)\exp[i(\alpha x-\omega t)],\qquad j=1,2. \tag{2.57}$$

Substitution of (2.57) into the linearized two-dimensional Navier-Stokes equations results in the Orr-Sommerfeld equations for the y-dependent functions $\phi_j(y)$,

$$\left[(-i\omega+i\alpha U_1)\left(\frac{\partial^2}{\partial y^2}-\alpha^2\right)-\frac{r}{mR}\left(\frac{\partial^2}{\partial y^2}-\alpha^2\right)^2-i\alpha U_1''\right]\phi_1=0,\qquad y\le 0, \tag{2.58}$$

$$\left[(-i\omega+i\alpha U_2)\left(\frac{\partial^2}{\partial y^2}-\alpha^2\right)-\frac{1}{R}\left(\frac{\partial^2}{\partial y^2}-\alpha^2\right)^2-i\alpha U_2''\right]\phi_2=0,\qquad y\ge 0, \tag{2.59}$$

i.e., equations (2.23) and (2.25) with $\beta=0$. Since (2.58), (2.59) are two fourth-order differential equations, eight boundary conditions are required. First, the conditions imposing a perturbation decay at the rigid channel walls or in the far field at infinity are

$$\phi_1=\frac{\partial\phi_1}{\partial y}=0\quad\text{at the lower boundary}\;\; y=-L_1, \tag{2.60}$$

$$\phi_2 = \frac{\partial \phi_2}{\partial y} = 0 \quad \text{at the upper boundary} \;\; y = L_2. \tag{2.61}$$

In addition, the interface conditions of continuity of the velocity and stress components coupling the two phases are imposed:

$$U_1 + u_1 = U_2 + u_2,$$

$$v_1 = v_2,$$

$$\frac{1}{mR}\left(\frac{\partial v_1}{\partial x} + \frac{\partial U_1}{\partial y} + \frac{\partial u_1}{\partial y}\right) = \frac{1}{R}\left(\frac{\partial v_2}{\partial x} + \frac{\partial U_2}{\partial y} + \frac{\partial u_2}{\partial y}\right),$$

$$-(P_2 + p_2) + \frac{2}{R}\frac{\partial v_2}{\partial y} + \frac{1}{r}(P_1 + p_1) - \frac{2}{mR}\frac{\partial v_1}{\partial y} = -S\frac{\partial^2 \hat{f}}{\partial x^2}.$$

The derivation of the interface conditions in terms of normal modes of the streamfunctions ψ_j defined in (2.57) is similar as in the three-dimensional case. The interface originally at $y = 0$ is perturbed to $\hat{f}(x,t) = f_{2D}\exp[i(\alpha x - \omega t)]$. Similar as for three-dimensional perturbations the above conditions can be evaluated at the unperturbed interface by means of a Taylor expansion in $\hat{f}$ around $y = 0$. Then the kinematic condition for the interface gives

$$f_{2D} = \alpha f \quad \text{with} \quad f = \frac{\phi_1(0)}{\omega - \alpha U_0}, \tag{2.62}$$

where $U_0 = U_1(0) = U_2(0)$. The continuity of cross-stream and streamwise velocities at the interface read as

$$\phi_1 = \phi_2, \tag{2.63}$$

and

$$\phi_1' - \phi_2' = \alpha[U_2' - U_1']f. \tag{2.64}$$

The continuity of tangential stresses gives

$$\left(\frac{\partial^2}{\partial y^2} + \alpha^2\right)\phi_1 + \alpha U_1'' f = m\left[\left(\frac{\partial^2}{\partial y^2} + \alpha^2\right)\phi_2 + \alpha U_2'' f\right]. \tag{2.65}$$

Finally, continuity of normal stresses imposes

$$\begin{aligned}\frac{1}{imR}(\phi_1''' - 3\alpha^2\phi_1') + \frac{1}{r}[\alpha U_1'\phi_1 + (\omega - \alpha U_0)\phi_1'] \\ -\frac{1}{iR}(\phi_2''' - 3\alpha^2\phi_2') - \alpha U_2'\phi_2 - (\omega - \alpha U_0)\phi_2' \;=\; \alpha^2[F + \alpha^2 S]f.\end{aligned} \tag{2.66}$$

When non-dimensionalization is performed with respect to fluid 1, in the governing ordinary differential equations and boundary conditions (2.58)-(2.66) the indices are interchanged and $1/r$, $1/m$ are replaced by r, m.

2.1.3 The Linearized Problem for Inviscid Parallel Two-Fluid Flows

The analogous equations to (2.15)-(2.18) for inviscid two-fluid flow are

$$\rho_j\left[\left(\frac{\partial}{\partial t} + U_j\frac{\partial}{\partial x}\right)\Delta v_j - U_j''\frac{\partial v_j}{\partial x}\right] = 0, \tag{2.67}$$

$$\rho_j\left[\left(\frac{\partial}{\partial t} + U_j\frac{\partial}{\partial x}\right)\eta_j + U_j'\frac{\partial v_j}{\partial z}\right] = 0, \qquad j = 1,2. \tag{2.68}$$

By substituting wavelike perturbations of the form

$$v_j(x,y,z,t) = \phi_j(y)\exp[i(\alpha x + \beta z - \alpha c t)], \qquad j = 1,2, \tag{2.69}$$

into (2.67), the Rayleigh equation is obtained in each layer:

$$\rho_j \left[(U_j - c) \left(\frac{\partial^2}{\partial y^2} - k^2 \right) - U_j'' \right] \phi_j = 0, \qquad j = 1, 2. \tag{2.70}$$

Note, that $c \equiv \omega/\alpha$ is the complex phase speed. For two-dimensional perturbations, i.e. $\beta = 0$, the equations (2.70) take the form

$$\rho_j \left[(U_j - c) \left(\frac{\partial^2}{\partial y^2} - \alpha^2 \right) - U_j'' \right] \phi_j = 0, \qquad j = 1, 2. \tag{2.71}$$

Since (2.71) are two second-order differential equations, four boundary conditions are required. First, the conditions imposing a perturbation decay at the rigid channel walls or in the far field at infinity are

$$\phi_1 = 0, \qquad \text{at the lower boundary} \quad y = -L_1, \tag{2.72}$$

$$\phi_2 = 0, \qquad \text{at the upper boundary} \quad y = L_2. \tag{2.73}$$

Additionally, two conditions are needed at the interface $y = 0$. First, continuity of the normal velocity is required, i.e.,

$$\phi_1 = \phi_2. \tag{2.74}$$

The second condition describes the continuity of normal stress at the interface:

$$\frac{1}{r}[U_1'\phi_1 + (c - U_0)\phi_1'] - U_2'\phi_2 - (c - U_0)\phi_2' = [F + \alpha^2 S]\frac{\phi}{c - U_0}. \tag{2.75}$$

It is equivalent to saying that, for an inviscid fluid, the pressure is continuous at $y = 0$.

2.2 Linear Equations of Single-Fluid Instability

The Linearized Problem for Viscous Fluids

If only a single fluid is present, the equations of viscous linear instability reduce accordingly. Neglecting, e.g., the lower layer, the stability of a three-dimensional perturbation is only given by equations (2.25) and (2.26) with $\phi \equiv \phi_2$, and $U \equiv U_2$:

$$\left[(-i\omega + i\alpha U) \left(\frac{\partial^2}{\partial y^2} - k^2 \right) - \frac{1}{R} \left(\frac{\partial^2}{\partial y^2} - k^2 \right)^2 - i\alpha U'' \right] \phi = 0, \tag{2.76}$$

$$\left[(-i\omega + i\alpha U) - \frac{1}{R} \left(\frac{\partial^2}{\partial y^2} - k^2 \right) \right] \eta = -i\beta U' \phi. \tag{2.77}$$

The conditions at the upper boundary $L \equiv L_2$ remain, i.e.,

$$\phi = \frac{\partial \phi}{\partial y} = \eta = 0 \qquad \text{at} \quad y = L. \tag{2.78}$$

In addition, the same three conditions are imposed at the lower boundary:

$$\phi = \frac{\partial \phi}{\partial y} = \eta = 0 \qquad \text{at} \quad y = 0. \tag{2.79}$$

Two-dimensional Perturbations

Neglecting the z direction for describing the linear instability of two-dimensional perturbations, one obtains the Orr-Sommerfeld equation (2.76) with $\beta = 0$,

$$\left[(-i\omega + i\alpha U)\left(\frac{\partial^2}{\partial y^2} - \alpha^2\right) - \frac{1}{R}\left(\frac{\partial^2}{\partial y^2} - \alpha^2\right)^2 - i\alpha U''\right]\phi = 0, \tag{2.80}$$

and boundary conditions

$$\phi = \frac{\partial \phi}{\partial y} = 0 \quad \text{at} \quad y = L, \tag{2.81}$$

$$\phi = \frac{\partial \phi}{\partial y} = 0 \quad \text{at} \quad y = 0. \tag{2.82}$$

The Linearized Problem for Inviscid Fluids

Similar to the viscous case, for a single inviscid fluid only one of the Rayleigh equations (2.71) is present:

$$\left[(U - c)\left(\frac{\partial^2}{\partial y^2} - \alpha^2\right) - U''\right]\phi = 0 \tag{2.83}$$

where again $\phi \equiv \phi_2$, and $U \equiv U_2$. The condition at the upper boundary $L \equiv L_2$ remain, i.e.,

$$\phi = 0 \quad \text{at} \quad y = L. \tag{2.84}$$

In addition, the same condition is required at the lower boundary:

$$\phi = 0 \quad \text{at} \quad y = 0. \tag{2.85}$$

2.3 Squire's Transformation and Squire's Theorem

2.3.1 Squire's Theorem in the Case of a Homogeneous Fluid

In case of a homogeneous fluid a relation between three-dimensional and two-dimensional perturbations in parallel viscous flow was given by Squire [55]. For showing this relation, instead of considering the complex frequency ω as the eigenvalue, the complex phase speed $c \equiv \omega/\alpha$ is used. Then, comparing the resulting slightly different version of the Orr-Sommerfeld equation (2.76),

$$\left[(U - c)\left(\frac{\partial^2}{\partial y^2} - k^2\right) - \frac{1}{i\alpha R}\left(\frac{\partial^2}{\partial y^2} - k^2\right)^2 - U''\right]\phi = 0,$$

for a homogeneous fluid with its two-dimensional analogue,

$$\left[(U - c)\left(\frac{\partial^2}{\partial y^2} - \tilde{\alpha}^2\right) - \frac{1}{i\tilde{\alpha}\tilde{R}}\left(\frac{\partial^2}{\partial y^2} - \tilde{\alpha}^2\right)^2 - U''\right]\phi = 0,$$

it is evident that the equations have identical solutions if

$$\tilde{\alpha} = k = \sqrt{\alpha^2 + \beta^2} \quad \text{and} \quad \tilde{\alpha}\tilde{R} = \alpha R. \tag{2.86}$$

Hence

$$\tilde{R} = \frac{\alpha}{k} R < R. \tag{2.87}$$

This states that each solution of the three-dimensional Orr-Sommerfeld equation corresponds to a two-dimensional Orr-Sommerfeld solution at a lower Reynolds number.

Squire's Theorem:
Let R_L denote the critical Reynolds number for the onset of linear instability for given α, β. Then, the Reynolds number R_c below which no exponential instabilities exist for any wave numbers satisfies

$$R_c \equiv \min_{\alpha,\beta} R_L(\alpha,\beta) = \min_{\alpha} R_L(\alpha,0). \tag{2.88}$$

Thus, parallel shear flows become unstable to two-dimensional wavelike perturbations at smaller Reynolds numbers than any value for which unstable three-dimensional perturbations exist [52].

The proof of this theorem follows directly from Squire's transformation (2.86) with the a priori knowledge that the Reynolds number is destabilizing for the considered problem.

2.3.2 Squire's Transformation in the Case of two Stratified Fluids

As in the single-fluid case, the complex phase speed $c = \omega/\alpha$ is considered as the eigenvalue. Then, comparing the slightly different versions of the Orr-Sommerfeld equations (2.23), (2.25) in layers 1 and 2 with its two-dimensional analogues again yields (2.86). No further relation is obtained, when comparing the conditions at the upper and lower boundaries, and (2.30), (2.31), (2.33) at the interface with its respective two-dimensional analogues. However, comparing the slightly different version of the normal stress interface condition (2.35) at $y = 0$,

$$\begin{aligned}&\frac{1}{im\alpha R}(\phi_1''' - 3k^2\phi_1') + \frac{1}{r}[U_1'\phi_1 + (c-U_0)\phi_1'] \\ &\quad -\frac{1}{i\alpha R}(\phi_2''' - 3k^2\phi_2') - U_2'\phi_2 - (c-U_0)\phi_2' \;=\; \frac{k^2}{\alpha^2}[F + k^2 S]\frac{\phi_1}{c-U_0},\end{aligned}$$

with its two-dimensional analogue,

$$\begin{aligned}&\frac{1}{im\tilde{\alpha}\tilde{R}}(\phi_1''' - 3\tilde{\alpha}^2\phi_1') + \frac{1}{r}[U_1'\phi_1 + (c-U_0)\phi_1'] \\ &\quad -\frac{1}{i\tilde{\alpha}\tilde{R}}(\phi_2''' - 3\tilde{\alpha}^2\phi_2') - U_2'\phi_2 - (c-U_0)\phi_2' \;=\; [F + \tilde{\alpha}^2 S]\frac{\phi_1}{c-U_0},\end{aligned}$$

one obtains the additional relations

$$\tilde{S} = \tilde{\alpha}^2 S/\alpha^2 \quad \text{and} \quad \tilde{F} = \tilde{\alpha}^2 F/\alpha^2. \tag{2.89}$$

Since $\tilde{\alpha} \geq \alpha$, it follows that three-dimensional waves oblique to the flow direction have a larger Reynolds number, $R \geq \tilde{R}$, smaller surface tension parameter, $S \leq \tilde{S}$, and provided that density stratification is stabilizing, i.e., $F > 0$ ($\rho_1 > \rho_2$), smaller gravity parameter, $F \leq \tilde{F}$, than do two-dimensional waves transverse to the flow direction.
Using the transformations (2.86) and (2.89), Yiantsios and Higgins [62] tried to prove a theorem in the spirit of Squire for two-fluid plane Poiseuille flow. For this particular problem they found, that interfacial tension is always stabilizing, and when the lower fluid is the more dense, gravity is also always stabilizing. Thus for Squire's theorem to exist, the Reynolds number must always be destabilizing. However, this needs not always be true [62]. Consequently, there is no Squire's theorem in this case, and in general three-dimensional stability analysis is required in order to determine whether two-dimensional disturbances are the most dangerous.

To summarize, although a Squire's transformation exists for the two-layer problem, in general no theorem is possible in this case due to the competing physical effects of shear, surface tension, and gravity; see also References [22] and [51]. Thus, one cannot state a priori what orientation the instability will take. Therefore, to check whether Squire's theorem holds, one would have to compute the neutral stability curve in the $\tilde{\alpha}$-$\tilde{R}$ plane for each data set.

2.4 Temporally and Spatially Growing Perturbations

In the classical linear stability theory the development of infinitesimal perturbations is considered around a given parallel basic flow. The perturbations are decomposed into elementary instability waves of complex frequency ω, and complex wave numbers α and β. The characteristic function relating the values α and ω is a dispersion relation of the form

$$D(\alpha, \omega) = 0. \tag{2.90}$$

For simple basic flows, (2.90) can be calculated explicitly. For more realistic velocity profiles, the dispersion relation is obtained by solving the linear stability equations given in Sections 2.1 and 2.2. Usually the following two special cases are of most interest:

- case T (time-dependent): $\alpha_i(T) = 0,\ \alpha = \alpha_r(T),\ \omega = \omega_r(T) + i\omega_i(T),$
- case S (spatially-dependent): $\omega_i(S) = 0,\ \omega = \omega_r(S),\ \alpha = \alpha_r(S) + i\alpha_i(S).$

Thus, for temporal modes $\omega(\alpha)$ the complex frequency $\omega = \omega_r + i\omega_i$ is determined as a function of the real wave number α. In contrast, spatial branches $\alpha(\omega)$ are obtained by solving for complex wave numbers $\alpha = \alpha_r + i\alpha_i$ when the frequency ω is given real [30]. For the neutral disturbance $\alpha_i = \omega_i = 0$, and both cases T and S have the same solution.

2.4.1 Temporal Generalized Eigenvalue Problem

In the temporal formulation the spatial structure of the wavelike perturbation is unchanged and the amplitude of the wave grows or decays as time progresses. For given real values of α the governing equations and boundary conditions constitute a generalized eigenvalue problem of the form

$$A\vec{q} = \omega B\vec{q} \tag{2.91}$$

with $A = A(\alpha)$, $B = B(\alpha)$ and complex eigenvalues $\omega = \omega_r + i\omega_i$.

2.4.2 Spatial Generalized Eigenvalue Problem

For the spatial spectrum one wishes to solve the governing equations and boundary conditions for α given a real frequency ω. In this case a generalized eigenvalue problem is obtained, where the eigenvalue α appears up to the fourth power in the normal velocity equation. Similar to reducing an nth order ordinary differential equation to n differential equations of first order, one can reduce the higher-order eigenvalue problem to a linear one as shown in Section 3.4. Finally, a linear generalized eigenvalue problem of the form

$$A\vec{q} = \alpha B\vec{q} \tag{2.92}$$

is obtained with $A = A(\omega)$, $B = B(\omega)$ and complex eigenvalues $\alpha = \alpha_r + i\alpha_i$.

2.4.3 Gaster's Transformation

As already mentioned, the general solution to the linearized stability equations at fixed parameters yields a dispersion relation between the wave number α and the frequency ω given by equation (2.90),

$$D(\alpha, \omega) = 0.$$

Suppose now that the frequency is a complex analytic (holomorphic) function of the wave number, i.e., $\omega = \omega(\alpha)$ is complex differentiable in a neighbourhood of every point in its domain.

If $\omega(\alpha_r+i\alpha_i) = \omega_r(\alpha_r,\alpha_i)+i\omega_i(\alpha_r,\alpha_i)$ is complex differentiable, then ω_r and ω_i have first partial derivatives with respect to α_r and α_i, which satisfy the Cauchy-Riemann equations

$$\frac{\partial\omega_r}{\partial\alpha_r} = \frac{\partial\omega_i}{\partial\alpha_i} \quad \text{and} \quad \frac{\partial\omega_r}{\partial\alpha_i} = -\frac{\partial\omega_i}{\partial\alpha_r}. \tag{2.93}$$

In addition, $\omega = \omega(\alpha)$ is infinitely differentiable and equal to its Taylor series in a neighbourhood of each point in its domain.
With relations (2.93) one can integrate over α_i from a state S with $\alpha_i > 0$ to a state T where $\alpha_i = 0$, keeping α_r fixed. Hence

$$\alpha_r(S) = \alpha_r(T). \tag{2.94}$$

Integration of the Cauchy-Riemann equations gives

$$\omega_i|_S^T = \int_S^T \frac{\partial\omega_r}{\partial\alpha_r}\, d\alpha_i \tag{2.95}$$

and

$$\omega_r|_S^T = -\int_S^T \frac{\partial\omega_i}{\partial\alpha_r}\, d\alpha_i. \tag{2.96}$$

Because $\omega_i(S) = 0$, and on the right hand side the T state corresponds to $\alpha_i = 0$, (2.95) can be simplified to

$$\omega_i(T) = \int_S^0 \frac{\partial\omega_r}{\partial\alpha_r}\, d\alpha_i.$$

Expanding $\partial\omega_r/\partial\alpha_r$ in a Taylor series about any point $0 \le \alpha_i^* \le \alpha_i(S)$, and, provided the S state is close to zero, keeping the leading order term only, results in

$$\omega_i(T) = -\int_0^S \frac{\partial\omega_r}{\partial\alpha_r}\, d\alpha_i \;\approx\; -\left.\frac{\partial\omega_r}{\partial\alpha_r}\right|_{\alpha_i^*} \alpha_i(S).$$

Defining a group velocity as

$$c_g = \frac{\partial\omega_r}{\partial\alpha_r}, \tag{2.97}$$

the above equation reads

$$\omega_i(T) = c_g\left\{-\alpha_i(S)\right\}, \tag{2.98}$$

where c_g can be evaluated at any point between T and S [13]. Equation (2.98) is called Gaster's transformation [20] and relates the temporal and spatial growth rates, $\omega_i(T)$ and $-\alpha_i(S)$, by means of the group velocity c_g. Similarly, (2.96) can be simplified to

$$\omega_r(T) - \omega_r(S) = \int_0^S \frac{\partial\omega_i}{\partial\alpha_r}\, d\alpha_i.$$

Expanding $\partial\omega_i/\partial\alpha_r$ in a Taylor series, keeping the leading order term only, and then taking the maximum of both sides, yields

$$|\omega_r(T) - \omega_r(S)| \le \max\left|\frac{\partial\omega_i}{\partial\alpha_r}\right| |\alpha_i(S)|.$$

Since the first term of the product on the right-hand side is bounded, and $|\alpha_i(S)|$ is small near a neutral mode, one has

$$\omega_r(T) \approx \omega_r(S). \tag{2.99}$$

Thus, provided one is in a small neighbourhood about the neutral line, the real part of the frequency for temporal modes is approximately equal to those for spatial modes [13].

Note finally, that the group velocity c_g must be positive when attempting to apply Gaster's transformation for the usual type of flows. In harmony with the assumption that disturbances grow in the downstream direction, positive group velocities correspond to waves traveling downstream. Contrary, negative group velocities travel upstream [13].

2.5 Linear Energy Rate Equation

As mentioned in Section 1.3, the linear instability of parallel viscous two-phase flows usually deals with different amplified perturbations. A linear perturbation is amplified when it obtains more energy from the basic flow than it dissipates. However, it is in general not clear by which mechanism this energy transfer takes place. An instability may receive its energy from the basic flow in the bulk of either of the two phases. This is similar to the mechanisms in single-phase flow. Alternatively, an instability can originate at the interface, or may be driven by more than one mechanism [7]. In order to identify the different instability mechanisms, the linear energy rate equation will be used. Assuming two-dimensional disturbances, the energy budget is derived for two stratified fluids, where gravitational effects are neglected, i.e. $F = 0$. The total perturbation energy in two-fluid flows is composed of the kinetic energy contributions in both phases. In addition, it involves a term due to the presence of the interface.
Starting with the derivation of the kinetic energy in the two layers, the dimensionless Navier-Stokes equations for the perturbation velocity components u_1 and v_1 can be written as

$$\frac{1}{r}\left(\frac{\partial u_1}{\partial t} + U_1\frac{\partial u_1}{\partial x} + v_1\frac{\partial U_1}{\partial y}\right) = -\frac{1}{r}\frac{\partial p_1}{\partial x} + \frac{2}{mR}\left(\frac{\partial}{\partial x}S_{xx}^{(1)} + \frac{\partial}{\partial y}S_{yx}^{(1)}\right),$$

$$\frac{1}{r}\left(\frac{\partial v_1}{\partial t} + U_1\frac{\partial v_1}{\partial x}\right) = -\frac{1}{r}\frac{\partial p_1}{\partial y} + \frac{2}{mR}\left(\frac{\partial}{\partial x}S_{xy}^{(1)} + \frac{\partial}{\partial y}S_{yy}^{(1)}\right).$$

Similarly, for u_2 and v_2 one has

$$\frac{\partial u_2}{\partial t} + U_2\frac{\partial u_2}{\partial x} + v_2\frac{\partial U_2}{\partial y} = -\frac{\partial p_2}{\partial x} + \frac{2}{R}\left(\frac{\partial}{\partial x}S_{xx}^{(2)} + \frac{\partial}{\partial y}S_{yx}^{(2)}\right),$$

$$\frac{\partial v_2}{\partial t} + U_2\frac{\partial v_2}{\partial x} = -\frac{\partial p_2}{\partial y} + \frac{2}{R}\left(\frac{\partial}{\partial x}S_{xy}^{(2)} + \frac{\partial}{\partial y}S_{yy}^{(2)}\right).$$

The rate-of-strain tensor in each fluid is equal to

$$S_{ij}^{(k)} = \frac{1}{2}\left(\frac{\partial u_{ki}}{\partial x_j} + \frac{\partial u_{kj}}{\partial x_i}\right).$$

Here $(x_1, x_2) = (x, y)$, and $(u_{k1}, u_{k2}) = (u_k, v_k)$, where the subscript $k = 1, 2$ refers to the phase. Multiplying the equations for u_k with u_k and those for v_k with v_k, adding both equations, and using the incompressibility in the pressure terms, one gets for the lower layer 1

$$\begin{aligned}&\frac{\partial}{\partial t}\frac{1}{2r}\left(u_1^2 + v_1^2\right) + \frac{\partial}{\partial x}\left[\frac{U_1}{2r}\left(u_1^2 + v_1^2\right) + \frac{u_1 p_1}{r} - \frac{2}{mR}\sum_{j=1}^{2} S_{xj}^{(1)} u_{1j}\right]\\ &= -\frac{\partial}{\partial y}\left(\frac{v_1 p_1}{r} - \frac{2}{mR}\sum_{j=1}^{2} S_{yj}^{(1)} u_{1j}\right) - \frac{2}{mR}\sum_{i,j=1}^{2} S_{ij}^{(1)} S_{ij}^{(1)} - \frac{u_1 v_1}{r}\frac{\partial U_1}{\partial y}.\end{aligned} \tag{2.100}$$

Similarly, for the upper layer 2 one has

$$\begin{aligned}&\frac{\partial}{\partial t}\frac{1}{2}\left(u_2^2 + v_2^2\right) + \frac{\partial}{\partial x}\left[\frac{U_2}{2}\left(u_2^2 + v_2^2\right) + u_2 p_2 - \frac{2}{R}\sum_{j=1}^{2} S_{xj}^{(2)} u_{2j}\right]\\ &= -\frac{\partial}{\partial y}\left(v_2 p_2 - \frac{2}{R}\sum_{j=1}^{2} S_{yj}^{(2)} u_{2j}\right) - \frac{2}{R}\sum_{i,j=1}^{2} S_{ij}^{(2)} S_{ij}^{(2)} - u_2 v_2\frac{\partial U_2}{\partial y}.\end{aligned} \tag{2.101}$$

Note that

$$\sum_{i,j=1}^{2} u_{kj}\frac{\partial}{\partial x_i}S_{ij}^{(k)} = \sum_{i,j=1}^{2}\left[\frac{\partial}{\partial x_i}\left(S_{ij}^{(k)}u_{kj}\right) - S_{ij}^{(k)}\frac{\partial u_{kj}}{\partial x_i}\right],$$

and

$$\sum_{i,j=1}^{2} S_{ij}^{(k)}\frac{\partial u_{kj}}{\partial x_i} = \sum_{i,j=1}^{2} S_{ij}^{(k)}S_{ij}^{(k)} = \left(\frac{\partial u_k}{\partial x}\right)^2 + \frac{1}{2}\left(\frac{\partial u_k}{\partial y}+\frac{\partial v_k}{\partial x}\right)^2 + \left(\frac{\partial v_k}{\partial y}\right)^2$$

represents the dissipation.
For calculating the interfacial energy contribution, the starting point is the kinematic condition

$$\frac{\partial \hat{f}}{\partial t} + U_0\frac{\partial \hat{f}}{\partial x} = v(x,0,t), \tag{2.102}$$

where $y = \hat{f}(x,t)$ denotes the position of the interface between the two phases. Taking the x-derivative of (2.102), and multiplying the result by $S(\partial\hat{f}/\partial x)$ one obtains after straightforward algebraic manipulations

$$\frac{\partial}{\partial t}\left[\frac{S}{2}\left(\frac{\partial \hat{f}}{\partial x}\right)^2\right] + \frac{\partial}{\partial x}\left[U_0\frac{S}{2}\left(\frac{\partial \hat{f}}{\partial x}\right)^2 - Sv\frac{\partial \hat{f}}{\partial x}\right] = -Sv\frac{\partial^2 \hat{f}}{\partial x^2}. \tag{2.103}$$

2.5.1 Energy Balance for Temporal Modes

In the temporal case, an energy analysis is based on the fact that, by definition, instability implies the increase of kinetic energy of an initially small disturbance with time. This idea has already been used by Boomkamp and Miesen [7] to classify the various instabilities in parallel two-phase flows. Their formulation for the energy budget applies for a spatially periodic, temporal eigenmode of given wavelength. It can be considered as a two-fluid extension of the Reynolds-Orr energy equation of a single viscous fluid [52]. Averaging (2.100) and (2.101) over a wavelength $\lambda = 2\pi/\alpha$, the terms that can be written as a divergence vanish. Integrating over the thicknesses L_1 and L_2 of both fluid layers, adding the two results together, and applying the divergence theorem of Gauss, the energy rate equation for infinitesimal temporal perturbations is obtained as

$$\frac{\partial E_k}{\partial t} = DIS_1 + DIS_2 + REY_1 + REY_2 + INT, \tag{2.104}$$

where

$$\frac{\partial E_k}{\partial t} = \frac{1}{\lambda}\frac{\partial}{\partial t}\int_0^{\lambda}\left(\frac{1}{r}\int_{-L_1}^{0}\left[\frac{1}{2}\left(u_1^2+v_1^2\right)\right]dy + \int_0^{L_2}\left[\frac{1}{2}\left(u_2^2+v_2^2\right)\right]dy\right)dx \tag{2.105}$$

denotes the spatially averaged rate of change of the total kinetic energy of perturbations, and

$$DIS_1 = -\frac{1}{\lambda}\frac{1}{mR}\int_0^{\lambda}\int_{-L_1}^{0}\left[2\left(\frac{\partial u_1}{\partial x}\right)^2 + \left(\frac{\partial u_1}{\partial y}+\frac{\partial v_1}{\partial x}\right)^2 + 2\left(\frac{\partial v_1}{\partial y}\right)^2\right]dy\,dx, \tag{2.106}$$

$$DIS_2 = -\frac{1}{\lambda}\frac{1}{R}\int_0^{\lambda}\int_{0}^{L_2}\left[2\left(\frac{\partial u_2}{\partial x}\right)^2 + \left(\frac{\partial u_2}{\partial y}+\frac{\partial v_2}{\partial x}\right)^2 + 2\left(\frac{\partial v_2}{\partial y}\right)^2\right]dy\,dx, \tag{2.107}$$

$$REY_1 = \frac{1}{\lambda}\frac{1}{r}\int_0^{\lambda}\int_{-L_1}^{0}\left[(-u_1v_1)\frac{\partial U_1}{\partial y}\right]dy\,dx, \tag{2.108}$$

$$REY_2 = \frac{1}{\lambda}\int_0^{\lambda}\int_{0}^{L_2}\left[(-u_2v_2)\frac{\partial U_2}{\partial y}\right]dy\,dx, \tag{2.109}$$

$$INT = \frac{1}{\lambda}\int_0^\lambda \left[-\frac{v_1 p_1}{r} + \frac{1}{mR}\left(2v_1\frac{\partial v_1}{\partial y} + u_1\frac{\partial v_1}{\partial x} + u_1\frac{\partial u_1}{\partial y}\right) + v_2 p_2 - \frac{1}{R}\left(2v_2\frac{\partial v_2}{\partial y} + u_2\frac{\partial v_2}{\partial x} + u_2\frac{\partial u_2}{\partial y}\right)\right]_{y=0} dx. \tag{2.110}$$

For an unstable flow, the kinetic energy E_k of initially small disturbances grows with time, and the rate of change $\partial E_k/\partial t$ is positive. The terms DIS_1 and DIS_2 represent the rates of viscous dissipation of the perturbed flow in each layer. Viscous dissipation opposes instability. Consequently, the expressions (2.106) and (2.107) are strictly negative. Since the Reynolds stress in the disturbed flow of each layer is given by

$$\tau_1^R(y) = \frac{1}{r}\int_0^\lambda (-u_1 v_1)\, dx \quad \text{and} \quad \tau_2^R(y) = \int_0^\lambda (-u_2 v_2)\, dx,$$

the terms REY_1 and REY_2 represent the rates at which Reynolds stress is transfering energy between the primary flow and the perturbation. Depending on the details of the problem, the terms (2.108) and (2.109) can either stabilize or destabilize the primary flow. Therefore, they can have a positive or negative sign. Characteristic for multiphase systems is the presence of INT. This contribution represents the transfer of energy from the basic flow to the perturbed flow at the interface, and can be decomposed as $INT = TAN + NOR$, where

$$TAN = \frac{1}{\lambda}\frac{1}{R}\int_0^\lambda \left[\frac{1}{m}\left(\frac{\partial v_1}{\partial x} + \frac{\partial u_1}{\partial y}\right)u_1 - \left(\frac{\partial v_2}{\partial x} + \frac{\partial u_2}{\partial y}\right)u_2\right]_{y=0} dx, \tag{2.111}$$

and

$$NOR = \frac{1}{\lambda}\int_0^\lambda \left[\left(-\frac{p_1}{r} + \frac{2}{mR}\frac{\partial v_1}{\partial y}\right)v_1 - \left(-p_2 + \frac{2}{R}\frac{\partial v_2}{\partial y}\right)v_2\right]_{y=0} dx. \tag{2.112}$$

The rate at which work is done by the disturbances in the direction normal to the interface is denoted by NOR, while TAN gives this rate for the disturbances in the tangential direction, i.e. in the direction of the primary flow.
Because $v_1(0) = v_2(0) \equiv v(0)$, and using the normal stress condition at the interface,

$$-\frac{p_1}{r} + \frac{2}{mR}\frac{\partial v_1}{\partial y} + p_2 - \frac{2}{R}\frac{\partial v_2}{\partial y} = S\frac{\partial^2 \hat{f}}{\partial x^2} - F\hat{f}, \tag{2.113}$$

in the absence of gravitational effects, $F = 0$, NOR can be written as

$$NOR = \frac{1}{\lambda}\int_0^\lambda \left[Sv\frac{\partial^2 \hat{f}}{\partial x^2}\right]_{y=0} dx. \tag{2.114}$$

Since temporal modes are studied here, the second term on the left-hand side of (2.103) vanishes. One obtains

$$NOR = -\frac{\partial E_p}{\partial t}; \qquad E_p \equiv \frac{1}{\lambda}\int_0^\lambda \left[\frac{S}{2}\left(\frac{\partial \hat{f}}{\partial x}\right)^2\right]_{y=0} dx. \tag{2.115}$$

Hence, NOR corresponds to the negative rate of change of surface tension energy E_p averaged over one wavelength. Adding (2.115) to (2.104), the total energy balance for temporal modes takes the form

$$\frac{\partial(E_k + E_p)}{\partial t} = DIS_1 + DIS_2 + REY_1 + REY_2 + TAN. \tag{2.116}$$

This interpretation of the energy budget is used later to identify and classify the various instabilities occurring in parallel two-phase flows. The expressions in equation (2.116) are given in

terms of the eigenfunctions ϕ_k, $k = 1, 2$, in Appendix A.1.1. Then, in (2.116) the time derivatives become multiplier by the temporal growth rate ω_i, see (A.1).
Because the streamfunctions in linear theory are arbitrarily normalized, only the relative values of the energy contributions have a physical meaning. Thus the production and dissipation terms in (2.116) have to be scaled. Here, scaling is performed, so that the sum of the destabilizing terms, i.e. the contributions with positive values, is unity. Finally, a natural estimate of the relative error of the numerical method is obtained by comparing the residual of equation (2.116) – as calculated by adding all energy terms – to the term with the largest absolute value [7].

2.5.2 Energy Balance for Spatial Modes

Similarly to temporal modes, an energy balance approach can be performed for spatial instabilities. To obtain such an energy budget, one averages equations (2.100) and (2.101) over one period $\gamma = 2\pi/\omega$, and with respect to y, i.e. over a plane $x = const.$ Then, the time derivatives drop out. Adding the expressions for both layers, one finds

$$MFL_1 + MFL_2 = DIS_1 + DIS_2 + REY_1 + REY_2 + TAN + NOR, \tag{2.117}$$

where

$$MFL_1 = \frac{1}{\gamma}\frac{\partial}{\partial x}\int_0^{\gamma}\int_{-L_1}^{0}\left[\frac{U_1}{2r}\left(u_1^2+v_1^2\right)+\frac{u_1 p_1}{r}-\frac{2}{mR}\sum_{j=1}^{2}S_{xj}^{(1)}u_{1j}\right]dy\;dt, \tag{2.118}$$

$$MFL_2 = \frac{1}{\gamma}\frac{\partial}{\partial x}\int_0^{\gamma}\int_{0}^{L_2}\left[\frac{U_2}{2}\left(u_2^2+v_2^2\right)+u_2 p_2-\frac{2}{R}\sum_{j=1}^{2}S_{xj}^{(2)}u_{2j}\right]dy\;dt, \tag{2.119}$$

$$DIS_1 = -\frac{1}{\gamma}\frac{1}{mR}\int_0^{\gamma}\int_{-L_1}^{0}\left[2\left(\frac{\partial u_1}{\partial x}\right)^2+\left(\frac{\partial u_1}{\partial y}+\frac{\partial v_1}{\partial x}\right)^2+2\left(\frac{\partial v_1}{\partial y}\right)^2\right]dy\;dt, \tag{2.120}$$

$$DIS_2 = -\frac{1}{\gamma}\frac{1}{R}\int_0^{\gamma}\int_{0}^{L_2}\left[2\left(\frac{\partial u_2}{\partial x}\right)^2+\left(\frac{\partial u_2}{\partial y}+\frac{\partial v_2}{\partial x}\right)^2+2\left(\frac{\partial v_2}{\partial y}\right)^2\right]dy\;dt, \tag{2.121}$$

$$REY_1 = \frac{1}{\gamma}\frac{1}{r}\int_0^{\gamma}\int_{-L_1}^{0}\left[(-u_1 v_1)\frac{\partial U_1}{\partial y}\right]dy\;dt, \tag{2.122}$$

$$REY_2 = \frac{1}{\gamma}\int_0^{\gamma}\int_{0}^{L_2}\left[(-u_2 v_2)\frac{\partial U_2}{\partial y}\right]dy\;dt, \tag{2.123}$$

$$TAN = \frac{1}{\gamma}\frac{1}{R}\int_0^{\gamma}\left[\frac{1}{m}\left(\frac{\partial v_1}{\partial x}+\frac{\partial u_1}{\partial y}\right)u_1-\left(\frac{\partial v_2}{\partial x}+\frac{\partial u_2}{\partial y}\right)u_2\right]_{y=0}dt, \tag{2.124}$$

$$NOR = \frac{1}{\gamma}\int_0^{\gamma}\left[\left(-\frac{p_1}{r}+\frac{2}{mR}\frac{\partial v_1}{\partial y}\right)v_1-\left(-p_2+\frac{2}{R}\frac{\partial v_2}{\partial y}\right)v_2\right]_{y=0}dt. \tag{2.125}$$

The left hand side in equation (2.117) represents the gradient of mean flux of energy across a fixed plane $x = const.$ It originates from a combination of advection by the mean flow, pressure and momentum diffusion. The right hand side gives the production and dissipation terms for this energy flux gradient. They are essentially the same as in the temporal case. Using again the normal stress condition at the interface (2.113), in the absence of gravitational effects, $F = 0$, NOR can be written as

$$NOR = \frac{1}{\gamma}\int_0^{\gamma}\left[Sv\frac{\partial^2 \hat{f}}{\partial x^2}\right]_{y=0}dt. \tag{2.126}$$

Since spatial modes are considered here, the first term on the left-hand side of (2.103) vanishes. One obtains

$$NOR = -MFL_0; \qquad MFL_0 \equiv \frac{1}{\lambda}\frac{\partial}{\partial x}\int_0^{\gamma}\left[U_0\frac{S}{2}\left(\frac{\partial \hat{f}}{\partial x}\right)^2 - Sv\frac{\partial \hat{f}}{\partial x}\right]_{y=0} dt. \tag{2.127}$$

Adding the above to equation (2.117), the total energy balance for spatial modes takes the form

$$MFL_1 + MFL_2 + MFL_0 = DIS_1 + DIS_2 + REY_1 + REY_2 + TAN. \tag{2.128}$$

All terms with $\partial/\partial x$ are grouped together on the left-hand side. Contrary to the temporal case they cannot be considered as kinetic and potential energies, and their physical interpretation is not obvious. The expressions on the right-hand side of the above equation are given in terms of the eigenfunctions ϕ_k, $k = 1, 2$, in Appendix A.1.2. Finally, as in the temporal case the expressions in (2.128) are scaled, so that the sum of the destabilizing terms is unity.

2.6 Local Instability Concepts

In this section the impulse response of a linear system at various streamwise locations is summarized. Consider the general dispersion relation (2.90),

$$D(\alpha, \omega) = 0,$$

which describes the dynamic behaviour of a linear system in space (characterized by the wave number α) and time (expressed by the frequency ω). The response of the linear system governed by the dispersion relation to an impulse at $x = 0$ and $t = 0$ is given by the Green's function $G(x, t)$, which satifies

$$D\left(-i\frac{\partial}{\partial x}, i\frac{\partial}{\partial t}\right) G(x, t) = \delta(x)\delta(t), \tag{2.129}$$

with δ denoting the Dirac delta function [30, 31]. The forcing initiated at $t = 0$ imposes the *causality condition*, that the associated physical linear response $G(x, t)$ must be zero for $t < 0$:

$$G(x, t) = 0 \quad \text{for} \quad t < 0. \tag{2.130}$$

In the limit $t \to +\infty$ three types of responses $G(x, t)$ to a localized initial state may occur:

- First, when the amplitude decays asymptotically in time in the entire domain, i.e.

$$\lim_{t\to\infty} G(x, t) = 0 \quad \text{along all rays} \quad x/t = const, \tag{2.131}$$

  the basic flow is said to be *linearly stable*. Otherwise it is called *linearly unstable*, i.e. when

$$\lim_{t\to\infty} G(x, t) = \infty \quad \text{along at least one ray} \quad x/t = const. \tag{2.132}$$

  In this case one may further distinguish between two sub-classes of linearly unstable flows, where now Green's function $G(x, t)$ is evaluated at a fixed spatial position x as $t \to \infty$:

- The basic flow is called *linearly convectively unstable*, when its impulse response is ultimately advected away from the source location so that

$$\lim_{t\to\infty} G(x, t) = 0 \quad \text{along the ray} \quad x/t = 0. \tag{2.133}$$

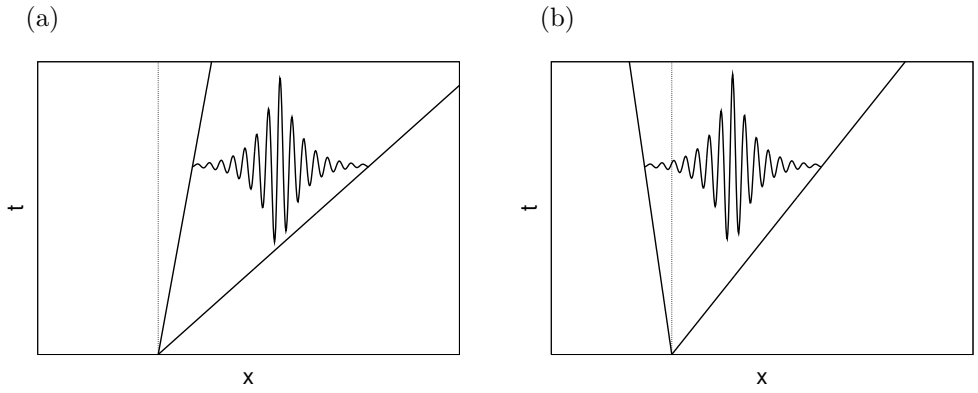

Figure 2.1: *Sketch of a typical impulse response: (a) convectively unstable flow; (b) absolutely unstable flow.*

- It is referred to as *linearly absolutely unstable*, when the impulse response becomes unbounded at the source and gradually contaminates the entire medium:

$$\lim_{t\to\infty} G(x,t) = \infty \quad \text{along the ray} \quad x/t = 0. \tag{2.134}$$

In other words, in linearly convectively unstable flows superimposed amplified perturbations are convected away so that the impulse response decays to zero at all points as $t \to \infty$. Contrary, for linearly absolutely unstable flows some perturbations increase in amplitude at all points in the limit $t \to \infty$ [31].
For illustration, in Figure 2.1 the amplified wave packet, generated by an impulse at the origin of the x-t diagram, is confined within a wedge bounded by the two rays of zero growth rate. Outside this wedge disturbances are algebraically decaying; in the wedge they grow exponentially. In a convectively unstable flow the edges of the wave packet travel in the same direction, e.g. in the positive x direction as in Figure 2.1(a). The ray $x/t = 0$ (the vertical axis in the Figure) must therefore lie outside the unstable packet. Contrary, the x-t diagram in Figure 2.1(b) shows the case of absolute instability. Here, the wave packet spreads in both the negative (upstream) and positive (downstream) x-directions, and contaminates the entire domain in the limit $t \to \infty$. The ray $x/t = 0$ must now be within the wedge [29].

If one Fourier- and Laplace-transforms (2.129) and formally reverts back to physical space, one obtains

$$G(x,t) = \frac{1}{(2\pi)^2} \int_L \int_F \frac{\exp[i(\alpha x - \omega t)]}{D(\alpha,\omega)}\, d\alpha\, d\omega, \tag{2.135}$$

where L denotes the inversion contour in the Laplace-ω-plane. Similarly, F is the inversion contour in the Fourier-α-plane [30, 31, 52]. Note, that the contours must be chosen so that both the convergence of (2.135) and the causality condition (2.130) are ensured.
Suppose the F contour is chosen on the α_r-axis. Then, focusing attention on the ω-plane integration in (2.135), the function

$$\frac{1}{2\pi} \int_L \frac{\exp(-i\omega t)}{D(\alpha_r,\omega)}\, d\omega \tag{2.136}$$

is examined, where the singularities of the integrand are given by $D(\alpha_r,\omega) = 0$, or equivalently by the temporal branches $\omega(\alpha_r) = \omega_r(\alpha_r) + i\omega_i(\alpha_r)$ with $\alpha_i = 0$. Choosing the path L in the plane of complex frequencies ω as a straight horizontal line located above the highest temporal branch $\omega(\alpha_r)$, the causality condition (2.130) is satisfied [4, 31]. When ω is varied along this path L in the complex frequency plane, none of the corresponding branches $\alpha(\omega_L) = \alpha_r(\omega_L) + i\alpha_i(\omega_L)$ in

the complex wave number plane can cross the real α-axis. Consequently, the generalized spatial branches are separated into two disjoint sets, where the modes located above and below the α_r-axis will be denoted $\alpha^+(\omega_L)$ and $\alpha^-(\omega_L)$, respectively. When $x > 0$ or $x < 0$, the contour F on the α_r-axis is closed in the upper or lower half α-plane, respectively, and the α-plane integration

$$\frac{1}{2\pi}\int_F \frac{\exp(i\alpha x)}{D(\alpha,\omega_L)}\,d\alpha \tag{2.137}$$

in (2.135) thus exhibits a division of the modes, where the spatial branches $\alpha^+(\omega_L)$ are associated with the dynamics downstream ($x > 0$), while the branches $\alpha^-(\omega_L)$ govern the perturbation behaviour upstream ($x < 0$) of the source [4, 30, 31].

2.6.1 Stability and Instability

Let $\omega_i^{\max}$ denote the maximum growth rate of all the temporal branches $\omega(\alpha_r)$ with $\alpha_i = 0$. Then, a given basic flow is

- linearly stable, if $\omega_i^{\max} < 0$,
- linearly unstable, if $\omega_i^{\max} > 0$.

Indeed, if the flow under consideration is linearly stable to small-amplitude perturbations, all the temporal branches $\omega(\alpha_r)$ possess a negative growth rate, $\omega_i(\alpha_r) < 0$, for all α_r. In this case, the integrand in (2.136) can be shown to decrease exponentially [31]. Consequently, the time-asymptotic response of $G(x,t)$ always vanishes in the limit $t \to \infty$. Contrary, in case of linear instability, at least one temporal branch $\omega(\alpha_r)$ has $\omega_i(\alpha_r) > 0$ for some values of α_r. In this case, the integral (2.136) blows up [31].
Hence, the stable/unstable nature of a flow can be determined by solving the dispersion relation for complex frequencies ω given real wave numbers α.

2.6.2 Convective and Absolute Instability

It was shown, that the unstable, time-asymptotic behaviour of $G(x,t)$ is determined by the singularities in the complex ω-plane between the L contour on the ω_r-axis. These singularities can prevent one from extending the region of convergence of the integral (2.135) into the lower half ω-plane without violating causality [4]. However, the discontinuities can be transformed by simultaneous, continuous deformations of the contours F and L without affecting the integration result. If $D(\alpha,\omega)$ is holomorphic with respect to α and ω, such deformations of L and F are possible without violating causality, provided the integration contours do not cross the corresponding generalized temporal and spatial modes [4, 31].
In the beginning of this transformation process suggested by Bers [4] and Briggs [10], the contours F and L are chosen as already discussed: F lies on the α_r-axis, and L is located above all the temporal branches $\omega(\alpha_r)$. Upon reducing ω_i, i.e. L is continously displaced downward, the $\alpha^+(\omega)$ and $\alpha^-(\omega)$ branches approach one another. Note that, for an unstable flow, when $\omega_i < \omega_i^{\max}$ at least one of the branches must necessarily cross the α_r-axis, and gives a band of spatially unstable frequencies. Hence, in the transformation process one must correspondingly deform the original F contour, until F becomes pinched between two branches $\alpha^+(\omega)$ and $\alpha^-(\omega)$ as ω_i is lowered. Pinching occurs precisely at the *absolute wave number* $\alpha^0 = \alpha_r^0 + i\alpha_i^0$. At this point the group velocity is zero [31],

$$\frac{\partial\omega}{\partial\alpha}\left(\alpha^0\right) = 0.$$

Correspondingly, a cusp appears in the plane of complex frequencies at $\omega^0 \equiv \omega(\alpha^0) = \omega_r^0 + i\omega_i^0$, which is called the *absolute frequency*. In this instance, any further lowering of L is illegal as the branches $\alpha^+(\omega)$ and $\alpha^-(\omega)$ would reconnect through a saddle point. The F contour would then cross a generalized spatial branch and hence violate causality [31].

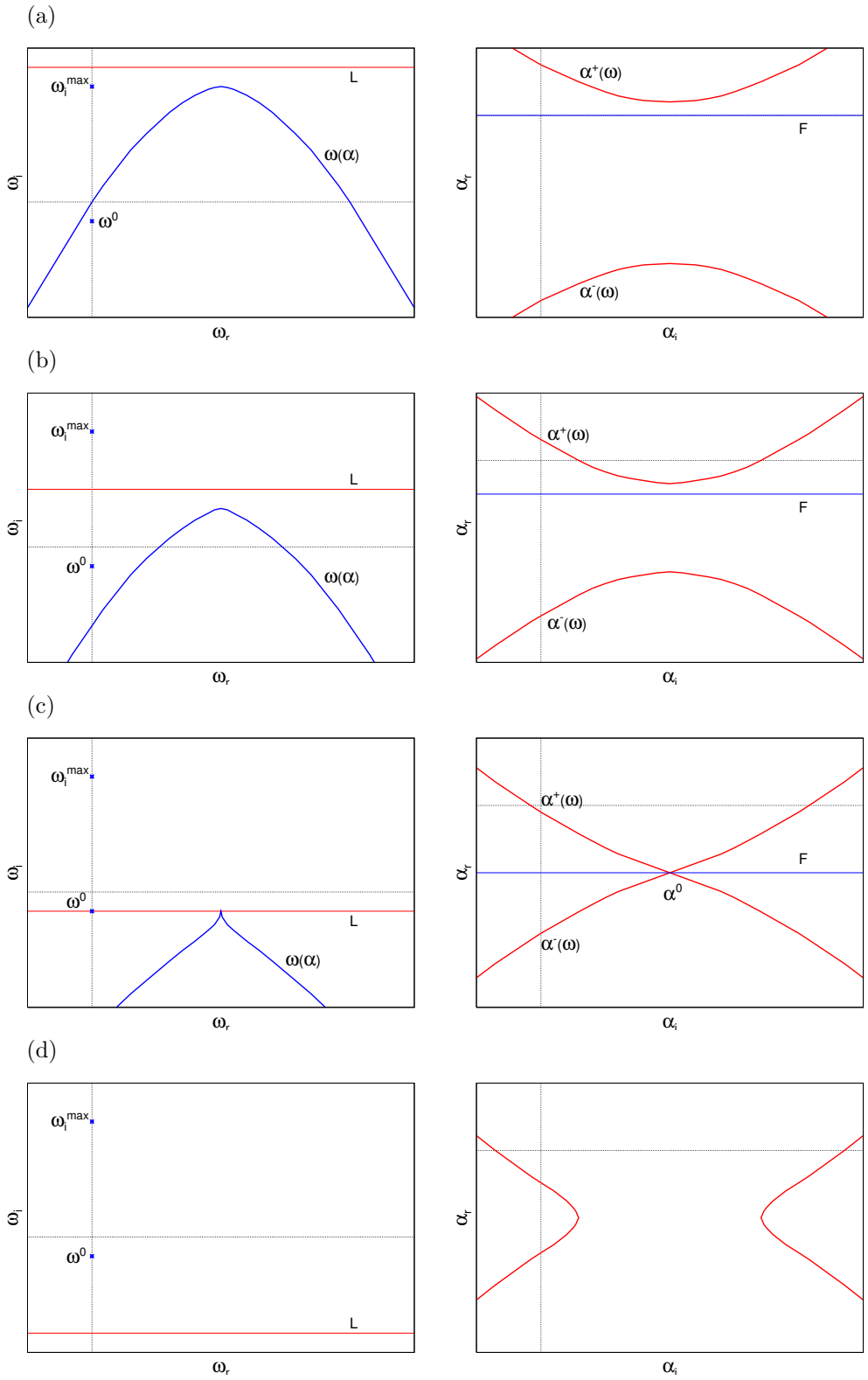

Figure 2.2: *Locus of generalized spatial branches as the L contour is lowered in the complex ω-plane. Case of convective instability. See text for details.*

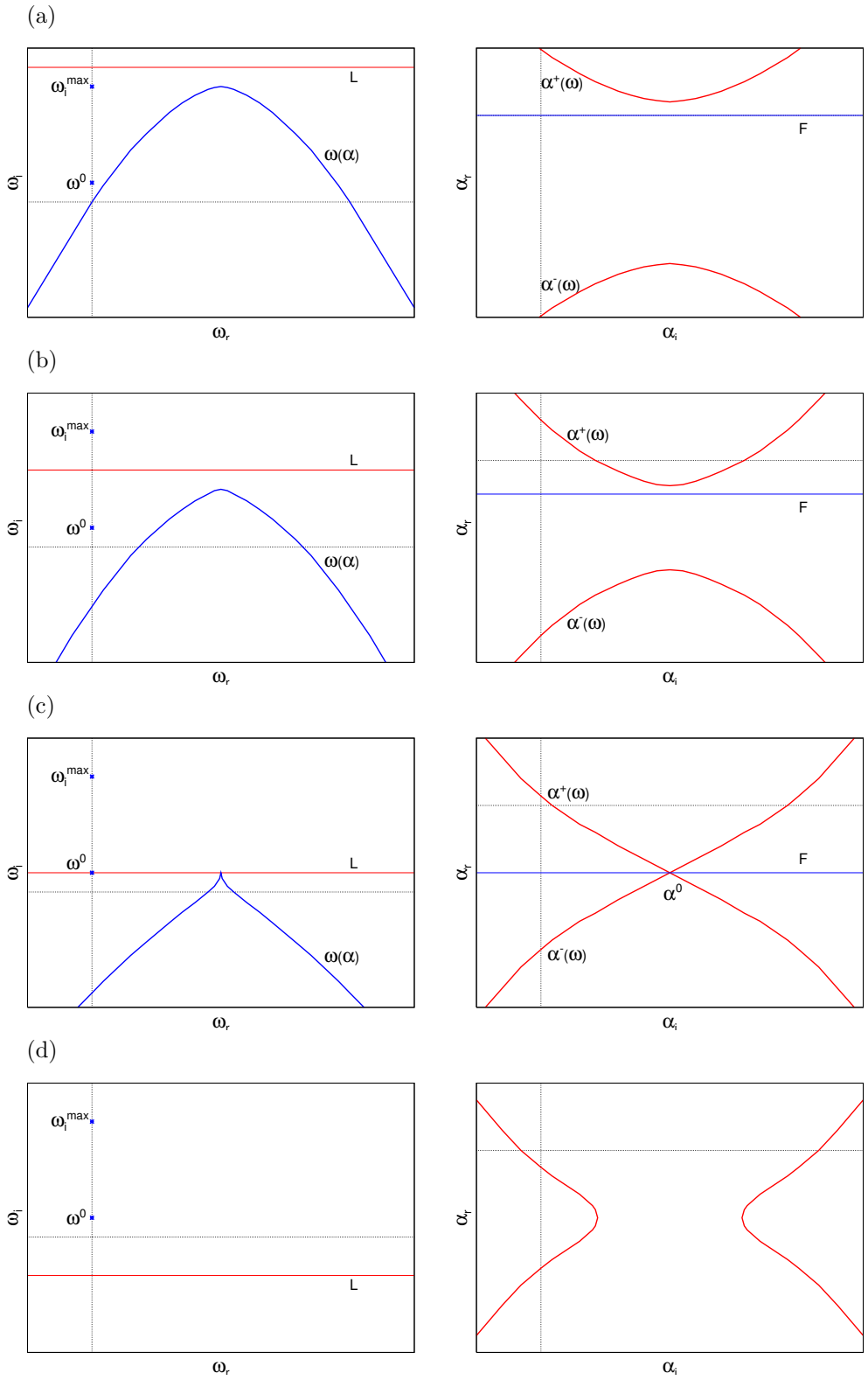

Figure 2.3: *Locus of generalized spatial branches as the L contour is lowered in the complex ω-plane. Case of absolute instability. See text for details.*

Thus, in the laboratory frame, i.e. at fixed position x, the impulse response $G(x,t)$ should be dominated by the complex absolute wave number α^0 and the complex absolute frequency ω^0 of zero group velocity. This can be seen by the following relation for the asymptotic impulse response along the ray $x/t = 0$ [31]:

$$G(x,t) \sim \frac{1}{\sqrt{2\pi}} \frac{\exp\left[\frac{i\pi}{4} + i(\alpha^0 x - \omega^0 t)\right]}{\frac{\partial D}{\partial \omega}(\alpha^0, \omega^0)} \left[t \frac{\partial^2 \omega}{\partial \alpha^2}(\alpha^0)\right]^{-1/2}. \tag{2.138}$$

Denoting the *absolute growth rate* by $\omega_i^0 \equiv \omega_i(\alpha^0)$, which characterizes the asymptotic growth of disturbances in the laboratory frame, relation (2.138) provides the following criterion on linear convective/absolute instability. An instability is

- convective, if $\omega_i^0 < 0$,
- absolute, if $\omega_i^0 > 0$.

Note that, in case of convective instability, the F contour can be deformed, such that all the corresponding branches $\omega(\alpha_F)$ lie in the lower half ω-plane. Then, L may be deformed to entirely lie in the lower half ω-plane as well. In this case, the mapping of the ω_r-axis into the complex α-plane exhibits all of the possible spatially amplifying waves: waves travelling downstream, i.e. for $x > 0$, lie above the deformed F contour and have $\alpha_i^+(\omega_r) < 0$ for a band of spatially unstable frequencies ω_r, whereas those travelling upstream, i.e. for $x < 0$, lie below the deformed F contour and have $\alpha_i^-(\omega_r) > 0$ for some values ω_r.
Hence, in case of convective instability, the unstable modes can be found by solving the dispersion relation for complex wave numbers α given real frequencies ω.

For illustration, a single unstable temporal mode $\omega(\alpha)$ with maximum growth rate $\omega_i^{\max} > 0$ is assumed, which exhibits a single second-order algebraic branch point ω^0 with two spatial branches $\alpha^+(\omega)$ and $\alpha^-(\omega)$. In the respective Figures 2.2 and 2.3, the transformation of contours L, F, and the branches involved is sketched in case of convective and absolute instability.

To summarize, just as the sign of the maximum growth rate $\omega_i^{\max}$ determines the unstable/stable nature of the flow, the sign of the absolute growth rate ω_i^0 determines its absolute/convective nature. It is noted, that since ω_i^0 characterizes the temporal evolution of the wave number α^0 observed at a fixed location in the limit $t \to \infty$, and $\omega_i^{\max}$ is observed following the peak of the wave packet, one necessarily has $\omega_i^0 \leq \omega_i^{\max}$ [30].
For convectively unstable flows, spatial branches associated with L lying on the ω_r-axis do have a physical meaning. Contrary, in case of absolute instability, spatial branches are meaningless, as they cannot be obtained in the transformation process without violating causality.

In inviscid theory the dispersion relation often takes simple analytical forms for piecewise linear velocity distributions. In this case, one can directly look for a complex pair (α^0, ω^0) of zero group velocity such that

$$\frac{\partial \omega}{\partial \alpha}(\alpha^0) = 0, \quad \text{and} \quad \omega^0 = \omega(\alpha^0). \tag{2.139}$$

This is done in Chapter 4 for piecewise linear mixing layer flows. However, in general the value of ω_i^0 can only be identified by detecting the cusp in the complex ω-plane [35], or the saddle point in the complex α-plane [29, 33]. The latter method is used in Chapter 5 to identify absolute instability in viscous mixing layer flow.

Chapter 3

Numerical Methods

Although the dispersion relation can be given analytically in inviscid flow for piecewise linear velocity profiles, see Chapter 4, this is not possible in the general case. The linear instability problem can then only be solved approximately using numerical methods, where the governing equations are discretized to give an algebraic generalized eigenvalue problem. Discretization can be performed by employing a finite difference technique, finite elements, or spectral methods. The latter can be distinguished by both the type of the method (Galerkin, collocation, or tau), and also the particular choice of the trial functions, e.g. trigonometric polynomials, Legendre polynomials, or Chebyshev polynomials [11].
For solving the viscous instability problem of two-phase mixing layers in Chapter 5, a Chebyshev spectral method is used. In this approach, an approximate solution of the governing equations is found by expanding the dependent variables in terms of Chebyshev polynomials. The usefulness and accuracy of this approach was demonstrated by Orszag [45] and Danabasoglu and Biringen [14] for solving the linear eigenvalue problem in plane Poiseuille flow for temporally and spatially growing perturbations, respectively. If the undisturbed velocity profile $U(y)$ is infinitely differentiable, approximations in Chebyshev polynomials are infinite-order accurate in the sense that errors decrease more rapidly than any power of $1/N$ as $N \to \infty$, where $N+1$ is the number of Chebyshev polynomials retained in the approximation [45].

The discretized equations of instability subject to the appropriate boundary conditions constitute a generalized algebraic eigenvalue problem. From a numerical point of view, there are two general concepts of finding its solutions:

- Local methods start with an initial guess for the eigenvalue and the original eigenvalue problem is solved as an initial value problem. By iteration, the initial guess is adjusted until the boundary conditions match the computed solution [52]. One example of a local iteration procedure is the *shooting method*, in which an initial guess is made for the eigenvalue, and then integration is performed over the domain. Local methods are highly accurate. However, a good initial guess is required to assure convergence. In addition, the determination of eigensolutions other than the least stable may be difficult.

- Global methods compute a large part of the eigenvalue spectrum for the fully discretized instability equations rather than a single eigenvalue only [52]. One such method is based on the generalized Schur decomposition (also called *QZ decomposition*), which factorizes the square matrices of a generalized eigenvalue problem $A\vec{q} = \lambda B\vec{q}$ as $A = QSZ^H$ and $B = QTZ^H$, where Q, Z are unitary, and S, T are upper triangular matrices. For $\vec{q} \neq 0$ the generalized eigenvalues can then be calculated as the ratio of the diagonal elements of S to those of T, i.e., $\lambda_i = S_{ii}/T_{ii}$, provided $T_{ii} \neq 0$ [21]. The QZ algorithm is implemented in the LAPACK routine $ZGGEV$, which is used for computing the eigenvalues of the viscous instability problem.

3.1 Expansion in Chebyshev Polynomials

As mentioned, in the present work the governing equations of linear instability are discretized using Chebyshev polynomials. These trial functions are orthogonal on the interval $[-1, 1]$. Further properties of Chebyshev polynomials are given in Appendix A.2.
The discretization of the dynamical equations and boundary conditions for both the tau method and the collocation method is given in Sections 3.2 and 3.3, respectively. For illustration, exept of Section 3.6, single-fluid flow is considered in this chapter. If the lengthscale L is chosen, so that the physical and numerical domains coincide, the Orr-Sommerfeld and Squire equations (2.76) and (2.77) governing the instability of three-dimensional perturbations are given for $-1 < y < 1$, and the boundary conditions (2.78) and (2.79) are imposed at $y = \pm 1$. Then, approximating the functions ϕ and η by a Chebyshev expansion,

$$\phi(y) = \sum_{j=0}^{N} a_j T_j(y), \qquad \eta(y) = \sum_{j=0}^{N} e_j T_j(y), \tag{3.1}$$

where a_j and e_j denote the expansion coefficients of ϕ and η, respectively, the stability eigenvalue problem is formulated either as tau or collocation method.

3.2 Chebyshev tau Method

The solutions of the linearized stability equations depend on the basic state velocity profile $U(y)$. For the tau method, as the eigenfunctions the velocity distribution is expanded in Chebyshev polynomials:

$$U(y) = \sum_{j=0}^{N} A_j T_j(y). \tag{3.2}$$

Because the basic flow is given, the coefficients A_j are known. Further, Chebyshev expansions of the derivatives $\phi^{(q)}$, $\eta^{(q)}$ and $U^{(q)}$, $q \geq 0$, can be formally defined as

$$\phi^{(q)}(y) = \frac{\partial^q \phi}{\partial y^q} = \sum_{j=0}^{N} a_j^{(q)} T_j(y), \qquad \eta^{(q)}(y) = \frac{\partial^q \eta}{\partial y} = \sum_{j=0}^{N} e_j^{(q)} T_j(y) \tag{3.3}$$

and

$$U^{(q)}(y) = \frac{\partial^q U}{\partial y^q} = \sum_{j=0}^{N} A_j^{(q)} T_j(y), \tag{3.4}$$

where $a_j^{(0)} = a_j$, $e_j^{(0)} = e_j$ and $A_j^{(0)} = A_j$. Using relations (3.1)-(3.4), the Orr-Sommerfeld and Squire equations (2.76) and (2.77) take the form

$$\begin{aligned} &\left[k^4 + i\alpha R k^2 \sum_{j=0}^{N} A_j T_j + i\alpha R \sum_{j=0}^{N} A_j^{(2)} T_j\right] \sum_{j=0}^{N} a_j T_j \\ &\quad - \left[2k^2 + i\alpha R \sum_{j=0}^{N} A_j T_j\right] \sum_{j=0}^{N} a_j^{(2)} T_j + \sum_{j=0}^{N} a_j^{(4)} T_j \;=\; i\omega R \left(k^2 \sum_{j=0}^{N} a_j T_j - \sum_{j=0}^{N} a_j^{(2)} T_j\right) \end{aligned} \tag{3.5}$$

and

$$\begin{aligned} &- \left[k^2 + i\alpha R \sum_{j=0}^{N} A_j T_j\right] \sum_{j=0}^{N} e_j T_j + \sum_{j=0}^{N} e_j^{(2)} T_j \\ &\qquad -i\beta R \left(\sum_{j=0}^{N} A_j^{(1)} T_j\right) \left(\sum_{j=0}^{N} a_j T_j\right) \;=\; -i\omega R \sum_{j=0}^{N} e_j T_j. \end{aligned} \tag{3.6}$$

The coefficients $a_j^{(q)}$, $e_j^{(q)}$ and $A_j^{(q)}$ in equations (3.5), (3.6) for $q > 0$ can be formulated in terms of a_j, e_j and A_j as follows [45]:

The derivatives of an infinitely differentiable function $h(y)$ expanded in Chebyshev polynomials can be represented formally as

$$h^{(q)}(y) = \frac{\partial^q}{\partial y^q} h(y) = \sum_{j=0}^{N} h_j^{(q)} T_j(y), \qquad q \geq 0,$$

with $h_j = h_j^{(0)}$. Using relation (A.22), i.e.

$$C_{j-1} h_{j-1}^{(q)} - h_{j+1}^{(q)} = 2j h_j^{(q-1)}, \qquad j \geq 1,$$

the coefficients of the derivatives, $h_j^{(q)}$, $q \geq 1$, can be expressed completely in terms of h_j, where $C_0 = 2$ and $C_j = 1$, $j \geq 1$. One obtains, for example,

$$C_j h_j^{(1)} = 2 \sum_{\substack{k = j+1 \\ k+j = 1 (mod 2)}}^{N} k h_k, \tag{3.7}$$

$$C_j h_j^{(2)} = \sum_{\substack{k = j+2 \\ k = j (mod 2)}}^{N} k(k^2 - j^2) h_k \tag{3.8}$$

and

$$C_j h_j^{(4)} = \frac{1}{24} \sum_{\substack{k = j+4 \\ k = j (mod 2)}}^{N} k[k^2(k^2-4)^2 - 3j^2k^4 + 3j^4k^2 - j^2(j^2-4)^2] h_k, \tag{3.9}$$

all with $j \geq 0$, see Appendix A.2. Further, in (3.5), (3.6) products of two functions and/or their derivatives expanded in Chebyshev polynomials occur. Let

$$U^{(p)}(y) = \sum_{j=0}^{N} A_j^{(p)} T_j(y) \quad \text{and} \quad h^{(q)}(y) = \sum_{j=0}^{N} h_j^{(q)} T_j(y).$$

Their product is given as

$$2\ U^{(p)}(y)\ h^{(q)}(y) = \sum_{j=0}^{N} g_j T_j(y), \tag{3.10}$$

where

$$g_j = \frac{1}{C_j} \sum_{k=0}^{N} \left(C_{|j-k|} A_{|j-k|}^{(p)} + C_{j+k} A_{j+k}^{(p)} \right) h_k^{(q)}, \tag{3.11}$$

and $A_j^{(p)} = 0$, $j > N$. Relation (3.11) is equivalent to formula (A7) in Orszag's paper [45].

Together with (3.7)-(3.11), relations (3.5), (3.6) are expressed in $2(N+1)$ equations only in terms of the coefficients $a_0, \ldots, a_N$ and $e_0, \ldots, e_N$. Using (A.15) and (A.16) the boundary conditions read

$$\sum_{j=0}^{N} (\pm 1)^j a_j = \sum_{j=0}^{N} j^2 (\pm 1)^j a_j = \sum_{j=0}^{N} (\pm 1)^j e_j = 0. \tag{3.12}$$

One would thus obtain $2(N+1)+6$ equations for only $2(N+1)$ unknown coefficients $a_0, \ldots, a_N$ and $e_0, \ldots, e_N$. Now, the idea of the tau method is to apply the Orr-Sommerfeld and Squire equations only for $j = 0, ..., N-4$, and $j = 0, ..., N-2$, respectively, whereas the high frequency (i.e. high j) behaviour of the solution is determined by the boundary conditions. As a result, one obtains $2(N+1)$ equations for $2(N+1)$ unknowns [45].

3.3 Chebyshev Collocation Method

For the collocation method only the eigenfunctions and its derivatives $\phi^{(q)}$ and $\eta^{(q)}$ are approximated by a series of Chebyshev polynomials,

$$\phi^{(q)}(y) = \frac{\partial^q \phi}{\partial y^q} = \sum_{j=0}^{N} a_j T_j^{(q)}(y), \quad \text{and} \quad \eta^{(q)}(y) = \frac{\partial^q \eta}{\partial y} = \sum_{j=0}^{N} e_j T_j^{(q)}(y), \qquad q \geq 0. \tag{3.13}$$

Then the dynamical equations (2.76) and (2.77) read

$$\begin{aligned} &\left[k^4 + i\alpha R k^2 U + i\alpha R U''\right] \sum_{j=0}^{N} a_j T_j \\ &- \left[2k^2 + i\alpha R U\right] \sum_{j=0}^{N} a_j T_j'' + \sum_{j=0}^{N} a_j T_j^{iv} \;=\; i\omega R \left(k^2 \sum_{j=0}^{N} a_j T_j - \sum_{j=0}^{N} a_j T_j'' \right), \end{aligned} \tag{3.14}$$

$$- \left[k^2 + i\alpha R U\right] \sum_{j=0}^{N} e_j T_j + \sum_{j=0}^{N} e_j T_j'' - i\beta R U' \sum_{j=0}^{N} a_j T_j = -i\omega R \sum_{j=0}^{N} e_j T_j, \tag{3.15}$$

where $' \equiv \partial/\partial y$. The derivatives of the Chebyshev polynomials can be obtained by formal differentiation of (A.12),

$$T_j(\tilde{y}) = \cos(j \arccos(\tilde{y})), \qquad j \geq 0.$$

Thus, for example,

$$T_j'(y) = \frac{\sin(j \arccos(y)) j}{\sqrt{1-y^2}},$$

$$T_j''(y) = -\frac{\cos(j \arccos(y)) j^2}{1-y^2} + \frac{\sin(j \arccos(y)) j y}{\sqrt{1-y^2}^3}.$$

Now, equations (3.14) and (3.15) for the functions ϕ and η are required at the Gauß-Lobatto points [11],

$$y_k = \cos\left(\frac{\pi k}{N}\right), \qquad k = 0, \ldots, N. \tag{3.16}$$

Consequently, the basic velocity profile and its derivatives need only be known at exactly these points y_k. In addition with the boundary conditions (3.12),

$$\sum_{j=0}^{N} (\pm 1)^j a_j = \sum_{j=0}^{N} j^2 (\pm 1)^j a_j = \sum_{j=0}^{N} (\pm 1)^j e_j = 0,$$

one would again result into $2(N+1)+6$ equations for only $2(N+1)$ unknowns. Equation (3.14) is therefore only required at the Gauß-Lobatto points $y_2, \ldots, y_{N-2}$, whereas the boundary conditions $\phi(\pm 1) = \phi'(\pm 1) = 0$ are introduced at y_0, y_1, y_{N-1}, y_N. Similarly, (3.15) is only imposed for $y_1, \ldots, y_{N-1}$, and the boundary conditions $\eta(\pm 1) = 0$ are introduced at y_0 and y_N.

3.4 Modified Equations of Linearized Stability

Since the Orr-Sommerfeld equation (2.76) involves the fourth order derivative of $\phi(y)$, for the tau method the terms in the discretization matrix grow like $O(N^7)$. This is evident from (3.9). In addition, the normal stress boundary condition in the linear stability problem for two-fluid flow involves third order derivatives, see Section 2.1. Then, in the discretization matrix the corresponding terms grow like $O(N^6)$ for both the tau method and the collocation method.

This is evident from (A.18). Since in the calculations often a large number of polynomials is required ($N \geq 100$), this growth rates can lead to serious round off error problems. Therefore, Dongarra et al. [16] suggest to reduce the order of the differential equations whenever possible. Writing the Orr-Sommerfeld equation (2.76) as two equations involving only derivatives up to the second order,

$$\xi(y) = \left(\frac{\partial^2}{\partial y^2} - \alpha^2 - \beta^2\right)\phi(y), \tag{3.17}$$

$$\left[(-i\omega + i\alpha U) - \frac{1}{R}\left(\frac{\partial^2}{\partial y^2} - \alpha^2 - \beta^2\right)\right]\xi(y) - i\alpha U''\phi(y) = 0, \tag{3.18}$$

for the tau method the terms in the discretization matrix for the single-fluid problem now grow at most like $O(N^3)$; see (3.8). Since the Squire equation (2.77) is already of second order, it remains unchanged. This modified system of the governing equations is written below to result into generalized eigenvalue problems $A(\alpha)\vec{q} = \omega B(\alpha)\vec{q}$ and $A(\omega)\vec{q} = \alpha B(\omega)\vec{q}$ for temporally growing and spatially growing modes, respectively.

3.4.1 Temporal Generalized Eigenvalue Problem

In the formulation (3.17), (3.18), (2.77), the frequency ω appears linearly in each equation. Since, for the temporal spectrum, the governing equations are solved for complex frequencies ω given real wave numbers α and β, the expressions involving ω are grouped together on the right-hand side of each equation to give a generalized eigenvalue problem of the form $A\vec{q} = \omega B\vec{q}$.

Chebyshev tau Formulation

In order to write the decomposed Orr-Sommerfeld equation (3.17), (3.18) as tau method, Chebyshev expansions of the introduced function ξ and its derivatives are required,

$$\xi^{(q)}(y) = \frac{\partial^q \xi}{\partial y^q} = \sum_{j=0}^{N} b_j^{(q)} T_j(y), \tag{3.19}$$

where $b_j^{(0)} = b_j$. Together with (3.1)-(3.4) one obtains

$$-\sum_{j=0}^{N} b_j T_j - \left[\alpha^2 + \beta^2\right]\sum_{j=0}^{N} a_j T_j + \sum_{j=0}^{N} a_j^{(2)} T_j = 0, \tag{3.20}$$

$$-\left[\alpha^2 + \beta^2 + i\alpha R\sum_{j=0}^{N} A_j T_j\right]\sum_{j=0}^{N} b_j T_j + \sum_{j=0}^{N} b_j^{(2)} T_j + i\alpha R\left(\sum_{j=0}^{N} A_j^{(2)} T_j\right)\left(\sum_{j=0}^{N} a_j T_j\right) = -i\omega R\sum_{j=0}^{N} b_j T_j. \tag{3.21}$$

Determining the high frequency (i.e. high j) behaviour of the solution by the boundary conditions (3.12) as in Section 3.2, the instability problem can be written as $3(N+1)$ equations for the $3(N+1)$ unknowns a_j, b_j and e_j with $0 \leq j \leq N$.
For comparison, because $\xi(y)$ is not needed in the traditional method of solving the Orr-Sommerfeld equation involving the fourth derivative, the matrices of the resulting generalized eigenvalue problem are of size $2(N+1)\times 2(N+1)$ only. However, for the tau method the growth rate of the derivative coefficients reduces from $O(N^7)$ for the traditional method to $O(N^3)$ for the recent method. Due to this reduced growth rate the modified method is more accurate.

In the respect of growth rate reduction, a formulation of the linearized instability equations as six equations involving only derivatives up to the first order would be even better, with terms growing only like $O(N)$. However, in this case the matrices of the resulting generalized eigenvalue problem would be of size $6(N+1) \times 6(N+1)$. Since the computer time required to use the QZ matrix eigenvalue routine is proportional to the cube of the number of polynomials, this further modification is not advantageous [16]. For the spatial formulation, however, it will be necessary to write the govering equations as eigenvalue problem of that size in order to result into the form $A\vec{q} = \alpha B\vec{q}$; see Section 3.4.2.

Chebyshev Collocation Formulation

Of course, analogous a Chebyshev collocation method based on the decomposed Orr-Sommerfeld equation can be formulated. With relations (3.13) and

$$\xi^{(q)}(y) = \frac{\partial^q \xi}{\partial y^q} = \sum_{j=0}^{N} b_j T_j^{(q)}(y) \tag{3.22}$$

for the new function ξ and its derivatives, equations (3.17), (3.18) read

$$-\sum_{j=0}^{N} b_j T_j - \left[\alpha^2 + \beta^2\right] \sum_{j=0}^{N} a_j T_j + \sum_{j=0}^{N} a_j T_j'' = 0, \tag{3.23}$$

$$-\left[\alpha^2 + \beta^2 + i\alpha RU\right] \sum_{j=0}^{N} b_j T_j + \sum_{j=0}^{N} b_j T_j'' + i\alpha RU'' \sum_{j=0}^{N} a_j T_j = -i\omega R \sum_{j=0}^{N} b_j T_j. \tag{3.24}$$

Applying each of the equations (3.23), (3.24), (3.15) at the Gauß-Lobatto points, $y_1, \ldots, y_{N-1}$, and adding the boundary conditions (3.12) at y_0 and y_N, one finally obtains $3(N+1)$ equations for $3(N+1)$ unknowns.

Generalized Eigenvalue Problem

For both the tau method and the collocation method, a generalized eigenvalue problem of the form

$$A\vec{q} = \omega B\vec{q} \tag{3.25}$$

is obtained with complex eigenvalues $\omega = \omega_r + i\omega_i$. In the case of three-dimensional perturbations, (3.25) reads

$$\begin{bmatrix} A_{11} & A_{12} & 0 \\ A_{21} & A_{22} & 0 \\ A_{31} & 0 & A_{33} \\ \star & \star & \star \end{bmatrix} \begin{bmatrix} \vec{a} \\ \vec{b} \\ \vec{e} \end{bmatrix} = \omega \begin{bmatrix} 0 & 0 & 0 \\ 0 & B_{22} & 0 \\ 0 & 0 & B_{33} \\ \star & \star & \star \end{bmatrix} \begin{bmatrix} \vec{a} \\ \vec{b} \\ \vec{e} \end{bmatrix}, \tag{3.26}$$

where the submatrices correspond to

$$A_{11} = \alpha^2 + \beta^2 - \frac{\partial^2}{\partial y^2}, \quad A_{12} = 1, \quad A_{21} = -i\alpha U'', \quad A_{22} = A_{33}, \quad B_{22} = i,$$

$$A_{31} = i\beta U', \quad A_{33} = i\alpha U + \frac{1}{R}\left(\alpha^2 + \beta^2 - \frac{\partial^2}{\partial y^2}\right), \quad B_{33} = i,$$

and the vectors $\vec{a} = [a_0, \ldots, a_N]^T$, $\vec{b} = [b_0, \ldots, b_N]^T$, and $\vec{e} = [e_0, \ldots, e_N]^T$ contain the Chebyshev coefficients of the functions ϕ, ξ and η, respectively. In addition, the symbols $\star$ refer to the boundary conditions. For two-dimensional perturbations $\beta = 0$, $\vec{q} = [\vec{a}, \vec{b}]^T$, and

$$A = \begin{bmatrix} A_{11} & A_{12} \\ A_{21} & A_{22} \\ \star & \star \end{bmatrix}, \quad B = \begin{bmatrix} 0 & 0 \\ 0 & B_{22} \\ \star & \star \end{bmatrix}.$$

In the resulting eigenvalue problem (3.25), the matrix B is generally singular, because it necessarily involves rows of zeros. This is both due to the way the boundary conditions are added to A, and as a result of equation (3.17) in the modified formulation. It leads to the production of spurious eigenvalues. These numbers are not solutions to the differential equation. They rather are approximations of infinite eigenvalues, and result when solving (3.25) by means of the QZ algorithm by decomposing the matrices as $A = QSZ^H$ and $B = QTZ^H$ [21]. Since the eigenvalues are obtained as the ratio of the diagonal elements of S to those of T, infinite eigenvalues have $T_{ii} = 0$, and can therefore easily be filtered out.

3.4.2 Spatial Generalized Eigenvalue Problem

In the formulation (3.17), (3.18), (2.77), the streamwise wave number α appears up to the second power in each equation. Since, for the spatial spectrum, the governing equations are solved for complex streamwise wave numbers α, the expressions involving α are grouped together on the right-hand side of each equation to give a generalized eigenvalue problem of the form

$$A(\omega)\vec{q} = \alpha B(\omega)\vec{q}. \tag{3.27}$$

Therefore, additional functions $\tilde{\phi}$, $\tilde{\xi}$ and $\tilde{\eta}$ need to be defined,

$$\tilde{\phi} = \alpha\phi, \qquad \tilde{\xi} = \alpha\xi, \qquad \tilde{\eta} = \alpha\eta, \tag{3.28}$$

and expanded in Chebychev polynomials as

$$\tilde{\phi}(y) = \sum_{j=0}^{N} c_j T_j(y), \qquad \tilde{\xi}(y) = \sum_{j=0}^{N} d_j T_j(y), \qquad \tilde{\eta}(y) = \sum_{j=0}^{N} f_j T_j(y). \tag{3.29}$$

Then, the instability equations linear in α read

$$\left(\frac{\partial^2}{\partial y^2} - \beta^2\right)\phi - \xi = \alpha\tilde{\phi}, \tag{3.30}$$

$$\left(\frac{\partial^2}{\partial y^2} - \beta^2 + i\omega R\right)\xi + iRU''\tilde{\phi} - iRU\tilde{\xi} = \alpha\tilde{\xi}, \tag{3.31}$$

$$\left(\frac{\partial^2}{\partial y^2} - \beta^2 + i\omega R\right)\eta - i\beta RU'\phi - iRU\tilde{\eta} = \alpha\tilde{\eta}. \tag{3.32}$$

The above equations including the boundary conditions $\phi(\pm1) = \phi'(\pm1) = \eta(\pm1) = 0$ can be formulated either as tau or collocation method as outlined in the previous sections. Then, in the case of three-dimensional perturbations, (3.27) reads

$$\begin{bmatrix} 0 & 0 & 0 & 1 & 0 & 0 \\ 0 & 0 & 0 & 0 & 1 & 0 \\ 0 & 0 & 0 & 0 & 0 & 1 \\ A_{41} & A_{42} & 0 & 0 & 0 & 0 \\ 0 & A_{52} & 0 & A_{54} & A_{55} & 0 \\ A_{61} & 0 & A_{63} & 0 & 0 & A_{66} \\ \star & \star & \star & \star & \star & \star \end{bmatrix} \begin{bmatrix} \vec{a} \\ \vec{b} \\ \vec{e} \\ \vec{c} \\ \vec{d} \\ \vec{f} \end{bmatrix} = \alpha \begin{bmatrix} 1 & 0 & 0 & 0 & 0 & 0 \\ 0 & 1 & 0 & 0 & 0 & 0 \\ 0 & 0 & 1 & 0 & 0 & 0 \\ 0 & 0 & 0 & 1 & 0 & 0 \\ 0 & 0 & 0 & 0 & 1 & 0 \\ 0 & 0 & 0 & 0 & 0 & 1 \\ \star & \star & \star & \star & \star & \star \end{bmatrix} \begin{bmatrix} \vec{a} \\ \vec{b} \\ \vec{e} \\ \vec{c} \\ \vec{d} \\ \vec{f} \end{bmatrix}, \tag{3.33}$$

where the submatrices correspond to

$$A_{41} = \frac{\partial^2}{\partial y^2} - \beta^2, \qquad A_{42} = -1, \qquad A_{52} = A_{41} + i\omega R, \qquad A_{54} = iRU'', \qquad A_{55} = -iRU,$$

$$A_{61} = i\beta RU', \qquad A_{63} = A_{52}, \qquad A_{66} = A_{55},$$

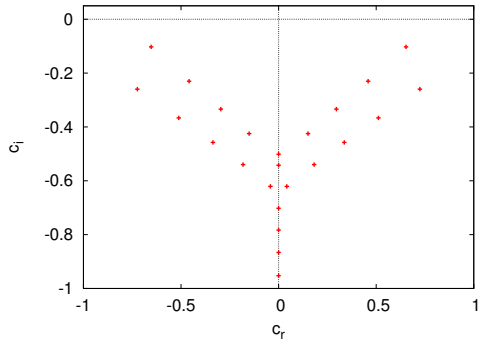

Figure 3.1: *Temporal Orr-Sommerfeld spectrum for plane Couette flow with* $\alpha = 1$, $\beta = 0$, *and* $R = 1500$. *The eigenvalues were computed using the Chebyshev tau method with* $N = 150$.

and the vectors $\vec{a} = [a_0, \ldots, a_N]^T$, $\vec{b} = [b_0, \ldots, b_N]^T$, $\vec{e} = [e_0, \ldots, e_N]^T$, $\vec{c} = [c_0, \ldots, c_N]^T$, $\vec{d} = [d_0, \ldots, d_N]^T$, and $\vec{f} = [f_0, \ldots, f_N]^T$ contain the Chebyshev coefficients of ϕ, ξ,η, $\tilde{\phi}$, $\tilde{\xi}$, and $\tilde{\eta}$ respectively. In addition, the symbols $\star$ refer to the boundary conditions. Note, that the matrices in the eigenvalue problem are of the size $6(N+1)\times 6(N+1)$. They are therefore twice as large as their temporal counterparts. For two-dimensional perturbations $\beta = 0$, $\vec{q} = [\vec{a}, \vec{b}, \vec{c}, \vec{d}]^T$, and

$$A = \begin{bmatrix} 0 & 0 & 1 & 0 \\ 0 & 0 & 0 & 1 \\ A_{41} & A_{42} & 0 & 0 \\ 0 & A_{52} & A_{54} & A_{55} \\ \star & \star & \star & \star \end{bmatrix}, \qquad B = \begin{bmatrix} 1 & 0 & 0 & 0 \\ 0 & 1 & 0 & 0 \\ 0 & 0 & 1 & 0 \\ 0 & 0 & 0 & 1 \\ \star & \star & \star & \star \end{bmatrix}.$$

Note finally, that in (3.27) there is no restriction to real values of the frequency ω. Indeed, in order to investigate the transition from convective to absolute instability, it is necessary to compute generalized spatial branches, i.e. instability curves for a given frequency with $\omega_i \neq 0$; see Section 3.5.3.

3.5 Application to Plane Couette-Poiseuille Flow

Before extending the numerical method to include a second layer in Section 3.6, for illustration the well known plane Couette-Poiseuille flow is reconsidered. In plane Poiseuille flow the basic flow is driven by a pressure gradient in the x-direction, whereas plane Couette flow is driven by the boundaries being sheared relative to each other. Choosing the half channel width as characteristic length scale L, the channel boundaries are located at $y = \pm 1$. Thus, the physical domain coincides with those of the Chebyshev polynomials. In addition, the characteristic velocity U^* is chosen to be the difference of centerline velocity and velocity at the walls. Then the dimensionless mean velocity profiles are $U(y) = y$ for plane Couette flow and $U(y) = 1 - y^2$ for plane Poiseuille flow. For the tau method, the basic velocity profile is given in terms of Chebyshev polynomials. In the case of plane Poiseuille flow, the expansion coefficients are

$$A_0 = 1/2, \qquad A_1 = 0, \qquad A_2 = -1/2, \qquad A_j = 0, \ j \geq 3.$$

In plane Couette flow one has

$$A_0 = 0, \qquad A_1 = 1, \qquad A_j = 0, \ j \geq 2.$$

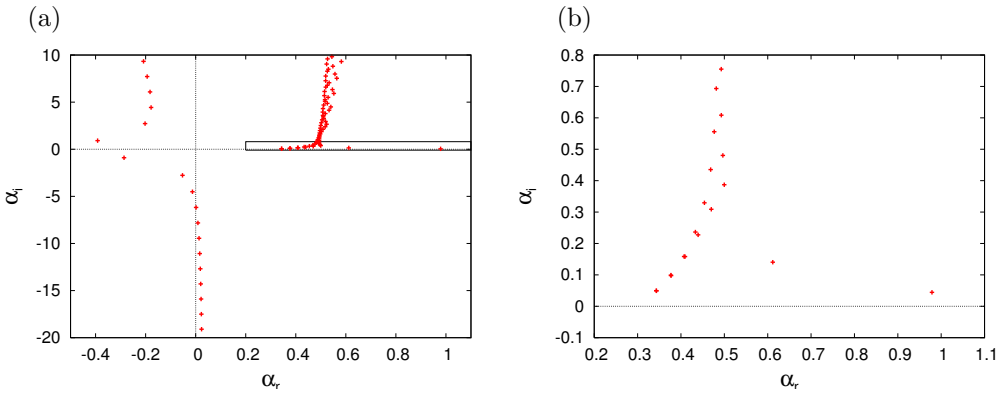

Figure 3.2: *Spatial Orr-Sommerfeld spectrum for plane Poiseuille flow with* $\omega = 0.3$, $\beta = 0$, *and* $R = 2000$. *(a) Entire spectrum, (b) blow up of region indicated in (a). The eigenvalues were computed using the Chebyshev collocation method with* $N = 150$.

For the collocation method the underlying basic velocity profiles are given at the Gauß-Lobatto points (3.16),

$$y_k = \cos\left(\frac{\pi k}{N}\right), \qquad k = 0, \ldots, N.$$

3.5.1 Temporal Spectra

As an example, the method presented in Section 3.4.1 is applied for two-dimensional perturbations in plane Couette flow. Therefore, the modified formulation (3.17), (3.18) of the Orr-Sommerfeld equation is solved subject to the boundary conditions $\phi(\pm 1) = \phi'(\pm 1) = 0$ for $\beta = 0$, and real values of α with a sufficient number of polynomials. For $\alpha = 1$ and $R = 1500$ the eigenvalues were computed using the tau method with $N = 150$. Their distribution in terms of the complex wave speed $c = c_r + ic_i = \omega/\alpha$ is shown in Figure 3.1. The quantity c_r is the phase speed of the perturbation, and αc_i is the temporal growth rate. The temporal eigenvalues distribute themselves along three branches. There are two branches of complex conjugate pairs and a third one, with eigenvalues having $c_r = 0$. Since the critical Reynolds number is $R_c = \infty$, plane Couette flow is linearly stable for all values of R, and $c_i < 0$ for all eigenvalues [17, 52].

3.5.2 Spatial Spectra

An example of a spatial Orr-Sommerfeld spectrum for two-dimensional perturbations ($\beta = 0$) is shown in Figure 3.2 for plane Poiseuille flow with $\omega = 0.3$, and $R = 2000$. The spatial eigenvalues were computed by applying the method presented in Section 3.4.2 using Chebyshev collocation with $N = 150$. Since $R < R_c \approx 5772$, the flow is linearly stable [17, 52]. Note, that the spatial spectrum displays a more complicated structure than the temporal one. In particular, there are eigenvalues in all four quadrants. The eigenvalues in quadrants I and IV have positive phase velocities, whereas those in quadrants II and III have negative phase velocities [52].

3.5.3 Generalized Spatial Branches

As in the temporal case, there exists a large number of complex eigenvalues α_j in plane Poiseuille flow for a given frequency $\omega = \omega_r + i\omega_i$, where $\omega_i = 0$ for spatial modes, and $\omega_i \neq 0$ for generalized spatial branches [29, 31]. Because of the symmetry in the problem, the curves $\alpha_j(\omega)$ are symmetric with respect to the imaginary α-axis. Therefore, further discussion is restricted to the case $\alpha_r \geq 0$. As shown in Section 2.6.2, the branches originate on both sides of the real α-axis, where as $\omega_i > \omega_i^{\max}$ decreases down to zero the curves $\alpha_j^-(\omega)$ originating in the

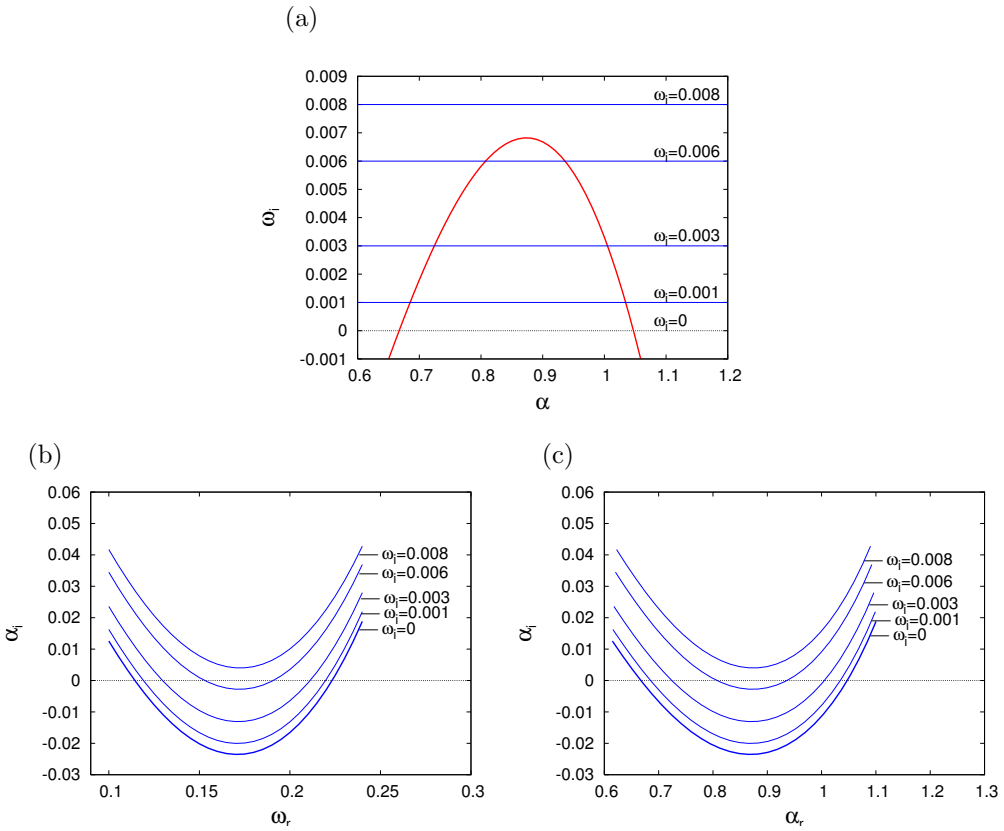

Figure 3.3: *(a) Temporal growth rate ω_i of the unstable eigenmode as a function of the streamwise wave number α. In (b) and (c) α_i is shown as a function of ω_r and α_r, respectively. The Reynolds number is $R = 20000$ and $\beta = 0$.*

lower half-plane move up, and the curves $\alpha_j^+(\omega)$ originating in the upper half-plane move down. However, only those branches that pass from one side of the α_r-axis to the other contribute to the spatial amplification. Therefore, the discussion is restricted to this spatially unstable modes.

As an example, for plane Poiseuille flow generalized spatial instability results are discussed for two-dimensional perturbations ($\beta = 0$), and $R = 20000$. Since $R > R_c \approx 5772$, the flow is linearly unstable, and the instability is of the Tollmien-Schlichting type [17, 52]. In Figure 3.3(a) the temporal growth rate ω_i of the only unstable eigenmode is shown as a function of the real streamwise wave number α. Amplifying waves exist in the range $0.665 \leq \alpha \leq 1.056$ [8], and the maximum growth rate $\omega_i^{\max} = 0.00682$ is realized at $\alpha^{\max} = 0.87$.

The spatial growth rate of the unstable mode is shown in Figures 3.3(b) and (c) as a function of the frequency ω_r and the streamwise wave number α_r, respectively. In addition, generalized spatial curves are presented for $\omega_i = 0.001$, $\omega_i = 0.003$, $\omega_i = 0.006$, and $\omega_i = 0.008$. As explained in Section 2.6.2, for the generalized spatial branch $\alpha_i(\omega_r) > 0$ in the case $\omega_i = 0.008 > \omega_i^{\max}$. As ω_i decreases, the unstable branch moves down, first touches the real α-axis at $\omega_i = \omega_i^{\max}$, and eventually enters the lower half-plane. Consequently, there exists a band of frequencies ω_r, so that $\alpha_i < 0$ for $\omega_i < \omega_i^{\max}$. For the spatial case ($\omega_i = 0$) amplifying waves exist for frequencies $0.114 \leq \omega_r \leq 0.223$ [8], and the maximum spatial growth rate $-\alpha_i^{\max} = 0.2353$ is realized at $\omega_r^{\max} \approx 0.17$ ($\alpha_r^{\max} \approx 0.87$); see Figures 3.3(b),(c). Since the curve $\alpha(\omega)$ passes the α_r-axis from above to below, the waves amplify for $x \to \infty$, i.e. downstream. Similarly, for $x \to -\infty$ the upstream contributions to the spatial amplification result from spatial branches $\alpha_j^-(\omega)$ that pass

from below to above the α_r-axis, as ω_i decreases. However, there are no waves that amplify upstream [8]. In addition, since the only unstable spatial branch does not pass the α_r-axis for $\omega_r = 0$, no stationary spatially amplifying waves exist in plane Poiseuille flow [8].
Finally, by numerical solution of the Orr-Sommerfeld equation in addition to an asymptotic analysis for large Reynolds numbers, Deissler [15] showed that there is no absolute instability in two-dimensional plane Poiseuille flow for any R. Hence, there is no collision of generalized spatial branches originating on opposite sides of the α_r-axis, as ω_i decreases from $\omega_i > \omega_i^{\max}$ to zero, indicating that plane Poiseuille flow is convectively unstable for $R_c < R < \infty$.

It is finally noted, that for flows in an unbounded domain a continuous spectrum may exist in addition to a disrete set of eigenvalues [13]. In both the temporal and spatial setting, the continuous spectrum is turned into a more or less dense discrete set of eigenvalues by means of the discretization. In the spatial case the continuous spectrum results into a branch cut along sections of the imaginary α-axis [52], and the approximation of this branch cut by discrete modes near the α_i-axis can modify the convective/absolute nature of a flow; see Section 5.5.

3.6 Numerical Method in Two-Phase Flows

In this section the numerical method for a single viscous fluid is extended to involve two fluids. First, general additional aspects in the numerics involving two phases are considered, followed by a reconsideration of two-fluid plane Poiseuille flow in order to validate the extended code.

3.6.1 General Considerations

Let the linearized equations governing the motion of perturbations in two-fluid flows, presented in Section 2.1, be given on the intervals $[-L_1, 0]$ and $[0, L_2]$ for the lower and upper layer, respectively. When introducing the functions ξ_1 and ξ_2 by

$$\xi_k(y) = \left(\frac{\partial^2}{\partial y^2} - \alpha^2 - \beta^2\right)\phi_k(y), \qquad k = 1, 2, \tag{3.34}$$

the Orr-Sommerfeld equations in each fluid can be decomposed into two equations involving only derivatives up to the second order, see Section 3.4. For using Chebyshev polynomials in order to expand the independent functions involved in the equations of two-fluid instability, the physical space has to be mapped onto the Chebyshev space $[-1, 1]$. This is achieved by changing the variable using a transformation function. Let y and $\tilde{y}$ denote the cross-stream variable in physical and numerical space, respectively. For example, when applying the linear transformations

$$y \in [-L_1, 0] \mapsto \tilde{y} \in [-1, 1]: \qquad \tilde{y} = \frac{2y}{L_1} + 1, \tag{3.35}$$

$$y \in [0, L_2] \mapsto \tilde{y} \in [-1, 1]: \qquad \tilde{y} = -\frac{2y}{L_2} + 1, \tag{3.36}$$

the governing equations in each layer are mapped onto $(-1, 1)$, the boundary conditions at $y = -L_1$ and $y = L_2$ are imposed at $\tilde{y} = -1$, and the interfacial conditions have to be applied at $\tilde{y} = 1$. Note, that the transformations (3.35) and (3.36) modify all terms in y:

Let $\phi(\tilde{y}) = \phi(y(\tilde{y}))$. Then

$$\frac{\partial \phi}{\partial \tilde{y}} = \frac{\partial \phi}{\partial y}\frac{\partial y}{\partial \tilde{y}} \tag{3.37}$$

by simple use of the chain differentiation rule. Using (3.37) and the product differentiation rule, the result for the second derivative is

$$\frac{\partial^2 \phi}{\partial \tilde{y}^2} = \frac{\partial^2 \phi}{\partial y^2}\left(\frac{\partial y}{\partial \tilde{y}}\right)^2 + \frac{\partial \phi}{\partial y}\frac{\partial^2 y}{\partial \tilde{y}^2}. \tag{3.38}$$

Since (3.35) and (3.36) are linear transformations, the second term in (3.38) vanishes. Then, y-differentiation changes to differentiation with respect to $\tilde{y}$,

$$\frac{\partial^q}{\partial \tilde{y}^q} = D_k^q \frac{\partial^q}{\partial y^q}, \qquad k, q = 1, 2, \tag{3.39}$$

where D_k, $k = 1, 2$, denote the ratios of the intervals involved in the linear transformations.

As for single-fluid flow, when expanding the dependent functions into a Chebyshev series, an eigenvalue problem (3.25),

$$A(\alpha)\vec{q} = \omega B(\alpha)\vec{q},$$

results for temporally growing perturbations. In the spatial case, when introducing the functions $\tilde{\phi}_k$, $\tilde{\xi}_k$ and $\tilde{\eta}_k$ as

$$\tilde{\phi}_k = \alpha\phi_k, \qquad \tilde{\xi}_k = \alpha\xi_k, \qquad \tilde{\eta}_k = \alpha\eta_k, \tag{3.40}$$

with $k = 1, 2$ refering to the phase, an eigenvalue problem (3.27),

$$A(\omega)\vec{q} = \alpha B(\omega)\vec{q},$$

linear in α is obtained. However, since the parameter f is explicitly included in the calculations using the kinematic condition, for both temporally growing and spatially growing perturbations $\vec{q} = [\vec{q}_1, \vec{q}_2, f]^T$, where $\vec{q}_1$, $\vec{q}_2$ contain the Chebyshev coefficients of the dependent functions. The matrices are of the form

$$A = \begin{bmatrix} A_1 & 0 & 0 \\ 0 & A_2 & 0 \\ \star & \star & \star \end{bmatrix}, \qquad B = \begin{bmatrix} B_1 & 0 & 0 \\ 0 & B_2 & 0 \\ \star & \star & \star \end{bmatrix},$$

where the submatrices A_k, B_k for each phase $k = 1, 2$ are coupled by the boundary conditions, denoted by $\star$. As for single-fluid flow, since the functions defined by relations (3.40) are included in the vectors $\vec{q}_k$ for the spatial eigenvalue problem, the matrices are about twice as large as those of the temporal system using the modified formulation.

3.6.2 Application to Two-Fluid plane Poiseuille Flow

For validation of the extended code, the temporal instability of plane Poiseuille flow of two superposed layers of fluids is reconsidered. This particular type of flow was investigated in a number of studies [16, 54, 59, 62]. In two-fluid plane Poiseuille flow the fluids are contained between two infinite parallel horizontal plates. Using the notation as in Reference [54], the dimensionless basic flow is given by

$$U_1(y) = C_\alpha + C_\beta y + C_\gamma y^2, \qquad 0 \le y \le 1, \tag{3.41}$$

$$U_2(y) = \tilde{C}_\alpha + \tilde{C}_\beta y + \tilde{C}_\gamma y^2, \qquad -n \le y \le 0, \tag{3.42}$$

where

$$C_\alpha = \tilde{C}_\alpha = \frac{1}{\tilde{V}}, \quad C_\beta = C_\alpha \frac{m - n^2}{n^2 + n}, \quad C_\gamma = -C_\alpha \frac{m + n}{n^2 + n}, \quad \tilde{C}_\beta = \frac{C_\beta}{m}, \quad \tilde{C}_\gamma = \frac{C_\gamma}{m},$$

and

$$\tilde{V} = 1 + \frac{(m - n^2)^2}{4(n^2 + n)(m + n)}, \qquad m \ge n^2,$$

or

$$\tilde{V} = 1 + \frac{(m - n^2)^2}{4m(n^2 + n)(m + n)}, \qquad m \le n^2.$$

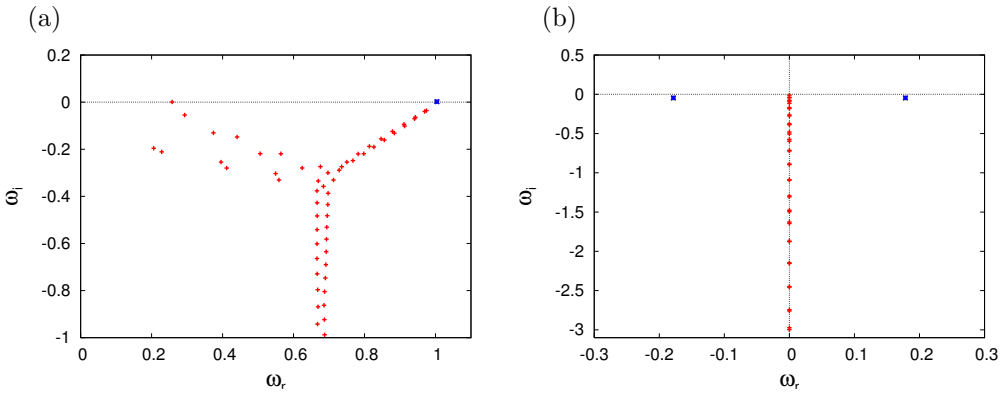

Figure 3.4: *Distribution of eigenvalues for two-fluid plane Poiseuille flow: (a) two-dimensional perturbations with* $\alpha = 1$, $\beta = 0$, $r = 1$, $m = 2$, $n = 1.2$, $R = 10000$, $S = 0$, *and (b) three-dimensional perturbations with* $\alpha = 0$, $\beta = 1$, $r = 0.9$, $m = 20$, $n = 1$, $R = 900$, $S = 0.1$.

Here $n = L_2/L_1$ denotes the ratio of the layer thickness of the lower fluid to those of the upper fluid. The additional dimensionless parameters are

$$r = \frac{\rho_2}{\rho_1}, \qquad m = \frac{\mu_2}{\mu_1}, \qquad R = \frac{\rho_1 U^* L_1}{\mu_1}, \qquad \text{and} \qquad S = \frac{s}{\rho_1 U^{*2} L_1},$$

where U^* denotes the maximum velocity of the mean profile $U(y)$. Gravity is neglected, $F = 0$.

When applying the tau method, the velocity profile (3.41), (3.42) must be mapped onto $[-1, 1]$, and expanded into Chebyshev polynomials as

$$U_1(\tilde{y}) = \sum_{j=0}^{N} A_j T_j(\tilde{y}), \qquad U_2(\tilde{y}) = \sum_{j=0}^{N} B_j T_j(\tilde{y}),$$

where

$$A_2 = \frac{1}{8} C_\gamma, \qquad A_1 = \frac{1}{2}(C_\gamma + C_\beta), \qquad A_0 = C_\alpha + A_1 - A_2,$$

$$B_2 = \frac{1}{8}\frac{n^2}{m} C_\gamma, \qquad B_1 = \frac{1}{2}\frac{n}{m}(nC_\gamma - C_\beta), \qquad B_0 = C_\alpha + B_1 - B_2,$$

and $A_j = B_j = 0$ for $j \geq 3$. Using Chebyshev collocation, the mean velocity profile is given at the Gauß-Lobatto points (3.16), i.e.

$$U(y) = \begin{cases} U_1(y(\tilde{y}_j)), & 0 \leq y \leq 1 \\ U_2(y(\tilde{y}_j)), & -n \leq y \leq 0 \end{cases} \qquad \text{and} \qquad \tilde{y}_j = \cos\left(\frac{\pi j}{N}\right), \quad j = 0, \ldots, N.$$

For validation, the two-fluid code is first performed for $r = m = n = 1$, and $S = 0$. In this limit the mean velocity profile (3.41), (3.42) reduces to the single-fluid profile $U(y) = 1 - y^2$, and Orszag's [45] linear stability results for two-dimensional perturbations ($\beta = 0$) in homogeneous flow are reproduced. Indeed, in the one-layer limit the eigenvalues of two-fluid plane Poiseuille flow are exactly the same as those for a single fluid, except that there is an additional neutral mode [63]. As is well known, the eigenvalues are distributed along three branches in the complex ω-plane, which meet at one confluence point.
In the presence of a viscosity contrast the Orr-Sommerfeld spectrum is modified. For $\alpha = 1$, $R = 10000$, $m = 2$ and $n = 1.2$ the temporal eigenvalue spectrum is shown in Figure 3.4(a). The eigenvalue distribution of two-fluid flow is similar as those for $m = n = 1$, except that the lower branch has split into two almost parallel branches. This splitting is observed as m increases

from 1, and is more pronounced as n increases. In addition to the red eigenvalues, which have a counterpart in the single-fluid formulation, the additional blue eigenvalue is associated with the deflected interface. Although this interfacial mode was shown to be neutrally stable in the single-fluid limit ($m = n = 1$), where $\omega = \alpha U(0)$, it is linearly unstable for $m = 2$ and $n = 1.2$. Thus, there are two distinct modes of possible instability in two-fluid plane Poiseuille flow if the Reynolds number is sufficiently high: one due to shear in the bulk of the fluids, whereas the other is due to the interface effect [63].
In addition, Figure 3.4(b) shows streamwise uniform three-dimensional disturbances ($\alpha = 0$). The remaining parameters are $\beta = 1$, $r = 0.9$, $m = 20$, $n = 1$, $R = 900$, and $S = 0.1$. The entire spectrum is located in the lower half-plane, and all but two modes have collapsed onto the axis $\omega_r = 0$. These two highly visible exceptions with $\omega_r \neq 0$ are shown in blue, and correspond to a pair of oppositely propagating weakly damped capillary waves [59].

3.6.3 Application to Two-Fluid Mixing Layers

For two-phase mixing layers the viscous velocity profile is parametrized by a combination of error functions; see Section 5.1. For this basic flow, it is advantageous to solve the instability problem using Chebyshev collocation, where one refers to the velocity profile at the Gauß-Lobatto points (3.16), i.e.

$$U(y) = \begin{cases} U_1(y(\tilde{y}_j)), & -L_1 \leq y \leq 0 \\ U_2(y(\tilde{y}_j)), & 0 \leq y \leq L_2 \end{cases} \quad \text{and} \quad \tilde{y}_j = \cos\left(\frac{\pi j}{N}\right), \quad j = 0, \ldots, N,$$

where $\tilde{y} \in [-1, 1]$. Contrary, for the tau method the mean velocity distribution $U(y)$ would have been expanded into a series of the Chebyshev trial functions as

$$U_1(\tilde{y}) = \sum_{j=0}^{N} A_j T_j(\tilde{y}), \qquad U_2(\tilde{y}) = \sum_{j=0}^{N} B_j T_j(\tilde{y}).$$

Since the error function cannot be given as a finite Taylor series, the above expansions are not exact for $N < \infty$. In addition, generally $A_j \neq 0$ and $B_j \neq 0$ for all $0 \leq j \leq N$.

Chapter 4

Instability of Inviscid Two-Phase Mixing Layers

Before analyzing the spatio-temporal instability of viscous two-phase mixing layer flows, an inviscid study is performed by adopting a piecewise linear velocity profile. The advantage of adopting such a basic flow is that the corresponding dispersion relation can be written in analytic form. The simplest piecewise linear flow configuration incorporates a basic velocity profile with uniform velocities in both phases with a density and velocity jump entirely located at the interface. This leads to the classical Kelvin-Helmholtz instability between different fluids due to shear [18].

In the experiments the shear between two initially nearly parallel streams having different velocities U_1^* and U_2^* is produced by accelerating the streams in distinct channels and merge them downstream. This method implies the formation of boundary layers with thicknesses δ_1 and δ_2. Thereafter phase 1 (resp. 2) is associated with the liquid (resp. gas). However, in the limit of a fast gas phase contacting a nearly quiescent liquid only the upper layer of thickness $\delta = \delta_2$ is of importance [49]. Thus, a more realistic extension of the Kelvin-Helmholtz basic flow includes a boundary layer of finite thickness, wherein the velocity increases monotonous from the minimum value U_1^* to the maximum value U_2^*. This modified piecewise linear velocity profile was analyzed in both the temporal [39, 49, 56] and spatial setting [1], where the latter study does not account for the effect of density stratification on both the spatially growing perturbations and the convective/absolute transition. Section 4.2 extends Balsa's [1] analysis by considering the influence of both density stratification, and surface tension. It also summarizes previous results [1, 39, 49, 56], and includes a comparison with temporal [42] and spatial results for the hyperbolic tangent velocity profile [40, 43, 44] including convective/absolute transition [29, 31].

However, from an experimental perspective the assumption that the velocity profile is monotonous in the cross-stream coordinate with velocity progressively increasing from the liquid to the gas side is questionable because liquid and gas are separated by a splitter plate before coming into contact as free streams. Hence a realistic basic velocity profile must include the fact that, inside the nozzle, the velocity, which is equal to U_1^* (resp. U_2^*) far way from the plate in phase 1 (resp. in phase 2), adjust to zero on the plate within the boundary layers of width δ_1 (resp. δ_2). Just behind the nozzle, both boundary layers keep characterizing the velocity distribution of the liquid and gas phases. Therefore, in Section 4.3 the liquid boundary layer, which was neglected so far, is taken into account. As a result, the interface velocity is variable. This extended piecewise linear model was also considered by Matas et al. [41], in order to compare with experimental results for air and water. However, the authors' focus was neither on a detailed study of the influences of all parameters involved in the instability problem nor on convective/absolute transition. Both aspects are investigated in detail in Section 4.3, which also includes a comparison with results for a smooth velocity profile including a wake [34].

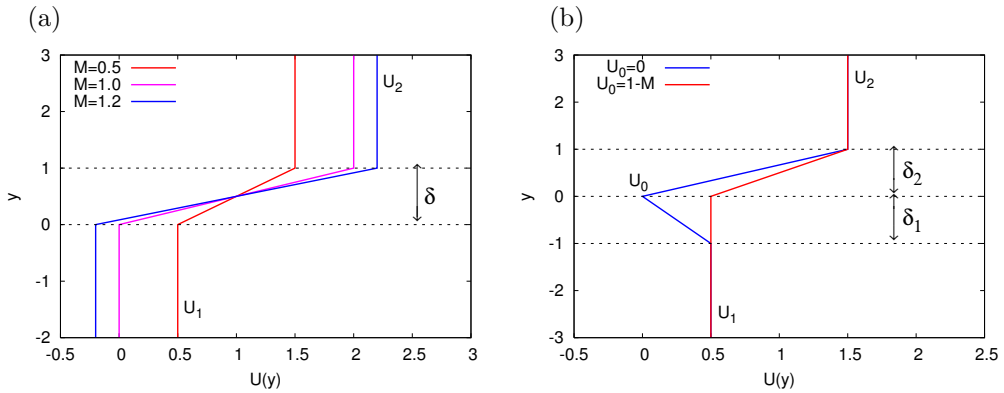

Figure 4.1: *(a) Broken line basic profile without liquid boundary layer for different values of velocity ratio M. (b) Broken line basic profile with equal boundary layer sizes ($n = 1$), velocity ratio $M = 0.5$, and different values of the interface velocity U_0.*

4.1 Inviscid Basic Velocity Profiles

As suggested in the above discussion, in this chapter two different piecewise linear velocity profiles are considered, which incorporate increasingly more features of the real flow.

4.1.1 Broken Line Profile without Liquid Boundary Layer

For a preliminary inviscid study, a basic flow with negligible liquid boundary layer is considered with the shear being entirely located in the rapid, light phase. In single-phase flows such a broken line profile is a caricature of the actual smooth velocity profile known to capture all the physics (wave number cut-off, growth rate, wave speed) of the instability [31]. The piecewise linear mixing-layer velocity profile is of the form

$$U(y) = \begin{cases} U_2^*, & y \geq \delta, \\ U_2^* - \frac{(\delta - y)}{\delta}(U_2^* - U_1^*), & 0 \leq y \leq \delta, \\ U_1^*, & y \leq 0. \end{cases} \tag{4.1}$$

U_1^* and U_2^* represent the asymptotic velocities in the lower liquid and upper gas phase, respectively. $U_2^* > U_1^*$ is assumed, and δ is the boundary layer thickness in the fast gas stream. For non-dimensionalization, δ is used as length scale, and the mean velocity $\bar{U} \equiv (U_2^* + U_1^*)/2$ is chosen as velocity scale. Based on these units, the dimensionless form of the basic velocity profile reads

$$U(y) = \begin{cases} 1 + M, & y \geq 1, \\ 1 + M - 2M(1 - y), & 0 \leq y \leq 1, \\ 1 - M, & y \leq 0. \end{cases} \tag{4.2}$$

The velocity ratio

$$M = \frac{\Delta U}{2\bar{U}} = \frac{U_2^* - U_1^*}{U_2^* + U_1^*} \tag{4.3}$$

is a measure of the magnitude of the shear across the layer. If $0 < M < 1$ the streams run in the same direction, while for $M > 1$ they flow in opposite directions; see Figure 4.1(a). When $M = 0$ there is no shear, and when $M = 1$ only one stream is present. For two-phase flows, in addition to the velocity ratio, the complete linearized dynamics depends also on two other dimensionless numbers representing the fluid properties (gravity is not considered here). These are the ratio of densities and the non-dimensional surface tension (which is the inverse of Weber

number), respectively, defined by

$$r = \frac{\rho_2}{\rho_1} \quad \text{and} \quad S = \frac{s}{\rho_2 \bar{U}^2 \delta}. \tag{4.4}$$

In this chapter, the reference of the upper and lower layers as the gaseous and liquid phases, respectively, suggests the restriction to values $0 < r \leq 1$, with $r = 1$ in the single-fluid limit.

Involving two fluids with, in general, different densities and surface tension, the dispersion relation for the velocity profile (4.2) can be written in analytic form as

$$\begin{aligned}(\alpha(1-M)-\omega)\left[\left(1+\frac{1}{r}\right)(\alpha-\omega)^2+\left(1-\frac{1}{r}\right)(\alpha-\omega)\left(1-e^{-2\alpha}\right)M\right.\\ -\left(\left(1+\frac{1}{r}\right)\alpha(\alpha-1)-2\alpha+2-\left[2+\left(1-\frac{1}{r}\right)\alpha\right]e^{-2\alpha}\right)M^2\Big]\\ +S\alpha^3\left[\left(1-\alpha-e^{-2\alpha}\right)M-(\alpha-\omega)\right]\;=\;0.\end{aligned} \tag{4.5}$$

A detailed derivation of the above equation is given in Appendix A.3.1. In general, the variables $\alpha = \alpha_r + i\alpha_i$ and $\omega = \omega_r + i\omega_i$ are both complex; α_r is the wave number, ω_r is the frequency of the disturbance, and $-\alpha_i$ and ω_i are the spatial and temporal growth rates, respectively. The case $\alpha_i = 0$ refers to the temporal instability results, whereas $\omega_i = 0$ corresponds to spatial instability. For the neutral disturbance $\alpha_i = \omega_i = 0$, and both cases have the same solution.

4.1.2 Broken Line Profile including a Liquid Boundary Layer

As already mentioned, a more general velocity profile has to take into account the presence of a liquid boundary layer. In this case the velocity at the interface U_0^* of the basic flow is variable. Therefore, for fixed asymptotic velocities U_1^* and U_2^* a family of velocity profiles can be defined differing only in the interface velocity. The broken line profile is

$$U(y) = \begin{cases} U_2^*, & y \geq \delta_2, \\ U_2^* - \frac{(\delta_2 - y)}{\delta_2}(U_2^* - U_0^*), & 0 \leq y \leq \delta_2, \\ U_1^* - \frac{(\delta_1 + y)}{\delta_1}(U_1^* - U_0^*), & -\delta_1 \leq y \leq 0, \\ U_1^*, & y \leq -\delta_1. \end{cases} \tag{4.6}$$

The boundary layers have thicknesses δ_1 and δ_2. For non-dimensionalization, δ_2 is used as length scale, and the mean velocity $\bar{U} \equiv (U_2^* + U_1^*)/2$ is again chosen as velocity scale. Based on these units, the dimensionless form of the basic velocity profile reads

$$U(y) = \begin{cases} 1 + M, & y \geq 1, \\ 1 + M - (1 - y)(1 + M - U_0), & 0 \leq y \leq 1, \\ 1 - M - (1 + ny)(1 - M - U_0), & -1/n \leq y \leq 0, \\ 1 - M, & y \leq -1/n; \end{cases} \tag{4.7}$$

see Figure 4.1(b). In comparison with the previous velocity profile, two additional dimensionless parameters are present:

$$U_0 = \frac{U_0^*}{\bar{U}} \quad \text{and} \quad n = \frac{\delta_2}{\delta_1} \tag{4.8}$$

denote the dimensionless interface velocity and the ratio of the boundary layer thicknesses. The remaining parameters M, r, and S were already introduced by relations (4.3) and (4.4). Note that the broken line velocity profile (4.2) can be understood as a special case of basic flow (4.7), when the interface velocity equals the mean speed in the lower liquid layer, i.e. $U_0^* = U_1^*$, or equivalently $U_0 = 1 - M$. In this case there is effectively no liquid boundary layer.

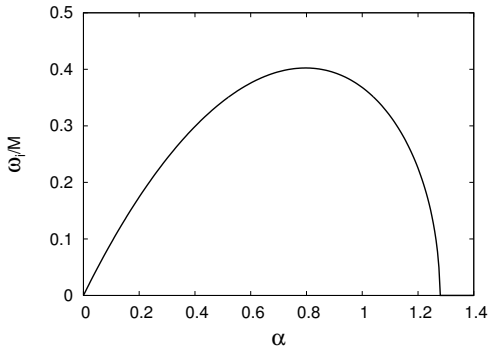

Figure 4.2: *Normalized unstable temporal mode $\omega_i(\alpha)/M$ for the inviscid piecewise linear profile without liquid boundary layer in the one-layer limit, $r = 1$, $S = 0$. The neutral point is located at $\alpha_N \approx 1.28$ [56]. Beyond this point the flow is precisely neutral.*

The dispersion relation for the broken line profile (4.7) including a liquid boundary can briefly be written as

$$\hat{a} + \hat{b} + \hat{c} + \hat{d} - \frac{S\alpha^3}{\alpha U_0 - \omega}(\hat{e} + \hat{f} + \hat{g} + \hat{h}) = 0. \tag{4.9}$$

The expressions for $\hat{a}$, $\hat{b}$, $\hat{c}$, $\hat{d}$, $\hat{e}$, $\hat{f}$, $\hat{g}$, and $\hat{h}$ are given in Appendix A.3.2. In the limit of no liquid boundary layer, the dispersion relation (4.9) reduces to equation (4.5).

4.2 Results for Profiles without Liquid Boundary Layer

In this section the boundary layer in the lower fluid is assumed to be negligible. Therefore the non-dimensional piecewise linear velocity profile is given by relation (4.2). The problem becomes considerably simpler by working with this assumption, because only three dimensionless parameters are involved in the problem, namely M, r, and S. Since the dispersion relation (4.5) is a third order equation with real coefficients for the complex variable ω, there exists only a single unstable mode.

4.2.1 Temporal Growth Rates

First, the influence of each of the three quantities M, r, and S on the temporal growth rates is considered. The temporal study on the inviscid broken line profile (4.2) was performed in detail by Villermaux [56] for small values of S. His results are summarized in the following paragraph.

Results in the Absence of Surface Tension

When the influence of surface tension is neglected, i.e. $S = 0$, then the temporal amplification rate of the unstable mode is exactly a linear function of M [31]. In other words, the dimensional temporal growth rate scales with the velocity difference $\Delta U \equiv U_2^* - U_1^*$ across the layer and does not depend on the average velocity $\bar{U}$ of the two streams. This feature justifies the choice of the average velocity as a reference scale. Figure 4.2 shows the temporal growth rate ω_i normalized by M as a function of the wave number for two fluids of equal density ($r = 1$). In this one-layer limit a single unstable mode is found for $0 \leq \alpha \leq \alpha_N \approx 1.28$. For $\alpha > \alpha_N$ the flow is precisely neutral. The neutral point α_N is also a square-root branch point, i.e. $\alpha_N = \alpha_B$, as necessarily implied by the coalescence of the unstable and stable modes in inviscid theory [1]. Because of the existence of a branch point, there must exist a branch cut in the complex wave number plane.

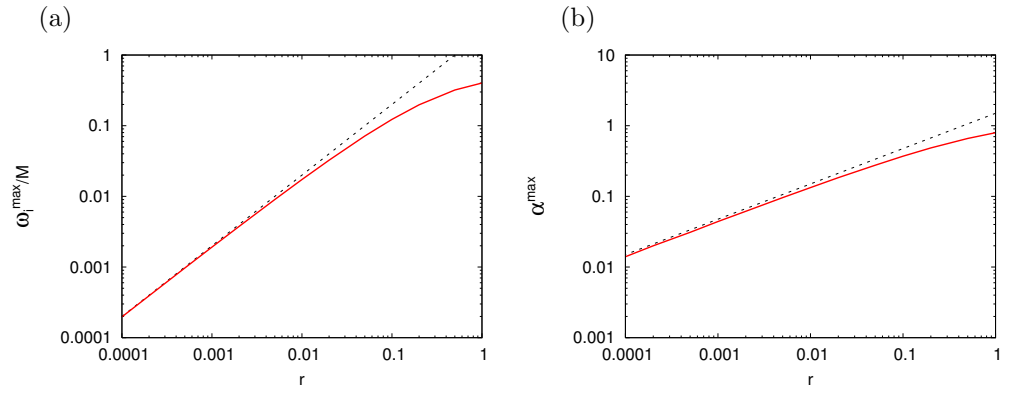

Figure 4.3: *Effect of density ratio variation on the temporal results for the piecewise linear velocity profile without liquid boundary layer in the absence of surface tension, $S = 0$: (a) normalized maximum growth rate $\omega_i^{\max}/M$, and (b) corresponding wave number $\alpha^{\max}$ both as a function of r. The asymptotic results (4.10) for $r \to 0$ are shown as dashed lines.*

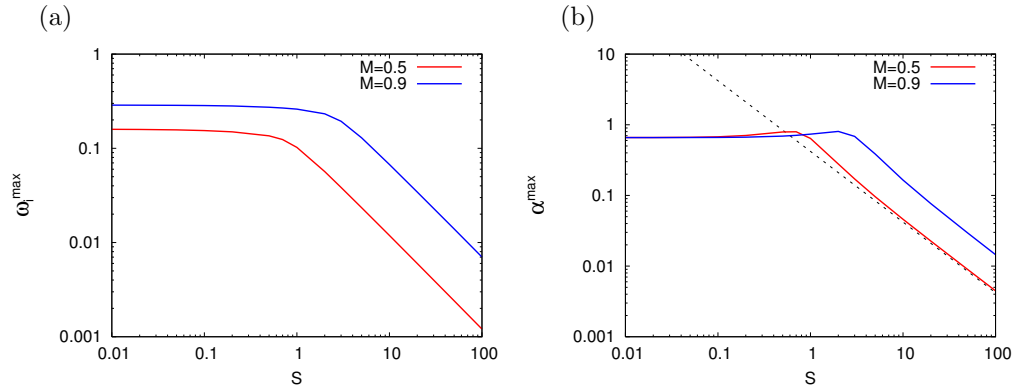

Figure 4.4: *Effect of surface tension variation on the temporal results for the piecewise linear velocity profile without liquid boundary layer for $r = 0.5$ and two different values of velocity ratio M: (a) maximum growth rate $\omega_i^{\max}$, and (b) corresponding wave number $\alpha^{\max}$ both as a function of S. The asymptotic result $\alpha^{\max} \propto S^{-1}$ [6] for $S \to \infty$ is shown as dashed line.*

The branch cut extends from $\alpha_N \approx 1.28$ to $+\infty$ along the real axis, and will be important in the spatial study.

Figure 4.2 further shows, that the dependence of the normalized growth rate for the only unstable mode on the wave number α displays a single maximum $\omega_i^{\max}/M$. In Figure 4.3(a) this maximum is given as a function of the density ratio r. The corresponding result for the wave number of maximum amplification $\alpha^{\max}$ is shown in Figure 4.3(b). For decreasing r, the maximum growth rate $\omega_i^{\max}/M$ and its associated wave numer $\alpha^{\max}$ both decrease, resulting into a preferred wavelength $\lambda^{\max} \equiv 2\pi/\alpha^{\max}$, which increases as r decreases. Although the instability is progressively damped for decreasing density ratios, it is never suppressed, except in the limit $r \to 0$, a case that amounts to the inviscid linear boundary-layer profile over a rigid plate, which is known to be linearly stable ($\omega_i^{\max} = 0$) [52]. In the limit $r \to 0$ the asymptotic behaviour

$$\alpha^{\max} \approx 1.5\sqrt{r}, \qquad \omega_i^{\max}/M \approx 2r \tag{4.10}$$

is found for the most unstable wave number and growth rate [39]. These asymptotic results are shown as dashed lines in Figure 4.3.

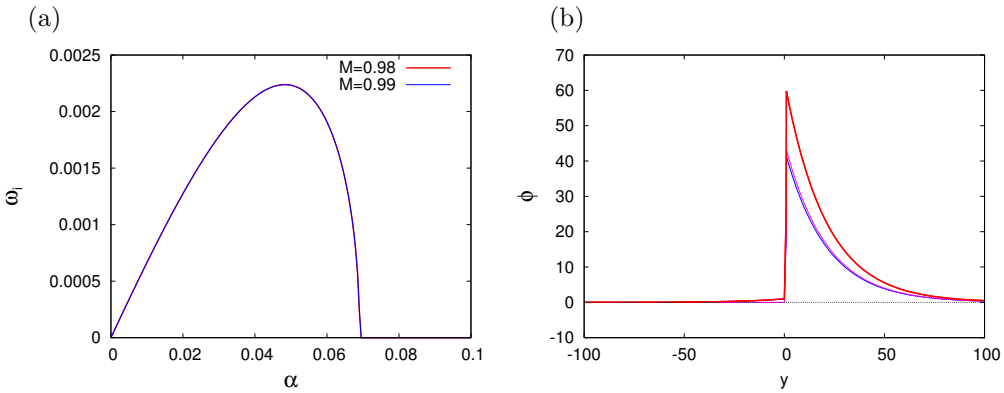

Figure 4.5: *Temporal inviscid results for the piecewise linear profile without liquid boundary layer for* $r = 0.0012$, $S = 1$*: (a) Unstable modes for* $M = 0.98$ *and* $M = 0.99$*. Note that both curves are visually indistinguishable. The neutral point is located at* $\alpha_N \approx 0.0691$*. (b) Eigenmode for* $M = 0.98$ *at the most amplified wave number* $\alpha^{\max} = 0.0485$ *normalized by* $\phi(0) = 1$*. The real and imaginary parts of the eigenfunction are shown in blue and magenta, respectively, and* $|\phi|$ *is plotted in red.*

Results in the Presence of Surface Tension

The effect of increasing surface tension is considered for two fluids with density ratio $r = 0.5$. For $S > 0$ the temporal growth rate of the unstable mode does not scale with M. Therefore, different values of the velocity ratio must be considered. For $M = 0.5$ and $M = 0.9$, in Figure 4.4 the maximum growth rate $\omega_i^{\max}$ and the associated wave number $\alpha^{\max}$ are shown as a function of S. The stabilizing effect of surface tension is apparent. For large $S > S_c$, $\alpha^{\max}$ is proportional to S^{-1} [6]. As shown in Figure 4.4, the value S_c depends on the velocity ratio M. S_c also depends on the density ratio [6], and the relation between both quantities is

$$S_c^{-1} \propto \sqrt{r}. \tag{4.11}$$

Finally, Figure 4.5 shows the temporal growth rates for a pair of inviscid fluids with $r = 0.0012$, $S = 1$, and two different values of the velocity ratio, namely $M = 0.98$ and $M = 0.99$. The chosen parameters are typical for experimental configurations involving a fast air stream over water moving at relatively lower velocity [3]. The increase of the velocity ratio M has almost no effect on the temporal amplification rates $\omega_i(\alpha)$, since both instability curves are visually indistinguishable, see Figure 4.5(a). As will be seen later, this is contrary to the spatial results. In addition, for $M = 0.98$ the temporal eigenmode at the wave number of maximum amplification $\alpha^{\max} = 0.0485$ is shown in Figure 4.5(b). The perturbation is clearly located in the upper gas phase ($y > 0$).

4.2.2 Spatial Growth Rates

As for the temporal case, the spatial study is started by considering the one-layer limit, i.e. $r = 1$, $S = 0$. In order to investigate the instability properties, one has to solve an eigenvalue problem for the complex wave number $\alpha = \alpha_r + i\alpha_i$ given a real frequency ω. For disturbances travelling and growing in the direction of the basic flow, attention can be restricted to values $0 < \alpha_r$, $\alpha_i < 0$, and $0 < \omega_r$.
In Figure 4.6 spatial growth rates for two different values of the velocity ratio are presented. For $M = 0.5$ and $M = 0.9$, Figure 4.6(a) shows the spatial instability curves in the complex α-plane. Along these curves $\omega_i = 0$, and the frequency ω_r increases monotonically. The curves of spatial instability originate at $\alpha = 0$, proceed to the right, and eventually intersect the branch cut at

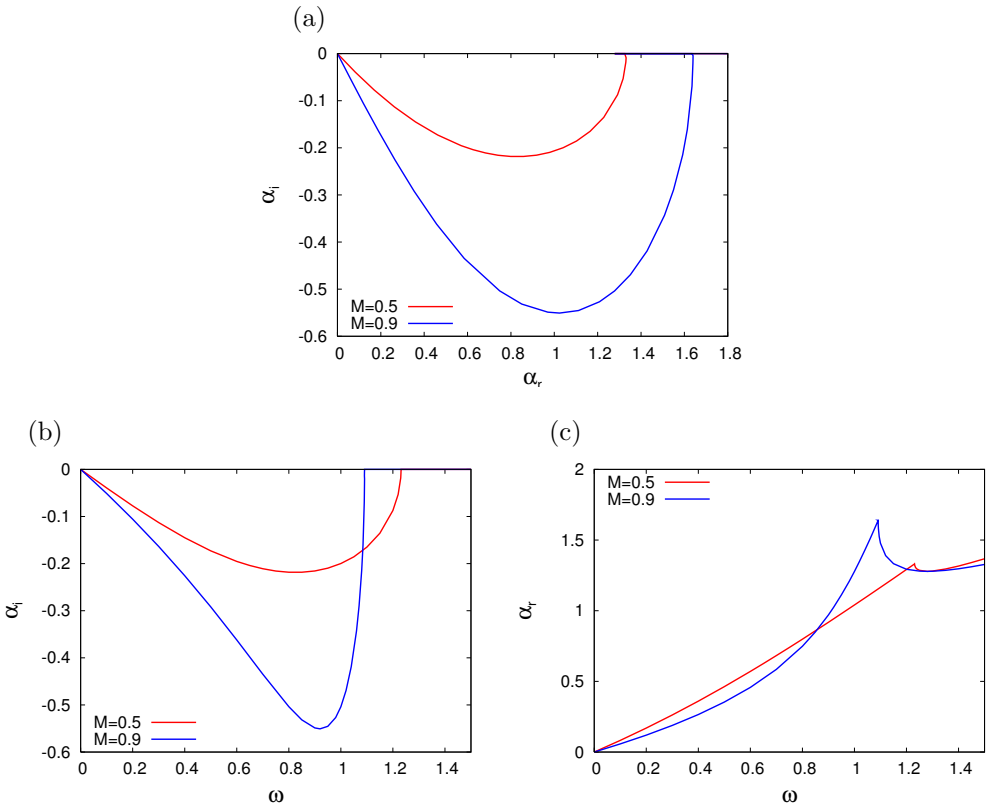

Figure 4.6: *Spatial inviscid results for the piecewise linear profile without liquid boundary layer in the one-layer limit, $r = 1$, $S = 0$: The unstable spatial modes for $M = 0.5$ and $M = 0.9$ are shown in (a). In (b) and (c), both α_i and α_r are shown as a function of the real frequency ω.*

$\alpha = \alpha_S > \alpha_N$. As in the temporal setting, the spatial growth rate $-\alpha_i$ is zero along the branch cut. Contrary to the temporal case, the spatial growth rate $-\alpha_i(\omega)$ does not scale with the velocity ratio. This is clearly seen in Figure 4.6(a), as the value α_S is different for $M = 0.5$ and $M = 0.9$. In addition, the neutral frequencies ω_N also differ for both values of M, see Figure 4.6(b). In each flow configuration the spatially unstable modes for $\omega < \omega_N$ become precisely neutral for frequencies larger than ω_N.

Further, the dependence of the spatial growth rate for the only unstable mode on the frequency ω displays a single optimum. As in the temporal case, the maximum growth rate $-\alpha_i^{\max}$ for $M = 0.9$ is larger than those for $M = 0.5$.

Finally, Figure 4.6(c) shows the dependence of the wave number α_r on the frequency ω. For both velocity ratios, the curves $\alpha_r(\omega)$ display a peak at the respective value α_S. In addition, a local minimum at the neutral wave number $\alpha_r = \alpha_N \approx 1.28$ is present. This value is the same for all velocity ratios M, since at α_N and the associated frequency both the temporal and spatial growth rates are zero.

It should be noted, that the existence of a branch cut can be easily sensed by plotting neighbouring curves in the complex wave number space. For $r = 1$, $S = 0$ and $M = 0.9$, Figure 4.7 shows the generalized spatial curves for $\omega_i = \pm 0.02$ in addition to those of spatial instability. (Note that the curve for $\omega_i = 0$ equals the blue curve in Figure 4.6(a)). It is important to note, that the curve for $\omega_i = -0.02$ remains in the lower halfplane. Contrary, the curve for $\omega_i = 0.02$ must leave the lower halfplane, but cannot cross the branch cut, which extends from $\alpha_N \approx 1.28$ to $+\infty$. It therefore must cross the α_r-axis at a wave number $\alpha_r < \alpha_N$.

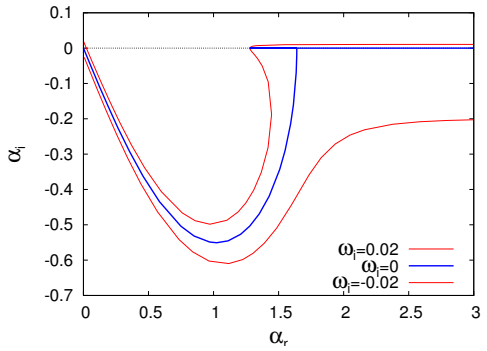

Figure 4.7: *The curve of spatial instability ($\omega_i = 0$) and neighbouring curves, $\omega_i = \pm 0.02$, for the piecewise linear profile without liquid boundary layer in the one-layer limit, $r = 1$, $S = 0$, where $M = 0.9$. Note, that the curve for $\omega_i = 0.02$ cannot cross the branch cut.*

Since, even for $S = 0$, there is no scaling with M in the spatial setting, the effect of the velocity ratio needs to be considered in this case. This is done first while keeping the remaining parameters fixed. Thereafter, r and S are changed keeping M fixed.

Velocity Ratio Variation

As shown in Figure 4.6, contrary to their temporal counterparts, in the case $r = 1$, $S = 0$ the spatial growth rates increase with the velocity ratio in a nontrivial manner. However, this result is not restricted to fluids of equal density, and applies whether interfacial tension is involved in the problem or not. For example, Figure 4.8(a) shows the spatial results for a pair of inviscid fluids with parameters corresponding approximately to air and water, $r = 0.0012$, $S = 1$. For this values, the effect of increasing the velocity ratio from $M = 0.98$ to $M = 0.99$ is considered. Recall from Figure 4.5(a), that this increase has almost no effect on the temporal growth rate for the parameters considered. On the other hand, the maximum spatial growth rate $-\alpha_i^{\max}$ for $M = 0.99$ is about 35% higher than those for $M = 0.98$, see Figure 4.8(a). However, this increase of the spatial growth rate with M is already suggested by Gaster's transformation (2.98),

$$-\alpha_i = \omega_i / c_g,$$

that relates temporal to spatial results in terms of the group velocity $c_g = \partial\omega_r/\partial\alpha_r$. Since there is no significant change in the temporal growth rates when the velocity ratio is increased from $M = 0.98$ to $M = 0.99$, according to Gaster's transformation, an increase of spatial amplification is then necessarily caused by a decrease in group velocity c_g. Figure 4.9(b) shows, that for a given wave number α_r the group velocity c_g is indeed smaller for $M = 0.99$ compared to those for $M = 0.98$. This causes the increased spatial growth rates calculated using Gaster's transformation for larger values of M. The comparison of these estimations with the spatial results obtained directly from the dispersion relation (4.5) is shown in Figure 4.9(a), where the approximation underestimates the spatial growth rates obtained from the numerical analysis. Note further, that, by definition, it is impossible for Gaster's transformation to predict spatial instability for wave numbers $\alpha > \alpha_N$, since then $\omega_i(\alpha) = 0$. Therefore, and due to the large growth rates involved, the qualitative agreement between direct solution and Gaster's leading order approximation is limited.

Finally, for $M = 0.98$ the eigenmode at the wave number of maximum spatial amplification $\alpha_r^{\max} = 0.0421$ is shown in Figure 4.8(b). As in the temporal case, the perturbation is clearly located in the upper gas phase ($y > 0$). Further, the shape of the spatial eigenfunction is very similar to its temporal counterpart; see Figure 4.5(b) for comparison.

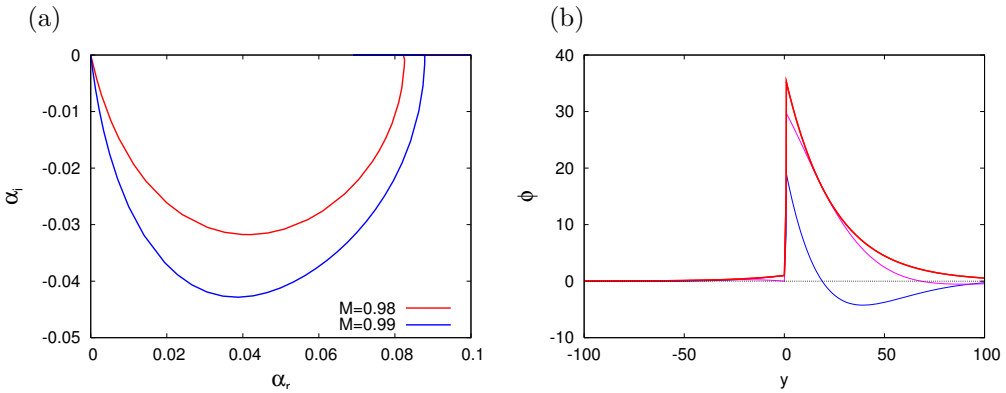

Figure 4.8: *Spatial inviscid results for the piecewise linear profile without liquid boundary layer for* $r = 0.0012$, $S = 1$*: (a) Convectively unstable modes for* $M = 0.98$ *and* $M = 0.99$. *(b) Eigenmode for* $M = 0.98$ *at the most amplified wave number* $\alpha_r^{\max} = 0.0421$ *normalized by* $\phi(0) = 1$. *The real and imaginary parts of the eigenfunction are shown in blue and magenta, respectively, and* $|\phi|$ *is plotted in red.*

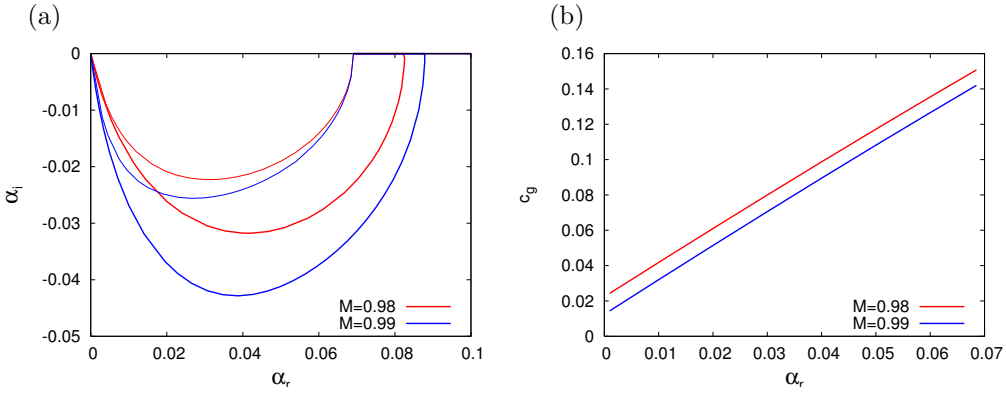

Figure 4.9: *Spatial inviscid results for the piecewise linear profile without liquid boundary layer for* $r = 0.0012$, $S = 1$ *and two different values of velocity ratio,* $M = 0.98$ *and* $M = 0.99$*: (a) the unstable spatial modes (thick) in comparison with the results using Gaster's transformation (thin), (b) the group velocity* c_g *as a funcion of wave number.*

After having identified the important effect of the velocity ratio on the spatial instability results, now M is kept constant, and both the effect of density ratio variation and the influence of interfacial tension on the spatial instability results are considered.

Density Ratio Variation

For spatial modes the effect of density ratio variation is considered for the following fixed values of the velocity ratio, and the surface tension parameter: $M = 0.5$, $M = 0.9$, and $S = 0$, $S = 1$. In Figure 4.10(a), for each parameter combination the maximum spatial growth rate $-\alpha_i^{\max}$ of the only unstable mode is given as a function of the density ratio r. The corresponding results for the associated wave number $\alpha_r^{\max}$ and frequency $\omega^{\max}$ are shown in Figure 4.10(b) and (c), respectively. The general trends observed in the temporal case are also found for spatial modes: both the most amplified wave number $\alpha_r^{\max}$ and its associated growth rate $-\alpha_i^{\max}$ decrease with r. As expected, the spatial growth rates for $M = 0.9$ are larger than those for $M = 0.5$. On the other hand, $\omega^{\max}$ is smaller for $M = 0.9$, see Figure 4.10(c). For both values of M, the wave numbers of maximum amplification $\alpha_r^{\max}$ are similar for sufficent small density ratios.

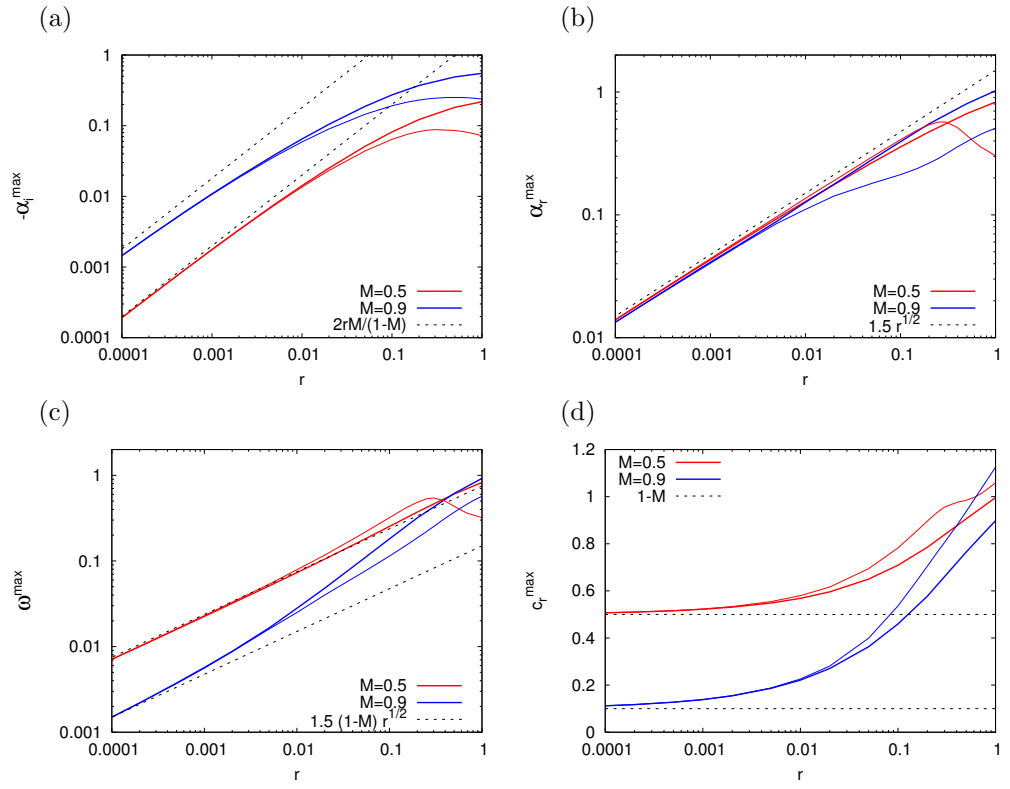

Figure 4.10: *Effect of density ratio variation on the spatial results for the piecewise linear velocity profile without liquid boundary layer for two different values of M and S: (a) maximum growth rate $-\alpha_i^{\max}$, and associated (b) wave number $\alpha_r^{\max}$ (c) frequency $\omega^{\max}$ and (d) wave speed $c^{\max}$ all as a function of r. Surface tension is $S = 0$ (thick) and $S = 1$ (thin). The asymptotic results (4.12)-(4.15) for $r \to 0$ are shown as dashed lines.*

Following equation (2.94), the wave number $\alpha_r^{\max}$ for the spatial case is approximately equal to the temporal value. Hence,

$$\alpha_r^{\max} \approx 1.5\sqrt{r} \tag{4.12}$$

in the limit $r \to 0$. In addition, the dispersion relation (4.5) yields $\omega_r = \alpha_r(1 - M)$ as $r \to 0$. Consequently, in this limit

$$\omega^{\max} \approx 1.5(1 - M)\sqrt{r}. \tag{4.13}$$

Next, using Gaster's relation (2.98), and assuming that the group velocity c_g can be approximated by the convection velocity

$$U_c \equiv \frac{1 - M + \sqrt{r}(1 + M)}{1 + \sqrt{r}},$$

estimated from the continuity of normal stresses at the interface [39], one obtains

$$-\alpha_i^{\max} \approx \frac{2Mr}{1 - M} \tag{4.14}$$

as $r \to 0$. Further, Figure 4.10(d) shows the variation of the wave speed $c^{\max} = \omega^{\max}/\alpha_r^{\max}$ with r. The wave speed decreases with the density ratio and, according to relations (4.12) and (4.13), approaches the minimum velocity of the mean flow (i.e. the velocity of the liquid) as $r \to 0$:

$$c^{\max} \to 1 - M. \tag{4.15}$$

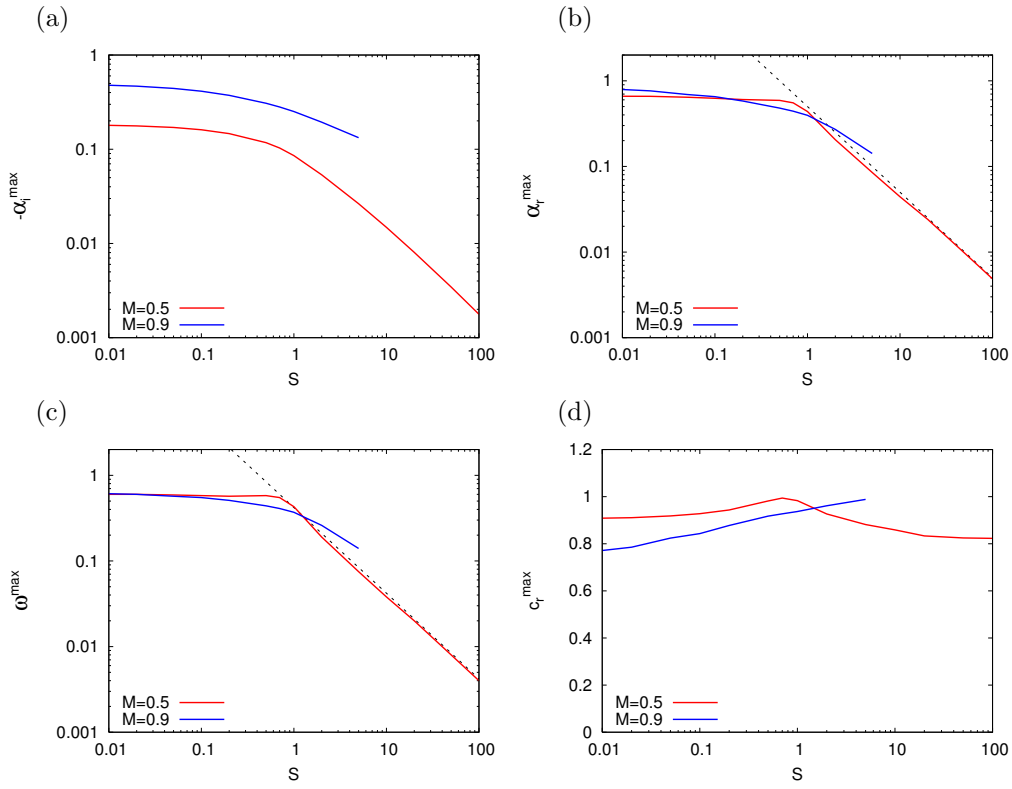

Figure 4.11: *Effect of surface tension variation on the spatial results for the piecewise linear velocity profile without liquid boundary layer for* $r = 0.5$ *and two different values of* M*: (a) maximum growth rate* $-\alpha_i^{\max}$ *and associated (b) wave number* $\alpha_r^{\max}$ *(c) frequency* $\omega^{\max}$ *and (d) wave speed* $c^{\max}$ *all as a function of* S*. The abrupt ending in the curves for* $M = 0.9$ *is due to absolute instability of the flow for* $S > S_0 \approx 6.5$*. The asymptotic results (4.16) for* $S \to \infty$ *are shown as dashed lines.*

The approximations (4.12)-(4.15) are shown in Figure 4.10 as dashed lines.
Finally, increasing surface tension from $S = 0$ to $S = 1$ only affects the results for large values of r. This clearly suggests the presence of a balance between the effects of density ratio variation and surface tension variation. In the limit $r \to 0$, the influence of surface tension is dominated by the strong density contrast, whereas in the case of small differences in the fluid densities, say $0.01 < r < 1$, the effect of interfacial tension is strong relative to the influence of density stratification.

Surface Tension Variation

For two fluids having a relatively weak contrast in densities given by $r = 0.5$, Figure 4.11 shows the effect of continuously increasing surface tension for the velocity ratios $M = 0.5$ and $M = 0.9$. It is therefore the spatial analogue to Figure 4.4. As in the temporal case, the spatial growth rate decreases as surface tension becomes increasingly dominant; the associated wave number and frequency also decrease. In the limit $S \to \infty$ one obtains the asymptotic results:

$$\alpha_r^{\max} \propto S^{-1}, \qquad \omega^{\max} \propto S^{-1}, \tag{4.16}$$

which are shown as dashed lines in Figures 4.11(b) and (c), respectively. The first relation is analogous to the temporal case and follows from equation (2.94). The latter result is obtained by considering the dispersion relation (4.5) in the limit $S \to \infty$. In addition, for spatially growing

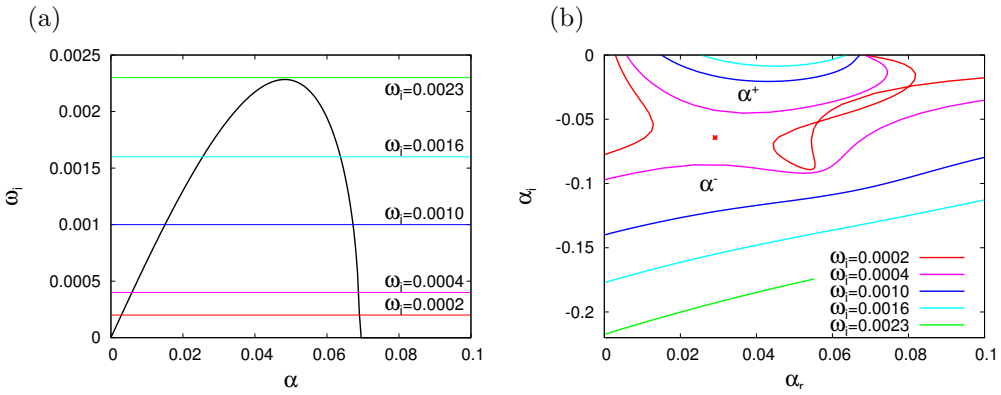

Figure 4.12: *Absolutely unstable inviscid results for the piecewise linear profile without liquid boundary layer with* $r = 0.0012$, $M = 1$, *and* $S = 1$*: (a) unstable temporal mode, (b) formation of a saddle point as a result of decreasing* ω_i*. The saddle point is* $\alpha^0 = 0.02912 - 0.06429i$, *and* $\omega^0 = 0.001862 + 0.0002786i$.

perturbations Figure 4.11(d) shows the wave speed $c^{\max}$ as a function of S. In contrast to variations of the density ratio, $c^{\max}$ is almost unaffected when surface tension is changed.
Note finally, that the curves for $M = 0.9$ end abruptely at some value $S = S_0 \approx 6.5$. This is important, since for $S > S_0$ the flow is absolutely unstable. In such cases no spatial growth rates exit. The transition between convectively and absolutely unstable flows is considered next.

4.2.3 Transition from Convective to Absolute Instability

Since a long time the piecewise linear mixing layer of a single fluid is known to be absolutely unstable for $M > 1$ [1, 31]. This case corresponds to the present broken-line velocity profile without liquid boundary layer, where $r = 1$ and $S = 0$. An extension of these result on convective/absolute instability for various density ratios can be stated as follows:

Consider the broken line velocity profile (4.2) in the absence of interfacial tension, $S = 0$. Then, independent of the density ratio r,

- each co-flow ($M < 1$) is convectively unstable, and
- each flow with $M \geq 1$ is absolutely unstable.

Therefore, the velocity ratio of convective/absolute transition is $M_t = 1$ independent of r. In this case the absolute wave number is $\alpha_r^0 \to \infty$ and the absolute frequency is

$$\omega^0 = \frac{2r}{r+1}. \tag{4.17}$$

A detailed derivation of this result is given in Appendix A.3.3.

When interfacial tension is included, the velocity ratio of convective/absolute transition M_t changes. For example, an inviscid air flow over water at rest ($r = 0.0012$, $M = 1$) is absolutely unstable for $S = 1$. For this flow a single unstable mode is found for $0 < \alpha < \alpha_N \approx 0.069$. The neutral point α_N is also a square-root branch point, and the branch cut extends from $\alpha_N \approx 0.069$ to $+\infty$ along the α_r-axis. Figure 4.12(a) shows the temporal growth rate $\omega_i(\alpha)$ of the unstable mode, which takes its maximum value $\omega_i^{\max} = 0.0022837$ at $\alpha^{\max} = 0.0485$. In Figure 4.12(b) the formation of a saddle point in the complex α-plane is shown by displaying generalized spatial branches with decreasing values of ω_i: First, when $\omega_i \geq \omega_i^{\max}$, the α^+ branch is entirely located

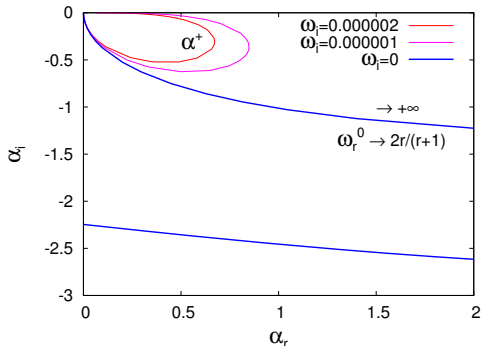

Figure 4.13: *Spatial instability curves for the absolutely unstable piecewise linear velocity profile without liquid boundary layer when* $r = 0.0012$, $M = 1$, *and* $S = 0$. *At* $\omega_r^0 = 2r/(r+1)$ *the wave number is* $\alpha_r^0 \to +\infty$.

in the upper halfplane (not shown), and the α^- branch lies in the lower one. The branches can be understood as functions of ω_r with fixed ω_i. When ω_i is lowered, the α^+ branch moves downwards and enters the lower halfplane when $\omega_i < \omega_i^{\max}$. Similarly, the α^- branch moves upwards. Note, that the α^+ branch cannot cross the branch cut, and therefore has to leave the lower halfplane at a wave number $\alpha_r < \alpha_N$. When ω_i is further decreased, the upper and lower branches consequently pinch for some value ω_i^0, which is negative for convectively unstable flows and positive in cases of absolute instability, see Section 2.6.2. Here, $\alpha^0 = 0.02912 - 0.06429i$ and $\omega^0 = 0.001862 + 0.0002786i$, indicating absolute instability. When ω_i is further decreased, the branches change their identity. In this case spatial results become non-physical due to violation of causality [31].

Keeping r and M as above, but neglecting surface tension, $S = 0$, the situation is different. The resulting absolutely unstable flow corresponds exactly to the convective/absolute transition case, i.e. $\omega_i^0 = 0$. Hence, the real absolute frequency ω^0 is given by relation (4.17), and the absolute wave number α_r^0 is infinite. Consequently, the curve of spatial instability ($\omega_i = 0$) extends to $+\infty$. On the other hand, as mentioned above, the curves for $\omega_i > 0$ must leave the lower halfplane at a wave number $\alpha_r < \alpha_N \approx 0.069$. Therefore, Figure 4.13 can be understood as the analogue of Figure 4.12(b) in the absence of surface tension.
This result of absolute instability for $S \to 0$ is consistent with the trend observed in Figure 4.8(a): For $r = 0.0012$ and $S = 0$ fixed, the wave number α_S, at which the spatial instability curve intersects the branch cut, is observed to move to the right as the velocity ratio M increases. By comparison with Figure 4.13, it becomes clear that α_S recedes to $+\infty$ as $M \to 1$, and, in this limit, the spatial curves in Figure 4.8(a) for $M < 1$ result into the α^+ branch for $\omega_i = 0$.
Note also the presence of a second branch below the α^+ branch in Figure 4.13. This curve originates at $\alpha_r = +\infty$ for $\omega = 2r/(r+1)$ and proceeds to the left for increasing frequency. It therefore connects to the α^+ branch in that sense, as this curve approaches infinity for the same frequency. The presence of such non-unique spatial instability curves for the piecewise linear velocity profile was already reported in the literature in the limit of a single fluid ($r = 1$, $S = 0$) [1].

Finally, Figure 4.14 shows the velocity ratio of convective/absolute transition M_t both (a) as a function of the density ratio r for several values of surface tension S, and (b) as a function of S for various r. M_t can be calculated by the procedure outlined in Appendix A.3.4. For a given velocity ratio M, this method provides both the absolute wave number $\alpha^0 = \alpha_r^0 + i\alpha_i^0$ and the absolute frequency $\omega^0 = \omega_r^0 + i\omega_i^0$. By changing M, M_t is obtained when the corresponding absolute frequency satisfies $\omega_i^0 = 0$.

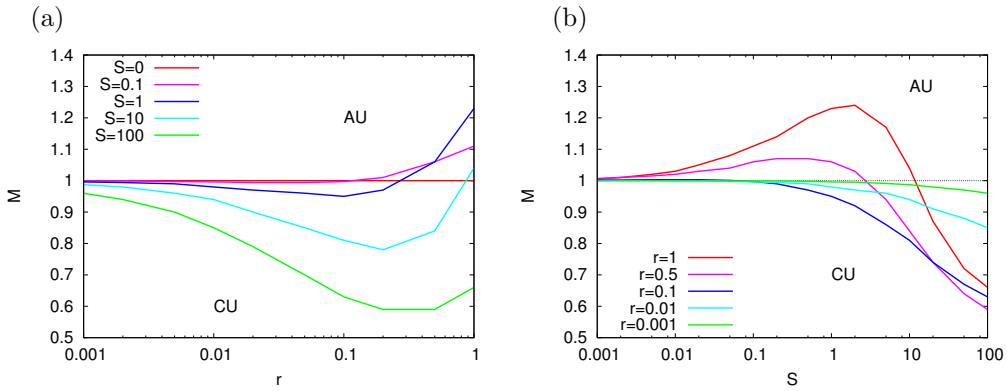

Figure 4.14: *Curves delimitating the convective/absolute transition for the piecewise linear velocity profile without liquid boundary layer (a) as a function of the density ratio r for different values of surface tension S, and (b) as a function of S for various r.*

As already mentioned, in the absence of surface tension $M_t = 1$, independent of r. This is shown by the red line in Figure 4.14(a). When the influence of interfacial tension is increased, M_t changes as follows: For small and moderate numbers of $S > 0$, there may be different ranges of the density ratio r, wherein absolutely unstable co-flows or convectively unstable counterflows exist. The latter cases correspond to $M_t > 1$ and occur preferably at weak density contrasts, i.e. for $r < 1$ close to unity. Contrary, $M_t < 1$ is typical for configurations with moderate and strong density contrasts. Thus, absolutely unstable co-flows preferably appear for small values of r, as, for example, in the case of air and water ($r = 0.0012$); see Figure 4.12.
With increasing S, an increasing number of co-flowing basic velocity profiles becomes absolutely unstable, see Figure 4.14(b). When surface tension exceeds a certain value, $M_t < 1$ for each density ratio r. Then, no convectively unstable counterflows exist. Such a situation is present in the case $S = 100$, for example. Contrary, in the limit $S \to 0$ one again finds $M_t \to 1$ independent of r. Finally, Figure 4.14 also shows, that $M_t \to 1$ independent of S as $r \to 0$.

The main results for the piecewise linear basic velocity profile (4.2) including only a gas boundary layer can be summarized as follows: In the absence of surface tension inviscid mixing layers are found to be convectively unstable in cases of co-flowing fluids for arbitrary density ratios r. Since spatially growing waves can only be observed in case of convective instability, this result suggests a restriction to cases with $M < 1$ for the inviscid study of the more complicated piecewise linear profile including a liquid boundary layer, whose instability analysis is performed in Section 4.3. It is noted here as well, that the same restriction on M is also assumed in the viscous study, which is presented in Chapter 5.

4.2.4 Comparison with Results for Smooth Velocity Profiles

The inviscid study of the piecewise linear profile (4.2) is finished by relating the previously presented results to those for velocity profiles, that are infinitely smooth. Such basic flows were studied extensively in the limit $S = 0$ for both uniform and nonuniform density distributions.

Uniform Density

Balsa [1] considered a velocity profile, that is very much like a piecewise linear one, but is modified so that the entire profile is infinitely differentiable. The inviscid piecewise-linear results are found to be robust and remain unaltered by the inclusion of both a small amount of viscosity and finite curvature of the velocity profile at the edges of the shear layer. In particular, when the Reynolds number is sufficiently high, the viscous temporal and spatial instabilities of the

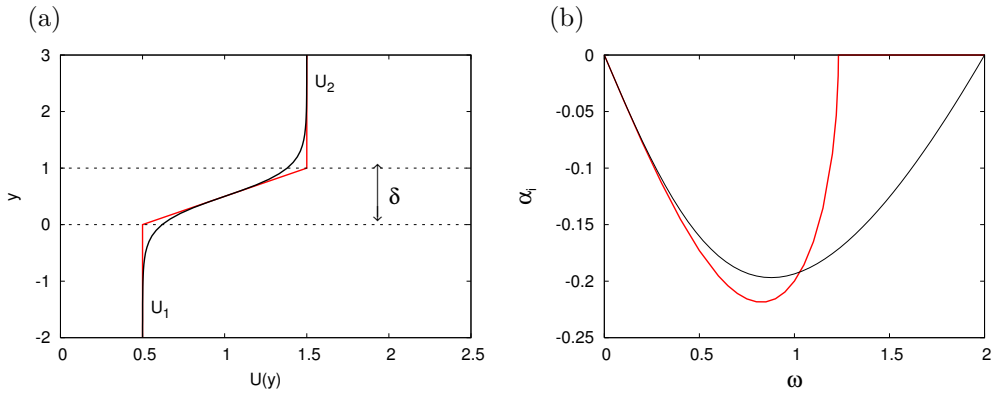

Figure 4.15: *(a) Piecewise linear basic flow without liquid boundary layer (red) vs. hyperbolic-tangent velocity profile (black) for $M = 0.5$. (b) Spatial growth rates as a function of the frequency ω for the convectively unstable profiles shown in (a). Note that $r = 1$, and $S = 0$.*

modified velocity profile are virtually identical to the inviscid instabilities of the piecewise linear basic flow. The solutions of the Orr-Sommerfeld equation for the modified profile further imply that an unstable mode for $\alpha < \alpha_N$ will become precisely neutral rather than damped for $\alpha > \alpha_N$ as $R \to \infty$. This is due to the fact that the velocity profile in the vicinity of $y = y_c = 1/2$ is perfectly straight [1]. The significance of $y = y_c$ is that the basic flow is antisymmetric about this point. Consequently, the phase velocity of the unstable mode is $c_r = U(y_c) = \bar{U}$. Balsa [1] finally showed that the square-root behaviour of the dispersion relation, i.e. $\omega \sim \sqrt{\alpha - \alpha_N}$, is unrelated to the piecewise nature of the velocity profile or to any unphysical feature arising from the Rayleigh equation. Instead, the square-root behaviour is a generic result which will occur whenever the basic flow is sufficiently linear near the shear-layer centerline at $y = y_c = 1/2$.
In addition, Balsa [1] noted, that the instability characteristics of the piecewise linear flow agree qualitatively with the inviscid results for the hyperbolic-tangent profile, when the shear layers are convectively unstable. The parallel *tanh* mixing-layer velocity profile matching the piecewise linear basic flow (4.2) in its generic features is given in dimensionless form by

$$U(y) = 1 + M\tanh(2y - 1). \tag{4.18}$$

The hyperbolic-tangent velocity profile is given in Figure 4.15(a) for $M = 0.5$. The corresponding piecewise linear basic flow is shown for comparison. For the *tanh* profile with $M = 1$, both the temporal and spatial instability problems were first investigated by Michalke [42, 43]. Like the broken-line profile, the smooth shear layer of an uniform fluid is unstable in a finite band of given wave numbers or frequencies in the temporal or spatial case, respectively. Monkewitz and Huerre [44] showed further, that, in contrast to their temporal counterparts, the spatial stability results cannot be extended to arbitrary values of M by translation of the frame of reference. Consequently, as for the piecewise linear basic flow, although the temporal growth rate of the *tanh* profile is exactly a linear function of the velocity ratio, the spatial stability characteristics depend on M in a nontrivial manner. Therefore, spatial growth rates do not scale with the velocity difference $\Delta U = U_2^* - U_1^*$ across the layer. However, when the average velocity $\bar{U}$ is chosen as a reference scale, for the hyperbolic-tangent velocity profile the range of unstable non-dimensional frequencies stays constant with M [44]. A qualitative comparison between the spatial growth rates of the *tanh* (black) and piecewise linear (red) profiles are shown in Figure 4.15(b) for $M = 0.5$. Although the range of frequencies for which the flow is unstable is narrower for the piecewise linear profile, the curves are very similar, and the maximum spatial growth rates are about the same. They also occur at about the same frequency. However, any quantitative difference between the results is attributable to the fact that the velocity profiles are not identical.

Finally, according to the results by Huerre and Monkewitz [29], the velocity ratio of convective/absolute transition for the hyperbolic-tangent profile is $M_t = 1.315$. For comparison, the broken-line velocity profile is absolutely unstable for any counterflow, i.e. $M_t = 1$. Thus, in contrast to the piecewise linear case, for the hyperbolic-tangent velocity profile spatially growing waves can be observed in the presence of a weak counterflow, whose magnitude is sufficiently small. However, for any larger counterflow, i.e. $M > M_t$, the *tanh* mixing layer is absolutely unstable, and the flow should then be described in terms of temporally growing disturbances.

Nonuniform Density

The case of a nonuniform density mixing layer between two uniform streams was considered by Maslowe and Kelly [40], who analyzed both temporal and spatial results for $M = 1$ and $S = 0$. The flow is unstable for all finite $r > 0$, and it was shown that variations in density can be destabilizing. More precisely, for the hyperbolic tangent velocity profile, when the stream with the higher velocity has the lower density, i.e. $r < 1$, both the wave number range of unstable disturbances and the maximum spatial growth rate can be increased relative to the case of homogeneous flow. An absolute maximum in the spatial amplification factor is achieved for $r \simeq 0.03$ and is approximately 1.64 times the amplification factor for homogeneous flow [40]. Such behaviour was not observed for the piecewise linear profile (4.2). In this case, both the range of unstable wave numbers and the maximum spatial growth rate $-\alpha_i^{\max}$ decrease in the absence of surface tension, $S = 0$. An increase of $-\alpha_i^{\max}$ with decreasing r was only observed for $S > 0$, and values of $r < 1$, close to unity, see Figure 4.10(a). However, the effect of interfacial tension was not considered by Maslowe and Kelly [40]. Apart from the fact that the velocity profiles are not identical, the discrepancies may also be attributable to the choice of the density distribution. When $r \neq 1$, in the present work the density distribution is always discontinuous across the interface. Contrary, Maslowe and Kelly [40] assumed a continuous density profile of the form $\exp[-\gamma\tanh(y)]$, where γ can be related to r.

4.3 Results for Profiles including a Liquid Boundary Layer

In this section, the piecewise linear velocity profile (4.7) is considered. In this case the presence of a liquid boundary layer is taken into account, and the dimensionless velocity at the interface U_0 is variable, where $U_0 \geq 0$ is assumed. The study is restricted to co-flowing systems. Hence, both fluids travel in the same direction, where $U_2^* > U_1^* > 0$, or, equivalently, $0 < M < 1$. Since the effects of both interfacial tension and density stratification on the inviscid instability results were already considered in Section 4.2, here surface tension is neglected, $S = 0$. In addition, three different fixed density ratios are considered: $r = 1$ (one-layer limit), $r = 0.0012$ (corresponding approximately to air/water), and $r = 0.02$ (corresponding approximately to hydrogen/liquid oxygen). Thus, the inviscid study of the profile (4.7) is focussed on varying the two additional parameters: the dimensionless interface velocity U_0, and the ratio of the boundary layer thicknesses n.

4.3.1 Temporal Growth Rates

The influence of the parameters U_0 and n is first considered in the temporal setting. By varying the interface velocity U_0 relative to the value of M, it will be shown in the following paragraph, that the effect of changing U_0 depends effectively on the velocity ratio M.

Variations of Interface Velocity and Velocity Ratio

In this paragraph both boundary layers are equal-sized, i.e. $n = 1$. First, in the limit of a single fluid ($r = 1$, $S = 0$) a family of basic profiles with fixed positive asymptotic velocities U_1^* and U_2^* is considered. The velocity ratio is $M = 0.5$, and only the interface velocity $U_0 > 0$

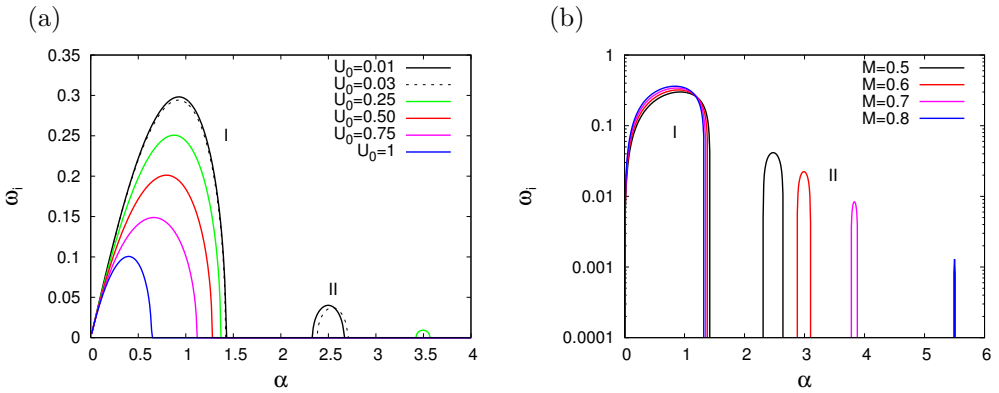

Figure 4.16: *Inviscid results for the piecewise linear basic flow including a liquid boundary layer in the one-layer limit, $r = n = 1$, $S = 0$: In (a) the temporal unstable modes for $M = 0.5$ are shown for different values of $U_0 > 0$. Note the presence of a second unstable mode for $U_0 < 0.5$. In (b) the effect of velocity ratio variation on the temporal results is shown. The interface velocity is $U_0 = 0$.*

changes. For these velocity profiles, Figure 4.16(a) shows the temporal growth rates ω_i as a function of the real wave number α. When $U_0 = 1 - M = 0.5$, the interface velocity equals the asymptotic velocity in the lower fluid. In this case, there is effectively no liquid boundary layer, and the corresponding stability curve is equivalent to those in Figure 4.2. When U_0 is decreased from this value, both the maximum temporal growth rate $\omega_i^{\max}$ and the range of unstable wave numbers increase. Furthermore, for $U_0 < 0.5$ a second unstable mode occurs at relatively larger values of α. These additional mode is referred to as mode II, whereas those already present in the absence of a liquid boundary layer is called mode I.
As mentioned above, the influence of U_0 needs to be related to the velocity ratio M. The relative effect of velocity ratio variation on the inviscid results is shown in Figure 4.16(b). Here $U_0 = 0$ is constant, and M varies. The effect on mode I is rather small. Contrary, mode II shifts towards larger wave numbers for increasing M, and both the interval of unstable wave numbers and the maximum growth rate $\omega_i^{\max}$ decrease. The latter result is clearly related to the reduced shear in the liquid boundary layer as M approaches unity. Additionally, for $U_0 = 0$ the dispersion relation (4.9) suggests the scaling

$$\alpha^{-1} \propto 1 - M \tag{4.19}$$

for mode II in the limit $M \to 1$. Consequently, since $\alpha \to \infty$ and $\omega_i^{\max} \to 0$ for mode II as $M \to 1$, only mode I is present for $M = 1$. This is exactly the mode shown in Figure 4.2, since the case $M = 1$, $U_0 = 0$ corresponds exactly to the basic flow given by relations (4.2) with $M = 1$.

For practical relevance, now the density ratio $r = 0.0012$ corresponding approximately to air and water is considered. As before, surface tension is neglected, $S = 0$. The basic flow has fixed asymptotic velocities, but different values of the dimensionless interface velocity. In Figure 4.17 temporal growth rates $\omega_i(\alpha)$ are shown for $M = 0.98$, and variable values of U_0. When $U_0 = 0.02$, the interface velocity equals the asymptotic velocity $U_1 = 1 - M$ in the lower fluid. In this case, there is effectively no liquid boundary layer, and the velocity profile is exactly those considered in Section 4.2. Hence, only mode I is present. As in the limit of equal densities, for decreasing U_0 the range of unstable wave numbers for mode I increases, and mode II occurs at higher wave numbers. When the interface velocity is slightly increased from $U_0 = 0.02$, there are also two modes present. A further increase of U_0 eventually results into the formation of a single curve. For $U_0 = 0.04$ modes I and II have merged, and only two local maxima remain.
Finally, for $U_0 = 0.01$ the eigenfunctions of both modes I and II are presented at the wave numbers of maximum temporal amplification. Mode I is shown in Figure 4.18(a). It is very

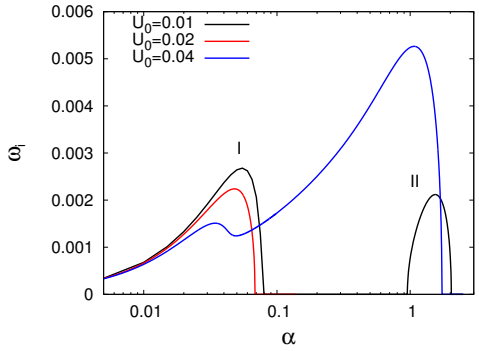

Figure 4.17: *Inviscid temporal growth rates for the piecewise linear velocity profile including a liquid boundary layer for air/water flow ($r = 0.0012$) with $n = 1$, $S = 0$, $M = 0.98$ and different values of the interface velocity U_0.*

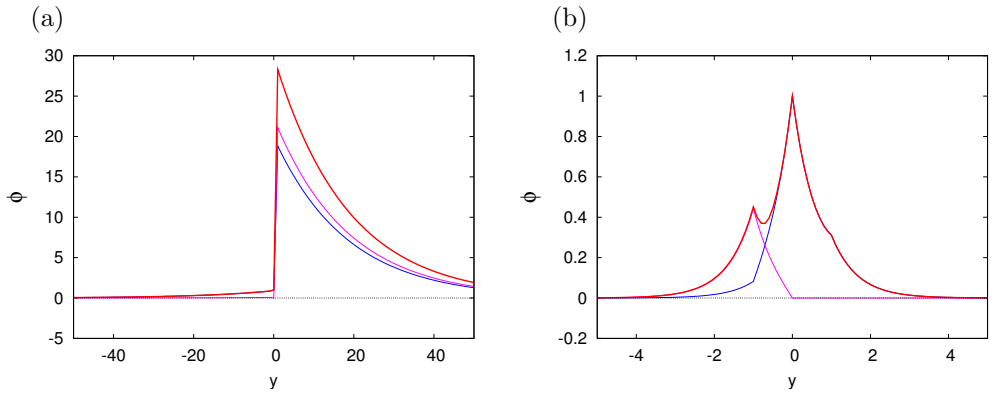

Figure 4.18: *Inviscid temporal eigenfunctions of the unstable modes at wave numbers of maximum amplification normalized by $\phi(0) = 1$ for air/water flow ($r = 0.0012$) with $n = 1$, $S = 0$, $M = 0.98$, and $U_0 = 0.01$: (a) mode I at $\alpha^{\max} = 0.055$, and (b) mode II at $\alpha^{\max} = 1.54$. The real and imaginary part of the eigenfunction are shown in blue and magenta, respectively, and $|\phi|$ is plotted in red.*

similar to the eigenmode in Figure 4.5(b) for the basic flow without liquid boundary layer. For mode I the perturbation is located in the upper gas phase, i.e. for $y > 0$. It is remarked, that usually the presence or absence of both surface tension and a velocity defect does not signifivantly modify the structure of the mode.
Contrary, the eigenfunction of mode II peaks at the interface, and has another local maximum in amplitude in the lower phase, i.e. for $y < 0$, see Figure 4.18(b). Mode II is therefore related to the presence of a boundary layer in the lower liquid phase. As a result, it cannot be observed when $U_0 = 1 - M$, since in this case there is effectively no liquid boundary layer.

Variations of the Boundary Layer Ratio

Until now the ratio of boundary layer thicknesses was $n = 1$. In this paragraph the influence of n on the temporal modes is studied. The ratio of densities and the asymptotic velocities in the free streams are fixed. For a change, the values $r = 0.02$ and $M = 0.9$ are chosen. These parameters are typical for flows involving hydrogen and liquid oxygen [28]. The effect of varying n is considered for three different values of the dimensionless interface velocity. Figures 4.19(a) and (b) show the temporal instability curves for $U_0 = 0.01$ and $U_0 = 0.15$, respectively. In these

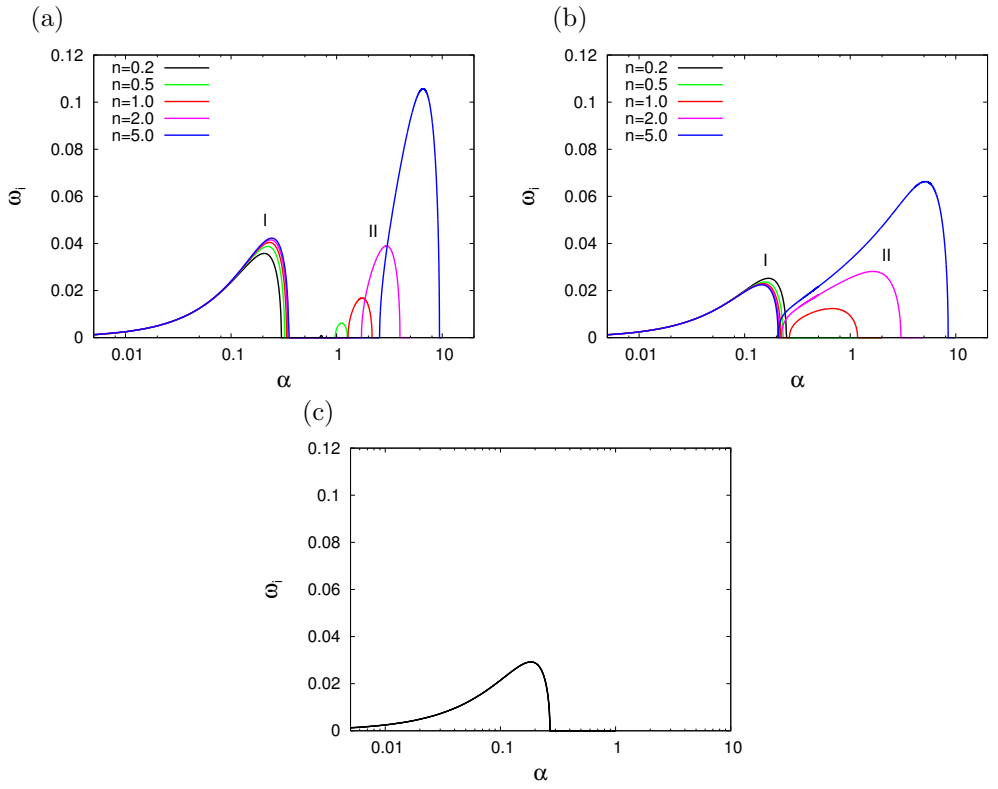

Figure 4.19: *Effect of boundary layer ratio variation on the temporal results for the piecewise linear velocity profile for* $r = 0.02$, $S = 0$, *and* $M = 0.9$. *The interface velocity is (a)* $U_0 = 0.01$, *(b)* $U_0 = 0.15$, *and (c)* $U_0 = 0.1$. *In the last case the results are insensitive to changes of* n.

cases the interface velocity is less and greater than the mean speed in the slower liquid layer, respectively. In addition, Figure 4.19(c) displays the results for $U_0 = 1 - M = 0.1$. In this case the basic flow has effectively no liquid boundary layer, and only mode I is present, whose stability characteristics are insensitive to changes of n. Hence, the growth rate $\omega_i(\alpha)$ is the same for all values of n. When the interface velocity does not equal the mean speed of the slower liquid phase, mode II may be present at relatively larger wave numbers. As already mentioned, the occurence of this mode is adressed to the presence of the liquid boundary layer. Consequently, keeping the remaining parameters fixed, mode II is strongly affected by variations of n: When increasing n, the boundary layer in the liquid becomes increasingly smaller compared to those in the gas phase. Thus, for given values of M and U_0, the fixed velocity difference in the lower phase is located in the decreasing interval $-1/n \leq y \leq 0$. As a consequence, the shear increases with n, leading to enhanced growth rates ω_i for mode II. This can be seen in Figures 4.19(a) and (b) for $U_0 = 0.01$ and $U_0 = 0.15$, respectively.

4.3.2 Spatial Growth Rates

In this section spatially growing disturbances are considered. For convectively unstable flows the spatial instability results are shown to share many characteristics with their temporal counterparts.

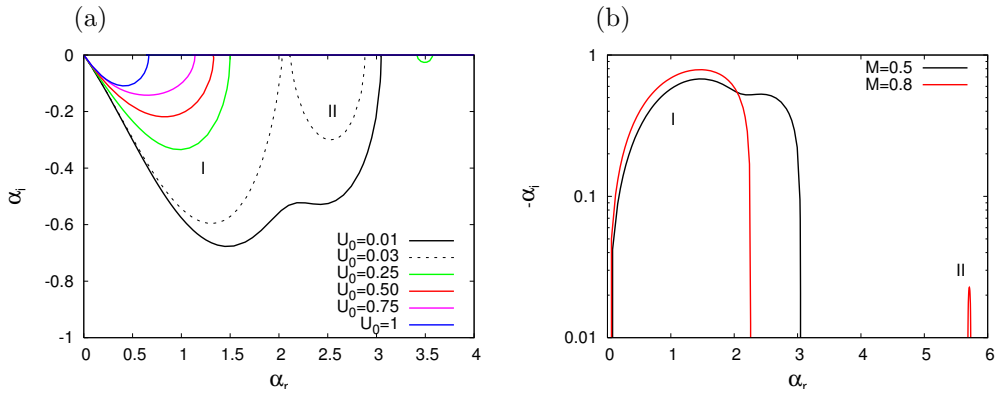

Figure 4.20: *Spatial growth rates for the piecewise linear basic flow including a liquid boundary layer in the one-layer limit, $r = n = 1$, $S = 0$ for (a) $M = 0.5$ and different values of $U_0 > 0$, and (b) $U_0 = 0.01$ and two different values of the velocity ratio, $M = 0.5$ and $M = 0.8$.*

Variations of Interface Velocity and Velocity Ratio

As in the temporal study, the single-fluid limit ($r = n = 1$, $S = 0$) is considered first. The velocity ratio is $M = 0.5$, and only the interface velocity U_0 changes. As long as $U_0 > 0$, the flow is convectively unstable. Figure 4.20(a) shows spatial growth rates $-\alpha_i(\omega)$ for flows having various values of U_0. When $U_0 = 1 - M = 0.5$, the interface velocity equals the asymptotic velocity in the lower fluid. In this case, there is effectively no liquid boundary layer, and the red stability curve is equivalent to those in Figure 4.6(a). As in the temporal case, both the range of unstable wave numbers and the maximum growth rate $-\alpha_i^{\max}$ increase for decreasing interface velocity. In addition, mode II occurs for $U_0 < 0.5$. When the interface velocity is not too small, the temporal and spatial results look very similar. In contrast, for $U_0 = 0.01$ modes I and II have merged into a single curve, and only two local maxima of spatial amplification remain.
The formation of a single unstable mode strongly depends on the velocity ratio M. For example, Figure 4.20(b) compares the spatial instability curves for $M = 0.5$ and $M = 0.8$, where the interface velocity is $U_0 = 0.01$ in both instances. Contrary to the case $M = 0.5$, the spatial stability curves of modes I and II do not form a single spatial mode for $M = 0.8$, and remain seperate in distinct intervals of the wave number α_r. Note further, that the maximum spatial growth rate $-\alpha_i^{\max}$ of mode II is much smaller than those of mode I. These observations confirm the result that a change of the interface velocity U_0 must be considered with respect to the velocity ratio M.

Figure 4.21(a) shows spatial results for air and water ($r = 0.0012$), where $S = 0$, and $n = 1$. The velocity ratio is $M = 0.98$, and only the interface velocity changes. Again, as long as $U_0 > 0$, the flow is convectively unstable. As in the temporal setting, there are two modes for $U_0 = 0.01$, whereas only one is present for both $U_0 = 0.02$ and $U_0 = 0.04$. Recall from Figure 4.17, that two local extrema are observed in the temporal plot for $U_0 = 0.04$. In the case of spatial instability, however, only the peak at large wave numbers remains, see Figure 4.21(a).

An important effect can be identified by considering the temporal and spatial instability curves for $U_0 = 0.01$. The maximum temporal growth rates can be identified to be $\omega_i^{(I)} \approx 0.00268$ for mode I, and $\omega_i^{(II)} \approx 0.00212$ for mode II, see Figure 4.17. The maximum spatial growth rates of modes I and II are $-\alpha_i^{(I)} \approx 0.0356$ and $-\alpha_i^{(II)} \approx 0.1444$, respectively. Therefore, $-\alpha_i^{(I)} < -\alpha_i^{(II)}$, whereas $\omega_i^{(I)} > \omega_i^{(II)}$. Hence, a mode being temporally less unstable than another, may be most unstable in the spatial setting. For the considered parameters, this effect can already be estimated by means of Gaster's transformation (2.98). In Figure 4.21(b) the calculated spatial results are compared with these approximation.

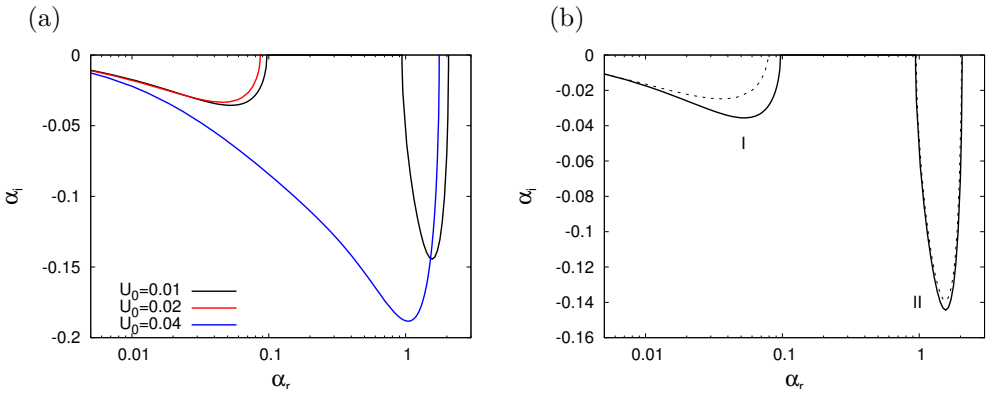

Figure 4.21: *Spatial growth rates for the basic velocity profile including a liquid boundary layer for air/water flow ($r = 0.0012$) with $M = 0.98$, $n = 1$, $S = 0$: (a) effect of varying the interface velocity U_0, (b) comparison of the spatial instability results for $U_0 = 0.01$ (solid) with Gaster's approximation (dashed).*

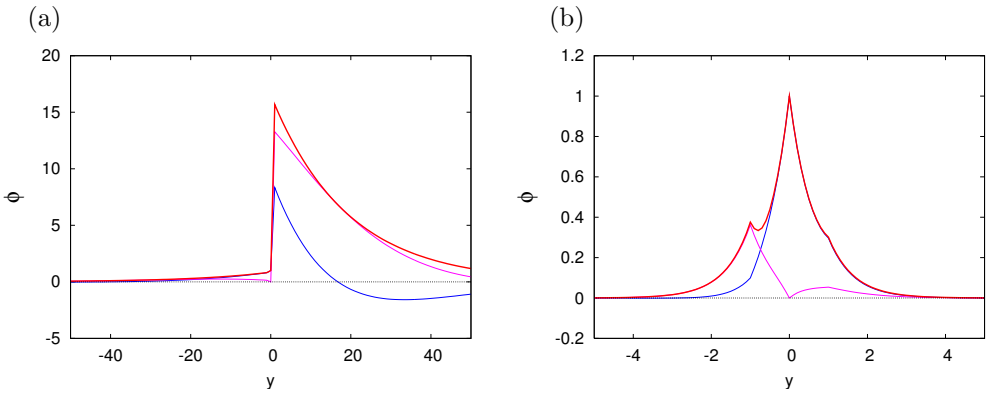

Figure 4.22: *Inviscid spatial eigenfunctions of the unstable modes at wave numbers of maximum amplification normalized by $\phi(0) = 1$ for air/water flow ($r = 0.0012$) with $n = 1$, $S = 0$, $M = 0.98$, and $U_0 = 0.01$: (a) mode I at $\alpha_r^{\max} = 0.0529$, and (b) mode II at $\alpha_r^{\max} = 1.5634$. The real and imaginary part of the eigenfunction are shown in blue and magenta, respectively, and $|\phi|$ is plotted in red.*

Finally, for $U_0 = 0.01$ the eigenfunctions of both modes I and II are given at the wave numbers of maximum spatial amplification. Mode I is shown in Figure 4.22(a). Its perturbation is located in the upper gas phase, i.e. for $y > 0$. As in the temporal setting, mode I has a counterpart in the flow without liquid boundary layer, since it is very similar to the eigenmode in Figure 4.8(b). As for mode I, there is no significant difference between the temporal and spatial eigenfunctions of mode II. The latter peaks at the interface and has another local maximum in amplitude in the lower phase, i.e. for $y < 0$, see Figure 4.22(b).

Variations of the Boundary Layer Ratio

As in the temporal setting, the effect of varying the ratio of boundary layer thicknesses is considered for parameters corresponding approximately to hydrogen and liquid oxygen: $r = 0.02$, $M = 0.9$. Figure 4.23 shows the spatial growth rates $-\alpha_i(\omega)$ for various n, and the same three values of the dimensionless interface velocity as in the temporal study: $U_0 = 0.01$, $U_0 = 0.1$, and $U_0 = 0.15$. The overall picture of the spatial results is essentially similar to those obtained for temporal modes; see Figure 4.19 for comparison.

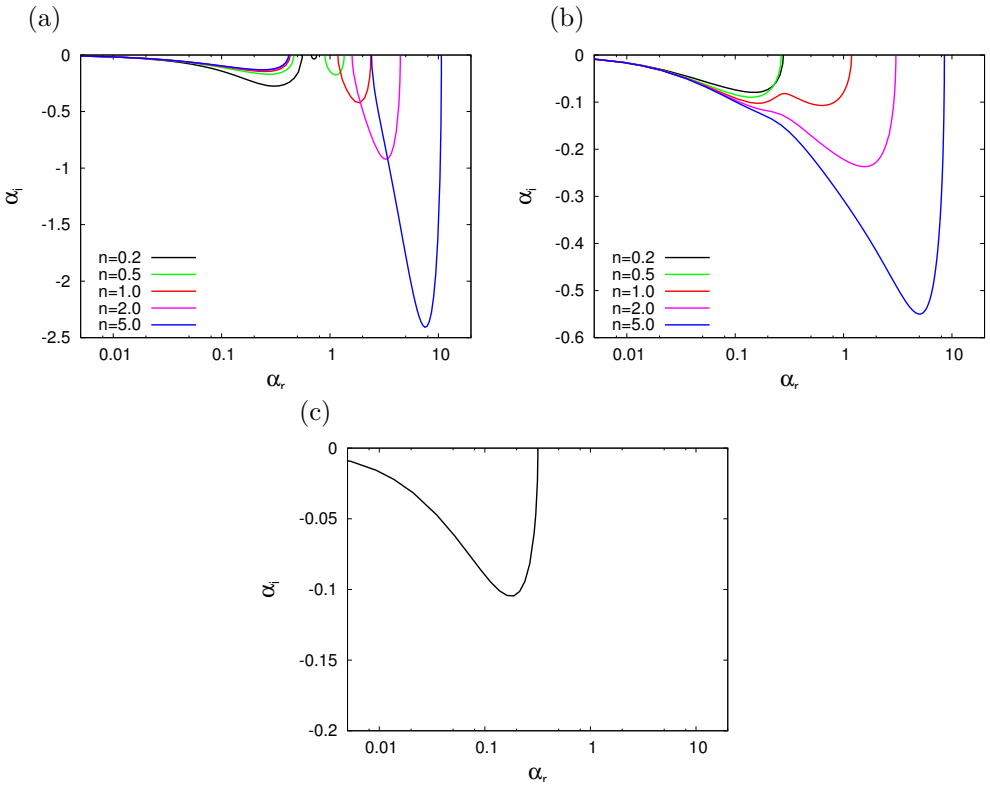

Figure 4.23: *Effect of boundary layer ratio variation on the spatial results for the piecewise linear velocity profile for* $r = 0.02$, $S = 0$, *and* $M = 0.9$. *The interface velocity is (a)* $U_0 = 0.01$, *(b)* $U_0 = 0.15$, *and (c)* $U_0 = 0.1$. *In the last case the results are insensitive to changes of* n.

4.3.3 Transition from Convective to Absolute Instability

Recall that, in the absence of surface tension, $S = 0$, the basic flow without liquid boundary layer, given by relations (4.2), is only convectively unstable for co-flows, i.e. when the velocity ratio $M < 1$. This result was shown to hold for each density ratio, and the absolute frequency is given by (4.17). It is possible to formulate an analoguous result for the velocity profile (4.7), which includes a boundary layer in the slower liquid phase:

Consider the piecewise linear velocity profile (4.7) including a liquid boundary layer in the absence of surface tension, $S = 0$. Then, for $M < 1$, and independent of the remaining parameters,

- each flow with positive interface velocity, $U_0 > 0$, is convectively unstable,
- each flow with $U_0 = 0$ is absolutely unstable.

In case of absolute instability the absolute wave number is $\alpha_r^0 \to \infty$ and the absolute frequency is

$$\omega^0 = \frac{r(1+M) + n(1-M)}{r+1}. \tag{4.20}$$

The derivation of this result is similar to those for relation (4.17), and is sketched briefly in Appendix A.3.5. Further, the above result can be combined with those of Section 4.2.3 to give the following condition for convectively unstable piecewise linear velocity profiles:

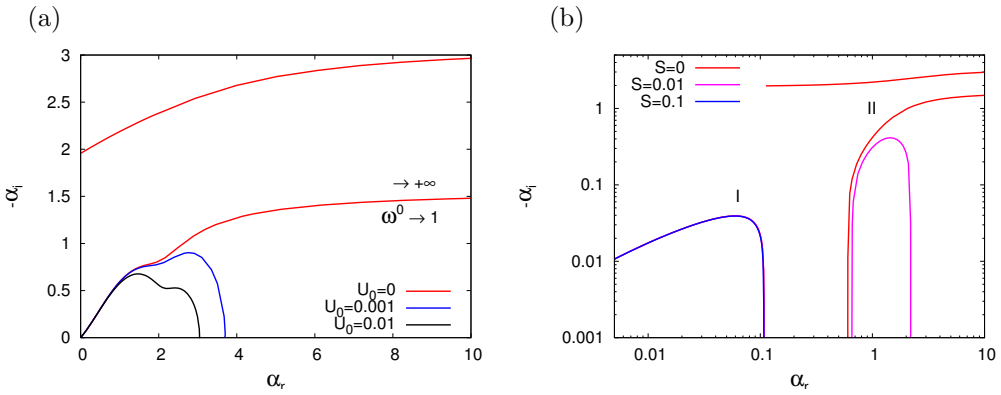

Figure 4.24: *Absolute instability for the piecewise linear velocity profile with equal boundary layer sizes, $n = 1$, (a) in the limit $U_0 \to 0$ when $S = 0$, and (b) in the limit $S \to 0$ for flows with $U_0 = 0$. In (a) the results for $r = 1$ and $M = 0.5$ are compared with those for $U_0 = 0.01$. In (b) the parameters correspond to air and water, $r = 0.0012$, $M = 0.98$ with various values of S.*

In the absence of surface tension, $S = 0$, for the piecewise linear velocity profiles considered in this chapter each convectively unstable flow must satisfy the condition

$$U(y) > 0, \quad \text{for all } y. \tag{4.21}$$

For both piecewise linear velocity profiles the above inequality is fullfilled when $M < 1$. In addition, $U_0 > 0$ is required for the basic flow including a liquid boundary layer. Further, as already mentioned, when $U_0 = 1 - M$, the interface velocity equals the asymptotic velocity in the lower fluid, and the basic flow (4.7) simplifies to those given by relations (4.2). In this case, the limit $U_0 \to 0$ is equivalent to $M \to 1$, and equation (4.17) can be obtained by placing $M = 1$ into relation (4.20). It is finally noted, that no result analogous to those given by relation (4.21) is possible for $S > 0$, since the inclusion of surface tension modifies the convective/absolute characteristics in a non-trivial manner, as was already shown in Section 4.2.3.

To summarize, the basic flow with liquid boundary layer is absolutely unstable, when both $S = 0$ and $U_0 = 0$. In this limit, Figure 4.24 shows the transition to absolute instability by considering the wave number α_S, at which the spatial instability curve intersects the branch cut.
For the basic flow (4.2) without liquid boundary layer, in the absence of surface tension, $S = 0$, α_S was shown to move to the right for increasing values of the velocity ratio, and recedes to $+\infty$ in the limit $M \to 1$. For both $S = 0$ and $M < 1$, a similar behaviour is observed for the velocity profile (4.7) including a liquid boundary layer, when U_0 is decreased to zero. Figure 4.24(a) shows the spatial instability curve for $U_0 = 0$ in the limit of a single fluid ($r = n = 1$) with $M = 0.5$. Absolute instability is present, and, by equation (4.20), the absolute frequency is $\omega^0 = 1$. For comparison, the instability curves for $U_0 = 0.001$ and $U_0 = 0.01$ are plotted as well. In these cases the flow is convectively unstable.
A similar observation as those in Figure 4.24(a) is expected for basic flows with zero interface velocity in the limit $S \to 0$. Figure 4.24(b) shows the spatial instability curves for flow of air and water ($r = 0.0012$) with $n = 1$, and $M = 0.98$. For these parameters and $U_0 = 0$, two unstable modes may be present, depending on the value of S. Mode I is almost unaffected by variations of S. On the other hand, mode II is damped for increasing values of S, and no more amplified for $S \geq 0.1$. Contrary, when S is decreased, mode II is present in an increasing interval of wave numbers α_r. Eventually, in the limit $S \to 0$, the intersection point of the spatial instability curve of mode II with the α_r-axis is at $+\infty$ for the absolute frequency value $\omega^0 = 0.0223492$, which again can be derived by equation (4.20). Hence, the flow is absolutely unstable for $S = 0$, whereas it is convectively unstable for $S > 0$.

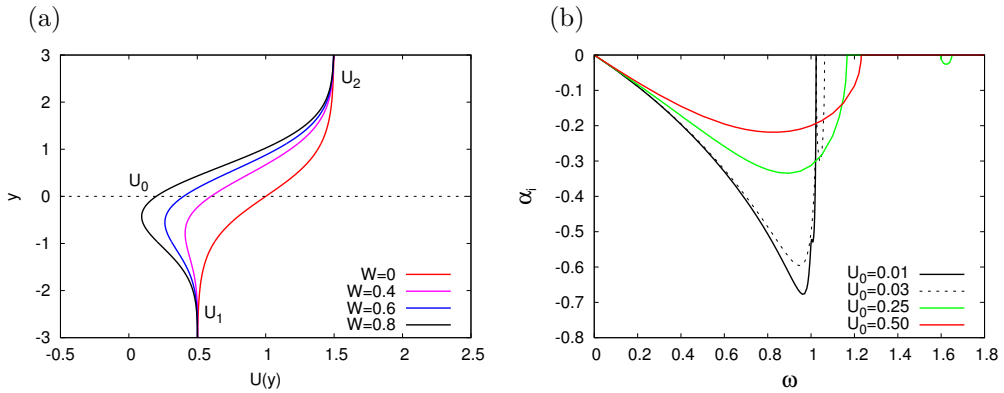

Figure 4.25: *(a) Mean velocity profiles given by relation (4.22) for $M = 0.5$, and different values of the normalized wake deficit W. (b) Spatial growth rates as a function of frequency ω for the piecewise linear velocity profile with $r = n = 1$, $S = 0$, $M = 0.5$ and different values of $0 < U_0 \leq 1 - M$. The curves correspond to those of the same colour in Figure 4.20(a).*

4.3.4 Comparison with Results for Smooth Velocity Profiles

The inviscid study of the piecewise linear profile (4.7) is finished by relating the presented results to those for velocity profiles, that are infinitely smooth. In order to account for the particular flow structure near the tip of the splitter plate, Koochesfahani and Frieler [34] investigated the linear instability characteristics of plane shear layers, whose smooth basic velocity profile includes a wake component. The parallel mean velocity profile is composed of the hyperbolic tangent profile plus a wake component represented by a Gaussian distribution. Its dimensionless form is given by

$$U(y) = 1 + M\tanh(y) - W\exp[-\ln(2)y^2], \tag{4.22}$$

where M is the velocity ratio, and W is the normalized wake deficit. The dimensionless interface velocity is $U_0 = 1 - W$. Contrary to the piecewise linear case, U_0 is, in general, not the minimum velocity of $U(y)$. Figure 4.25(a) shows mean velocity profiles given by (4.22) for $M = 0.5$, and different values of W. The profiles can be thought of as representing the evolution of the mean velocity profile due to viscous diffusion. Starting near the splitter lip, a profile with a large wake deficit, e.g. $W = 0.8$, evolves into one with no wake component, $W = 0$, as the flow convects downstream. In addition, the mean density profile is assumed to have a hyperbolic-tangent profile given by

$$\rho(y) = 1 + \Lambda\tanh\left(\frac{y - y_0}{\sigma}\right), \tag{4.23}$$

where $\Lambda = (\rho_2 - \rho_1)/(\rho_1 + \rho_2)$. The parameters y_0 and σ adjust the lateral position and thickness of the density profile relative to the velocity profile. Koochesfahani and Frieler [34] calculated the range of unstable frequencies and wave numbers of the linear instability using inviscid spatial stability analysis for both uniform and nonuniform density flows.

Uniform Density

When the density is uniform across the layer, the effect of the depth of the wake deficit on the spatial instability characteristics of the shear layer (4.22) was considered for a fixed velocity ratio M. In the presence of the wake component, two unstable modes are found as opposed to one for the pure hyperbolic-tangent profile [34]. However, in the limit $W = 0$ mode I approaches the *tanh* profile solution, while mode II vanishes. In general, the growth rate of mode II is dominated by that of mode I. Both modes are amplified for frequencies in certain ranges, $0 < \omega < \omega_N^I$ and $0 < \omega < \omega_N^{II}$, where the upper bounds of the intervals are usually distinct, i.e. $\omega_N^I \neq \omega_N^{II}$. As

the wake deficit increases, the neutral point ω_N^I of mode I moves to lower frequencies and its maximum amplification rate $-\alpha_i^{\max}$ increases [34]. The same effect is observed for the piecewise linear velocity profile (4.7) with $r = 1$, when the interface velocity U_0 is decreased. This is shown in Figure 4.25(b). Contrary to the smooth basic flow (4.22), the modes of the piecewise linear profile are usually amplified in distinct ranges of frequencies, where those for mode II are larger. However, as was shown in Figure 4.20(a), for decreasing values of U_0, the spatial instability curves of the unstable modes can merge, and eventually form a single one. In this case, the interval of unstable frequencies for mode II moves towards those for mode I, until a single range of unstable frequencies, $0 < \omega < \omega_N$, remains for the coalesced mode.

Nonuniform Density

In investigating the effect of nonuniform density, a specific velocity profile with fixed velocity ratio M and wake deficit W was considered. The density profile (4.23) was chosen to have its inflection point at the minimum of the velocity profile (4.22), and its thickness much smaller than that of the velocity profile. These conditions are expected to hold near the splitter lip. However, as long as the density profile is sufficiently thin relative to the velocity profile, the qualitative features of the results are not sensitive to these conditions [34].
Recall, that in flows of uniform density, the spatial growth rate of mode II was shown to be dominated by that of mode I. When the high-density fluid is on the high-speed side, mode I remains dominant for the wake velociy profile (4.22). However, if the density of the low-speed stream is larger than that of the high-speed stream, the spatial amplification rate of mode II can become comparable or even stronger than that of mode I [34]. The same result is found for the piecewise linear velocity profile; see e.g. the solid curve in Figure 4.21(b). The result corresponds to flow of air and water ($r = 0.0012$) with $M = 0.98$ and $U_0 = 0.01$.

4.4 Summary

In this chapter an invisicd spatio-temporal instability analysis is performed for two piecewise linear velocity profiles. The generalized profile (4.7) includes boundary layers in both the gas and liquid layer. It further includes the basic flow (4.2) as a special case, when the dimensionless interface velocity equals the mean liquid velocity, i.e. $U_0 = 1 - M$. For this particular choice of U_0 there is effectively no liquid boundary layer.
For the generalized velocity profile (4.7), in general, two unstable modes I and II are present. Mode I is associated with the boundary layer δ_2 in the gas, whereas mode II, which occurs at relatively larger wave numbers, is related to the boundary layer δ_1 in the liquid.

In the absence of a liquid boundary layer, only mode I is unstable. In the absence of surface tension, $S = 0$, its temporal growth rate is exactly a linear function of the velocity ratio M. Contrary, in the spatial case the growth rates increase with M in a nontrivial manner. However, the dependency of the maximum growth rates and its associated wave number with both the density ratio r and surface tension S are generally similar in both the temporal and the spatial setting. More precisely, in the limit $r \to 0$ the growth rates are proportional to r, and the associated wave number decreases as $\sqrt{r}$. Further, the effect of surface tension is much more pronounced for relatively large density ratios, say $r \geq 0.01$.
When $U_0 \neq 1 - M$, for both temporally and spatially growing perturbations, both the growth rate and the unstable wave number range of mode I generally increase with decreasing U_0. In addition, mode II may be unstable. In contrast to mode I, its instability characteristics strongly depend on n. It is also observed, that in some cases, the two unstable branches I and II have merged into a single curve. This formation of a single unstable mode depends on the parameters and can be found in both the temporal and the spatial setting.

In addition, the dominant modes in the temporal and in the spatial analyses are not necessarily identical. This effect can be explained using Gaster's transformation (2.98), which states that the ratio of temporal and spatial growth rates is approximately equal to the group velocity c_g.

Finally, in the absence of surface tension, $S = 0$, for convective instability the piecewise linear velocity profile (4.7) must satisfy

$$U(y) > 0, \quad \text{for all } y.$$

In this case, the absolute wave number is $\alpha_r^0 \to +\infty$, and the absolute frequency is given by (4.20),

$$\omega^0 = \frac{r(1+M) + n(1-M)}{r+1}.$$

Note, that for $S > 0$ there is no analogous result possible, since the inclusion of surface tension modifies the convective/absolute characteristics in a nontrivial manner. However, interfacial tension usually promotes absolute instability for small or moderate r.

Chapter 5

Instability of Viscous Two-Phase Mixing Layers

In this chapter viscosity is taken into account, and a more realistic velocity distribution as in the inviscid piecewise linear approach is introduced. The viscous basic velocity profile includes both viscous boundary layers adjacent to the interface to satisfy continuity of velocity and shear stress at the interface, and a velocity defect describing a wake generated by the no-slip condition upstream of the splitter plate edge. This velocity defect decreases with increasing distance from the nozzle since the slower liquid phase is accelerated by the fast gas stream. As for the inviscid piecewise linear approach a spatio-temporal stability analysis is performed including the determination of the transition from convective to absolute instability. [1]

5.1 Viscous Basic Velocity Profile

The modeling of the basic velocity distribution behind the splitter plate depends on the level of detail and realism one wishes to achieve. In this work, the viscous basic velocity profile is modeled to include the fact that, inside the nozzle, the velocities U_1^* and U_2^* far away from the plate in the liquid (phase 1) and the gas (phase 2) adjust to zero on the plate within boundary layers of width δ_1 and δ_2. Just behind the nozzle, both boundary layers – mathematically modelled by a function $U_s(y)$ – keep characterizing the velocity distribution of the liquid and gas phases. However, this velocity field is not sufficient since the distribution $U_s(y)$ would have a discontinuous slope on the liquid-gas interface $y = 0$. To account for the effect of finite plate thickness and to satisfy continuity of velocity and shear stress at the interface, a splitter plate wake correction $U_d(y)$ is added to the distribution $U_s(y)$. This correction $U_d(y)$ is centered on the interface and represents a finite vorticity layer of vanishing total circulation.
To keep the mathematical and numerical complexity of the problem manageable, the functions U_s and U_d are analytically modeled by simple functions so that the velocity profile $U_s + U_d$ mimics the complex experimental structure. The distribution U_s is represented by error functions centered on the interface, i.e.

$$U_s(y) = -U_1^* \operatorname{erf}\left(\frac{y}{\delta_1}\right), \qquad y \leq 0, \tag{5.1}$$

$$U_s(y) = U_2^* \operatorname{erf}\left(\frac{y}{\delta_2}\right), \qquad y \geq 0, \tag{5.2}$$

[1] Most of the content of this chapter is included in "Viscous instability of a sheared liquid-gas interface: dependence on fluid properties and basic velocity profile" [46], which was submitted to Phys. Fluids.

where the error function is defined by

$$\mathrm{erf}\,(z) = \frac{2}{\sqrt{\pi}} \int_0^z \exp\left(-\xi^2\right) d\xi. \tag{5.3}$$

Error functions are building blocks of the exact solutions of the first Stokes problem. They thus describe an impulsively started flow adjacent to a flat plate. The function U_d is chosen to be

$$U_d = U_0^* \left[1 + \mathrm{erf}\left(\frac{y}{\delta_d^*}\right)\right], \qquad y \le 0, \tag{5.4}$$

$$U_d = U_0^* \left[1 - \mathrm{erf}\left(\frac{y}{\delta_d^*}\right)\right], \qquad y \ge 0. \tag{5.5}$$

It is characterized by a velocity U_0^*, which is the interface velocity since $U_s(0) = 0$, and a width δ_d^*. This velocity distribution decays to zero on either side of the interface when the distance $|y|$ is large ($|y| > \delta_d^*$). It is based on the simplest smooth vorticity distribution $\eta(y,t)$ of a wake with vanishing total circulation,

$$\eta = -\frac{2U_0^*}{\sqrt{\pi}\delta_d^*} \exp\left(-\frac{y^2}{\delta_d^*}\right), \qquad y \le 0, \tag{5.6}$$

$$\eta = \frac{2U_0^*}{\sqrt{\pi}\delta_d^*} \exp\left(-\frac{y^2}{\delta_d^*}\right), \qquad y \ge 0. \tag{5.7}$$

Near the splitter plate edge, δ_d^* must be close and physically related to the plate thickness. At larger downstream distance it increases. In the present work, it is a parameter in the parallel flow approximation.
The total velocity $U = U_s + U_d$ is clearly continuous on the interface. The continuity of the shear stress

$$\mu_1 \left.\frac{\partial U}{\partial y}\right|_{y=0-} = \mu_2 \left.\frac{\partial U}{\partial y}\right|_{y=0+}. \tag{5.8}$$

is enforced, if the interface velocity U_0^* is imposed to be equal to

$$U_0^* = \frac{\frac{\mu_2 U_2^*}{\delta_2} + \frac{\mu_1 U_1^*}{\delta_1}}{\mu_2 + \mu_1}\, \delta_d^*. \tag{5.9}$$

This quantity is thus related to the width δ_d^*. As a summary, the basic velocity field is given by

$$U_1(y) = -U_1^* \,\mathrm{erf}\left(\frac{y}{\delta_1}\right) + U_0^* \left[1 + \mathrm{erf}\left(\frac{y}{\delta_d^*}\right)\right], \qquad y \le 0, \tag{5.10}$$

$$U_2(y) = U_2^* \,\mathrm{erf}\left(\frac{y}{\delta_2}\right) + U_0^* \left[1 - \mathrm{erf}\left(\frac{y}{\delta_d^*}\right)\right], \qquad y \ge 0. \tag{5.11}$$

As in the inviscid case, only results for co-current flows where the upper gas velocity is larger than the lower liquid velocity are considered, i.e. $U_2^* > U_1^* > 0$. In addition, the length δ_d^* is assumed to be smaller than the boundary layer sizes,

$$0 < \delta_d^* \le \delta_1, \qquad 0 < \delta_d^* \le \delta_2, \tag{5.12}$$

to ensure that the velocity profile maintains a single local extremum. Without these assumptions, e.g., when $\delta_d^* > \delta_2$, the velocity in the gas boundary layer would be locally larger than its asymptotic velocity U_2^* in the gas, which would not be very realistic.

For non-dimensionalization, δ_2 is used as length scale, and the mean velocity $\bar{U} \equiv (U_2^* + U_1^*)/2$ is chosen as velocity scale. Based on these units, the non-dimensional viscous basic velocity profile reads

$$U_1(y) = -(1-M)\ \mathrm{erf}\,(ny) + U_0\left[1 + \mathrm{erf}\left(\frac{n}{\delta_0}y\right)\right], \qquad y \le 0, \tag{5.13}$$

$$U_2(y) = (1+M)\ \mathrm{erf}\,(y) + U_0\left[1 - \mathrm{erf}\left(\frac{n}{\delta_0}y\right)\right], \qquad y \ge 0, \tag{5.14}$$

where

$$M = \frac{U_2^* - U_1^*}{U_2^* + U_1^*} \tag{5.15}$$

quantifies the velocity ratio, and

$$n = \frac{\delta_2}{\delta_1}, \qquad \delta_0 = \frac{\delta_d^*}{\delta_1} \tag{5.16}$$

respectively denote the ratio between boundary layer sizes and the ratio between the plate width δ_d^* and the boundary layer size in the liquid δ_1. The dimensionless interface velocity U_0 is determined by

$$U_0 = \frac{U_0^*}{\bar{U}} = \frac{\frac{m}{n}(1+M) + (1-M)}{m+1}\ \delta_0, \tag{5.17}$$

where

$$m = \frac{\mu_2}{\mu_1} \tag{5.18}$$

denotes the ratio of dynamic viscosities. The non-dimensional viscous basic profile thus depends on the four variables M, n, δ_0, and m. According to the assumptions on velocities and boundary layer sizes, the dimensionless interface velocity U_0 remains positive, the velocity ratio M is in the range $0 \le M \le 1$, and finally $\delta_0 \le 1$ and $\delta_0 \le n$.

A basic velocity profile with fixed velocity ratio M, and various U_0 represents different stages of the downstream spatial evolution of the basic flow, see Figure 5.1. Near the splitter plate the defect width δ_0 is small and, by consequence, U_0 is small. This implies that the velocity defect, quantified by $U(\infty) - U(0)$, is larger than further downstream. Getting away from the splitter plate, δ_0 increases as well as U_0. Finally, when all boundary layers have diffused, all thicknesses are equal ($n = \delta_0 = 1$) and the basic velocity simplifies into

$$U_1(y) = U_0 + \frac{2m}{m+1} M\ \mathrm{erf}(y), \qquad y \le 0, \tag{5.19}$$

$$U_2(y) = U_0 + \frac{2}{m+1} M\ \mathrm{erf}(y), \qquad y \ge 0, \tag{5.20}$$

where

$$U_0 = 1 + M\frac{m-1}{m+1}.$$

The above profile differs from those studied previously [6, 61] only by the uniform velocity offset U_0 and a rescaled amplitude. This specific case will be thereafter called the *Stokes solution* and will be useful for direct comparison with the results reported in Reference [6].

Now some characteristics of the basic profile are discussed. First, note that the Stokes solution has no local minimum at finite y, i.e. the slope or shear rate at any y location is always positive across the entire profile. Contrary, as soon as $\delta_0 < 1$ a unique local minimum is present in the flow for $y < |\infty|$. When $n < (1+M)/(1-M)$, this minimum is located within the lower liquid (fluid 1). Otherwise, it appears in the gas (fluid 2). For the case $n = 1$ generally studied in this chapter, the local minimum y_m is in the liquid, and its location is shown in Figure 5.2(a) for $M = 0.5$ and $M = 0.9$ as a function of the defect width δ_0. As a consequence the shear becomes

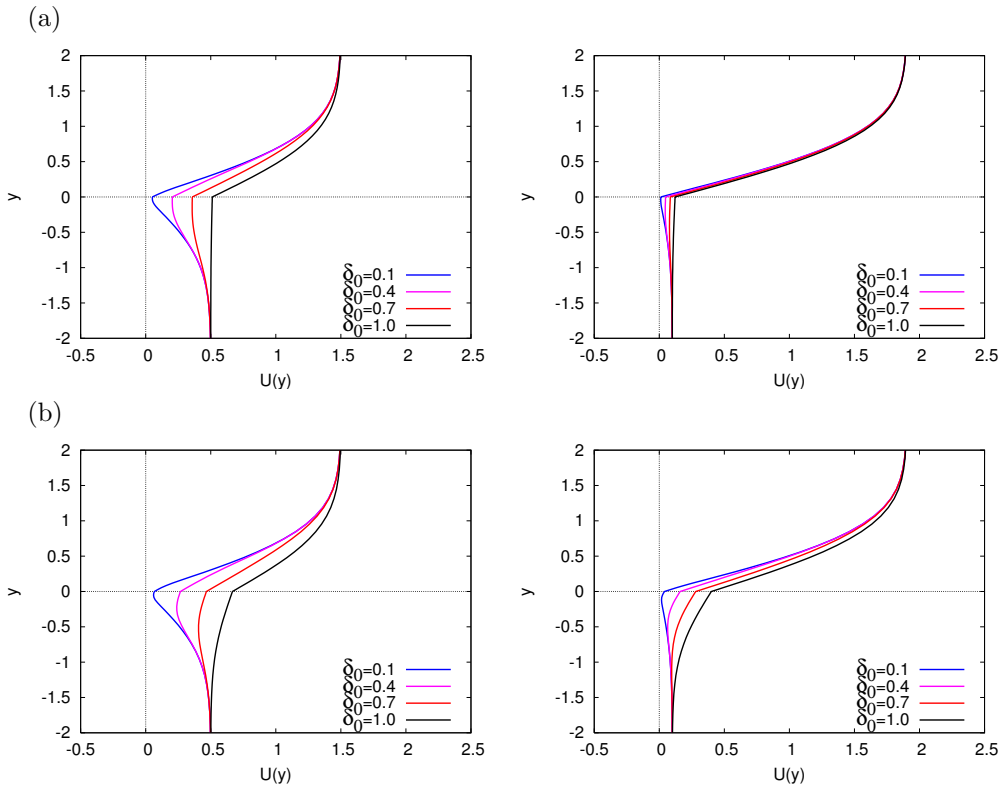

Figure 5.1: *Viscous basic velocity profiles for different values of δ_0 and velocity ratios $M = 0.5$ (left) and $M = 0.9$ (right) for (a): $m = 0.012$, $n = 1$, and (b) $m = 0.2$, $n = 1$. The upper layer corresponds to the less viscous fluid. Note, that the velocity defect is much more pronounced for the smaller velocity ratio $M = 0.5$.*

negative in the liquid for $y < y_m < 0$ and remains positive elsewhere. By reducing δ_0 from 1, the shear at the interface is modified since the velocity defect is increased. This effect depends on the velocity ratio M, see Figure 5.1. When M is close to unity, the free-stream velocities are very different and there is almost no change with δ_0 in the shear rate at the interface. Contrary, for moderate values of M the parameter δ_0 can significantly change the shear in the gas.
More importantly, the reduction of the defect width δ_0 introduces inflection points located at

$$y_i^{(1)} = -\sqrt{\frac{2\ln\left(\frac{\gamma_1}{\delta_0}\right)}{n^2\left(\frac{1}{\delta_0^2}-1\right)}}, \qquad \gamma_1^2 = \frac{\frac{m}{n}(1+M)+(1-M)}{(m+1)(1-M)}, \tag{5.21}$$

$$y_i^{(2)} = \sqrt{\frac{2\ln\left(\frac{\gamma_2}{\delta_0}\right)}{\frac{n^2}{\delta_0^2}-1}}, \qquad \gamma_2^2 = \frac{mn^2(1+M)+n^3(1-M)}{(m+1)(1+M)}, \tag{5.22}$$

see Figure 5.2(b). For the examples of Figure 5.2, where $m = 0.012$ (approximatively the value for air and water), $n = 1$ and $M = 0.5$ or $M = 0.9$, it is seen that $\gamma_2 < 1 < \gamma_1$. In addition, the inflection point located within the liquid moves from $y = -\infty$ towards the interface as δ_0 is reduced, and within the gas an inflection point bifurcates from $y = 0$ when $\delta_0 < \gamma_2$. Finally, a decrease of the velocity ratio M favours the appearance of the gas inflection point since $\gamma_2 = 0.253$ for $M = 0.9$ meanwhile $\gamma_2 = 0.584$ for $M = 0.5$. The existence of these inflection points is shown below to modify the behaviour and properties of certain unstable modes.

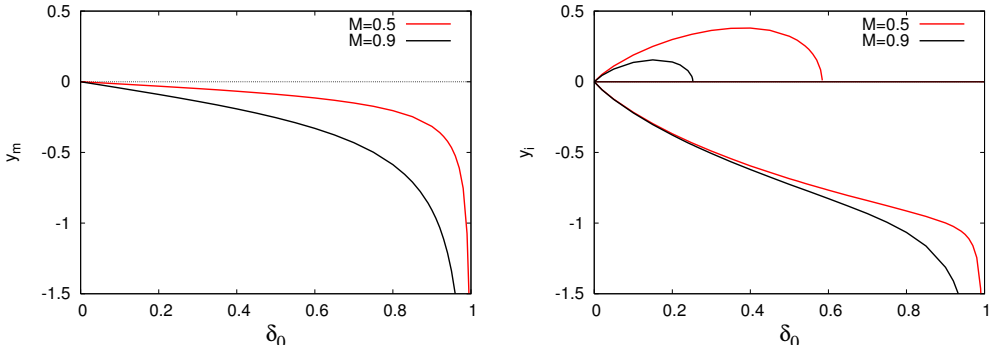

Figure 5.2: *Location of (a) local minimum y_m, and (b) inflection points y_i of the velocity profile both as function of δ_0. The figures correspond to two velocity ratios $M = 0.5$ and $M = 0.9$ with parameters $m = 0.012$, and $n = 1$.*

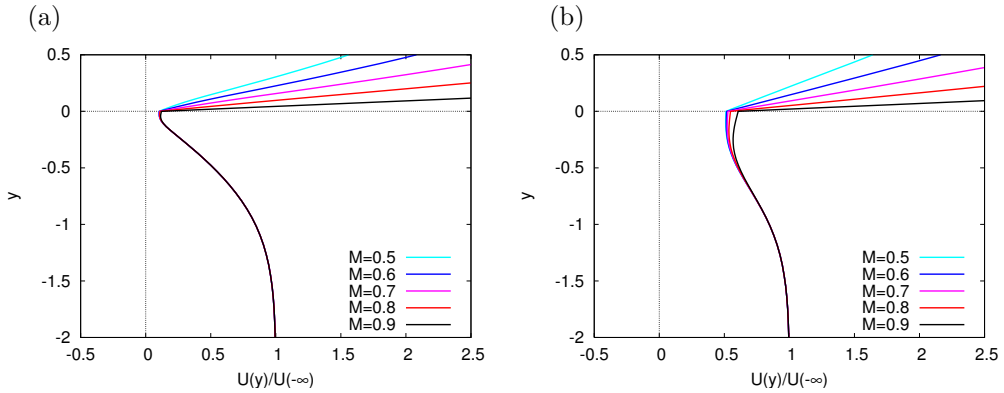

Figure 5.3: *Rescaled basic velocity distribution for $m = 0.012$, $n = 1$. The velocity is normalized such that it approaches unity at $y = -\infty$. The defect width is (a) $\delta_0 = 0.1$, and (b) $\delta_0 = 0.5$.*

The velocity distribution has another characteristic feature that turns out to be relevant for the stability properties. For small viscosity ratios m, and when the defect width δ_0 is sufficiently small, the dimensional velocity profile in the liquid scales with U_1^* except in a small region near the interface. This is shown in Figure 5.3 since the rescaled velocity profile $U(y)/U(-\infty)$ is not affected by M. The agreement improves as δ_0 becomes smaller.
In addition to the four variables M, δ_0, n, and m, the complete linearized dynamics depend also on the density ratio

$$r = \frac{\rho_2}{\rho_1}, \tag{5.23}$$

the Reynolds number

$$Re = \frac{\rho_2 \Delta U \delta_2}{\mu_2}, \tag{5.24}$$

based on $\Delta U \equiv U_2^* - U_1^*$, and the non-dimensional surface tension

$$S = \frac{s}{\rho_2 \bar{U}^2 \delta_2}. \tag{5.25}$$

Gravity is not considered here, $F = 0$. Because the parameter space is very large (7 variables), the description of the temporal and spatial analyses is restricted as follows. In this chapter, the boundary layer sizes are assumed to be equal, $n = 1$. By considering the remaining parameters,

- the effect of shear is considered by analyzing results obtained for two velocity ratios: a large one, $M = 0.9$, and a smaller one, $M = 0.5$,
- the presence of a wake in the velocity profile is usually studied by considering three values of δ_0: $\delta_0 = 0.1$ (large velocity defect), $\delta_0 = 0.5$, $\delta_0 = 1$ (Stokes flow).
- the effect of viscosity is considered by varying the Reynolds number Re.

5.2 Instability problem

The viscous linear instability problem is formulated in two dimensions for viscous incompressible fluids. Perturbations about the basic flow (5.13), (5.14) are given in the form of streamfunctions ψ_j, $j = 1, 2$, where the streamwise u_j and cross-stream v_j velocity components are defined by relations (2.56). Because the primary flow $U_j(y)$ only depends on the y-coordinate, streamfunctions assume the form of normal modes (2.57). Substitution of (2.57) into the linearized Navier-Stokes equations results in the Orr-Sommerfeld equations (2.58), (2.59) for the y-dependent functions $\phi_j(y)$, where R is the Reynolds number based on the mean velocity,

$$R = \frac{\rho_2 \bar{U} \delta_2^*}{\mu_2}. \tag{5.26}$$

It is related to Re by the relation $R = Re/(2M)$. In addition, the conditions (2.60), (2.61) impose a decay of perturbations at $\pm\infty$. Finally, the interface conditions (2.62)-(2.66) coupling the two phases are required, where $U_1''(0) = U_2''(0) = 0$, and $F = 0$ in the present case.
As was shown in Section 3.4, for the numerical treatment it is advantageous to reduce the order of the Orr-Sommerfeld differential equations and boundary conditions. For the temporal problem the functions ξ_j are introduced by equations

$$\xi_j(y) = \left(\frac{\partial^2}{\partial y^2} - \alpha^2 \right) \phi_j(y), \qquad j = 1, 2. \tag{5.27}$$

In order to obtain an eigenvalue problem linear in α in the spatial case, additionally

$$\tilde{\phi}_j = \alpha \phi_j, \qquad \tilde{\xi}_j = \alpha \xi_j, \qquad j = 1, 2, \tag{5.28}$$

are defined. For the numerical treatment boundaries are introduced at finite distances $y = -L_1$ and $y = L_2$ away from the interface, and the modified formulation of the Orr-Sommerfeld problem is solved numerically using Chebyshev collocation. The resulting generalized linear eigenvalue problem is coded in FORTRAN and solved using the LAPACK routine $ZGGEV$. Details about the implementation are summarized in Appendices A.4.1 and A.4.2 for the temporal and spatial formulation, respectively.
For temporally growing perturbations, the eigenvalue problem consists in finding complex frequencies $\omega = \omega_r + i\omega_i$ in terms of real wave numbers α. For the spatial problem, the eigenvalues are complex wave numbers $\alpha = \alpha_r + i\alpha_i$ for given real frequencies ω. For the temporal calculations, typically $N = 150$ was used for each layer. With an identical number of Chebyshev polynomials, the matrix for the eigenvalue solver is of a larger size for the spatial than for the temporal problem. For the spatial case, a resolution of $N = 100$ was usually enough to guarantee convergence of the results. However, in some instances more points ($N = 150$) were necessary. In addition, quadruple precision was used in some calculations. Finally, in the computations discussed below, $L_1 = L_2 = 15$ was usually chosen. Different choices of L_1 and L_2 are explicitly noted. It is remarked, that this numerical confinement may lead to some problems to determine the convective/absolute transition in the unconfined case, see Section 5.5.

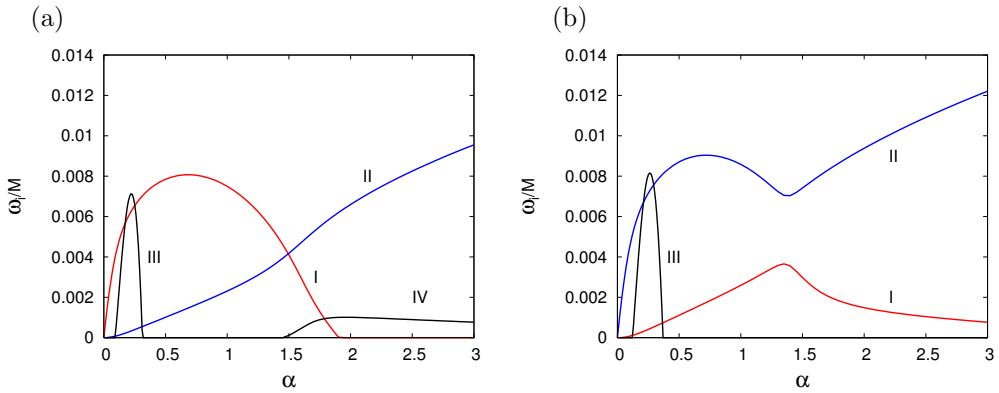

Figure 5.4: *Normalized growth rates ω_i/M of the viscous temporal instability modes for the Stokes solution ($n = \delta_0 = 1$) with $r = 0.0012$, $m = 0.012$, and no surface tension, $S = 0$: (a) $Re = 59280$, and (b) $Re = 29640$.*

5.3 Temporal Instability Results

As already mentioned, $n = 1$ throughout this chapter. In Sections 5.3.1 - 5.3.3, the effects of M, δ_0, and Re on the temporal results are studied for the specific density ratio $r = 0.0012$ and viscosity ratio $m = 0.012$. These fluid parameters were used in a previous study by Boeck and Zaleski [6] for air-water. In addition, interfacial tension is neglected, i.e. $S = 0$. Contrary, the effects of the parameters r, m, and S are considered in Section 5.3.4.

5.3.1 The Stokes Solution

First the results of the *Stokes solution* (5.19), (5.20) for $n = \delta_0 = 1$ are discussed. This basic velocity distribution equals those used by Boeck and Zaleski [6] up to an offset velocity, i.e. the interface velocity, which bears no consequences for the temporal growth rates ω_i, and up to a multiplicative factor $1/M$. This factor can be scaled out in the stability equation, indicating that ω_i is proportional to M for this particular flow. Figure 5.4 shows normalized temporal growth rates ω_i/M for $Re = 59280$ and $Re = 29640$. These values compare very well with those obtained by Boeck and Zaleski [6] for their corresponding Reynolds numbers $Re^{BZ} = 60000$, and $Re^{BZ} = 30000$, thus providing a good check for the present computations.

The different unstable branches seen in Figure 5.4 are briefly recalled here as a foundation for future analysis. The most unstable branch II predominates at high wave numbers. This mode is essentially caused by the viscosity-contrast mechanism [26, 27], and is called H mode in [6]. The unstable branches I and III appear at relatively lower wave numbers than mode II, and can be more unstable than this mode in this wave number range. Mode I originates from the inviscid Kelvin-Helmholtz mechanism [6]. This identification was made by comparing high Reynolds number results with purely inviscid results for the very same basic flow. Note, however, that by lowering Re, a switch between the branches of modes I and II is observed around $\alpha = 1.5$. Because of this branch switch, mode I is also driven by the H mechanism at low or moderate Reynolds numbers. This will be shown in detail in the next section. Contrary, mode III remains distinct from the other modes, and has been attributed to the Tollmien-Schlichting mechanism by its characteristic Reynolds number dependence [6].

Finally mode IV is always much weaker. It becomes unstable near $\alpha \approx 1.6$ when the Reynolds number exceeds $Re \approx 40000$, and thereafter switches branches with mode I around $Re \approx 50000$. It is interpreted in [6] as the result of the interaction between the inviscid mode and damped modes due to finite viscosity. Since mode IV only appears for rather large Reynolds numbers and is never dominant, it will not be discussed any further.

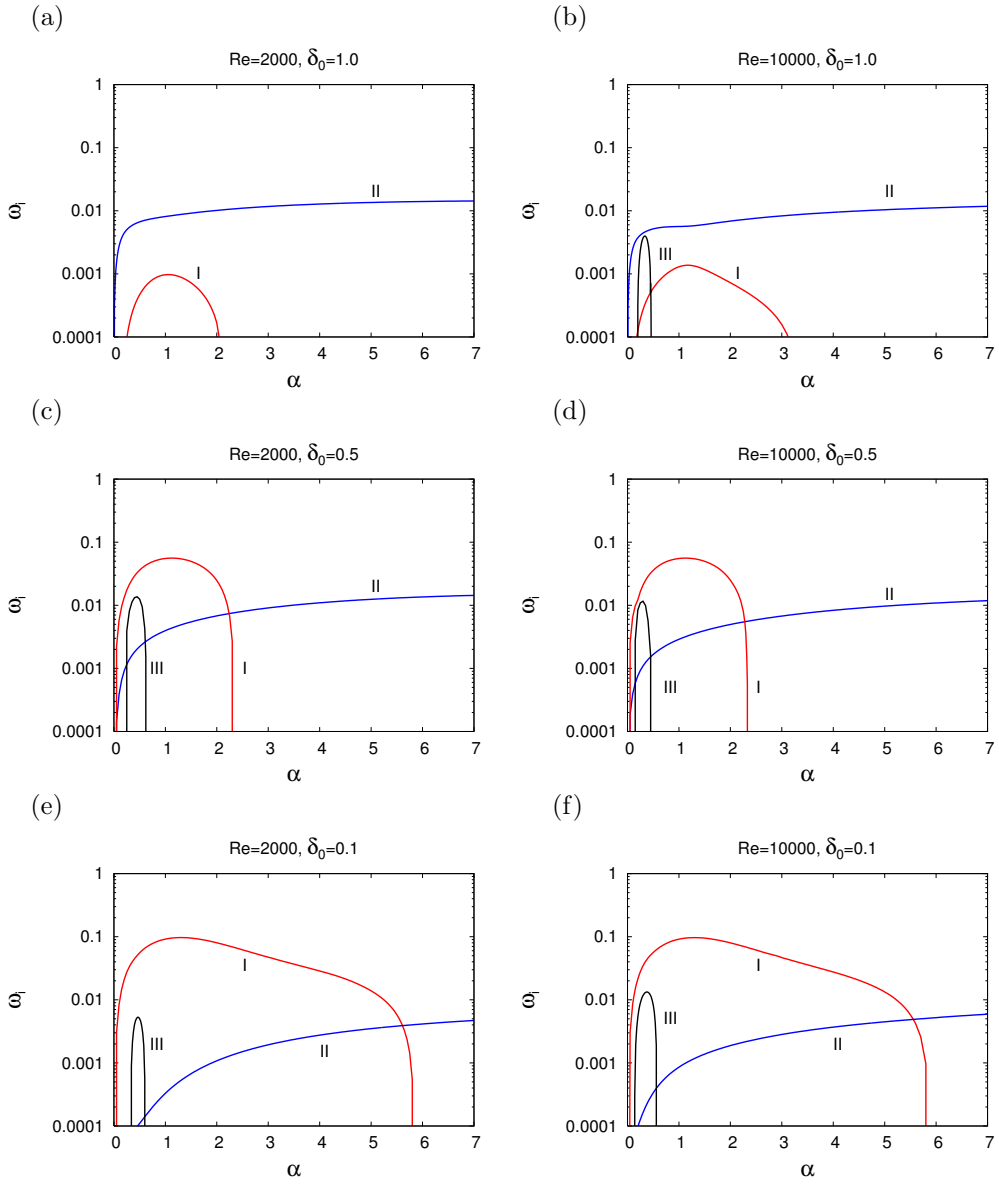

Figure 5.5: *Temporal growth rates ω_i as a function of the wave number α for $M = 0.5$. Each plot corresponds to a different width δ_0 and Reynolds number Re. The remaining parameters are $r = 0.0012$, $m = 0.012$, $n = 1$, and $S = 0$. Note that mode III is not amplified for case (a).*

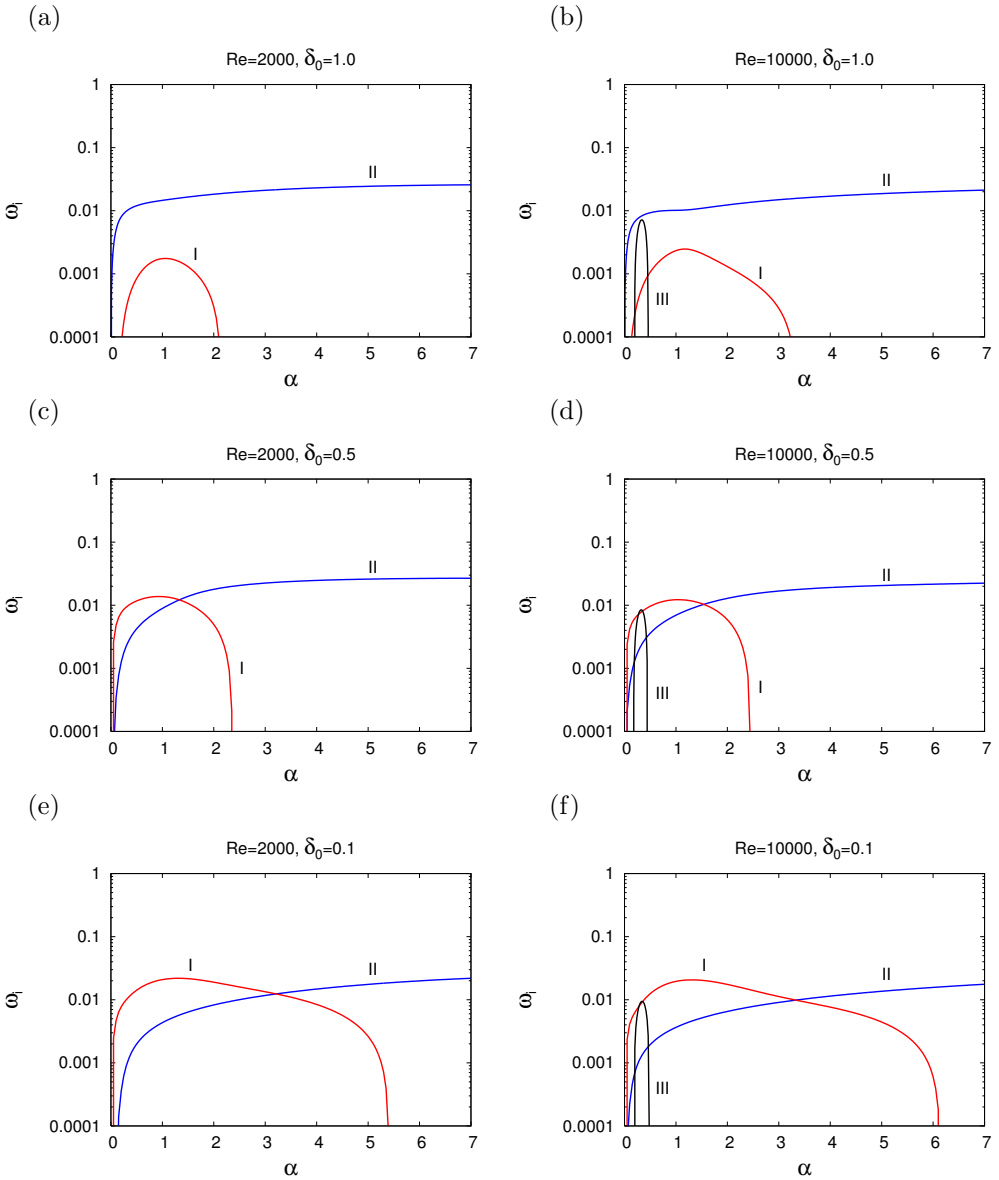

Figure 5.6: *Idem that Figure 5.5 but for* $M = 0.9$. *Note that mode III is not amplified for* $Re = 2000$.

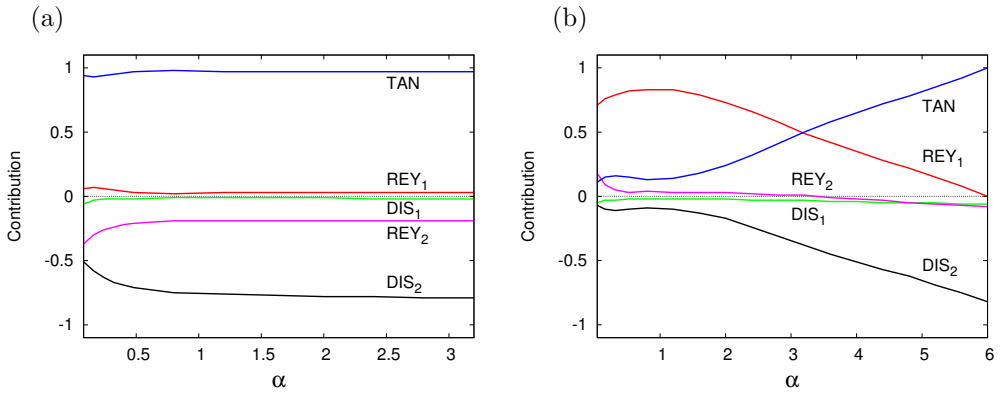

Figure 5.7: *Energy contributions for mode I as a function of the streamwise wave number* α. *The parameters are* $r = 0.0012$, $m = 0.012$, $n = 1$, $Re = 10000$, $S = 0$, *and* $M = 0.9$. *The defect width is (a)* $\delta_0 = 1$, *and (b)* $\delta_0 = 0.1$.

5.3.2 Dependency on the Velocity Distribution

When the defect width δ_0 becomes less than one, the basic flow differs from the Stokes solution since it displays a velocity defect near $y = 0$, see Figure 5.1. Contrary to the Stokes solution, when $\delta_0 < 1$ the growth rates of all modes are no more proportional to the velocity ratio M; see Figures 5.5 and 5.6. In addition, the various modes behave differently with respect to this parameter: an increase of M leads to a decrease of mode I, a weaker decrease of mode III, and an increase of mode II. Mode IV is not present here since the Reynolds number is much lower than in Figure 5.4. For a systematic discussion, first the unstable modes I and III at low wave numbers are considered. The properties of mode II at relatively larger α are discussed later on.

Mode I

The most significant change for mode I is caused by the presence of the velocity defect; see Figures 5.5 and 5.6. The maximum growth rate $\omega_i^{\max}$ always increases with decreasing δ_0. When the defect width is reduced to $\delta_0 = 0.5$, the range of unstable wave numbers is not much affected but, when δ_0 is sufficiently small, the unstable bandwidth is considerably wider: it extends to $\alpha \approx 6$ for $\delta_0 = 0.1$. Contrary to the Stokes case, for $\delta_0 = 0.5$ or $\delta_0 = 0.1$ an increasing velocity ratio M reduces the growth rate. In addition, the unstable wave number bandwidth varies only slightly with M. Similarly to the Stokes profile, mode I is affected by the Reynolds number for δ_0 close to 1. This is due to the H-mechanism, which contributes to mode I via branch switching with mode II. This switching of branches between modes I and II occurs at some value of the defect width between $\delta_0 = 1$ and $\delta_0 = 0.5$, and should be apparent in Figures 5.5 and 5.6. For smaller values ($\delta_0 \leq 0.5$), the growth rate does not change much by increasing the Reynolds number from $Re = 2000$ to $Re = 10000$.
As seen from this Reynolds number dependence, for $\delta_0 = 0.5$ or $\delta_0 = 0.1$ mode I is probably generated by an instability mechanism of inviscid origin. To substantiate this interpretation, the temporal energy budget (2.116) of mode I is discussed. To do so, the integrals introduced in Section 2.5.1 are considered. In Figure 5.7, this energy budget is illustrated for $M = 0.9$ and $Re = 10000$ as function of the wave number α. Here the integrals are displayed for each wave number α once normalized by the sum of all destabilizing (i.e. positive) terms. For $\delta_0 = 1$, the destabilizing contributions for mode I originate almost entirely from the interfacial shear (TAN term), i.e. the H mechanism is dominant. For $\delta_0 = 0.1$ and $M = 0.9$, TAN is the leading contribution for large wave numbers only, whereas up to $\alpha \approx 3$ the Reynolds stress REY_1 in the liquid dominates. Mode I is therefore mixed, and the influence of the different destabilizing mechanisms changes with α. When $\delta_0 = 0.1$ and $M = 0.5$, the Reynolds stress REY_1 contributes

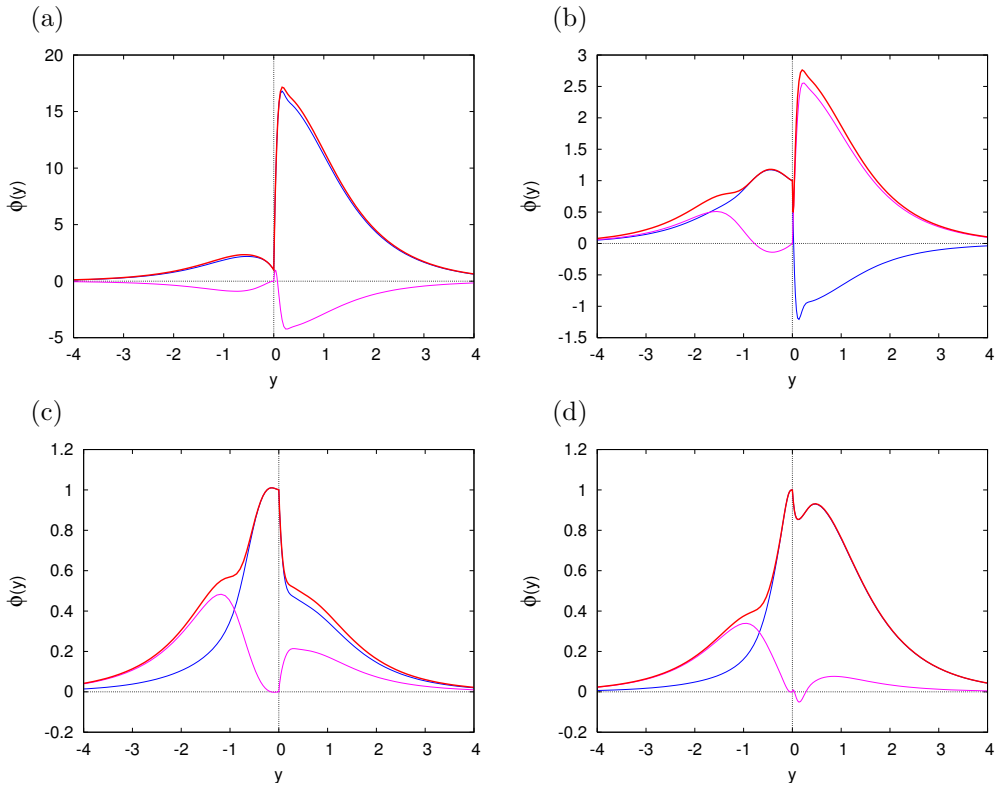

Figure 5.8: *Temporal eigenfunctions of mode I at* $\alpha = 1$ *normalized by* $\phi(0) = 1$ *for (a)* $\delta_0 = 1$, *(b)* $\delta_0 = 0.9$, *(c)* $\delta_0 = 0.5$, *and (d)* $\delta_0 = 0.1$. *Case with* $r = 0.0012$, $m = 0.012$, $n = 1$, $Re = 2000$, $S = 0$, *and* $M = 0.5$. *The real and imaginary part of the eigenfunction are shown in blue and magenta, respectively, and* $|\phi|$ *is plotted in red.*

even more: it corresponds to 95% to the sum of the destabilizing contributions over the entire unstable wave number range (not shown). Studying the energy budget thus indicates, that the inviscid destablizing effect mainly originates within the liquid phase.

One may also look at the spatial structure of mode I for different values of the defect width δ_0; see Figure 5.8. For the Stokes case, the eigenfunction shows a significantly different amplitude in the liquid and in the gas. This is due to the H mechanism which is associated with vorticity perturbations differing by a factor of order m on either side of the interface. In that case, the curvature of the eigenfunctions reaches a very high value on the gas side (i.e. for $y > 0$) close to the interface, and a comparatively low value on the liquid side (i.e. for $y < 0$). As the inviscid mechanism becomes dominant upon decreasing δ_0, the amplitudes approach one another on either side of the interface, which shows a coupling between the two phases. From the energy budget, one may infer that it is only a one-way coupling: the low inertia of the gas suggests an essentially passive role of the gas phase which simply conforms to the motion transmitted by the liquid phase.

All this can be related to the existence of a region of opposite velocity gradient including an inflection point in the liquid for $\delta_0 < 1$; see Figures 5.1 and 5.2. Moreover, steep gradients observed for the mode structure are present in the zone of strong reversed shear of the basic velocity profile containing the inflection point; see Figure 5.8. The independence of M of the rescaled velocity distribution $U_1(y)/U_1(-\infty)$ in the liquid, demonstrated in Figure 5.3, implies that $\omega(\alpha)/U_1(-\infty)$ is independent of M. This can be seen by taking the inviscid limit of the Orr-Sommerfeld equation (2.58) for $y \leq 0$, assuming that only the liquid phase matters for the instability. Since $U_1(-\infty) = 1 - M$, the growth rate should be proportional to this factor, and

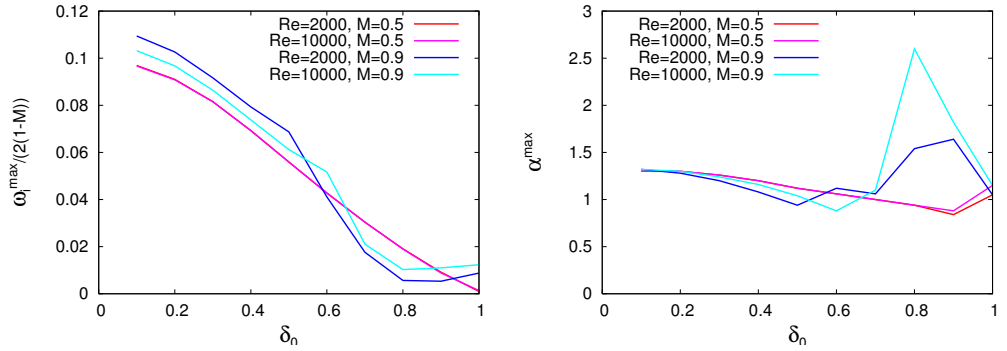

Figure 5.9: *Rescaled maximum temporal growth rate (left) and corresponding wave number (right) for mode I as a function of* δ_0 *with* $M = 0.5$, $M = 0.9$, *and* $Re = 2000$, $Re = 10000$. *The remaining parameters are* $r = 0.0012$, $m = 0.012$, $n = 1$, *and* $S = 0$.

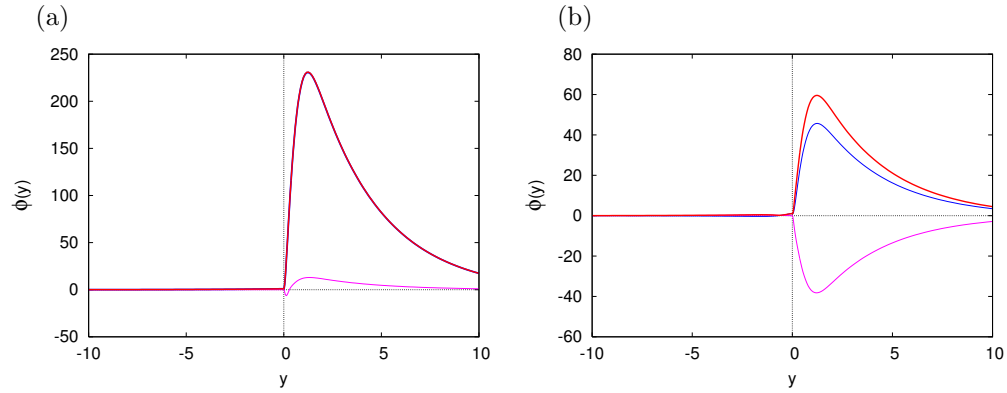

Figure 5.10: *Temporal eigenfunctions of mode III at* $\alpha = 0.3$ *normalized by* $\phi(0) = 1$ *for (a)* $\delta_0 = 1$, *and (b)* $\delta_0 = 0.1$. *Case with* $r = 0.0012$, $m = 0.012$, $n = 1$, $Re = 10000$, $S = 0$, *and* $M = 0.5$. *The real and imaginary part of the eigenfunction are shown in blue and magenta, respectively, and* $|\phi|$ *is plotted in red.*

the range of unstable wave numbers should not depend on M. This can be seen qualitatively in Figures 5.5 and 5.6. The predicted scaling with $1 - M$ is verified quantitatively in Figure 5.9.

To summarize, for $\delta_0 = 0.5$ and $\delta_0 = 0.1$, mode I is an inviscid mode related to an inflection point instability in the liquid phase. For δ_0 close to 1 and low Reynolds numbers Re, there exists a branch switching with mode II. In that case, the instability is due to a mixture of inviscid and H mechanisms and its growth depends on the Reynolds number.

Mode III

Contrary to mode I, mode III is largely controlled by the velocity profile in the gas, since the eigenfunctions have an appreciable amplitude in the gas only (i.e. for $y > 0$); see Figure 5.10. The dependency on the Reynolds number Re is different for Stokes flow and the case $\delta_0 = 0.1$; see Figure 5.11. For both instances, the unstable mode III appears only when the Reynolds number is sufficiently large (e.g. the branch III is not present at $Re = 2000$ in Figure 5.6). For $\delta_0 = 1$, however, the maximum growth rate of mode III first increases with Re, and then starts to decrease above a critical Reynolds number. This behaviour may be related to a Tollmien-Schlichting instability mechanism. In the case $\delta_0 = 0.1$, this attenuation of mode III with

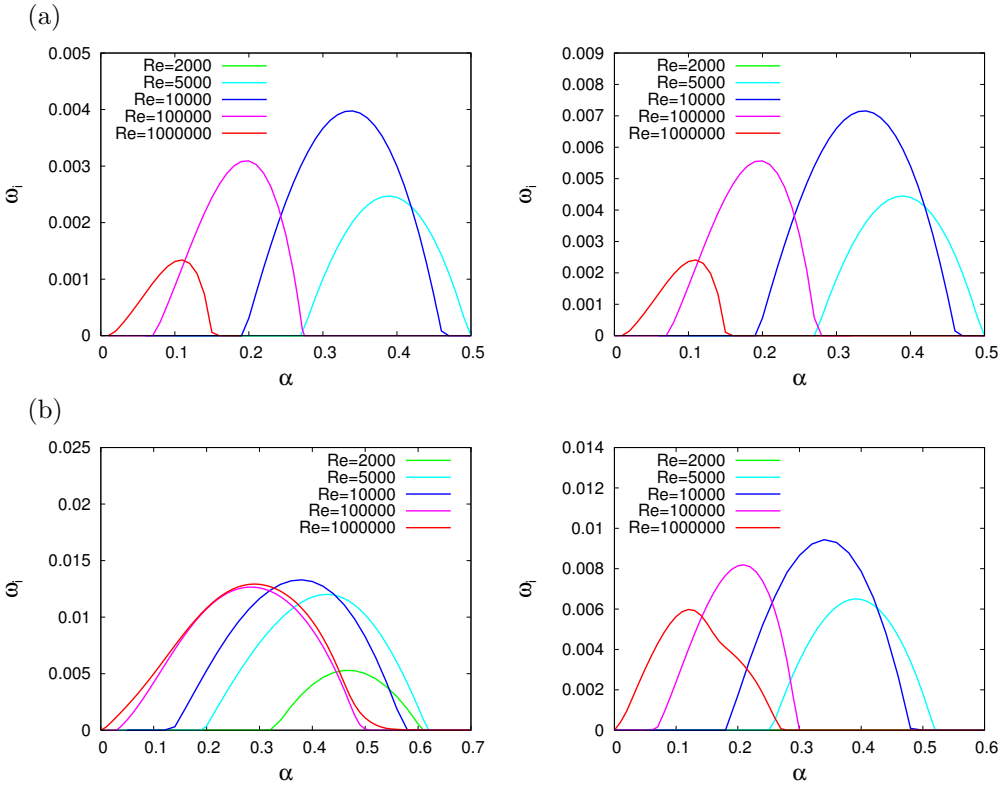

Figure 5.11: *Reynolds number dependence of mode III for* $M = 0.5$ *(left) and* $M = 0.9$ *(right): (a)* $\delta_0 = 1$*, (b)* $\delta_0 = 0.1$*. The remaining parameters are* $r = 0.0012$*,* $m = 0.012$*,* $n = 1$*,* $S = 0$*.*

increasing Re is less accentuated: it is even not present for $M = 0.5$, where mode III maintains its growth rate for large Reynolds numbers. This feature may be due to the additional inviscid destabilization caused by the inflection point in the gas for small values of δ_0.

Except for the Stokes case, an increase of M leads to a weak decrease of mode III. This is shown in Figures 5.5 and 5.6. For $M = 0.9$ the growth rate curve does not change much, when the defect width δ_0 is reduced. This can be interpreted by the fact, that the shear within the gas only slightly increases with decreasing δ_0 when $M = 0.9$. For the lower value $M = 0.5$, the growth rate of mode III at $Re = 10000$ is enhanced when reducing the defect width between $\delta_0 = 1$ and $\delta_0 = 0.5$, and then stays almost the same. This can be accounted for as follows: for $M = 0.5$ the basic velocity shear in the gas can be significantly increased when the defect width is reduced from $\delta_0 = 1$.

The energy budget confirms the above interpretation; see Figure 5.12. For $M = 0.5$ it shows, that the destabilizing contributions are the Reynolds stress terms REY_2 and REY_1, although the latter is positive only for small δ_0 and low M. TAN is small approximatively of 1%. For $\delta_0 = 0.1$ and $M = 0.5$, REY_1 reaches a maximum contribution of 26% to the sum of REY_1 and REY_2 at a wave number $\alpha \approx 0.35$. The result for $M = 0.9$ is not shown, because in this case the dominant contribution REY_2 remains close to 100% over the entire range of unstable wave numers for both $\delta_0 = 0.1$ and $\delta_0 = 1$.

To summarize, mode III is a Tollmien-Schlichting mode in the gas phase. For $\delta_0 < 1$, however, it depends on the basic velocity shear and the existence of an inflection point in the gas phase, which modifies its property with respect to the Reynolds number Re and the velocity ratio M.

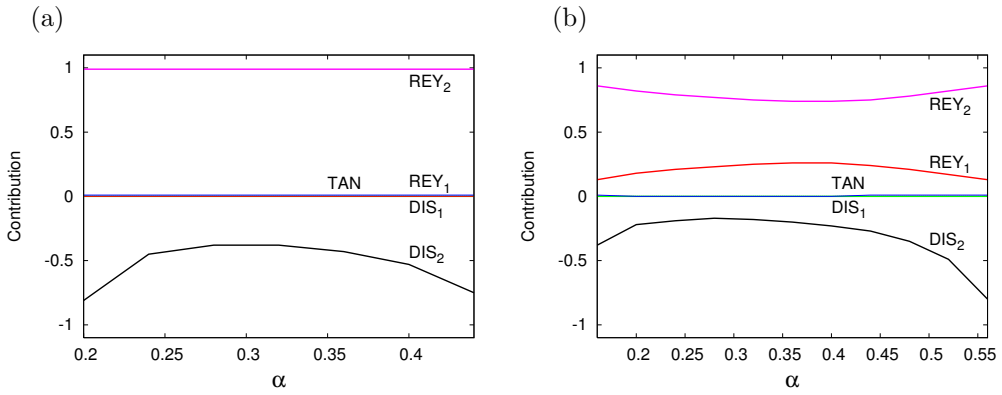

Figure 5.12: *Energy contributions for mode III as a function of the streamwise wave number* α. *The parameters are* $r = 0.0012$, $m = 0.012$, $n = 1$, $Re = 10000$, $S = 0$, *and* $M = 0.5$. *The defect width is (a)* $\delta_0 = 1$, *and (b)* $\delta_0 = 0.1$.

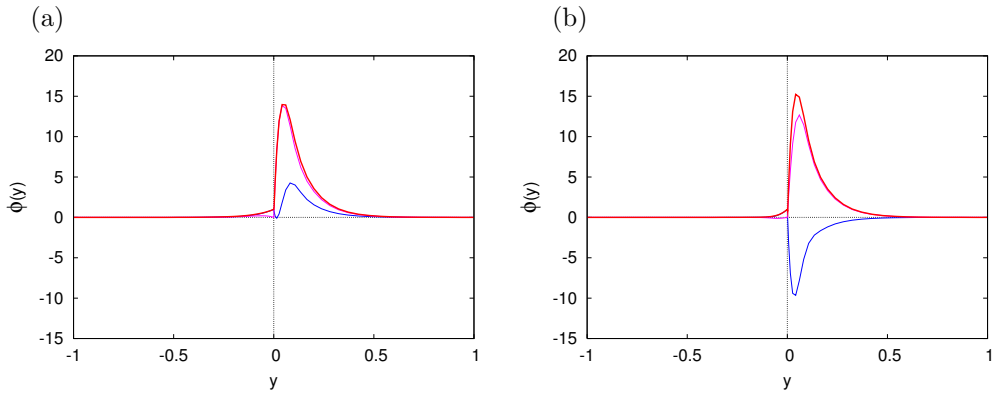

Figure 5.13: *Temporal eigenfunctions of mode II at* $\alpha = 10$ *normalized by* $\phi(0) = 1$*: (a)* $\delta_0 = 1$, *(b)* $\delta_0 = 0.1$. *Case* $r = 0.0012$, $m = 0.012$, $n = 1$, $Re = 2000$, $S = 0$, *and* $M = 0.5$. *The real and imaginary part of the eigenfunction are shown in blue and magenta, respectively, and* $|\phi|$ *is plotted in red.*

Mode II

Finally, mode II is considered, which predominates at high wave numbers. In Figure 5.13 the eigenfunction is shown for $\alpha = 10$. It is localized near the interface and its amplitude is significantly larger on the side of the less viscous gas (i.e. for $y > 0$) than in the liquid phase. In Figure 5.14 the growth rates ω_i are shown in semi-logarithmic plots as a function of the wave number α. For Stokes flow, the growth rate curves are shifted to higher wave numbers but retain their shape when the Reynolds number Re is increased. In particular, the maximum growth rate $\omega_i^{\max}$ remains unchanged and, as demonstrated in Figure 5.15, the corresponding wave number scales as

$$\alpha^{\max} \sim Re^{1/2}. \tag{5.29}$$

As pointed out by Boeck and Zaleski [6], this scaling can be associated with the viscosity contrast between the liquid and gas phases [26, 27]. More precisely, this mode is associated to the continuity of shear stress on the interface and its characteristic length scale is $\sqrt{\nu_2/\mathcal{S}}$, where $\mathcal{S}$ denotes the shear rate at the interface. Hence, the structure of the basic velocity distribution only matters from the interface up to a distance of order $\sqrt{\nu_2/\mathcal{S}}$. This implies that the H mechanism "zooms in" on the interface when the Reynolds number is increased, where it

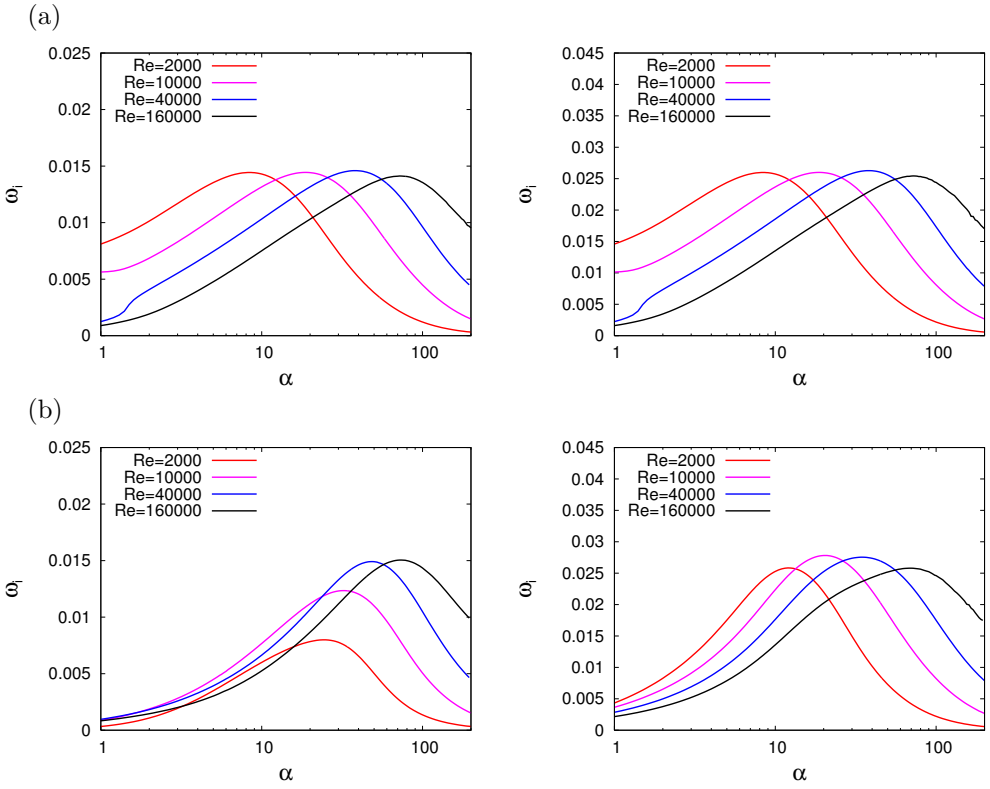

Figure 5.14: *Temporal growth rates of mode II as a function of the wave number* α *for* $M = 0.5$ *(left) and* $M = 0.9$ *(right): (a)* $\delta_0 = 1$*, (b)* $\delta_0 = 0.1$*. The remaining parameters are* $r = 0.0012$*,* $m = 0.012$*,* $n = 1$*, and* $S = 0$*.*

ultimately perceives a piecewise linear profile. The generic configuration for this instability is therefore unbounded, two-fluid Couette flow, which was considered by Hooper and Boyd [27] and Hinch [26]. The similarity of the curves arises because the "active" part of the velocity profile is the linear part close to the interface. The scaling for the wave number $\alpha^{\max}$ corresponding to the maximum growth rate on Re follows from the present choice of the external length scale δ_2 as unit of length. The time scale of the instability is set by the shear rate itself and is independent of the Reynolds number.

When introducing a width $\delta_0 < 1$, one can still identify a shift towards higher wave numbers for the growth rate curves of mode II. Nevertheless, the nearly perfect match between the shapes of growth rate curves at different Reynolds numbers is not present anymore, see Figure 5.14. However, for $M = 0.9$, one recovers this similarity at large Reynolds numbers. The same is true for $M = 0.5$ but for even larger Re. This is confirmed when looking at the maximum growth rate $\omega_i^{\max}$ as function of the Reynolds number Re in Figure 5.15: for different defect widths δ_0 the scaling (5.29) is found for both $M = 0.5$ and $M = 0.9$ when Re is sufficiently large.

For the general cases $\delta_0 < 1$, the velocity profile retains a more complicated structure as long as the viscous shear length $\sqrt{\nu_2/\mathcal{S}}$ is not small compared with the defect width δ_0. This explains, why the growth rate curves initially change their shape with Re. Note also, that, for small δ_0, the most amplified wave number $\alpha^{\max}$ of mode II increases in comparison with the value for the Stokes solution, and the maximum growth rate decreases. Again this can be accounted for as follows: the H instability mechanism becomes effective when the instability mode is located in the region where the two-fluid Couette flow is a good approximation. This imposes, that the wavelength must be smaller than $\max(\delta_0, \sqrt{\nu_2/\mathcal{S}})$ to be fully effective. When this constraint is satisfied, the growth rate for a given wave number α is identical for different defect widths δ_0.

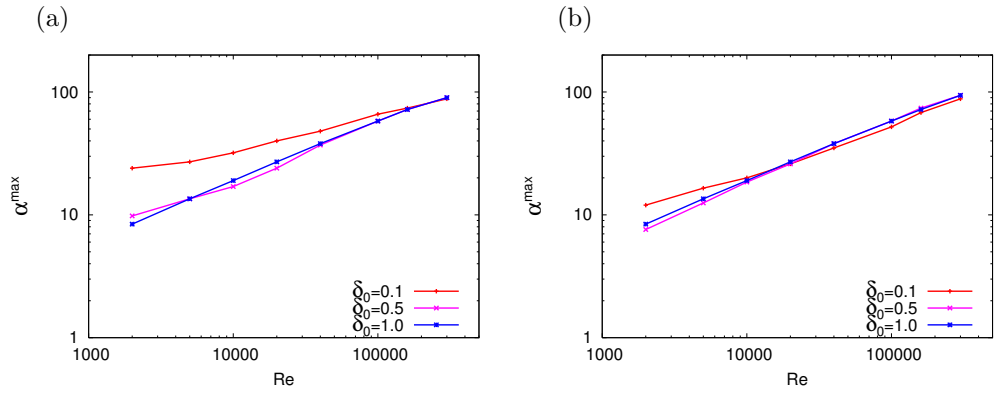

Figure 5.15: *Wave number $\alpha^{\max}$ of maximum temporal growth rate of mode II as a function of Re for various defect widths δ_0. The velocity ratio is (a) $M = 0.5$, and (b) $M = 0.9$. The remaining parameters are $r = 0.0012$, $m = 0.012$, $n = 1$, and $S = 0$.*

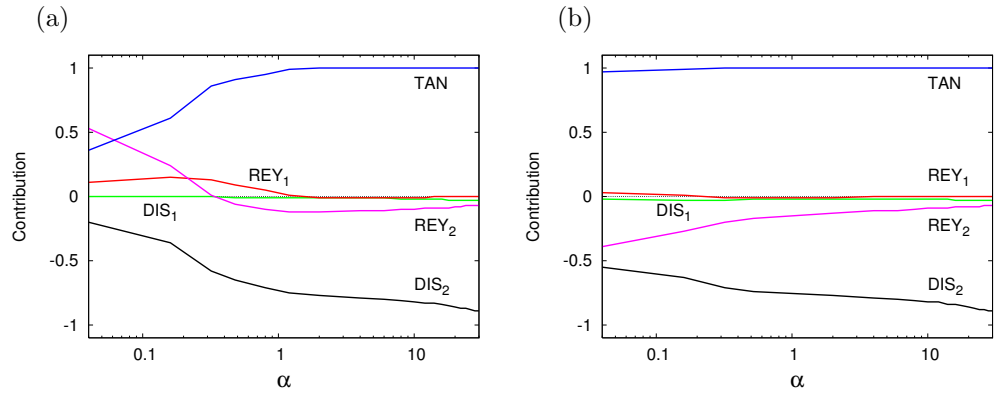

Figure 5.16: *Energy contributions for mode II as a function of the streamwise wave number α. The parameters are $r = 0.0012$, $m = 0.012$, $n = 1$, $Re = 10000$, $S = 0$, $M = 0.9$. The defect width is (a) $\delta_0 = 1$, (b) $\delta_0 = 0.1$.*

Finally, the energy budget for mode II is shown in Figure 5.16 for $M = 0.9$. In the Stokes case, the terms REY_1 and REY_2 only contribute at low wave numbers $\alpha < 1$. This mirrors the branch switching with mode I, which mixes the inviscid and viscosity-contrast mechanisms. For small defect widths δ_0, as expected, this mixing is absent, and the term TAN provides the entire destabilizing contribution. The case $M = 0.5$, $\delta_0 = 0.1$ is not shown, as it differs only slightly from those for $M = 0.9$.

To summarize, mode II is, as for the Stokes case, due to the viscosity-constrast instability mechanism near the interface. At small defect widths δ_0, however, the mechanism can be attenuated at lower wave numbers since the mode does not "see" a two-fluid Couette flow as for the Stokes case.

5.3.3 The Dominant Mode

The mode with the largest eigenvalue does not necessarily remain the same as δ_0 is varied. To highlight this feature, additional computations with more than the three values of δ_0 considered so far were carried out. In Figure 5.17, the largest eigenvalues for modes I and II are shown for different Reynolds numbers as a function of δ_0. Mode III is not shown as it is never dominant.

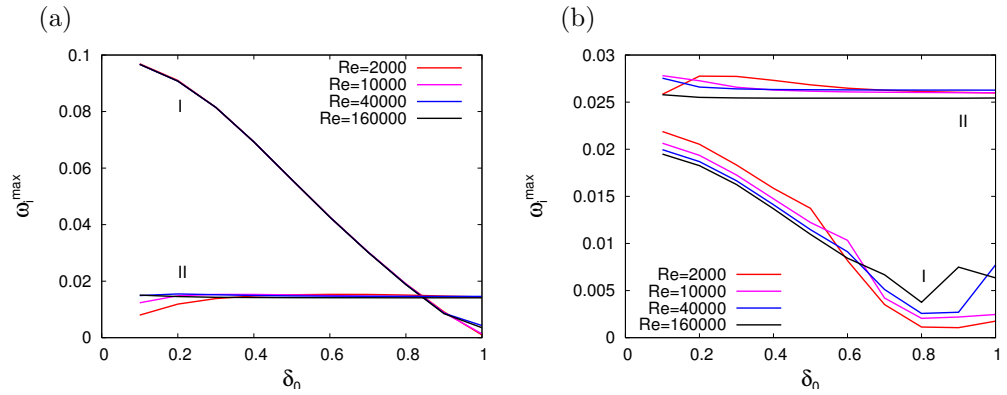

Figure 5.17: *Maximum temporal growth rate* $\omega_i^{\max}$ *for modes I and II as function of the defect width* δ_0*: (a)* $M = 0.5$*, and (b)* $M = 0.9$*. The remaining parameters are* $r = 0.0012$*,* $m = 0.012$*,* $n = 1$*, and* $S = 0$*.*

For $M = 0.9$, mode II remains dominant for all defect widths down to the last computed value $\delta_0 = 0.1$. Contrary, for $M = 0.5$, as soon as δ_0 is decreased and one gets away from the Stokes case, mode I possesses the largest growth rate.
To summarize, the velocity defect always favours mode I, but M needs to be not too large for mode I to predominate. As a side remark, it is noted that the complicated structure of the maximum growth rate of mode I near $\delta_0 = 1$ and $M = 0.9$ at $Re = 40000$ and $Re = 160000$ is caused by an additional exchange in the low-wave number branches of modes I and II.
The leading eigenvalue and the associated mode will be the focus in the next section on the influence of the fluid properties.

5.3.4 Influence of Fluid Properties

Inviscid and viscosity-contrast mechanisms, which both contributes to instability, are sensitive to fluid properties. Therefore, in this section different values of the ratios of densities and dynamic viscosities than $r = 0.0012$ and $m = 0.012$ are examined. In addition, $S > 0$ is considered as well. A detailed description of the unstable modes is not given, unless there is a significant alteration of the general behaviour described in the previous section. Instead, the focus is on the largest growth rate $\omega_i^{\max}$, the corresponding wave number $\alpha^{\max}$, and their dependency on the density ratio r, the viscosity ratio m, and surface tension S.

Density Ratio Variation

To simplify the discussion, the influence of the density ratio r is considered for the two fixed viscosity ratios $m = 0.01$ (corresponding approximately to air and water), and $m = 0.1$ (corresponding approximately to hydrogen and liquid oxygen), whereby the modification of the basic velocity distribution is only related to the parameters M and δ_0. The choice of the parameters is again guided by Boeck and Zaleski [6], who studied the effect of r for the Stokes case ($n = \delta_0 = 1$).

First, results for $m = 0.01$, and velocity ratio $M = 0.9$ are considered. In Figure 5.18 it is shown that, gradually increasing the density ratio r from zero, the growth rate $\omega_i^{\max}$ stays constant until a critical density ratio $r_1^{(t)}$. Thereafter $\omega_i^{\max}$ starts increasing. For $r < r_1^{(t)}$, the wave number $\alpha^{\max}$ is constant. At $r_1^{(t)}$ it jumps, and thereafter decreases before jumping again at a density ratio $r_2^{(t)}$ of order 0.1. These transitions correspond to changes of the nature of the dominant mode with the density ratio. Note that $r_1^{(t)}$ and $r_2^{(t)}$ are functions of δ_0 and M. The

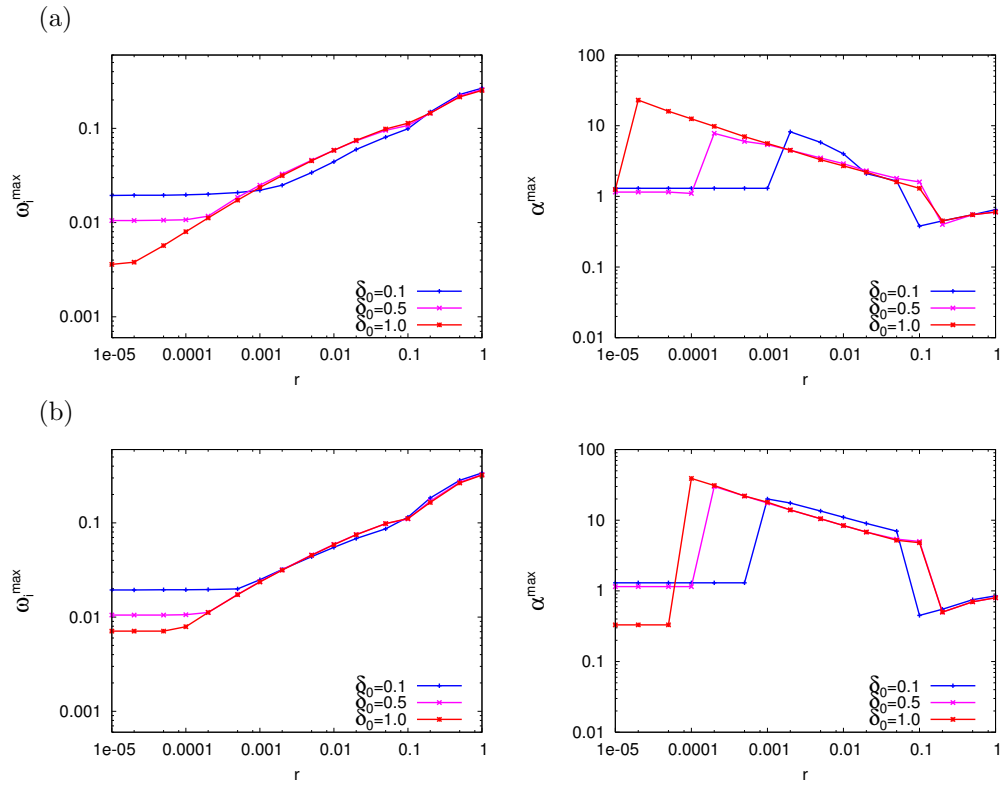

Figure 5.18: *Maximum temporal growth rates* $\omega_i^{\max}$ *(left), and corresponding wave numbers* $\alpha^{\max}$ *(right) as function of the density ratio* r *for two Reynolds numbers: (a)* $Re = 1000$*, and (b)* $Re = 10000$*. The remaining parameters are* $m = 0.01$*,* $n = 1$*,* $S = 0$*, and* $M = 0.9$*.*

type of dominant mode is identified through both the typical dependences of $\omega_i^{\max}$ and $\alpha^{\max}$ on the Reynolds number, and the energy budget for each mode.

As mentioned in the previous section, $\alpha^{\max}$ for mode II increases with Re, and its growth rate $\omega_i^{\max}$ remains unchanged with Re. This behaviour is observed in Figure 5.18 for the broad range of density ratios $r_1^{(t)} < r < r_2^{(t)}$ by comparing the results for $Re = 1000$ and $Re = 10000$. For $r_1^{(t)} < r < r_2^{(t)}$, this indicates that, mode II is dominant, and that its wave number $\alpha^{\max}$ decreases with increasing density ratio r.

For $r > r_2^{(t)}$, $\alpha^{\max}$ does not follow this behaviour but increases with r and shows no difference between $Re = 1000$ and $Re = 10000$. This indicates that the dominant instability is inviscid [6]. Moreover the energy budget is dominated by the REY_2 term. It is caused by an instability in the gas boundary layer. This inviscid mode is thus of another type than those already presented. Its eigenfunction is shown in Figure 5.19 for $r = 0.5$ and $\delta_0 = 1$ at $\alpha = 0.55$.

For $r < r_1^{(t)}$, both $\alpha^{\max}$ and $\omega_i^{\max}$ are independent of r. For $Re = 10000$ and $\delta_0 = 1$, mode III in the gas has maximum growth rate. In the other cases presented, mode I becomes dominant leading to a larger value for $\alpha^{\max}$ compared to those for mode III.

When decreasing δ_0, the transition point $r_2^{(t)}$ is only slightly shifted. However, significant differences appear for $r_1^{(t)}$. Since a small defect width enhances the growth rate of mode I, as discussed in the previous section, whereas $\omega_i^{\max}$ remains almost constant for mode II, it is not surprising that $r_1^{(t)}$ increases.

The impact of the defect width $\delta_0 < 1$ is more significant at the lower velocity ratio $M = 0.5$; see Figure 5.20. In contrast to $M = 0.9$, for $\delta_0 = 0.5$ and $\delta_0 = 0.1$, mode II is never the leading mode, and mode I becomes dominant over most part of the range of density ratios. Note,

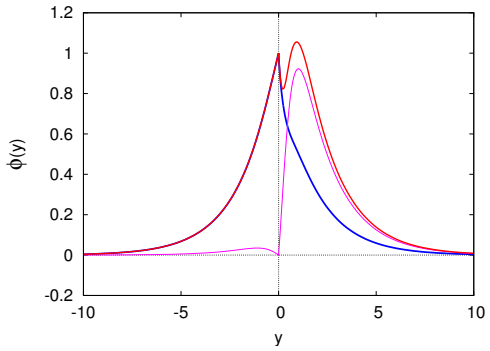

Figure 5.19: *Temporal eigenfunctions of the inviscid gas mode at* $\alpha = 0.55$ *normalized by* $\phi(0) = 1$. *Case with* $r = 0.5$, $m = 0.01$, $n = 1$, $Re = 10000$, $S = 0$, $M = 0.9$, *and* $\delta_0 = 1$. *The real and imaginary part of the eigenfunction are shown in blue and magenta, respectively, and* $|\phi|$ *is plotted in red.*

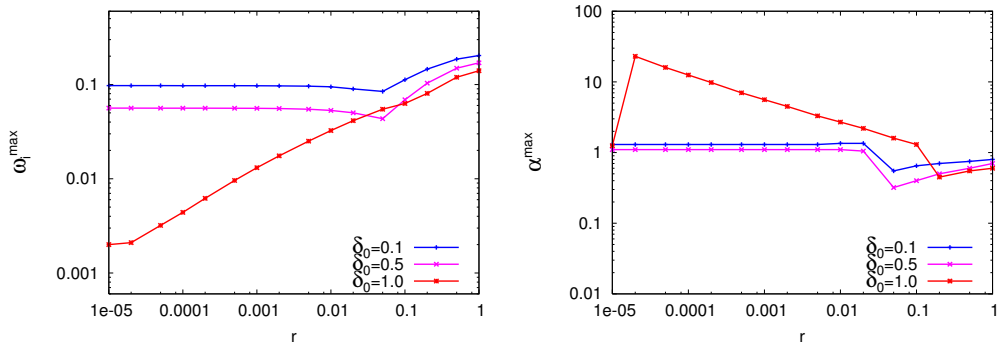

Figure 5.20: *Maximum temporal growth rates* $\omega_i^{\max}$ *(left), and corresponding wave numbers* $\alpha^{\max}$ *(right) as function of the density ratio* r *for* $Re = 1000$. *The remaining parameters are* $m = 0.01$, $n = 1$, $S = 0$, *and* $M = 0.5$.

that the growth rates $\omega_i^{\max}$ of this mode are larger for the smaller velocity ratio M; compare also with Figure 5.17. Finally, for r close to unity the inviscid mode in the gas is again dominant.

The same analysis was repeated for the larger viscosity ratio $m = 0.1$. Exemplary results are shown in Figure 5.21 for $Re = 1000$. Note that, the density ratio interval $r_1^{(t)} < r < r_2^{(t)}$ is narrower than for $m = 0.01$. Nevertheless, in general, similar conclusions about the influence of the density ratio are obtained.

Viscosity Ratio Variation

Now the effect of varying the viscosity ratio m is considered for a fixed density ratio r. Recall, that now the basic velocity profile is not only changed by the parameters δ_0 and M, but it also depends on m itself. Figure 5.22 shows the maximum growth rate $\omega_i^{\max}$ and corresponding wave number $\alpha^{\max}$ as a function of the viscosity ratio m for $r = 0.01$, $Re = 1000$, and the two velocity ratios $M = 0.9$ and $M = 0.5$. For the Stokes case ($\delta_0 = 1$), the H mechanism is not dominant for large m. It is, however, dominant for the values $m < 0.1$ considered. Mode II has its largest growth rate below $m \approx 0.1$, and its wave number $\alpha^{\max}$ increases with m. Since this characteristic signature of the viscosity-contrast mechanism for $m < 0.1$ is also present for

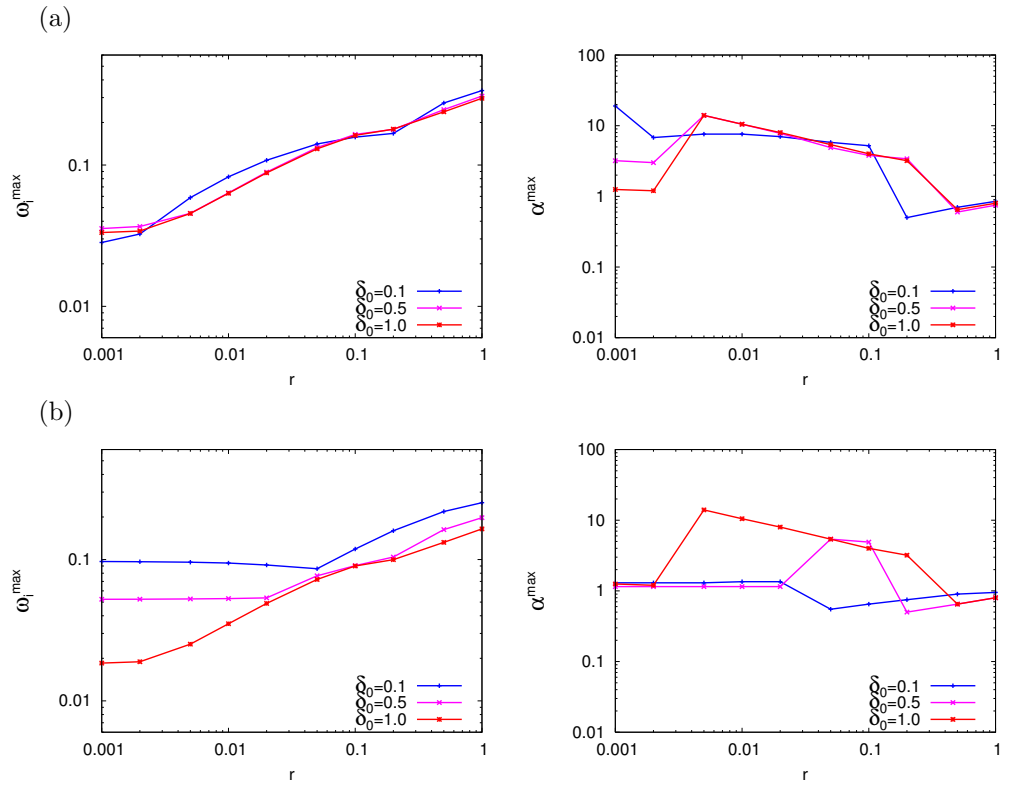

Figure 5.21: *Maximum temporal growth rates* $\omega_i^{\max}$ *(left), and corresponding wave numbers* $\alpha^{\max}$ *(right) as function of the density ratio* r *with a different viscosity contrast* $m = 0.1$*. Case with* $Re = 1000$*,* $n = 1$*, and* $S = 0$*. The velocity ratio is (a)* $M = 0.9$*, and (b)* $M = 0.5$*.*

$\delta_0 < 1$ when $M = 0.9$, mode II remains dominant in this case. Contrary, for $M = 0.5$, $\omega_i^{\max}$ is realized by mode I for $\delta_0 < 1$ and the smaller viscosity ratios.

Effect of Surface Tension

Finally, for the parameters in Section 5.3.3 the influence of surface tension is considered. Since interfacial tension is stabilizing for large wave numbers only, the growth rates of mode II strongly decrease, whereas those of modes I and III, which are unstable at low values of α, remain almost unaffected by variations of S. Figure 5.23 shows the maximum growth rate $\omega_i^{\max}$ of modes I and II as a function of the defect width δ_0 for $M = 0.5$ and $M = 0.9$ with $S = 0.01$; it is thus the analogue of Figure 5.17 for $S = 0$. The unstable Tollmien-Schlichting-type mode III for sufficient large Reynolds numbers is not shown in the figure, as it is never dominant for $S = 0.01$. As a result of the reduced maximum growth rate $\omega_i^{\max}$ for mode II compared to the case $S = 0$, mode I becomes dominant over a wider range of small values of δ_0. Note also that, as in Figure 5.17, branch switches between the modes also occur for $S = 0.01$. This is apparent for $M = 0.9$ and $Re = 40000$.

When surface tension is further increased, and the Reynolds number is neither too small nor too large for the Tollmien-Schlichting instability mechanism to be important, mode III may become most unstable (not shown). However, this effect is more pronounced for $M = 0.9$ and can only occur for defect widths close to unity when $M = 0.5$, since otherwise the maximum growth rate of mode I is much larger than those of both modes II and III.

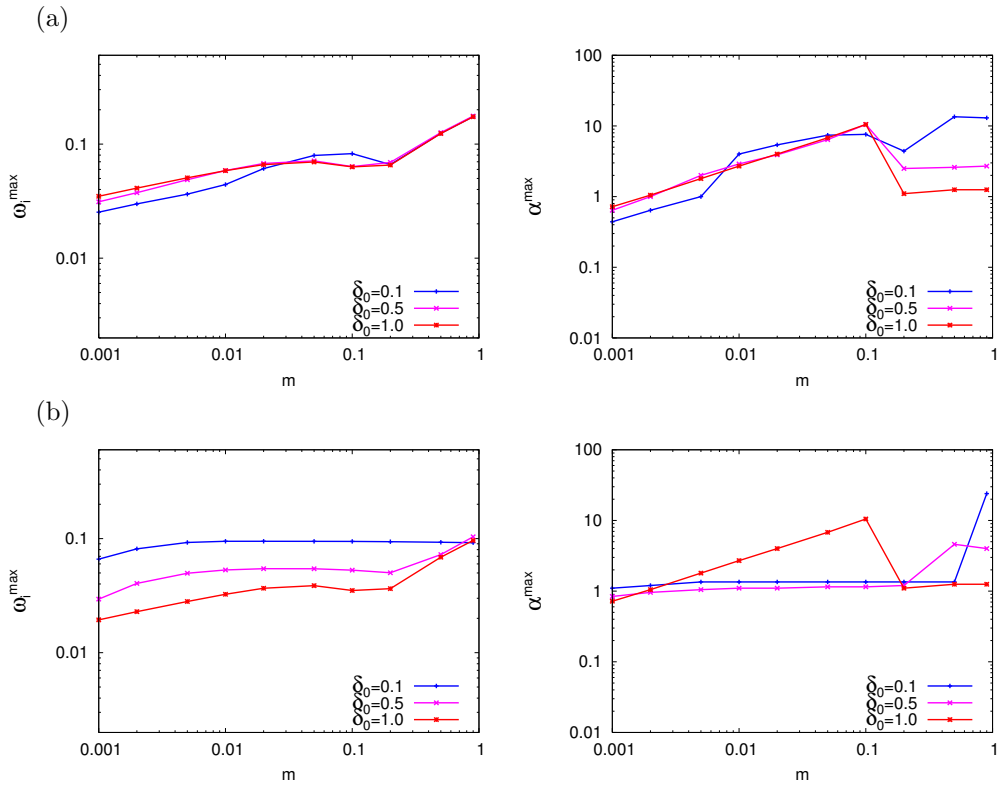

Figure 5.22: *Maximum temporal growth rates* $\omega_i^{\max}$ *(left), and corresponding wave numbers* $\alpha^{\max}$ *(right) as function of the viscosity ratio* m *with* $r = 0.01$. *Case with* $Re = 1000$, $n = 1$, *and* $S = 0$. *The velocity ratio is (a)* $M = 0.9$, *and (b)* $M = 0.5$.

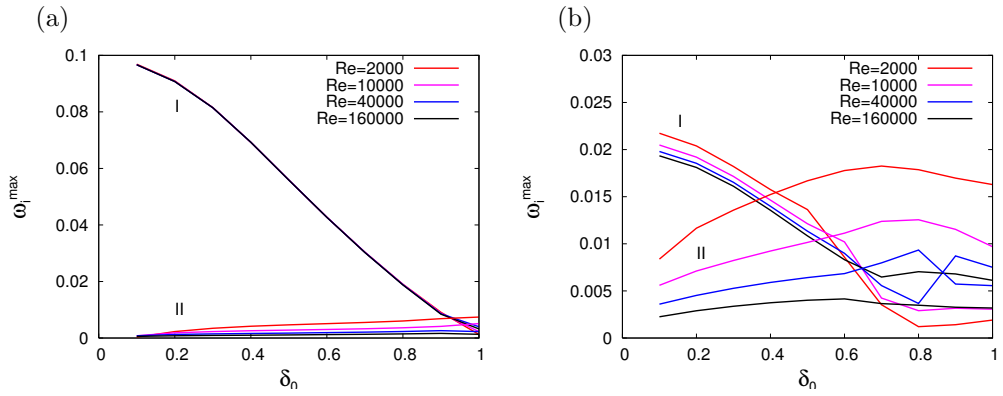

Figure 5.23: *Maximum temporal growth rate* $\omega_i^{\max}$ *for modes I and II as function of the defect width* δ_0: *(a)* $M = 0.5$, *and (b)* $M = 0.9$. *The remaining parameters are* $r = 0.0012$, $m = 0.012$, $n = 1$, *and* $S = 0.01$.

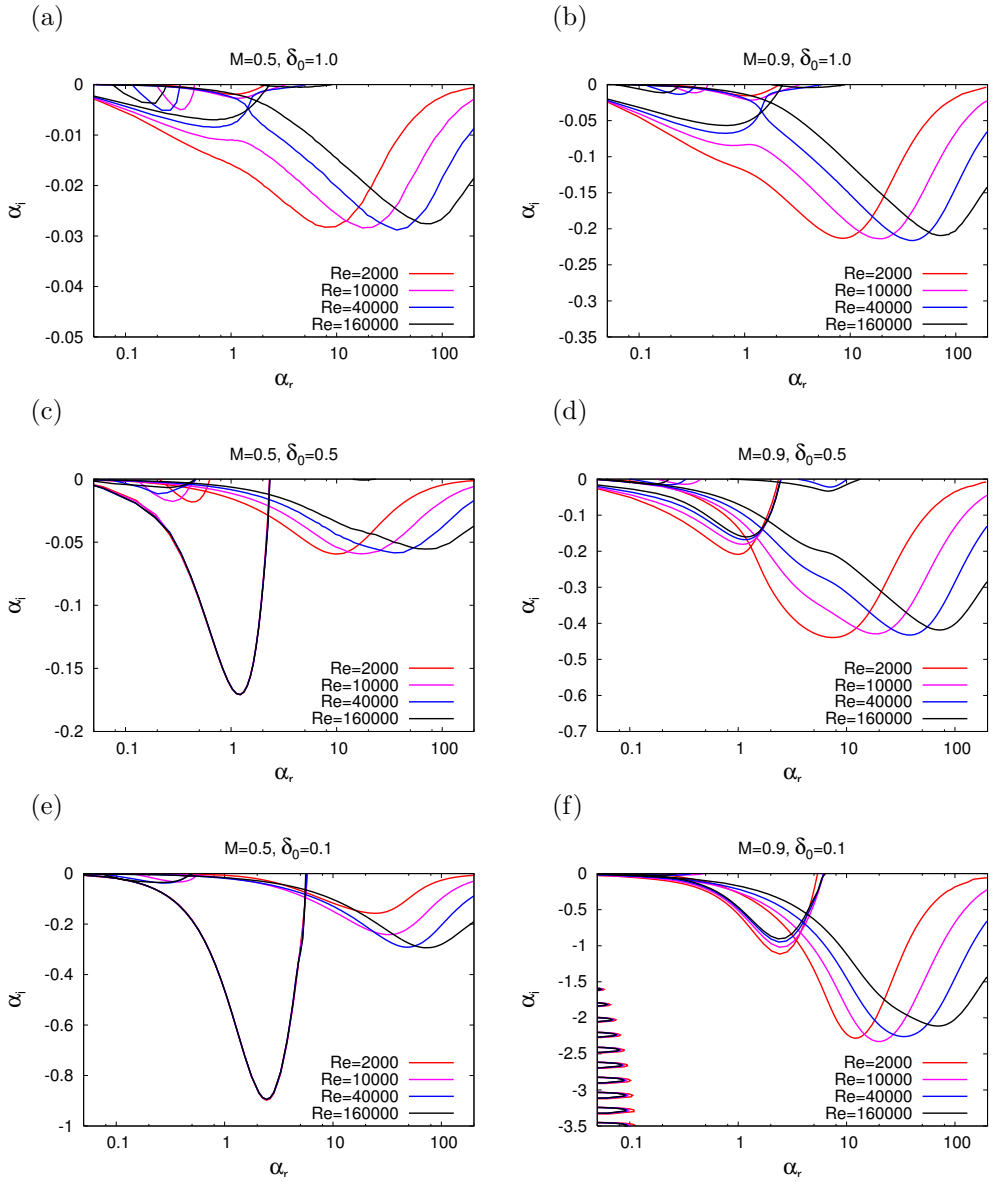

Figure 5.24: *Spatial growth rates α_i as a function of real wave numbers α_r for different Reynolds numbers, defect widths δ_0, and velocity ratios M. Case with $r = 0.0012$, $m = 0.012$, $n = 1$, and $S = 0$. Note the confinement branches in (f).*

5.4 Spatial Instability Results

In this section the growth rates of spatially developing disturbances are investigated, assuming that the flow under consideration is convectively unstable. The transition from convectively to absolutely unstable flows is studied in Section 5.5.

Spatial instability, which provides the complex wave number α for a given real frequency ω, is considered assuming that the flow is always convectively unstable. This has been checked studying the convective/absolute transition; see Section 5.5. The parametric study is identical to those performed in the temporal case: the influences of shear and the defect width are studied by considering the velocity ratios $M = 0.5$, $M = 0.9$, and the three values $\delta_0 = 0.1$, $\delta_0 = 0.5$, $\delta_0 = 1$, respectively. For each of the six parameter combinations, the dependency of the spatial growth rates on the Reynolds number Re, the density ratio r, and the viscosity ratio m is studied. Similarly to the temporal case, the boundary layer thicknesses are assumed equal, $n = 1$. In Sections 5.4.1 and 5.4.2, the discussion is performed for the parameters $r = 0.0012$, $m = 0.012$. Contrary, the effects of both r and m are considered in Section 5.4.3. Note that, surface tension is neglected throughout this section, i.e. $S = 0$. It is, however, included in Section 5.5 and Chapter 6, when discussing convective/absolute transition and comparing the numerical results with experimental data.

5.4.1 Dependency on the Velocity Distribution

The spatial growth rates $-\alpha_i(\omega)$ of unstable modes are displayed in Figure 5.24 as a function of the real part of the complex wave number $\alpha_r(\omega)$. Thanks to the logarithmic scale for α_r, this figure gives a complete overview of all unstable spatial modes for four different Reynolds numbers. First, one identifies two spatial branches which dominate the dynamics: they correspond to the unstable temporal modes I and II. Mode I is present for relatively low wave numbers, whereas mode II peaks at fairly large α_r, which increases with Re. This is typical for the viscosity-contrast mechanism. As in the temporal analysis, one also finds modes III and IV; see, e.g., Figure 5.24(d). Since their growth rates $-\alpha_i(\omega)$ are fairly low, the focus is exclusively on modes I and II.

A difference between temporal and spatial analysis is the appearance of additional spatial branches near the imaginary axis in Figure 5.24(f). They are also present in the other cases in Figure 5.24, but outside the axes range. These branches are the result of the distant walls at $y = -L_1$ and $y = L_2$ necessitated by the numerical method. In the unconfined case, there would be a continuous spectrum on the imaginary axis representing waves propagating in the cross-stream direction. The confinement turns it into a discrete set. In keeping with the physical origin of these solutions, their streamwise wave number range is limited to values of order $1/L$, where $L = \min(L_1, L_2)$. Hence, by increasing the values of the computational domain L_1 and L_2, the spacing between eigenvalues characterizing the confinement becomes smaller and they are closer to the imaginary axis. The properties of such confinement branches have been discussed in several recent works on inviscid spatial instability of single phase and two-phase flows [24, 25, 32, 33]. When the confining walls are sufficiently far away, these branches do not interfere with the regular spatial branches identified as modes I-IV above. As long as the flow is convectively unstable, these additional branches may be disregarded since they do not describe spatial growth in the streamwise direction. However, they have to be taken into consideration for identifying absolute instability in Section 5.5.

As in the temporal analysis, mode II dominates in the Stokes case ($\delta_0 = 1$). When the defect width δ_0 is lowered, the growth rates $-\alpha_i$ of modes I and II are both enhanced, see Figure 5.24. For a given defect width $\delta_0 < 1$, decreasing the velocity ratio M decreases the growth rate of mode II substantially. This is not observed for mode I. As a consequence, mode II remains

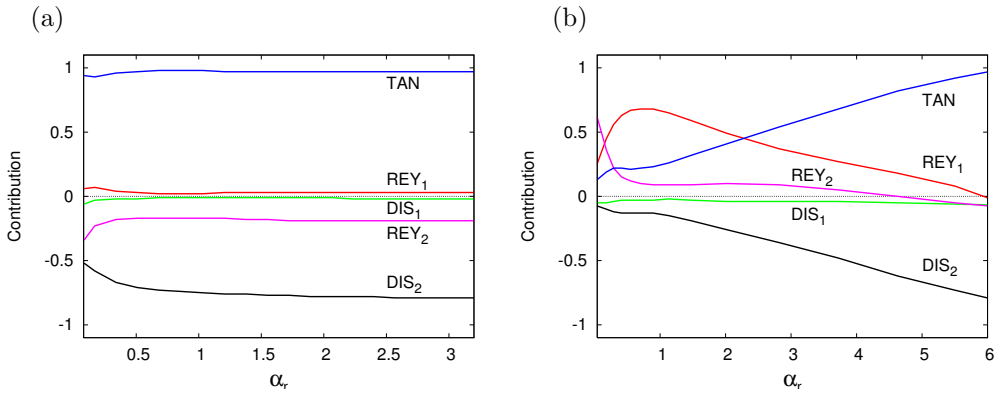

Figure 5.25: *Spatial energy contributions for mode I as a function of the streamwise wave number* $\alpha_r(\omega)$. *The parameters are* $r = 0.0012$, $m = 0.012$, $n = 1$, $Re = 10000$, $S = 0$, *and* $M = 0.9$. *The defect width is (a)* $\delta_0 = 1$, *and (b)* $\delta_0 = 0.1$.

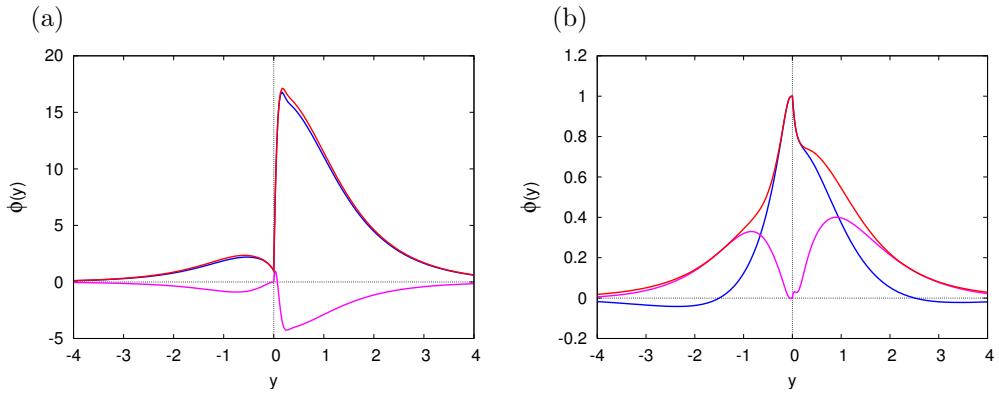

Figure 5.26: *Spatial eigenfunctions of mode I at* $\alpha_r(\omega) \approx 1$ *normalized by* $\phi(0) = 1$ *for (a)* $\delta_0 = 1$, *(b)* $\delta_0 = 0.1$. *Case with* $r = 0.0012$, $m = 0.012$, $n = 1$, $Re = 2000$, $S = 0$, *and* $M = 0.5$. *The real and imaginary part of the eigenfunction are shown in blue and magenta, respectively, and* $|\phi|$ *is plotted in red.*

dominant for all the defect widths presented for $M = 0.9$. Contrary, for $M = 0.5$ mode I quickly overcomes mode II when the defect width δ_0 decreases.

Mode I

In the Stokes case, the dependency of mode I with respect to the Reynolds number is twofold. For sufficiently high Re, it becomes independent of the Reynolds number. For low Reynolds numbers, it varies with Re. This is due to an exchange of the low-wave number branches of modes I and II occuring between $10000 < Re < 40000$ in Figure 5.24. For $Re \leq 10000$ mode I is therefore mainly caused by the H mechanism. In the presence of a velocity deficit, when Re is varied, mode I remains unchanged for $M = 0.5$ and is only mildly modified for $M = 0.9$. As for the temporal case, mode I is then of inviscid type. The different driving instability mechanisms for $\delta_0 = 1$ and $\delta_0 = 0.1$ can be identified by plotting the eigenfunction and/or the contributions of the spatial energy budget. For $M = 0.9$ and $Re = 10000$, the spatial energy contributions of equation (2.128) are shown in Figure 5.25 as function of the wave number $\alpha_r(\omega)$. Contrary, in Figure 5.26 spatial eigenfunctions are shown at $\alpha_r \approx 1$ for $M = 0.5$ and $Re = 2000$. Note, that these plots are very similar to their temporal analogues, Figures 5.7 and 5.8. Hence, similar conclusions as in the temporal case are obtained.

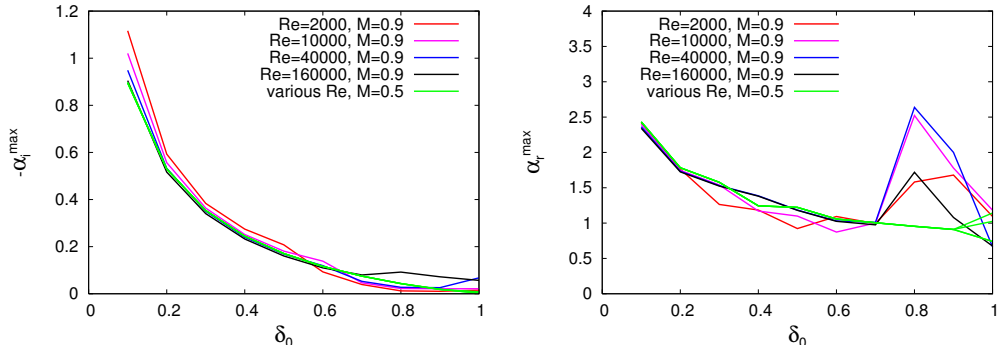

Figure 5.27: *Maximum spatial growth rate* $-\alpha_i^{\max}$ *(left) and corresponding wave number* $\alpha_r^{\max}$ *(right) of mode I as a function of the velocity defect* δ_0*. The remaining parameters are* $r = 0.0012$*,* $m = 0.012$*,* $n = 1$*, and* $S = 0$*.*

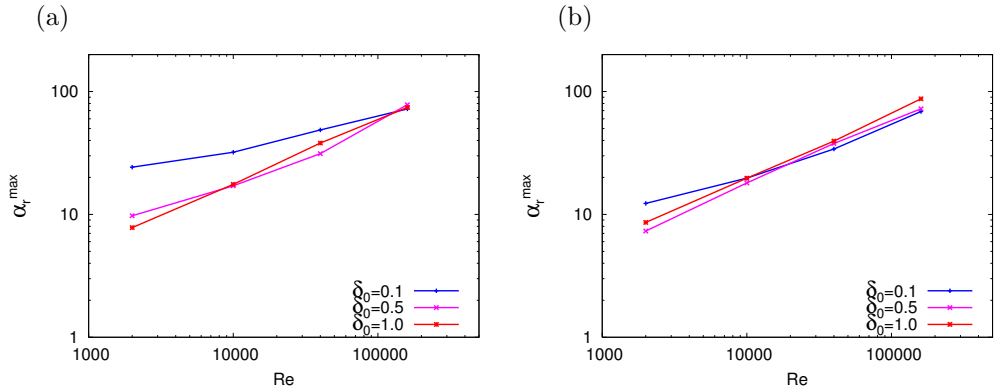

Figure 5.28: *Wave number* $\alpha_r^{\max}$ *of maximum spatial growth rate of mode II as function of Re for various defect widths* δ_0*. The velocity ratio is (a)* $M = 0.5$*, and (b)* $M = 0.9$*. The remaining parameters are* $r = 0.0012$*,* $m = 0.012$ $n = 1$*, and* $S = 0$*.*

Further, given $\delta_0 < 1$ the spatial growth rate of mode I does not change significantly with M. This is shown in Figure 5.27, where the maximum growth rate and corresponding wave number of mode I are presented as a function of δ_0. These quantities effectively collapse on a single curve for different M and Re when $\delta_0 \leq 0.6$. However, when one approaches the Stokes case for $M = 0.9$, there are some differences caused by branch switches between modes I and II. This quasi independence of M in the spatial case has the same origin as for the temporal case and can be seen by taking the inviscid limit of the Orr-Sommerfeld equation (2.58) for $y \leq 0$: From the independence on M of the rescaled basic velocity distribution in the liquid $U_1(y)/U_1(-\infty)$ for small m, one concludes that the eigenvalue α depends only on $\omega/U_1(-\infty)$. Thereby the maximum spatial growth rate $-\alpha_i^{\max}$ and the corresponding wave number $\alpha_r^{\max}$ cannot depend on M while the corresponding frequency $\omega^{\max}$ does depend on M via $U_1(-\infty) = 1 - M$.
Finally, an estimate α_i^G of the spatial growth rate is computed from the temporal growth rate ω_i and the group velocity c_g using Gaster's relation,

$$\alpha_i^G = -\frac{\omega_i}{c_g}, \qquad c_g = \frac{d\omega_r}{d\alpha}, \tag{5.30}$$

The predictions using (5.30) are in good quantitative agreement with the spatial analysis. E.g., for $M = 0.5$, $Re = 2000$ and the two values $\delta_0 = 1$ and $\delta_0 = 0.1$, the peaks in the spatial growth rates of mode I agree to within 10% in real and imaginary parts of the complex wave number.

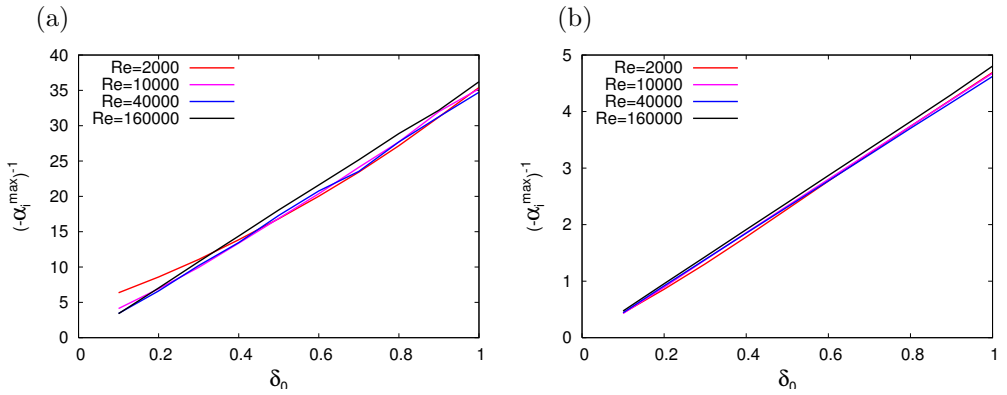

Figure 5.29: *Inverse maximum growth rate* $(-\alpha_i^{\max})^{-1}$ *of mode II as a function of the defect width* δ_0 *for (a)* $M = 0.5$*, and (b)* $M = 0.9$*. The remaining parameters are* $r = 0.0012$*,* $m = 0.012$*,* $n = 1$*, and* $S = 0$*.*

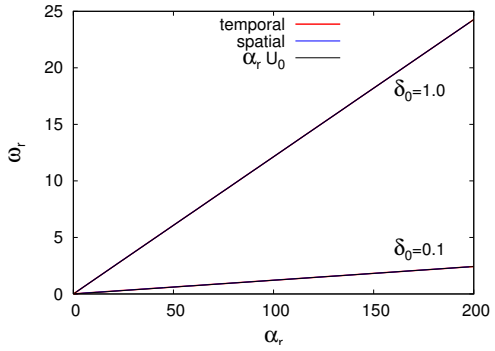

Figure 5.30: *Mode II: Dependency of the frequency* ω *on the real part of the wave number from temporal and spatial analysis for* $M = 0.9$*,* $Re = 10000$*. The remaining parameters are* $r = 0.0012$*,* $m = 0.012$*,* $n = 1$*, and* $S = 0$*.*

Mode II

The behaviour of mode II in Figure 5.24 is completely analogous to the temporal case as far as the effect of the Reynolds number is concerned. Upon increasing Re, the maximum growth rate is essentially unchanged and the corresponding wave number $\alpha^{\max}$ increases as $\sqrt{Re}$, see Figure 5.28, which resembles Figure 5.15 for the temporal case very closely. Only for small defect widths δ_0, moderate velocity ratios, and low Reynolds numbers there are some deviations from this behaviour. As in the temporal problem, they arise when the viscous length scale of the H instability mechanism is comparable with the defect width.

In the temporal case, maximum growth rates $\omega_i^{\max}$ are hardly changed by the defect width, see Figure 5.14. Contrary, the maximum spatial growth rates $-\alpha_i^{\max}$ turn out to be inversely proportional to δ_0, see Figure 5.29. This observation can be explained from the particular properties of the H mechanism in combination with Gaster's relation. If one assumes, as noted by Hinch [26], that the perturbation resulting from the viscosity-contrast mechanism does not propagate in the reference system in which the interface is at rest, then the group velocity c_g should be equal to the interface velocity U_0 itself. Good agreement of phase and group velocities with the interface velocity is illustrated in Figure 5.30 for a typical parameter combination. Because of equation (5.17), $U_0 \sim \delta_0$. Consequently, because the temporal growth rate ω_i is essentially constant, Gaster's relation (5.30), provides an inverse proportionality of the spatial

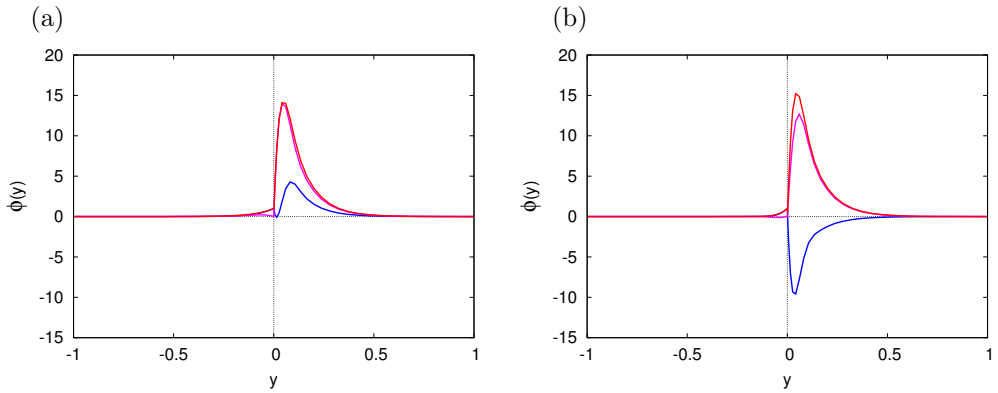

Figure 5.31: *Spatial eigenfunctions of mode II at* $\alpha_r(\omega) \approx 10$ *normalized by* $\phi(0) = 1$*: (a)* $\delta_0 = 1$*, (b)* $\delta_0 = 0.1$*. Case* $r = 0.0012$*,* $m = 0.012$*,* $n = 1$*,* $Re = 2000$*,* $S = 0$*, and* $M = 0.5$*. The real and imaginary part of the eigenfunction are shown in blue and magenta, respectively, and* $|\phi|$ *is plotted in red.*

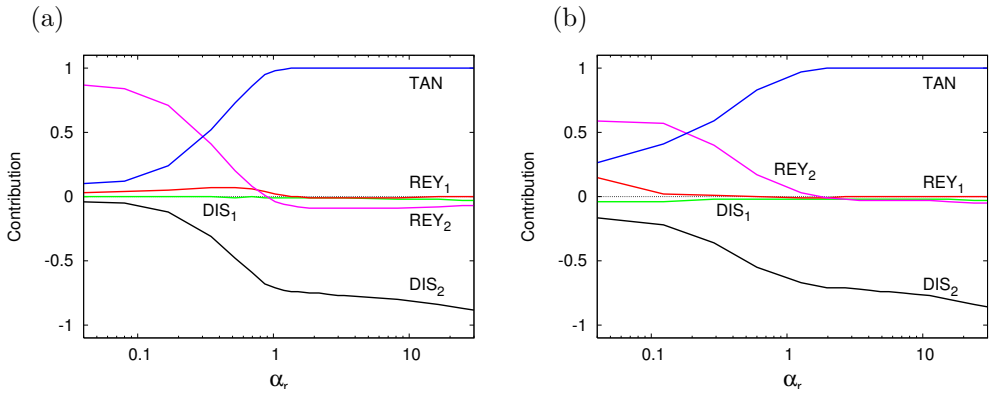

Figure 5.32: *Spatial energy contributions for mode II as a function of the streamwise wave number* $\alpha_r(\omega)$*. The parameters are* $r = 0.0012$*,* $m = 0.012$*,* $n = 1$ *,* $Re = 10000$*,* $S = 0$*,* $M = 0.9$*. The defect width is (a)* $\delta_0 = 1$*, (b)* $\delta_0 = 0.1$*.*

growth rate with respect to the defect width δ_0,

$$-\omega_i = c_g \alpha_i^G \sim \delta_0 \alpha_i^G. \tag{5.31}$$

This relation is very well satisfied in Figure 5.29. Deviations occur for the same parameter combinations noted in the $\sqrt{Re}$ scaling of the optimal wave number $\alpha_r^{\max}$.

Finally, for $M = 0.5$, $Re = 2000$, and the two defect widths $\delta_0 = 1$ and $\delta_0 = 0.1$, Figure 5.31 shows the spatial eigenfunctions of mode II for $\alpha_r \approx 10$. Note that, the structure of the mode is very similar to its temporal counterpart shown in Figure 5.13. For the larger velocity ratio $M = 0.9$, $Re = 10000$, and both $\delta_0 = 1$ and $\delta_0 = 0.1$, Figure 5.32 shows the spatial energy contributions of equation (2.128) as function of the wave number $\alpha_r(\omega)$. Comparing the results with its temporal analogue in Figure 5.32, one finds that for spatial modes the Reynolds stress contribution REY_2 in the gas is stronger than in the temporal case. This effect is found for both $\delta_0 = 1$ and $\delta_0 = 0.1$, where in the latter case REY_2 is destabilizing for spatial modes, whereas it is stabilizing for temporal growing perturbations.

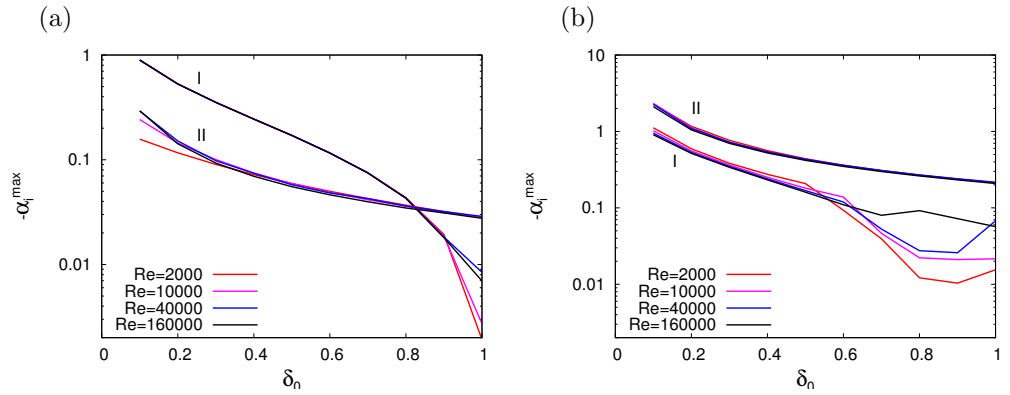

Figure 5.33: *Maximum spatial growth rate* $-\alpha_i^{\max}$ *for modes I and II as function of the defect width* δ_0*: (a)* $M = 0.5$*, and (b)* $M = 0.9$*. The remaining parameters are* $r = 0.0012$*,* $m = 0.012$*,* $n = 1$*, and* $S = 0$*.*

5.4.2 The Dominant Mode

The maximum spatial growth rates of modes I and II are presented in Figure 5.33 as function of the defect width δ_0. As in the temporal analysis, for the small velocity ratio $M = 0.5$, mode I becomes dominant when δ_0 is decreased. For the large velocity ratio $M = 0.9$, mode II remains dominant even when the defect width is small.
However, there are certain differences between temporal and spatial results. For the temporal case, modes I and II have comparable growth rates for $M = 0.9$ and small δ_0. This trend is not confirmed by the spatial growth rates for $M = 0.9$, where mode II is consistently larger by a factor of two or larger, see Figure 5.33(a). This can be justified by Gaster's relation. Since the group velocity of mode II is proportional to the defect width, the spatial growth rate is enhanced by reducing δ_0. The group velocity of mode I is less sensitive to δ_0. Temporal analysis alone may therefore lead to inappropriate or misleading conclusions on the importance of the defect width or other parameters as well as about the relevant instability mechanisms.
As noted in the temporal analysis, the particular features of the δ_0-dependence for mode I in Figure 5.33 are related to exchanges of the low-wave number branches of modes I and II. For $M = 0.5$, such an exchange occurs only for low Reynolds numbers and when the velocity profile is still close to the Stokes case, i.e. for $\delta_0 < 1$ close to unity; see Figure 5.24. For $M = 0.9$ the switch of these branches occurs at smaller $\delta_0 \approx 0.5$, and produces a distinct change in slope in the dependence of $-\alpha_i^{\max}$ on δ_0 for mode I.
It is finally noted, that the effect of increasing surface tension on the maximum spatial growth rates $-\alpha_i^{\max}$ is the same as in the temporal setting (not shown): Assuming that the flow remains convectively unstable for $S > 0$, the growth rates for large wave numbers α_r are strongly damped. However, as for inviscid flow, surface tension is shown to alter the convective/absolute nature of the flow; see Section 5.5.

In the absence of surface tension, $S = 0$, the leading spatial eigenvalue and the associated mode will be the focus in the next section on the influence of the fluid properties.

5.4.3 Influence of Fluid Properties

Now, the influence of the ratios of both densities and viscosities on the dominant spatial mode is considered. Although this aspect has already been examined in the temporal case, the results from spatial computations may differ from the temporal ones because the velocity ratio M and the defect width δ_0 affect the inviscid and H mechanisms and the associated modes in distinct ways. As for the temporal case, the spatial growth rate $-\alpha_i^{\max}$, and the corresponding wave

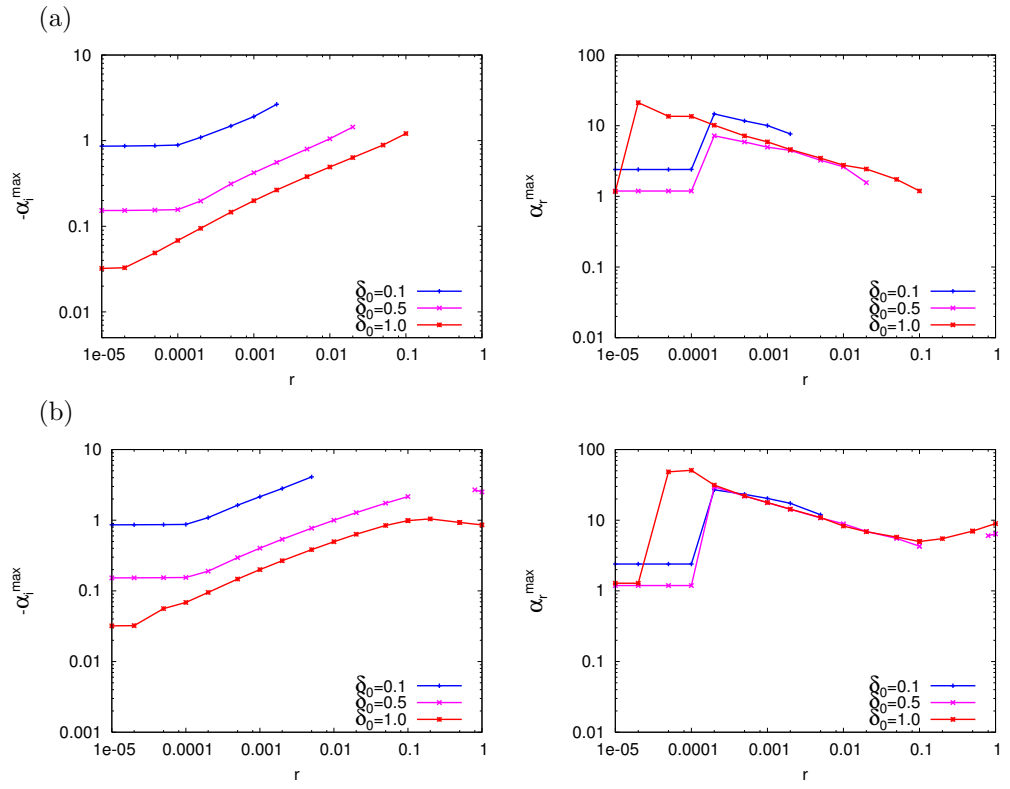

Figure 5.34: *Maximum spatial growth rates* $-\alpha_i^{\max}$ *(left), and corresponding wave numbers* $\alpha_r^{\max}$ *(right) as function of the density ratio* r *for two Reynolds numbers: (a)* $Re = 1000$*, and (b)* $Re = 10000$*. The remaining parameters are* $m = 0.01$*,* $n = 1$*,* $S = 0$*, and* $M = 0.9$*. The abrupt ending in some of the curves with is due to a change to absolute instability.*

number $\alpha_r^{\max}$ of the leading eigenmode are studied for $m = 0.01$ and $m = 0.1$, and a large interval of density ratios r. Thereafter, the dependency of these quantities on the viscosity ratio m is investigated for the fixed density ratio $r = 0.01$.

Density Ratio Variation

First, $m = 0.01$ is considered. Figure 5.34 shows the largest spatial growth rate $-\alpha_i^{\max}$ and the corresponding wave number $\alpha_r^{\max}$ as functions of the density ratio r for $M = 0.9$ and $M = 0.5$ at two different Reynolds numbers. For $M = 0.9$, there exists an intermediate range of density ratios, $r_1^{(s)} < r < r_2^{(s)}$, such that $-\alpha_i^{\max}$ increases and $\alpha_r^{\max}$ decreases with growing r. This corresponds to a dominant mode II. Note that the wave numbers for mode II do not depend on the defect width δ_0, but, contrary to the temporal case, the spatial growth rates do differ. This is related to the fact that the interface velocity U_0 is modified by δ_0, and hence the H-mode group velocity. For $r < r_1^{(s)}$, mode I becomes dominant as for temporal analysis, and both $\alpha_r^{\max}$ and $-\alpha_i^{\max}$ become independent of r. As in the temporal case, $r_1^{(s)}$, which is close to $r_1^{(t)}$, has values of order 10^{-4} and increases as δ_0 is reduced. Contrary, $r_2^{(s)}$ is typically different from the temporal value $r_2^{(t)}$. On the one hand, for the Stokes flow at $Re = 10000$ mode II is dominant up to $r = 1$, although its spatial growth rate starts to decrease with r for $r > 0.1$. On the other hand, for $\delta_0 = 0.5$ and $\delta_0 = 0.1$ the limit $r_2^{(s)}$ indicates transition from convective to absolute instability for $M = 0.9$. This limit is shifted towards smaller density ratios for $Re = 1000$.
In addition, Figure 5.35 shows the dependency of $-\alpha_i^{\max}$ and $\alpha_r^{\max}$ on the density ratio for

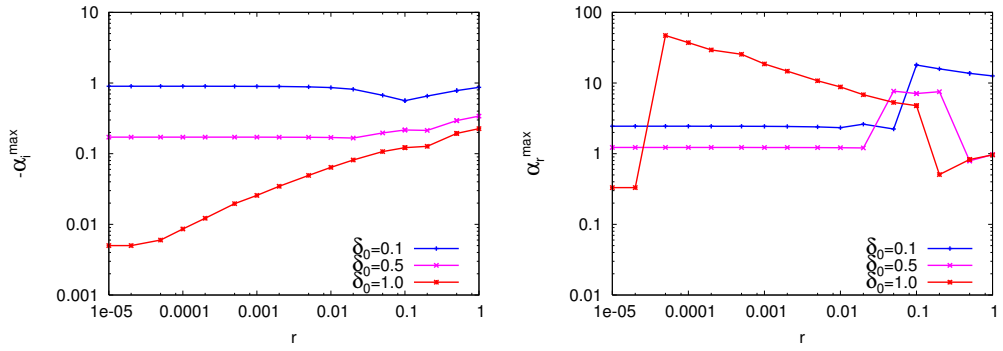

Figure 5.35: *Maximum spatial growth rates* $-\alpha_i^{\max}$ *(left), and corresponding wave numbers* $\alpha_r^{\max}$ *(right) as function of the density ratio* r *for* $Re = 10000$*. The remaining parameters are* $m = 0.01$, $n = 1$, $S = 0$, $M = 0.5$*. Quadruple precision was necessary for* $\delta_0 = 1$ *and* $r \leq 0.0002$*.*

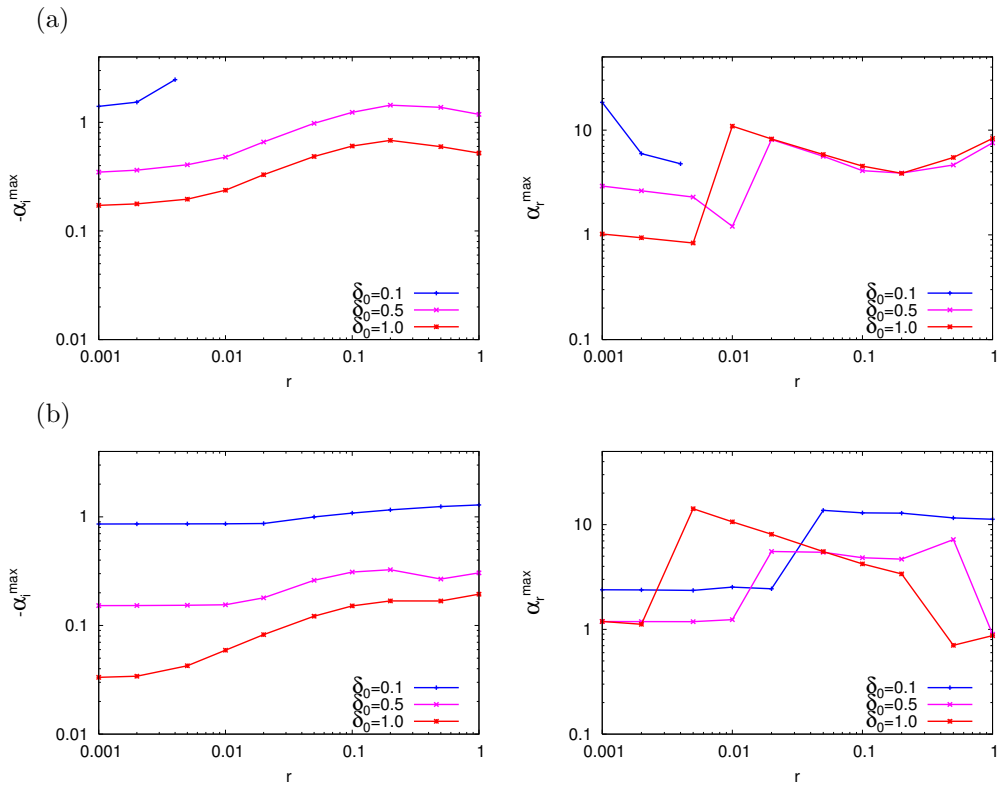

Figure 5.36: *Maximum spatial growth rates* $-\alpha_i^{\max}$ *(left), and corresponding wave numbers* $\alpha_r^{\max}$ *(right) as function of the density ratio* r *with a different viscosity contrast* $m = 0.1$*. Case with* $Re = 1000$, $n = 1$, *and* $S = 0$*. The velocity ratio is (a)* $M = 0.9$, *and (b)* $M = 0.5$*. The abrupt ending of the curves for* $M = 0.9$ *and* $\delta_0 = 0.1$ *is due to a change to absolute instability.*

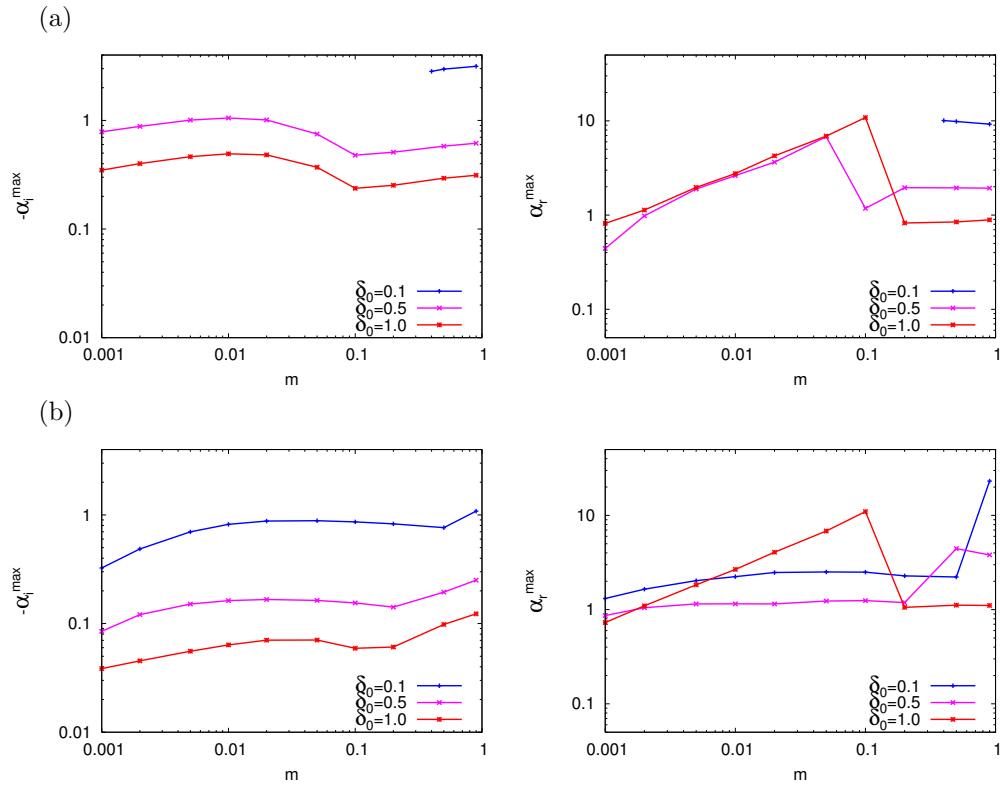

Figure 5.37: *Maximum spatial growth rates* $-\alpha_i^{\max}$ *(left), and corresponding wave numbers* $\alpha_r^{\max}$ *(right) as function of the viscosity ratio* m *with* $r = 0.01$*. Case with* $Re = 1000$*,* $n = 1$*, and* $S = 0$*. The velocity ratio is (a)* $M = 0.9$*, and (b)* $M = 0.5$*. The abrupt ending of the curves for* $M = 0.9$ *and* $\delta_0 = 0.1$ *is due to a change to absolute instability.*

$Re = 10000$, and $M = 0.5$. For this smaller velocity ratio the values $r_1^{(s)}$ are larger than for $M = 0.9$. Contrary to the temporal case, there is a range of density ratios near $r \approx 0.1$, where mode II is dominant for the values $\delta_0 < 1$ considered. In addition, the plateau near $r = 10^{-5}$ for $\delta_0 = 1$ is caused by mode III, which is absent for $Re = 1000$ (not shown). Finally, the transition to absolute instability is never reached for $M = 0.5$.

For completeness, in Figure 5.36 the case $m = 0.1$ is shown for both $M = 0.9$ and $M = 0.5$ at $Re = 1000$. Note that, the general observations are very similar to those for the lower viscosity ratio $m = 0.01$.

Viscosity Ratio Variation

Finally, Figure 5.37 shows the maximum spatial growth rate $-\alpha_i^{\max}$ and corresponding wave number $\alpha^{\max}$ as a function of the viscosity ratio m for the fixed density ratio $r = 0.01$, $Re = 1000$, and the two velocity ratios $M = 0.9$ and $M = 0.5$. The general observations are very similar to the temporal case shown in Figure 5.22, but, as for the variation of the density ratio, the spatial growth rates differ for different values of the defect width δ_0. Note, that for $M = 0.9$ and $\delta_0 = 0.1$ absolute instability is present for a wide range of viscosity ratios $m \leq 0.3$.

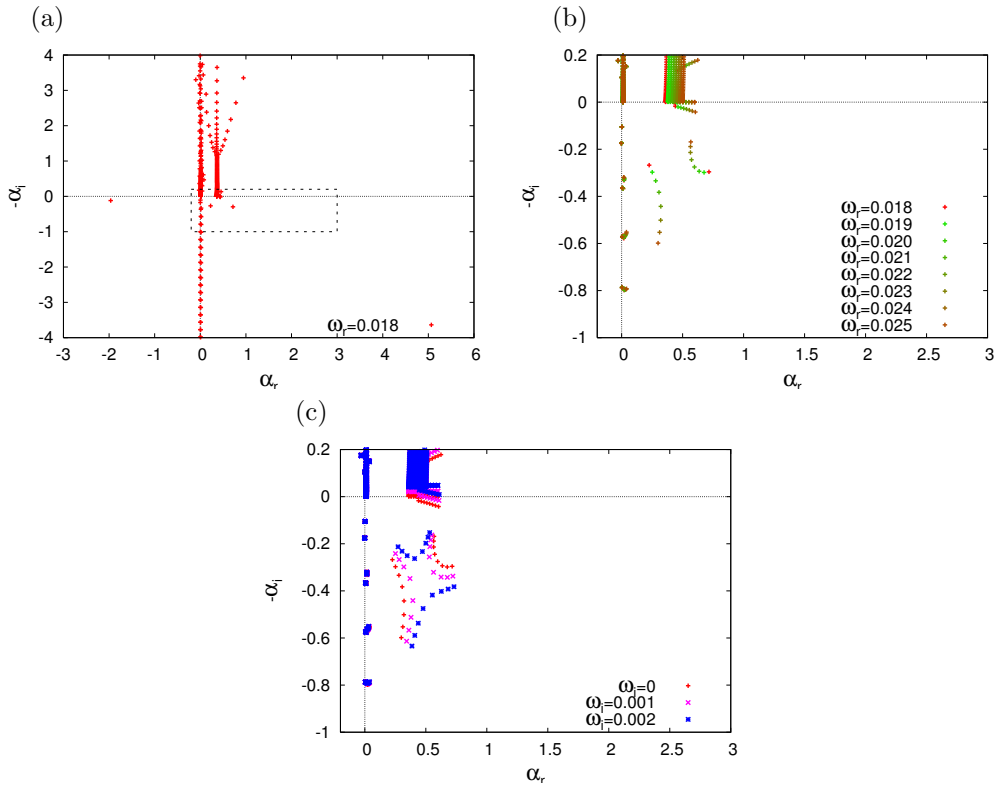

Figure 5.38: *Spatial eigenvalues for (a)* $\omega = 0.018$*, and (b)* $0.018 \leq \omega \leq 0.025$*. In (c) generalized spatial eigenvalues for* $\omega_i = 0.001$*,* $\omega_i = 0.002$ *are shown in addition to the spatial results. The parameters are* $r = 0.0012$*,* $m = 0.018$*,* $n = 1$*,* $Re = 700$*,* $S = 1$*,* $M = 0.95$*, and* $\delta_0 = 0.5$*.*

5.5 Transition from Convective to Absolute Instability

In open flows, the convective/absolute transition is an important feature. Only for convectively unstable flows, classical spatial branches are meaningful. A search for the transition boundary in parameter space (δ_0,M) has been performed for $r = 0.0012$, $m = 0.018$, $n = 1$, two different Reynolds numbers $Re = 700$, $Re = 10000$, and two surface tension numbers $S = 0$, $S = 1$. Note, that the case $Re = 700$, $S = 1$ is well in the range of the experiments for air and water performed by Matas et al. [41].

The transition from convective to absolute instability is determined by the method based on the behaviour of generalized spatial branches $\alpha(\omega)$ in the plane of complex wave numbers; see Section 2.6.2. Let ω^0 denote the value, such that, when ω_i is lowered to ω_i^0, two generalized spatial branches originating in different halfplanes reconnect through a saddle point. When $\omega_i^0 > 0$, the flow is absolutely unstable; otherwise it is convectively unstable [4, 29, 31]. This reconnection is also referred to as *pinching*, because any contour F in the complex wave number plane that passes from $\alpha_r = -\infty$ to $\alpha_r = +\infty$ between the sets of $\alpha_j^-(\omega)$ and $\alpha_j^+(\omega)$ branches would become pinched by these generalized branches as ω_i is lowered to zero. Such an integration contour is required in order for the response to a time-periodic localized source to be computed without violating causality; see Section 2.6.2. Detection of pinching at $\omega_i^0 > 0$ means that no such contour exists [30, 31].

From the above discussion, it becomes clear, that spatial analyses require considerably more effort than the traditional temporal stability analysis of periodic disturbances. The process of

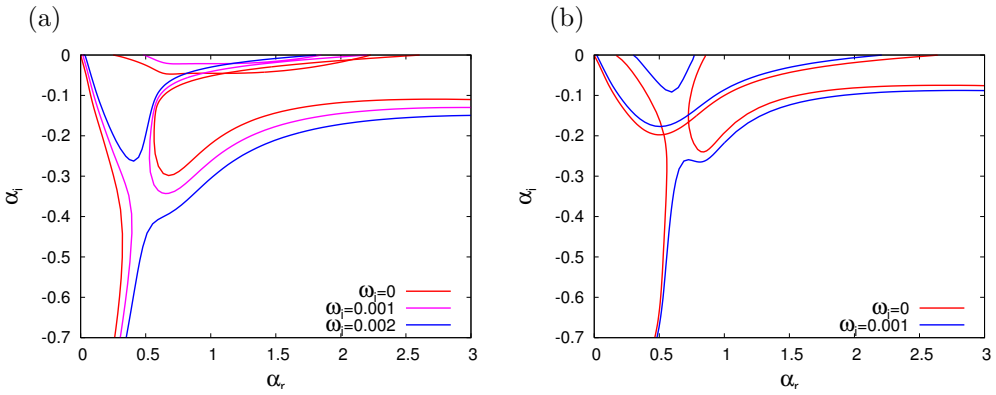

Figure 5.39: *Two instances of absolute instability: generalized spatial branches reconnect before the imaginary part ω_i is reduced to zero for (a) $M = 0.95$, $\delta_0 = 0.5$; (b) $M = 0.92$, $\delta_0 = 0.1$. The remaining parameters are $r = 0.0012$, $m = 0.018$, $n = 1$, $Re = 700$, and $S = 1$.*

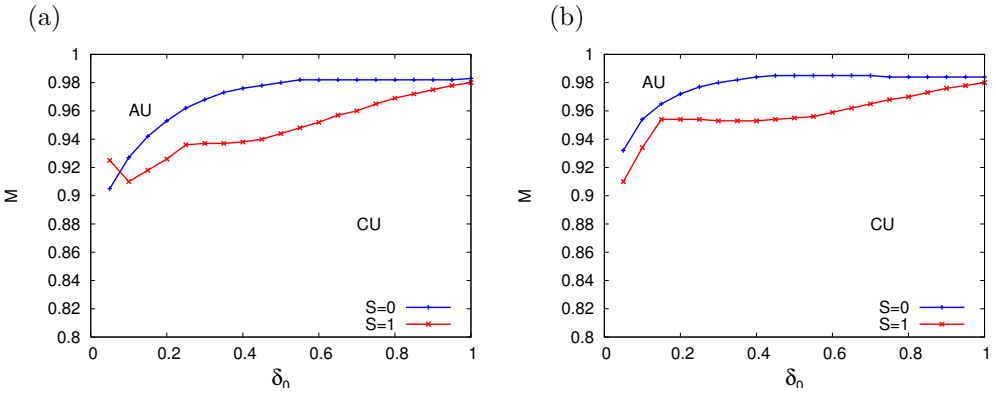

Figure 5.40: *Curves in the parameter plane (δ_0,M) delimitating the convective/absolute transition for $S = 0$ and $S = 1$. The Reynolds number is (a) $Re = 700$, and (b) $Re = 10000$. The remaining parameters are $r = 0.0012$, $m = 0.018$, and $n = 1$. The numerical results are computed with $L_1 = L_2 = 30$.*

finding a saddle point in the complex wave number plane is illustrated in Figure 5.38 for the absolutely unstable unstable case $Re = 700$, $S = 1$, $M = 0.95$, and $\delta_0 = 0.5$. For these set of parameters, the temporal analysis (not shown) indicates that modes I and II are unstable.

In Figure 5.38(a) a typical plot of spatial eigenvalues (i.e. $\omega_i = 0$) in the complex α-plane is presented for the fixed frequency $\omega_r = 0.018$. First, the eigenvalues in quadrant I are damped spatial modes. There may also exist eigenvalues in quadrants II and III, corresponding to negative wave numbers. However, none of these eigenvalues is of further interest. In addition, the spatial eigenvalues near the imaginary axis are the result of the distant walls at $y = -L_1$ and $y = L_2$ necessitated by the numerical method. In the unconfined case, there would be a continuous spectrum on the imaginary axis representing waves propagating in the cross-stream direction. The confinement turns it into a discrete set. These eigenvalues are important, since they have the potential to alter the convective/absolute transition, as will be shown below.

In Figure 5.38(b) consideration is restricted to the region indicated in (a). In addition, the eigenvalues are given for a set of real freqencies $0.018 \leq \omega \leq 0.025$. In quadrant IV three spatial branches are observed, whose origin is revealed by considering generalized spatial branches with $\omega_i > 0$. For $\omega_i = 0.001$ and $\omega_i = 0.002$, Figure 5.38(c) shows the formation of a saddle point for frequencies in the interval $0.018 \leq \omega_r \leq 0.025$. The complete generalized spatial branches are

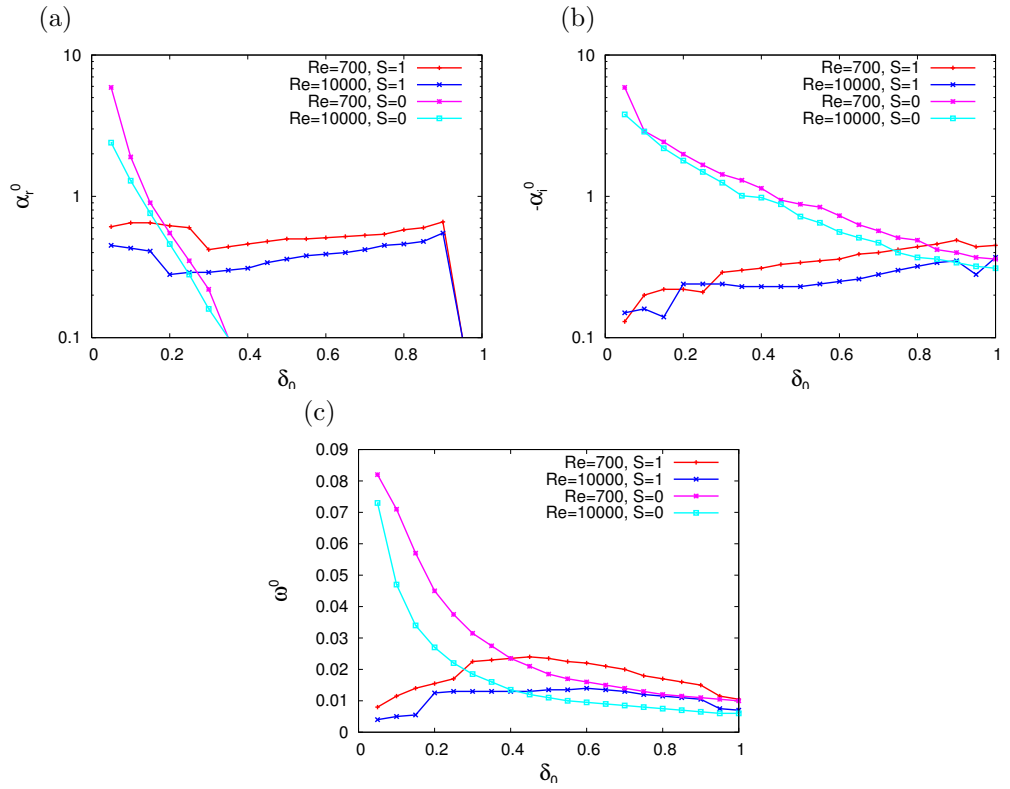

Figure 5.41: *Pinch point location along the convective/absolute transition curves in Figure 5.40: (a) α_r^0, (b) $-\alpha_i^0$, and (c) the absolute frequency ω^0 as a function of δ_0.*

plotted in Figure 5.39(a). (Note, that the confinement branches near the α_i-axis are eliminated from this plot for clarity.) From this figure the three branches observed can be identified as a generalized α^- branch and two unstable α^+ branches corresponding to modes I and II. Note, that the saddle point is formed by the α^- branch and the generalized spatial branch II.
However, as is evident from Figure 5.39, the convective/absolute transition can occur from modes of different nature. For example, in the case $\delta_0 = 0.1$ and $M = 0.92$ it is the generalized mode I that forms the saddle, whereas it is mode II for $\delta_0 = 0.5$ and $M = 0.95$.
In addition, the detection of absolute instability through pinching of generalized spatial branches turns out to be affected by the additional branches near the imaginary axis by the confinement introduced in the numerical method; see Figure 5.24(f). For some values of δ_0, pinching first occurs between an α^+-branch and one of the additional spatial confinement branches near the imaginary axis when M is increased for a given defect width δ_0. This is unpleasant, since in this work the focus is on the behaviour of unconfined mixing layer flows. However, it was recently elucidated by Healey [24, 25] and Juniper [32, 33] for certain classes of inviscid flows that these pinching points have a physical meaning and cannot be ignored. A detailed interpretation and discussion of this and related issues including examination of spatio-temporal impulse responses is provided in these works. Pertinent to the present study, Healey [25] found that symmetric confinement tends to promote absolute instability in a single-phase mixing layer unless the walls are rather close. For the problem at hand, it therefore seems plausible that the critical velocity ratio M_t for the convective/absolute transition associated with a pinching point of a confinement branch should actually be lower than without confinement.

The main results for convective/absolute transition are shown in Figure 5.40. Absolute instability is typically encountered for $M > 0.9$, and surface tension promotes the transition, except

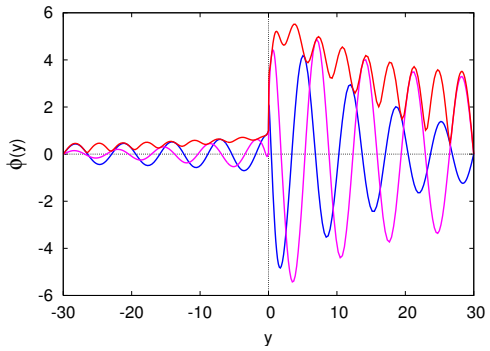

Figure 5.42: *Eigenfunction of a confinement branch normalized by* $\phi(0) = 1$ *for* $r = 0.0012$, $m = 0.018$, $n = 1$, $Re = 10000$, $M = 0.978$, $\delta_0 = 0.25$, *and* $S = 0$. *The numerical results are computed with* $L_1 = L_2 = 30$. *The real and imaginary part of the eigenfunction are shown in blue and magenta, respectively, and* $|\phi|$ *is plotted in red.*

at small defect widths δ_0 and $Re = 700$. This can be interpreted by the presence of capillary waves that are able to spread upstream [50]. Moreover, if again one excepts the case (small δ_0, $Re = 700$ and $S = 1$), the threshold value M_t for convective/absolute transition remains constant or decreases when decreasing the defect width from $\delta_0 = 1$, i.e. for enhanced wake contribution to the basic flow. This behaviour is in line with single-phase flows, where wake flows tend to be absolutely unstable without counterflow, whereas pure mixing layers usually require counterflow for absolute instability [13, 29].
Note also that, for $S = 1$ the curves for both Reynolds numbers change slope near $\delta_0 = 0.2$. This corresponds to a change of modes producing the saddle point from mode I ($\delta_0 \leq 0.2$) to mode II ($\delta_0 \geq 0.3$). This trend between modes I and II is also apparent from Figure 5.41, which shows the location of the saddle points and corresponding frequencies.
Without surface tension, $S = 0$, for $\delta_0 \leq 0.15$, absolute instability is caused by a pinch of mode I ($Re = 10000$) or mode II ($Re = 700$); for $\delta_0 \geq 0.15$ it is caused by mode II only. For $\delta_0 \geq 0.35$ and both Reynolds numbers there is a pinch with confinement branches, which appears at small values $\alpha_r < 0.1$ outside the axis range in Figure 5.41(a). To ensure that there is no significant effect by the confinement in the other cases, two different wall distances are used, namely $L_1 = L_2 = 15$ and $L_1 = L_2 = 30$. Except for the confinement branches, eigenvalues of other modes are unaffected for $\alpha_r \geq 0.15$ by this change of the computational domain. For $\delta_0 > 0.9$ and $S = 1$ there is pinching with confinement branches as for $S = 0$, see Figure 5.41.

For completeness, Figure 5.42 shows the eigenfunction of a confinement branch for the parameters given in the caption. Since the confinement branches represent waves propagating in the cross-stream direction which are reflected by the outer boundaries, their eigenfunctions display a number of peaks in amplitude in both the liquid and the gas phase.

5.6 Summary

In this chapter the viscous linear instability of gas-liquid mixing layers was considered. The work extends two previous studies by three features. First it incorporates viscous boundary layers, and accounts for the particular flow structure near the nozzle by an adjustable velocity deficit on the interface. Second it performs an analysis of spatially growing perturbations, and third it determines the transition from convective to absolute instability.
The viscous linear stability problem typically provides three characteristic unstable modes in different wave number intervals. They are caused by the inviscid Kelvin-Helmholtz mechanism

due to the free-stream velocity difference, the Tollmien-Schlichting mechanism in the gas boundary layer, the viscosity-contrast or H mechanism, and an additional inviscid mechanism due to the appearance of inflection points in both liquid and gas.
In the absence of surface tension, $S = 0$, in both the temporal and spatial setting modes I and II are predominant. Generally, mode I provides the strongest amplification when a velocity deficit is present and the velocity ratio is moderate. By contrast, mode II is strongest when the deficit is absent, or when the velocity ratio is large.
Finally, for parameters corresponding approximately to air and water, absolute instability is encountered for velocity ratios in the range of typical gas-assisted atomization experiments, and both the velocity deficit and surface tension usually promote absolute instability. It is further shown, that the convective/absolute transition can originate from modes of different nature. In addition, the detection of absolute instability through pinching of generalized spatial branches may be affected by the additional confinement branches near the imaginary axis necessitated by the numerical method.

Chapter 6

Comparison with Experiments

In this chapter the formulation of both the viscous and inviscid spatial instability problem is applied to air-water mixing layers in order to compare the numerical results with recent experiments. Two such experiments are considered. The first one has been performed by Marmottant and Villermaux [39] using a concentric nozzle with a round water jet surrounding by an annular air stream. In the second experiment by Matas et al. [41] planar air and gas streams emanate from a rectangular nozzle with the width/height ratio of 10. In both works, the authors have recorded the evolution of the deforming interface near the nozzle with a high-speed camera and obtained dominant frequencies and spatial growth rates of the wavy perturbations. In the experiments, the velocities, U_1^* and U_2^* can be directly controlled. The boundary layer sizes δ_1 and δ_2 depend on these velocities and the particular nozzle or splitter plate geometry. In both experiments, only the gas boundary layer thickness δ_2 has been measured at a location close to the end of the separating wall. The authors obtain the relation

$$\delta_2 = \gamma \sqrt{\frac{H_2 \mu_2}{\rho_2 U_2^*}}, \tag{6.1}$$

between δ_2 and U_2^*, where H_2 denotes the width of the gas stream within the nozzle and the coefficient γ accounts for the geometry. The specific values are $\gamma = 5.6$, $H_2 = 1.7\,\text{mm}$ in the experiments of Marmottant and Villermaux [39] and $\gamma = 6$, $H_2 = 10\,\text{mm}$ in those of Matas et al. [41]. The thickness δ_1 of the liquid boundary layer is not known, but is presumably roughly the same as for the gas phase [41].

6.1 Experimental Results

Experimental results are given in Table 6.1 for the concentric nozzle [39] and in Table 6.2 for the planar nozzle geometry [41]. Table 6.2 is the orginal data set given by the authors. It has frequencies and growth rates for all combinations of the velocities U_1^* and U_2^*. This is not the case for the other experiment. The frequencies and growth rates in Table 6.1 were extracted from Figures 5(b) and 6(b) of Reference [39]. The latter plot shows the amplitude of the liquid interface displacement as function of the dimensionless downstream distance x/D_1 with $D_1 = 7.8\,\text{mm}$ denoting the diameter of the round inner nozzle [39]. Note, that only the lowest four curves of that figure are used, because they have relatively pronounced exponential growth from $0.625 \leq x/D_1 \leq 0.875$. The growth rates have been determined by an exponential fit in this interval. The velocity combinations in Figure 6(b) of Reference [39] are not shown in Figure 5(b) of that paper. Finally, the data from Figure 22(b) of Reference [39] is not used, because the growth rates reported there correspond to $M > 0.97$ on account of the low liquid velocity U_1^*. For these large values of M the viscous stability computations indicate absolute instability, i.e. a growth rate cannot be predicted.

Case	U_1^* [m/s]	U_2^* [m/s]	δ_2 [mm]	f [Hz]	$-\alpha_i^{\exp}$ [1/m]	M	Re	S
$A1$	0.80	14.1	0.239	125.6		0.893	210	4.56
$A2$	0.45	14.7	0.234	101.4		0.941	221	4.50
$A3$	0.32	14.4	0.236	73.6		0.957	220	4.72
$A4$	0.20	13.9	0.241	33.6		0.972	218	5.06
$B1$	1.69	23.3	0.186	306.2		0.865	266	2.08
$B2$	0.80	24.2	0.182	238.6		0.936	283	2.12
$B3$	0.45	26.1	0.176	150.0		0.966	298	1.95
$B4$	0.32	25.6	0.177	112.9		0.975	297	2.03
$B5$	0.20	24.6	0.181	84.9		0.984	292	2.17
$C1$	0.94	18	0.211		130	0.901	239	3.19
$C2$	0.94	21	0.196		384	0.914	260	2.57
$C3$	0.94	25	0.179		500	0.928	286	2.00
$C4$	0.94	27	0.173		615	0.933	298	1.79

Table 6.1: Parameters for the experiments in the axisymmetric configuration performed by Marmottant and Villermaux [39].

Case	U_1^* [m/s]	U_2^* [m/s]	δ_2 [mm]	f [Hz]	$-\alpha_i^{\exp}$ [1/m]	M	Re	S
$A1$	0.95	12	0.67	35.7	50.57	0.853	493	2.14
$A2$	0.76	12	0.67	26.2	56.89	0.881	501	2.21
$A3$	0.50	12	0.67	16.8	103.5	0.920	513	2.30
$A4$	0.37	12	0.67	15.1	150.0	0.940	518	2.35
$A5$	0.31	12	0.67	13.6	151.4	0.950	521	2.37
$A6$	0.26	12	0.67	11.7	126.0	0.958	523	2.39
$B1$	0.95	17	0.57	37.6	130.6	0.894	601	1.33
$B2$	0.76	17	0.57	32.2	174.7	0.914	608	1.36
$B3$	0.50	17	0.57	24.5	211.5	0.943	618	1.40
$B4$	0.37	17	0.57	19.7	215.4	0.957	623	1.42
$B5$	0.31	17	0.57	17.8	200.1	0.964	625	1.43
$B6$	0.26	17	0.57	16.0	174.8	0.970	627	1.44
$C1$	0.95	22	0.50	47.9	313.5	0.917	693	0.92
$C2$	0.76	22	0.50	39.5	265.2	0.933	699	0.94
$C3$	0.50	22	0.50	29.4	328.8	0.956	708	0.96
$C4$	0.37	22	0.50	23.5	323.2	0.967	712	0.97
$C5$	0.31	22	0.50	20.7	366.6	0.972	714	0.98
$C6$	0.26	22	0.50	18.9	341.2	0.977	716	0.98
$D1$	0.95	27	0.45	64.1	566.1	0.932	774	0.69
$D2$	0.76	27	0.45	54.4	512.3	0.945	780	0.70
$D3$	0.50	27	0.45	39.8	569.9	0.964	787	0.71
$D4$	0.37	27	0.45	32.4	614.6	0.973	791	0.72
$D5$	0.31	27	0.45	31.6	640.6	0.977	793	0.72
$D6$	0.26	27	0.45	28.8	612.6	0.981	795	0.73

Table 6.2: Parameters for the experiments in the planar configuration performed by Matas et al. [41].

In the following two sections the experimental results are compared with spatial instability computations for both the viscous and the inviscid setting. For the comparison the following material properties are used: $r = 0.0012$, $m = 0.0182$, $\rho_1 = 998.2\,\mathrm{kg/m^3}$, $\mu_1 = 1.002 \cdot 10^{-3}\,\mathrm{Pa\ s}$ and $s = 0.0728\,\mathrm{N/m}$. These values correspond to air and water at 20°C [53]. The Reynolds and surface tension numbers listed in Tables 6.1 and 6.2 are based on these parameters.
In the planar configuration (Table 6.2) four sets of cases labeled *A*-*D* are considered. Each label corresponds to a fixed gas velocity. Then the Reynolds number Re and the surface tension parameter S vary only slightly for each of the four sets. For the axisymmetric configuration (Table 6.1) the cases labelled with A and B also correspond to approximately fixed gas velocities, whereas case C correspond to a fixed liquid velocitiy. Note further, that, compared with the values for the planar geometry, in Table 6.1 the Reynolds numbers are significantly smaller and the surface tension parameter is larger.
With exception of Figure 6.8 the computations have been performed with $n = 1$ as assumed by Matas et al. [41]. In addition, the effect of the velocity deficit is considered:

- Inviscid spatial instability results are shown for two different values of the dimensionless interface velocity: $U_0 = 0$, and $U_0 > 0$ chosen to satisfy equation (5.17) for the viscous error-function profile with $\delta_0 = 1$.
- Viscous spatial instability results are presented for four selected values of the defect width δ_0: 1, 0.7, 0.4, 0.1.

All results are shown as functions of M. For convectively unstable flows, the maximum spatial growth rate $-\alpha_i^{\max}$ and its associated frequency $\omega^{\max}$ are computed. For absolute unstable flows, the absolute frequency ω^0 is given instead of $\omega^{\max}$ and clearly no spatial growth rates can be calculated. The change from convective to absolute instability is indicated by a change from full to dashed lines and may be accompanied by a visible discontinuity in the frequency curve. The curves of spatial growth rates stop at these points.

6.2 Inviscid Numerical Results vs. Experiments

In this section the experimental data are compared with the maximum growth rates and corresponding frequencies obtained from inviscid theory. In Figures 6.1-6.3 two values of the dimensionless interface velocity are considered in order to account for the effect of the velocity deficit: $U_0 = 0$, and $U_0 > 0$. In the latter case, U_0 is chosen to satisfy equation (5.17) for the error-function profile with $\delta_0 = 1$ in order to compare with the viscous results for the Stokes case; see Section 6.3. Note, that for this choice of U_0 the interface velocity is greater than the mean speed in liquid, and the increase in velocity is larger in the gas boundary layer than in the liquid one. For comparison, the case $U_0 = 0$, $S = 0$ is also included in the figures. In this situation the piecewise linear velocity profile is absolutely unstable, and the absolute frequency ω^0 is given by equation (4.20).

Axisymmetric Experimental Setup

For the axisymmetric configuration, in Figure 6.1 the experimental frequencies are compared with the computed values from the inviscid spatial stability analysis using nondimensional units. Note, that the measured frequencies decrease with M.
In the absolutely unstable case $S = 0$, $U_0 = 0$, the absolute frequencies ω^0 significantly exceed the experimental values. On the other hand, for $S > 0$ all cases with $U_0 = 0$ are convectively unstable. In addition, with the exception of case $B1$, there is only a single unstable mode, where $\omega^{\max} < 0.02$. For the exceptional case, however, mode II at the relatively larger frequency $\omega \approx 0.125$ is most unstable. This mode is damped by the action of surface tension in the other cases. Contrary to the case with zero interface velocity, for $U_0 > 0$ there is always a single unstable mode. In addition, absolute instability appears above $M \approx 0.97$. However,

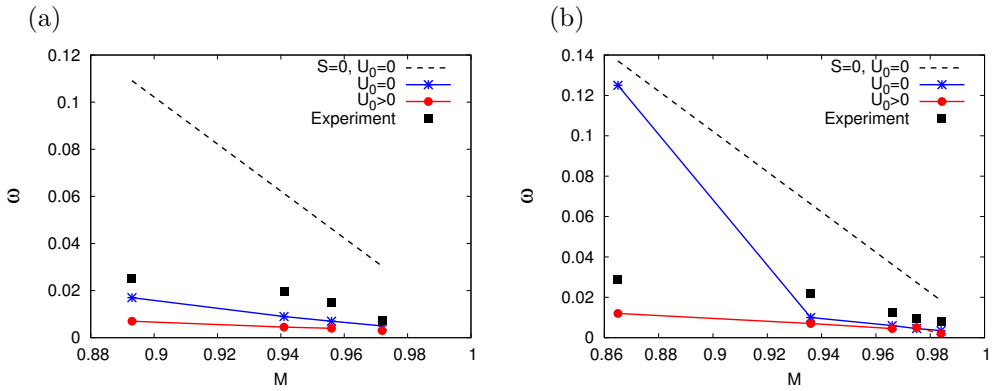

Figure 6.1: Inviscid numerical and experimental frequencies as a function of the velocity ratio M for parameter combinations from Table 6.1: (a) $A1$-$A4$, (b) $B1$-$B5$.

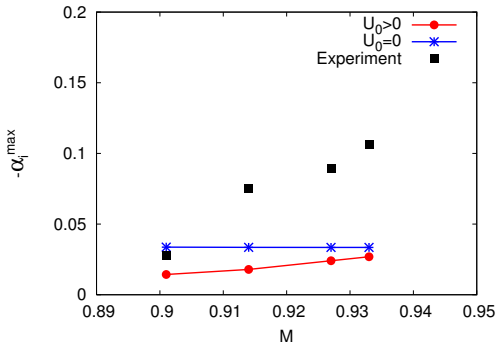

Figure 6.2: Inviscid numerical and experimental growth rates as a function of the velocity ratio M for parameter combinations $C1$-$C4$ from Table 6.1.

the calculated frequencies for both $U_0 > 0$ and $U_0 = 0$ (with the exception of case $B1$) are systematically smaller than the experimental values.

The maximum spatial growth rates in Figure 6.2 correspond to case C from Table 6.1, in which the liquid velocity is fixed. For all cases $C1$-$C4$, the flow is convectively unstable for $S > 0$, and both $U_0 = 0$ and $U_0 > 0$. In addition, a single unstable mode is present, whose maximum spatial growth rate $-\alpha_i^{\max}$ is shown in the figure. The computed inviscid growth rates as a function of M agree neither qualitatively nor quantitatively with the measured values for both $U_0 = 0$ and $U_0 > 0$. In particular, the discrepancy between the inviscid and experimental values increases with the velocity ratio M.

Planar Experimental Setup

As for the axisymmetric configuration, the measured frequencies decrease with M. In addition, for cases A and B the experimental growth rates increase with the velocity ratio up to $M \approx 0.95$ and decay for larger values of M. For cases C and D there is an initial decrease followed by a monotonous increase with a peak close to $M = 0.98$. Generally, there is considerably less variation in the experimental growth rates for C and D.

In Figure 6.3 both the frequencies (left) and growth rates (right) from the inviscid stability analysis are compared with the experimental values using nondimensional units. Again, for

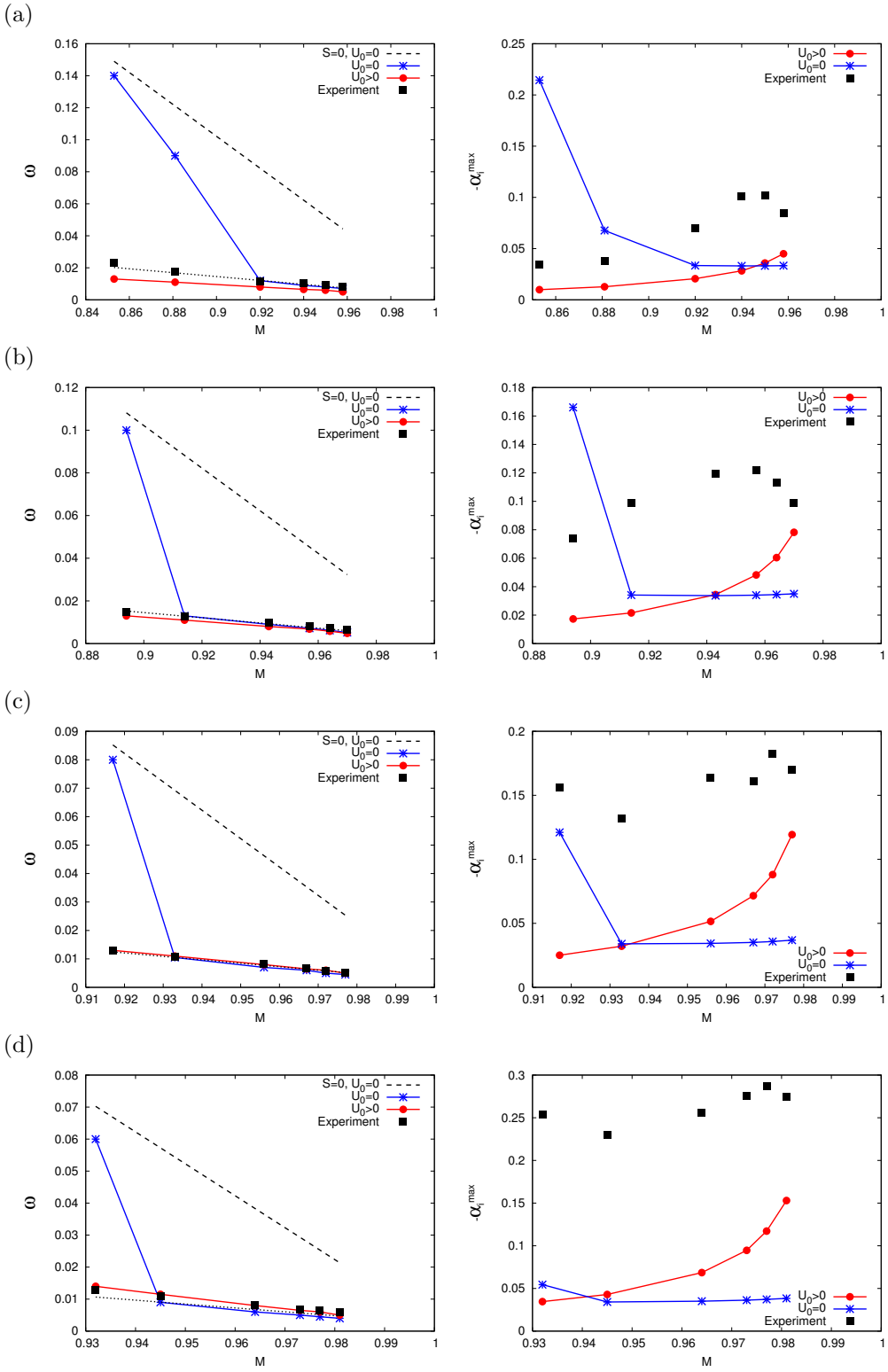

Figure 6.3: Invisicd numerical and experimental results for the frequencies (left) and growth rates (right) as a function of the velocity ratio M for parameter combinations from Table 6.2: (a) $A1$-$A6$, (b) $B1$-$B6$, (c) $C1$-$C6$, (d) $D1$-$D6$. In the left plots, the dotted lines close to the experimental values correspond to Matas' [41] approximation (6.2).

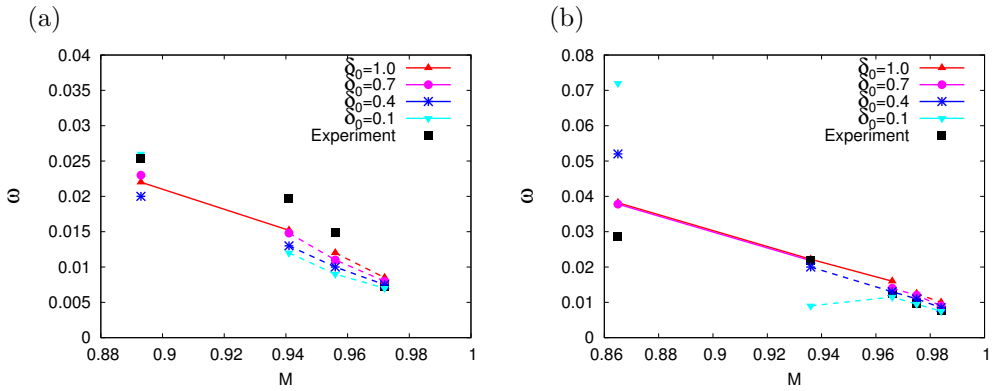

Figure 6.4: Viscous numerical and experimental frequencies as a function of the velocity ratio M for parameter combinations from Table 6.1: (a) $A1$-$A4$, (b) $B1$-$B5$.

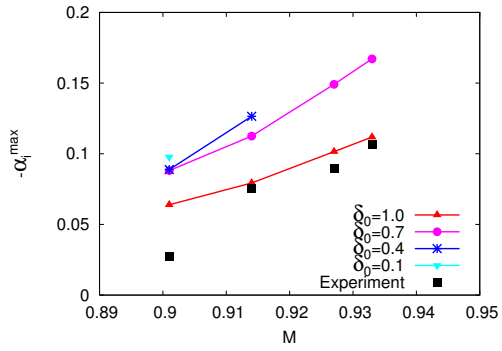

Figure 6.5: Viscous numerical and experimental growth rates as a function of the velocity ratio M for parameter combinations $C1$-$C4$ from Table 6.1.

$U_0 = 0$ and $S = 0$ all cases are absolutely unstable, and the absolute frequencies ω^0 significantly exceed the experimental values. Contrary, for $S > 0$ all cases are convectively unstable for both $U_0 > 0$ and $U_0 = 0$. In addition, for most experimental cases a single unstable mode is present at small frequencies for both $U_0 > 0$ and $U_0 = 0$. In the latter case, however, mode II at relatively larger frequencies is unstable for small velocity ratios M. As long as only a single unstable mode is present, the values $\omega^{\max}$ match the measured frequencies very well for both $U_0 > 0$ and $U_0 = 0$. On the other hand, when mode II is unstable, both its growth rate $-\alpha_i^{\max}$ and the corresponding frequency $\omega^{\max}$ exceed the values of mode I as well as the experimental data. The presence of mode II seems to be completely ignored by Matas et al. [41], since they refer to a favourable comparison of the inviscid freqencies to the experimental data. In addition, assuming $U_0 = 0$ they suggest the approximation

$$\omega \approx r(1+M)\left[1+\frac{5}{2}\sqrt{2}\left(r\frac{1+2M+M^2}{1-2M+M^2}\right)^{-1/2}\right] \tag{6.2}$$

for the measured frequency [41]. This result is shown as dotted line in the frequency plots of Figure 6.3, and agrees very well with the measured values.

Finally, the calculated maximum spatial growth rates usually underpredict the measured values, where the curve $-\alpha_i^{\max}(M)$ for $U_0 > 0$ agrees better with the experimental data.

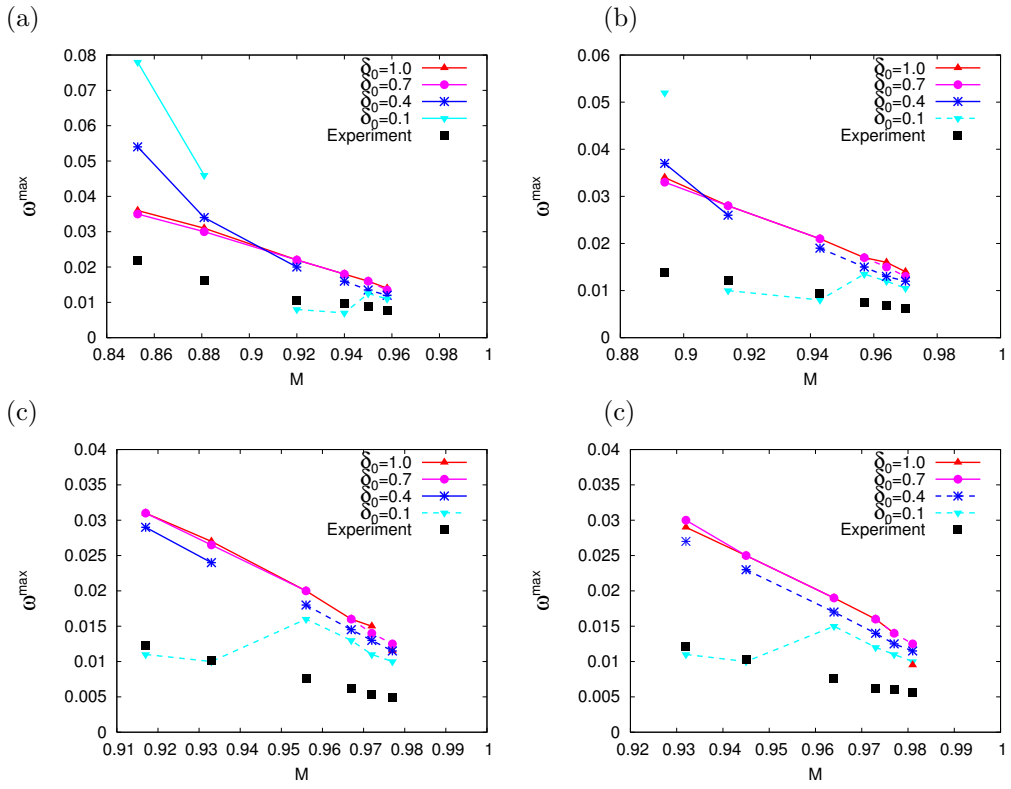

Figure 6.6: Viscous numerical and experimental results for the dominant frequency as a function of the velocity ratio M for parameter combinations from Table 6.2: (a) $A1$-$A6$, (b) $B1$-$B6$, (c) $C1$-$C6$, (d) $D1$-$D6$.

6.3 Viscous Results vs. Experiments

In Figures 6.4-6.8 the experimental data are presented together with spatial instability results from viscous theory for four selected defect widths δ_0: 1, 0.7, 0.4, 0.1.
As in the previous section, when the flow is convectively unstable, plotted frequencies correspond to those associated to the maximum spatial growth rates (solid lines), whereas they correspond to absolute frequencies for an absolutely unstable flow (dashed lines). In addition, plotted growth rates correspond to $-\alpha_i^{\max}$ for convectively unstable flows only.

Axisymmetric Experimental Setup

For the axisymmetric configuration, Figure 6.4 shows the comparison of the experimental and numerical frequencies for cases A and B from Table 6.1 using nondimensional units. The agreement with the experiments is fairly good for all values of M when δ_0 is close or equal to unity. For $M < 0.9$, the flow is convectively unstable for all values of the defect width δ_0. Turning to relatively larger velocity ratios, the flow may become absolutely unstable for small values $\delta_0 < 1$, but it remains convectively unstable up to $M \approx 0.96$ when $\delta_0 = 1$. The calculated frequency shows a monotonous dependence on M except for the small value $\delta_0 = 0.1$ in case $B2$, where absolute instability is associated with the viscous mode I instead of mode II as usual.
The maximum spatial growth rates in Figure 6.5 correspond to case C from Table 6.1, in which the liquid velocity is fixed. The computed growth rates are only slightly above the measured values, and the discrepancy increases with decreasing δ_0. The best agreement is obtained for the curve with $\delta_0 = 1$. The corresponding dominant spatial mode is mode II.

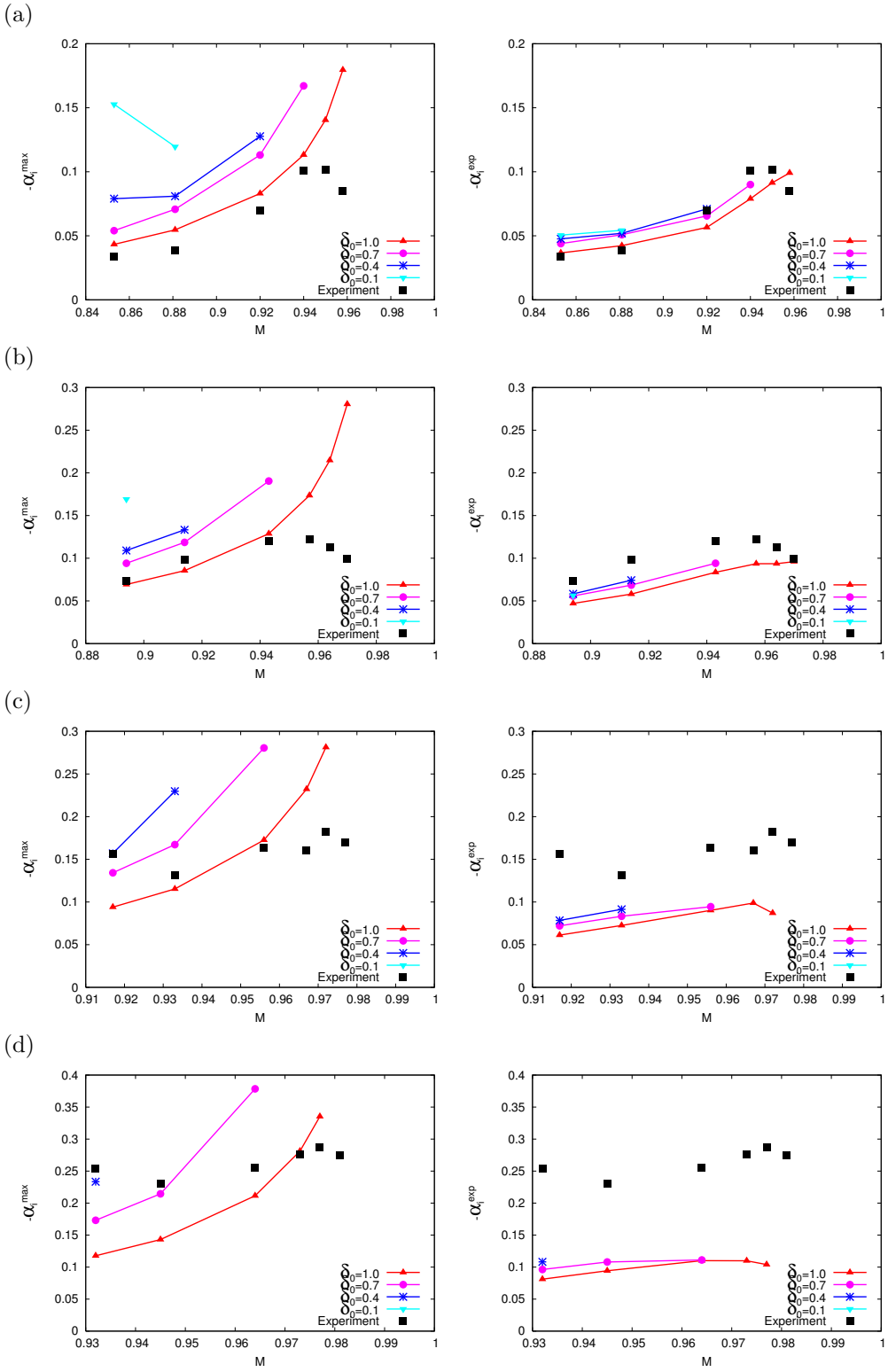

Figure 6.7: Viscous numerical and experimental results for the growth rate as a function of the velocity ratio M for parameter combinations from Table 6.2: (a) $A1$-$A6$, (b) $B1$-$B6$, (c) $C1$-$C6$, (d) $D1$-$D6$. The left column shows the maximum growth rates from stability theory. The right column shows the largest growth rate corresponding to the experimenal value of the frequency.

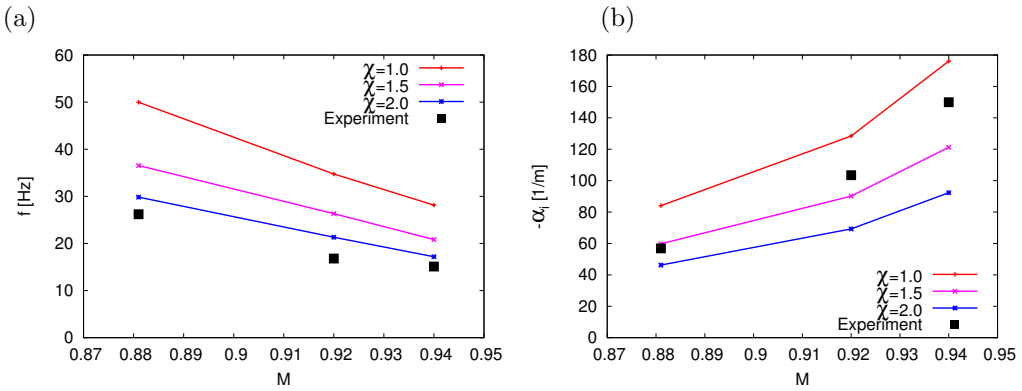

Figure 6.8: Comparison between viscous results and the experimental cases $A2$-$A4$ from Table 6.2 assuming a gas boundary layer thickness $\chi\delta_2$ and different values of χ: (a) dimensional frequencies, and (b) dimensional growth rate. The results for $\chi = 1$ correspond to those in Figure 6.6(a) and 6.7(a).

Planar Experimental Setup

For the planar configuration, in Figure 6.6 the frequencies $\omega^{\max}$ from the viscous stability analysis are compared with the experimental values using nondimensional units. Absolute instability appears above $M \approx 0.97$ and $M \approx 0.9$ for $\delta_0 = 1$ and $\delta_0 = 0.1$, respectively.
Although the computed frequencies and the experimental values both decrease with M, generally no favorable agreement with the experiment is observed for $\delta_0 = 1$. Instead, the predicted frequencies are systematically higher. This is contrary to the axisymmetric geometry. However, there is good agreement for $\delta_0 = 0.1$ in a certain range around $M \approx 0.93$ in all cases A-D. For these parameters, the flow is absolutely unstable, and the absolute frequency originates from the generalized branch corresponding to mode I. At larger velocity ratios the absolute instability for $\delta_0 = 0.1$ is caused by mode II, and the corresponding frequencies again exceed the experimental values. All frequencies for larger δ_0 are also associated with mode II.

In view of the differences between the measured and the theoretical frequencies (at least for δ_0 close to unity) both the maximum growth rates and the largest growth rates corresponding to the experimentally measured frequencies were computed.
The plots in the left column of Figure 6.7 display the maximum growth rates for the different values $\delta_0 \leq 1$. The results for $\delta_0 = 1$ represent the same trends as in the experiments in cases A and B for $M < 0.95$, and the agreement in the numerical values is fairly good. However, the theoretical maximum growth rates increase monotonously with M and do not reproduce the decay for $M > 0.95$. Since the values $-\alpha_i^{\max}$ increase with decreasing defect width, agreement with the experiments is generally worse for relatively smaller values $\delta_0 < 1$. In cases C and D the theoretical growth rates follow the same trend with M as for cases A and B, which is not seen in the experimental values. In particular, the initial decrease in the experimental growth rates at the lower values of M is not reproduced.
The right column of Figure 6.7 shows the growth rates computed with the experimental frequencies. For case A and $\delta_0 = 1$ there is fairly good overall agreement with the measured growth rates at all velocity ratios, although the small peak near $M = 0.95$ is not reproduced. The differences for $\delta_0 < 1$ are also fairly minor. For increasing gas velocity, i.e. from cases B to D, there is a systematically increasing discrepancy between theoretical and measured values. Nevertheless, the dependence on M resembles that of the experiment to a better degree than that of the maximum growth rates from the stability analysis.
The differences between the measurements by Matas et al. [41] and the stability analysis might be caused by an underestimation of the gas boundary layer width δ_2 in the experiments since it

is measured in the nozzle. It is conceivable that the actual width is somewhat larger outside the nozzle. In order to test this idea, δ_2 is increased by a factor $\chi \geq 1$ in the selected cases $A2$-$A4$ from Table 6.2. Since δ_2 is used for non-dimensionalization, dimensional quantities have to be used in Figure 6.8 to facilitate a comparison. The defect width is kept at $\delta_0 = 1$ since this value captures the dependence of the growth rate on M satisfactorily for $M < 0.95$ in Figure 6.7. The dimensional width δ_1 of the liquid boundary layer is also kept constant. Figure 6.8 indeed shows that increasing δ_2 reduces the maximum frequency and therefore improves the agreement between theory and experiment. However, the agreement for the growth rates deteriorates significantly. Therefore, underestimation of the gas boundary layer width δ_2 does not satisfactorily account for the overprediction of the frequencies in the stability analysis. Note, that the results of Figure 6.8 have also been computed by increasing δ_1 in proportion with δ_2. They essentially coincide with those for fixed δ_1.

It is finally remarked, that the inclusion of a realistic amount of gravity into the viscous calculations for some experimental cases shows almost no effect on the results, since the spatial instability curves for $F = 0$ are visually indistinguishable from those including gravity.

6.4 Summary

In this chapter, the numerical results for both viscous and inviscid spatial theory are compared with experimental data for both the axisymmetric [39] and the planar configuration [41]. It is found that, with the exception of the frequencies in the planar case, the growth rates and wavelengths observed in experiments can be predicted much better when applying a viscous study of spatially growing disturbances. Hence, the inviscid piecewise linear approach is a generally inadequate model in order to predict the experimental results. This suggests, that the presence of viscosity, particularly the viscosity-contrast mechanism, which by definition is excluded in inviscid theory, plays an important role in the experiments considered.
It is also found, that the experimental data is best reproduced, when the velocity distribution increases monotonously from the liquid to the gas side, i.e. for $\delta_0 = 1$. Assuming convective instability, this suggests that in the experiments the compensation of the velocity deficit near the interface is much faster than the growth of the initially small perturbations, which occurs almost entirely on the relaxed velocity profile.

Chapter 7

Summary and Conclusions

The characteristics of liquid atomization by a fast gas stream at all stages depend on the nature and properties of the initial stage of the atomization process, which is considered as a linear stability analysis of small wavelike perturbations. As in most other references [6, 34, 39], the assumption of a time-independent parallel basic flow with known basic velocity profile $U(y)$ is also adopted in this work, since it reduces the stability problem to one inhomogeneous direction in space. In addition, although, in general, no Squire's theorem exists for the two-fluid problem, the instability of two-phase mixing layers is considered for two-dimensional perturbations only. This choice is guided by recent atomization experiments with air and water [39, 41], where the fast gas stream leads to the breakup of the liquid, and the wavy perturbations at the deformed interface evolve in the streamwise direction only.
Since so far neither inviscid theory nor previous viscous studies of temporally growing disturbances [6, 61] are fully capable in predicting all the characteristic features (length scales, growth rates and wave speeds of the most amplified linear perturbations) present in the initial stage of the atomization process observed in experiments, the claim of the present work is to overcome the discrepancy between experiment and theory by adopting a viscous instability analysis of spatially growing disturbances.

If one wishes to account for viscous effects in the stability analysis, realistic basic velocity profiles need to include viscous boundary layers adjacent to the interface to satisfy both continuity of velocity and shear stress on the interface. In addition, the work extends previous studies of such two-phase mixing layers [6, 61] by taking into account the particular wake-like structure of the planar basic velocity distribution near the nozzle by an adjustable velocity deficit on the interface. All these conditions are fullfilled by the viscous error function velocity distribution defined in Section 5.1, which also contains the monotonous smooth velocity profile from [6, 61] as a special case when the velocity deficit is absent. For given viscosity ratio, the generalized profile depends on the velocity ratio M of the free streams, the thicknesses of the boundary layers in liquid and gas, and the defect width δ_0 characterizing the velocity deficit. A similar basic flow was used in an inviscid study by Koochesfahani and Frieler [34]. Their basic velocity profile is composed of the hyperbolic tangent profile plus a wake component represented by a Gaussian distribution. Note that, in a fully rigorous treatment a spatially developing, two-dimensional basic flow $U(x, y)$ should be studied, which depends on the downstream distance from the splitter lip. In the present work, however, the consequences of a given defect size is considered, and the problem is reduced using the standard parallel flow hypothesis.

Additionally, the instability of piecewise linear basic flow is considered in order to compare with both the viscous results and previous inviscid results. Therefore, two families of piecewise linear velocity profiles are defined, which match increasingly more characteristic features of the viscous error-function profile, and differ only in the vicinity of the interface, see Section 4.1.

As a consequence of using the standard parallel flow hypothesis, the instability equations constitute a generalized eigenvalue problem, see Section 2.4. The eigenvalues resulting from either the temporal or spatial instability formulation are determined as the eigenvalues of linear algebraic equations. In the inviscid piecewise linear approach these equations take more or less simple analytical forms, see Section 4.1. For viscous flows, however, generally the dispersion relation cannot be given analytically, and the eigenvalues must be determined by means of appropriate numerical methods, see Chapter 3. The viscous instability problem is solved using Chebyshev collocation.

For both the viscous and the inviscid case it is shown, how the structure of the basic velocity distribution modifies the temporal and spatial stability properties. In addition, transition from convective to absolute instability is determined by computing generalized spatial branches. In this considerations surface tension is taken into account but gravity effects are neglected.

Inviscid Results

For the piecewise linear velocity profile (4.7), in general, two unstable modes I and II are present. Mode I is associated with the boundary layer δ_2 in the gas, whereas mode II, which occurs at relatively larger wave numbers, is related to the boundary layer δ_1 in the liquid.
When the dimensionless interface velocity equals the mean liquid velocity, i.e. $U_0 = 1 - M$, there is effectively no liquid boundary layer. Hence, in this case only mode I is unstable. In the absence of surface tension, $S = 0$, the temporal growth rate ω_i of mode I is exactly a linear function of the velocity ratio M [31], and the normalized maximum growth rate $\omega_i^{\max}/M$, and its associated wave number $\alpha^{\max}$ both decrease with the density ratio r [39]. Contrary, when $S > 0$, ω_i depends on M in a nontrivial manner. In the spatial case, however, the growth rates $-\alpha_i$ do not scale with the velocity ratio, even for $S = 0$, and the rate of maximum spatial amplification $-\alpha_i^{\max}$ increases with M. The dependency of the maximum spatial growth rate and its associated wave number with both r and S is generally similar to the temporal case. More precisely, for spatial modes all $-\alpha_i^{\max}$, $\alpha_r^{\max}$, and the associated frequency $\omega^{\max}$ decrease with r, whereas the wave speed $c^{\max} = \omega^{\max}/\alpha_r^{\max}$ approaches the dimensionless mean velocity in the liquid, i.e. $c^{\max} \to 1 - M$, as $r \to 0$. Further, the effect of surface tension is much more pronounced for relatively large density ratios, say $r \geq 0.01$.
When $U_0 \neq 1 - M$, for both temporally and spatially growing perturbations, both the growth rate and the unstable wave number range of mode I generally increase with decreasing U_0. In addition, mode II may be unstable, where, contrary to mode I, its instability characteristics strongly depend on n. It is also observed, that for some cases the two unstable branches I and II have merged into a single curve. This formation of a single unstable mode depends on the parameters and can be found in both the temporal and the spatial setting. It is further observed, that the dominant modes in the temporal and in the spatial analyses are not necessarily identical. This effect can be explained using Gaster's transformation (2.98), which states that the ratio of temporal and spatial growth rates is approximately equal to the group velocity c_g.

Further, for $S = 0$ a necessary condition for convective instability of the piecewise linear velocity profile (4.7) is

$$U(y) > 0, \quad \text{for all } y.$$

Hence, when $U_0 \neq 1 - M$ and $M < 1$, in case of convective instability $U_0 > 0$, whereas $U_0^t = 0$ is the interface velocity of convective/absolute transition, which is independent of r and n. In this case, the absolute wave number is $\alpha_r^0 \to +\infty$, and the absolute frequency is given by (4.20),

$$\omega^0 = \frac{r(1+M) + n(1-M)}{r+1}.$$

Since $\alpha_r^0 \to +\infty$, for $S = 0$ there must exist a spatial instability curve, whose interval of unstable wave numbers increases with decreasing interface velocity, and the upper bound α_S approaches $+\infty$ in the limit $U_0 \to 0$. A similar behaviour is observed for basic flows with $U_0 = 0$ as $S \to 0$. In the special case $U_0 = 1 - M$, i.e. there effectively does not exist a boundary layer in the liquid, the condition $U_0^t = 0$ results into $M_t = 1$, and (4.20) simplifies to $\omega^0 = 2r/(r+1)$. In this case, each co-flow ($M < 1$) is convectively unstable independent of the density ratio r. Thus, when increasing the velocity ratio to the limit of convective/absolute transition, $M \to M_t = 1$, the value α_S of the only unstable mode I approaches infinity.
Note finally, that for $S > 0$ there is no analogous result possible, since the inclusion of surface tension modifies the convective/absolute characteristics in a nontrivial manner. However, interfacial tension usually promotes absolute instability for small or moderate r.

Viscous Results

The viscous linear instability analysis extends two previous studies by three features. First it incorporates viscous boundary layers, and accounts for the particular flow structure near the nozzle by an adjustable velocity deficit on the interface. This basic flow contains the monotonous smooth velocity profile from [6, 61] as a special case when the velocity deficit is absent. For given viscosity ratio, the generalized profile depends on the velocity ratio M of the free streams, the thicknesses of the boundary layers in liquid and gas, and on the velocity deficit parameter δ_0. Second it performs a spatial stability analysis and third it determines the transition from convective to absolute instability.
For the monotonous, smooth velocity profile from [6, 61], it typically provides three characteristic unstable modes in different wave number intervals. They are caused by the inviscid Kelvin-Helmholtz mechanism due to the free-stream velocity difference, the Tollmien-Schlichting mechanism in the gas boundary layer, and the viscosity-contrast mechanism, which has also been called the H mechanism in [6]. At finite Reynolds numbers Re the different modes are generally mixed. They only become distinct and exclusively generated by the three mechanisms in the limiting case of large Reynolds number.
For $\delta_0 = 1$, the temporal growth rates ω_i of all modes are proportional to the velocity ratio M. Contrary, when the basic flow displays a velocity defect near $y = 0$ ($\delta_0 < 1$), the growth rates are no more proportional to M, and the various modes behave differently with respect to the dimensionless parameters. The presence of the velocity deficit also modifies the effectiveness of the three basic mechanisms and introduces an additional inviscid mechanism due to the appearance of inflection points in both liquid and gas. As a result, one is confronted with a fairly complex interplay of instability mechanisms, which makes the interpretation of the different modes somewhat cumbersome.
In the temporal stability analysis the effects of the dimensionless parameters is systematically examined. The predominant modes turn out to be modes I and II, which are localized at small and large wave numbers, respectively. On the basis of their characteristic dependence on Re, the defect width, and also by the perturbation energy budget, they are shown to be primarily caused by the inviscid and H mechanisms. By contrast to mode II, the velocity deficit can boost mode I significantly. Mode I therefore provides the strongest amplification when a velocity deficit is present and the velocity ratio is moderate. Mode II is strongest when the deficit is absent, or when the velocity ratio is large. Mode III is usually weaker than modes I and II.
Modes I and II can also be identified in the spatial stability analysis. In contrast to the temporal amplification, both modes receive a boost from the velocity deficit. As in the inviscid case, the dominant modes in the temporal and in the spatial analyses are not necessarily identical. While agreement is found for moderate or low density ratios, the results for density ratios near unity frequently differ. Moreover, for large velocity ratios M, absolute instability precludes a comparison between temporal and spatial results. In this range of density ratios, the spatial analysis for convectively unstable flows tends to provide a dominant mode II in contrast to the temporal analysis with a dominant inviscid mode, which originiates in the gas phase. Although

the corresponding parameters r and m are probably not realized in experiments and applications, it is nevertheless remarkable that such a disagreement exists.

The transition from convective to absolute instability has been exclusively studied for density and viscosity ratios corresponding to air and water. Absolute instability is typically encountered for $M > 0.9$, and the velocity deficit leads to absolute instability at a smaller velocity ratio. This result is in line with the behavior for single-phase flows, where wake flows tend to be absolutely unstable without counterflow, whereas pure mixing layers usually require counterflow for absolute instability [13, 29]. In addition, surface tension usually promotes absolute instability because of capillary waves that may travel upstream [50]. The critical velocity ratios where transition appears are in the range of typical gas-assisted atomization experiments.
It is further shown, that the convective/absolute transition can originate from modes of different nature. In addition, depending on the parameters, the detection of absolute instability through pinching of generalized spatial branches may be affected by the additional confinement branches near the imaginary axis. These branches are the result of the distant walls at $y = -L_1$ and $y = L_2$ necessitated by the numerical method [24, 25, 32, 33]. In the unconfined case, there would be a continuous spectrum on the imaginary axis representing waves propagating in the cross-stream direction. The confinement turns it into a discrete set. Since symmetric confinement usually tends to promote absolute instability in single-phase mixing layers [25], it seems plausible for the problem at hand, that the critical velocity ratio M_t for the convective/absolute transition associated with a pinching point of a confinement branch should actually be lower than without confinement.

Comparison with Experiments

Finally, in Chapter 6 the numerical results for both viscous and inviscid spatial theory are compared with experimental data available in the literature [39, 41]. Compared with the inviscid piecewise linear model, the discrepancy between theory and experiment is much less when applying a viscous study of spatially growing disturbances. It is also found, that the agreement between measured frequencies and the viscous results is better for the axisymmetric configuration [39] compared with the planar experimental setup [41]. Finally, the experimental data is best covered for the Stokes case $\delta_0 = 1$.

However, the direct comparison of dominant frequencies and growth rates with experiments leaves room for interpretation. For the axisymmetric nozzle configuration [39] there is fairly good agreement for both frequencies and growth rates without velocity deficit, but the experimental data set is insufficient to verify simultaneous agreement in both quantities. Nevertheless, the viscous results are superior to the inviscid temporal predictions.
For the planar nozzle geometry studied by Matas et al [41], the frequencies are systematically overestimated by at least 50 % in the viscous spatial analysis. However, there is good agreement at some values of the velocity ratio when a strong velocity deficit is assumed. In these cases the flow is absolutely unstable. In addition, the inviscid analysis reproduces the frequencies satisfactorily. On the other hand, the comparison for the growth rates is favorable for low air velocities when the experimental frequencies are used and only a small or moderate velocity deficit is assumed. In particular, the viscous computations reproduce the increase of growth rate with decreasing liquid velocity when the air velocity is fixed. These two seemingly contradictory observations might be reconciled by the following interpretation. The frequency should be determined at the end of the splitter plate, where the flow is expected to be locally absolutely unstable because the velocity deficit is largest. Further downstream, where the growth rate is measured, the velocity deficit has been reduced, and the flow should be convectively unstable. However, it may still be dominated by the frequency generated upstream. The dominance of the inviscid mechanism in the immediate vicinity of the nozzle might be due to non-parallel effects. The viscosity-contrast mechanism might therefore be neutralized in this region.

The given interpretation does not resolve the differences between experimental and theoretical growth rates at the larger gas velocities in the experiment of Matas et al [41]. The experimental values are larger than the numerical predictions in these cases, and the difference increases with the gas velocity. One may think of a number of reasons for this systematic difference. One reason might be that the gas flow becomes turbulent when the streams come into contact at the larger gas velocities, which should imply stronger friction and higher shear. Other reasons could be that the interplay between the evolution of the basic velocity distribution and the perturbations becomes nonlinear at an earlier stage, and that the parallel flow approximation is more inaccurate when the gas velocity is larger. Theoretical investigation of these issues requires accurate nonlinear simulations of the evolving gas-liquid mixing-layer in at least two dimensions. Experiments at lower gas velocities could be useful as a test of the speculative interpretation of the linear dynamics in the planar nozzle configuration.

Acknowledgement

I am grateful to my supervisor, Thomas Boeck, and Maurice Rossi for introducing me to hydrodynamic instability, for valuable discussions over the past years, and their help and advice concerning the completition of the manuscript. Maurice Rossi is further acknowledged for suggesting the consideration of spatial instabilities.
I am also grateful to Milena Pfafferott for overlooking the manuscript in order to improve readability and to reduce the number of spelling mistakes.
Finally, I would like to thank my wife, my parents, relatives and friends for their support and encouragement.

The present work has been supported by the Deutsche Forschungsgemeinschaft (Emmy-Noether grant Bo 1668/2).

Appendix A

A.1 Energy Balance

A.1.1 Energy Balance for Temporal Modes

In terms of the eigenfunctions the temporal energy expressions in equation (2.116) take the form

$$\frac{\partial(E_k+E_p)}{\partial t} = \omega_i \left[\frac{1}{r}\int_{-L_1}^{0}\left(\phi_1'^*\phi_1' + \alpha^2\phi_1^*\phi_1\right)dy + \int_0^{L_2}\left(\phi_2'^*\phi_2' + \alpha^2\phi_2^*\phi_2\right)dy + S\alpha^4 f^* f\right]\exp(2\omega_i) \tag{A.1}$$

$$DIS_1 = -\frac{1}{m}\left[\frac{1}{R}\int_{-L_1}^{0}\left(4\alpha^2\phi_1'^*\phi_1' + \phi_1''^*\phi_1'' + \alpha^2(\phi_1''^*\phi_1 + \phi_1^*\phi_1'') + \alpha^4\phi_1^*\phi_1\right)dy\right]\exp(2\omega_i), \tag{A.2}$$

$$DIS_2 = -\left[\frac{1}{R}\int_0^{L_2}\left(4\alpha^2\phi_2'^*\phi_2' + \phi_2''^*\phi_2'' + \alpha^2(\phi_2''^*\phi_2 + \phi_2^*\phi_2'') + \alpha^4\phi_2^*\phi_2\right)dy\right]\exp(2\omega_i), \tag{A.3}$$

$$REY_1 = \frac{1}{r}\left[\frac{i\alpha}{2}\int_{-L_1}^{0}\left((\phi_1'^*\phi_1 - \phi_1^*\phi_1')\frac{\partial U_1}{\partial y}\right)dy\right]\exp(2\omega_i), \tag{A.4}$$

$$REY_2 = \left[\frac{i\alpha}{2}\int_0^{L_2}\left((\phi_2'^*\phi_2 - \phi_2^*\phi_2')\frac{\partial U_2}{\partial y}\right)dy\right]\exp(2\omega_i), \tag{A.5}$$

$$TAN = \frac{1}{2R}\left[\frac{1}{m}\left(\alpha^2(\phi_1'^*\phi_1 + \phi_1^*\phi_1') + \phi_1''^*\phi_1' + \phi_1'^*\phi_1''\right) - \alpha^2(\phi_2'^*\phi_2 + \phi_2^*\phi_2') - \phi_2''^*\phi_2' - \phi_2'^*\phi_2''\right]_{y=0}\exp(2\omega_i). \tag{A.6}$$

A.1.2 Energy Balance for Spatial Modes

In terms of the eigenfunctions the spatial energy terms on the right-hand side of equation (2.128) read

$$DIS_1 = -\frac{1}{m}\left[\frac{1}{R}\int_{-L_1}^{0}\left(4\alpha^*\alpha\phi_1'^*\phi_1' + \phi_1''^*\phi_1'' + \alpha^2\phi_1''^*\phi_1 + \alpha^{*2}\phi_1^*\phi_1'' + (\alpha^*\alpha)^2\phi_1^*\phi_1\right)dy\right]\exp(-2\alpha_i), \tag{A.7}$$

$$DIS_2 = -\left[\frac{1}{R}\int_0^{L_2}\left(4\alpha^*\alpha\phi_2'^*\phi_2' + \phi_2''^*\phi_2'' + \alpha^2\phi_2''^*\phi_2 + \alpha^{*2}\phi_2^*\phi_2'' + (\alpha^*\alpha)^2\phi_2^*\phi_2\right)dy\right]\exp(-2\alpha_i), \tag{A.8}$$

$$REY_1 = \frac{1}{r}\left[\frac{i}{2}\int_{-L_1}^{0}\left((\alpha\phi_1'^*\phi_1 - \alpha^*\phi_1^*\phi_1')\frac{\partial U_1}{\partial y}\right)dy\right]\exp(-2\alpha_i), \tag{A.9}$$

$$REY_2 = \left[\frac{i}{2}\int_0^{L_2}\left((\alpha\phi_2'^*\phi_2 - \alpha^*\phi_2^*\phi_2')\frac{\partial U_2}{\partial y}\right)dy\right]\exp(-2\alpha_i), \tag{A.10}$$

$$TAN = \frac{1}{2R}\left[\frac{1}{m}(\alpha^2\phi_1'^*\phi_1 + \alpha^{*2}\phi_1^*\phi_1' + \phi_1''^*\phi_1' + \phi_1'^*\phi_1'') - \alpha^2\phi_2'^*\phi_2 - \alpha^{*2}\phi_2^*\phi_2' - \phi_2''^*\phi_2' - \phi_2'^*\phi_2''\right]_{y=0}\exp(-2\alpha_i). \tag{A.11}$$

A.2 Some Properties of Chebyshev Polynomials

Chebyshev polynomials are defined on $[-1,1]$ usually in terms of trigonometric functions,

$$T_j(\tilde{y}) = \cos(j\arccos(\tilde{y})). \tag{A.12}$$

Using definition (A.12), the trigonometric identity $\cos([j+1]\theta) + \cos([j-1]\theta) = 2\cos(\theta)\cos(j\theta)$ with $\theta = \arccos(y)$ gives the recurrence relation

$$T_0(\tilde{y}) = 1, \quad T_1(\tilde{y}) = \tilde{y}, \quad T_{j+1}(\tilde{y}) = 2\tilde{y}T_j(\tilde{y}) - T_{j-1}(\tilde{y}), \quad j \geq 1. \tag{A.13}$$

On the interval $[-1,1]$ the Chebyshev polynomials are orthogonal with respect to the weight function $(1-\tilde{y}^2)^{-1/2}$, i.e.,

$$\int_{-1}^{1} T_j(\tilde{y})T_l(\tilde{y})\frac{d\tilde{y}}{\sqrt{1-\tilde{y}^2}} = \begin{cases} 0, & j \neq l, \\ \pi, & j = l = 0, \\ \pi/2, & j = l \neq 0. \end{cases} \tag{A.14}$$

At the boundaries the Chebyshev polynomials satisfy

$$T_j(\pm 1) = (\pm 1)^j, \tag{A.15}$$

$$T_j'(\pm 1) = j^2(\pm 1)^j, \tag{A.16}$$

$$T_j''(\pm 1) = \frac{1}{3}j^2(j^2-1)(\pm 1)^j, \tag{A.17}$$

$$T_j'''(\pm 1) = \frac{1}{15}j^2(j^2-1)(j^2-4)(\pm 1)^j, \tag{A.18}$$

where $' \equiv \partial/\partial\tilde{y}$. Further, the derivative of a Chebyshev polynomial can be written as a linear combination of lower order Chebyshev polynomials:

The derivatives of a function $h(y)$ expanded in Chebyshev polynomials can be represented formally as

$$h^{(q)}(y) = \frac{\partial^q}{\partial y^q}h(y) = \sum_{j=0}^{\infty} h_j^{(q)}T_j(y), \quad q \geq 0, \tag{A.19}$$

with $h_j = h_j^{(0)}$, where

$$C_j h_j^{(1)} = 2 \sum_{\substack{k=j+1 \\ k+j=1(mod2)}}^{\infty} k h_k, \qquad j \geq 0, \tag{A.20}$$

gives the coefficients of the first derivative. These expression is a consequence of the relation

$$2T_j(y) = \frac{C_j}{j+1} T'_{j+1}(y) - \frac{\tilde{C}_{j-2}}{j-1} T'_{j-1}(y), \qquad j \geq 0, \tag{A.21}$$

with $C_0 = 2$, $\tilde{C}_0 = 1$, $C_j = \tilde{C}_j = 1$ and $C_{-j} = \tilde{C}_{-j} = 0$, where $j \geq 1$. Due to (A.12) and

$$T'_j(y) = \frac{\sin(j \arccos(y))j}{\sqrt{1-y^2}},$$

(A.21) is a different form of the trigonometric identity $2\sin(\theta)\cos(j\theta) = \sin([j+1]\theta) - \sin([j-1]\theta)$, and $\theta = \arccos(y)$. Consequently, from (A.19) and (A.21) one has

$$\begin{aligned} \frac{\partial}{\partial y} \sum_{j=0}^{\infty} h_j^{(q-1)} T_j(y) \quad &= \quad \frac{\partial^q h}{\partial y^q} = \sum_{j=0}^{\infty} h_j^{(q)} T_j(y) \\ & \qquad \frac{\partial}{\partial y} \frac{1}{2} \sum_{j=0}^{\infty} h_j^{(q)} \left[\frac{C_j}{j+1} T'_{j+1}(y) - \frac{\tilde{C}_{j-2}}{j-1} T'_{j-1}(y) \right], \end{aligned}$$

so that equating coefficients of $T_j(y)$ for $j \geq 1$ gives

$$C_{j-1} h_{j-1}^{(q)} - h_{j+1}^{(q)} = 2j h_j^{(q-1)}, \qquad j, q \geq 1; \tag{A.22}$$

whence (A.20) follows [45]. Further, it follows from (A.20) and (A.22) that

$$C_j h_j^{(2)} = \sum_{\substack{k=j+2 \\ k=j(mod2)}}^{\infty} k(k^2 - j^2) h_k, \qquad j \geq 0. \tag{A.23}$$

Similarly, it may be shown that

$$C_j h_j^{(4)} = \frac{1}{24} \sum_{\substack{k=j+4 \\ k=j(mod2)}}^{\infty} k[k^2(k^2-4)^2 - 3j^2k^4 + 3j^4k^2 - j^2(j^2-4)^2] h_k, \qquad j \geq 0. \tag{A.24}$$

A.3 Relations for the Piecewise Linear Profiles

The linearized instability equation for two-dimensional perturbations in each layer is given by (2.67),

$$\rho_j \left[\left(\frac{\partial}{\partial t} + U_j \frac{\partial}{\partial x} \right) \Delta v_j - U_j'' \frac{\partial v_j}{\partial x} \right] = 0, \qquad j = 1, 2.$$

By substituting

$$v_j(x, y, t) = \frac{\partial}{\partial x} \psi_j(y, t) \exp(i\alpha x), \qquad j = 1, 2, \tag{A.25}$$

into the above equation, one obtains

$$\rho_j \left[\left(\frac{\partial}{\partial t} + i\alpha U_j \right) \Delta \psi_j - i\alpha U_j'' \psi_j \right] = 0, \qquad j = 1, 2. \tag{A.26}$$

For piecewise linear velocity profiles the second derivative of the basic flow is zero, and the solutions of equations (A.26) can be found analytically. Since $U_j'' = 0$, and because $\exp(\pm\alpha y)$ is an eigenfunction of $\Delta = \partial^2/\partial y^2 - \alpha^2$, the solution is a linear combination of the exponentials $\exp(\pm\alpha y)$ for each segment of the piecewise linear profile, i.e.

$$\psi_j(y,t) = \zeta(t)\exp(\pm\alpha y), \qquad j = 1,2.$$

In addition, at the interface continuity of both pressure and normal velocity is required. Further, the same conditions must be applied at each intersection points between the segments. Apart from this, one finally has to impose conditions on the outer boundaries, ideally at $y = \pm\infty$. However, since the inviscid piecewise linear problem can be solved analytically, one easily demands that the perturbations decay for $y \to \pm\infty$.

A.3.1 Derivation of Dispersion Relation (4.5)

The solution is different in each phase and inside and outside the boundary layer. For the velocity profile (4.1) without liquid boundary layer one finds

$$\begin{aligned} y \geq \delta: &\qquad \psi_2^+ = C(t)\exp(-\alpha y),\\ 0 \leq y \leq \delta: &\qquad \psi_2^- = A(t)\exp(\alpha y) + B(t)\exp(-\alpha y),\\ y \leq 0: &\qquad \psi_1 = D(t)\exp(\alpha y), \end{aligned}$$

where ψ_2^+ and ψ_2^- refer to the solutions outside and inside the boundary layer in the gas, respectively. The coefficients A, B, C, and D are determined by the boundary conditions. For inviscid flow, the normal components of velocity and stress are continuous on interfaces. Continuity of the normal velocity means that ψ is continuous at $y = 0$ and $y = \delta$:

$$y = \delta: \qquad A\exp(\alpha\delta) + B\exp(-\alpha\delta) = C\exp(-\alpha\delta), \tag{A.27}$$

$$y = 0: \qquad A + B = D. \tag{A.28}$$

For the continuity of the normal stress, the expressions

$$i\alpha\hat{p}_j = -\frac{i\rho_j}{\alpha}\frac{\partial}{\partial y}\frac{\partial\psi_j}{\partial t} + \rho_j U_j\frac{\partial\psi_j}{\partial y} - \rho_j\psi_j U_j', \qquad j = 1,2, \tag{A.29}$$

are used, where $p_j(x,y,t) = \hat{p}_j(y,t)\exp(i\alpha x)$. Equations (A.29) are the inviscid analogues of (2.54) and (2.55). Let $\dot{}$ denote a time-derivative. Then at the interface one has

$$\begin{aligned} i\alpha\hat{p}_1 &= -i\rho_1\dot{D} + \rho_1\alpha U_0^* D,\\ i\alpha\hat{p}_2 &= -i\rho_2(\dot{A} - \dot{B}) + \rho_2\alpha U_0^*(A - B) - \rho_2(A + B)\frac{U_2^* - U_1^*}{\delta}, \end{aligned}$$

where $U_0^* \equiv U_1^*(0) = U_2^*(0)$. The normal stress condition at $y = 0$ then reads

$$\hat{p}_1 - \hat{p}_2 = s\alpha^2 f, \tag{A.30}$$

where the interface displacement f satisfies the kinematic condition

$$\dot{f} + i\alpha U_0^* f = i\alpha(A + B). \tag{A.31}$$

In addition, the pressure must be continuous at $y = \delta$, i.e.,

$$\hat{p}_2^+ = \hat{p}_2^-, \tag{A.32}$$

where $\hat{p}_2^+$ and $\hat{p}_2^-$ denote the pressure outside and inside the gas boundary layer, respectively, and

$$\begin{aligned} i\alpha\hat{p}_2^+ &= i\rho_2\dot{C}\exp(-\alpha\delta) - \rho_2\alpha U_2^*(\delta)C\exp(-\alpha\delta), \\ i\alpha\hat{p}_2^- &= -i\rho_2\left[\dot{A}\exp(\alpha\delta) - \dot{B}\exp(-\alpha\delta)\right] + \rho_2\alpha U_2^*(\delta)\left[A\exp(\alpha\delta) - B\exp(-\alpha\delta)\right] \\ &\quad -\rho_2\frac{U_2^* - U_1^*}{\delta_2}\left[A\exp(\alpha\delta) + B\exp(-\alpha\delta)\right]. \end{aligned}$$

Writing the time-dependent variables A, B, C, D, and f as $Q(t) = \hat{Q}\exp(-i\omega t)$, equations (A.27)-(A.32) read

$$\begin{aligned} \hat{A} + \hat{B} - \hat{D} &= 0, \\ \hat{A}\exp(\alpha\delta) + \hat{B}\exp(-\alpha\delta) - \hat{C}\exp(-\alpha\delta) &= 0, \\ \rho_1\hat{D}(\alpha U_0^* - \omega) - \rho_2(\hat{A} - \hat{B})(\alpha U_0^* - \omega) + \rho_2(\hat{A} + \hat{B})\frac{U_2^* - U_1^*}{\delta} - s\alpha^2\hat{f} &= 0, \\ (\alpha U_0^* - \omega)\hat{f} - \alpha\hat{A} - \alpha\hat{B} &= 0, \\ (\alpha U_2^*(\delta) - \omega)\left[\hat{A}\exp(\alpha\delta) - \hat{B}\exp(-\alpha\delta)\right] & \\ -\frac{U_2^* - U_1^*}{\delta}\left[\hat{A}\exp(\alpha\delta) + \hat{B}\exp(-\alpha\delta)\right] + (\alpha U_2^*(\delta) - \omega)\hat{C}\exp(-\alpha\delta) &= 0. \end{aligned}$$

These relations can be written completely in terms of $\hat{A}$ and $\hat{B}$. Using $r = \rho_2/\rho_1$, $\Delta U = U_2^* - U_1^*$, and $V_j = \alpha U_j^* - \omega$, with $j = 1, 2$, one obtains

$$\left[-\left(1 - \frac{1}{r}\right)V_1 + \frac{\Delta U}{\delta} - \frac{s\alpha^3}{\rho_2 V_1}\right]\hat{A} + \left[\left(1 + \frac{1}{r}\right)V_1 + \frac{\Delta U}{\delta} - \frac{s\alpha^3}{\rho_2 V_1}\right]\hat{B} = 0, \tag{A.33}$$

$$\left(2V_2 - \frac{\Delta U}{\delta}\right)e^{\alpha\delta}\hat{A} - \frac{\Delta U}{\delta}e^{-\alpha\delta}\hat{B} = 0. \tag{A.34}$$

Upon setting the corresponding determinant equal to zero, and introducing $\bar{U} = (U_1^* + U_2^*)/2$, then $U_1^* = \bar{U} - \Delta U/2$, $U_2^* = \bar{U} + \Delta U/2$, and the following dispersion relation ensues:

$$\begin{aligned} &2\left(1 + \frac{1}{r}\right)\delta^2(\alpha\bar{U} - \omega)^2 + \left(1 - \frac{1}{r}\right)\delta(\alpha\bar{U} - \omega)\left(1 - e^{-2\alpha\delta}\right)\Delta U \\ &-\left(\frac{1}{2}\left(1 + \frac{1}{r}\right)\alpha\delta(\alpha\delta - 1) - \alpha\delta + 1 - \left[1 + \frac{1}{2}\left(1 - \frac{1}{r}\right)\alpha\delta\right]e^{-2\alpha\delta}\right)(\Delta U)^2 \\ &+\frac{s\alpha^3\delta}{\rho_2\left[\alpha\left(\bar{U} - \frac{1}{2}\Delta U\right) - \omega\right]}\left[\left(1 - \alpha\delta - e^{-2\alpha\delta}\right)\Delta U - 2(\alpha\bar{U} - \omega)\delta\right] = 0. \end{aligned} \tag{A.35}$$

For non-dimensionalization, δ and $\bar{U}$ are chosen as length and velocity scale, respectively. Upon making the substitutions $\alpha\delta \mapsto \alpha$, $\omega/\bar{U} \mapsto \omega$, and introducing the velocity ratio M by definition (4.3), the dispersion relation in terms of dimensionless parameters may be written as

$$\begin{aligned} &\left(1 + \frac{1}{r}\right)(\alpha - \omega)^2 + \left(1 - \frac{1}{r}\right)(\alpha - \omega)\left(1 - e^{-2\alpha}\right)M \\ &-\left(\left(1 + \frac{1}{r}\right)\alpha(\alpha - 1) - 2\alpha + 2 - \left[2 + \left(1 - \frac{1}{r}\right)\alpha\right]e^{-2\alpha}\right)M^2 \\ &+\frac{S\alpha^3}{\alpha(1 - M) - \omega}\left[\left(1 - \alpha - e^{-2\alpha}\right)M - (\alpha - \omega)\right] = 0. \end{aligned} \tag{A.36}$$

When multiplying (A.36) with $(\alpha(1 - M) - \omega)$ the final form (4.5) is obtained.

A.3.2 Derivation of Dispersion Relation (4.9)

For the basic flow (4.6) the solution in each phase inside and outside the boundary layer is

$$\begin{aligned} y \geq \delta_2 : \quad & \psi_2^+ = C_2(t)\exp(-\alpha y), \\ 0 \leq y \leq \delta_2 : \quad & \psi_2^- = A_2(t)\exp(\alpha y) + B_2(t)\exp(-\alpha y), \\ -\delta_1 \leq y \leq 0 : \quad & \psi_1^+ = A_1(t)\exp(\alpha y) + B_1(t)\exp(-\alpha y), \\ y \leq -\delta_1 : \quad & \psi_1^- = C_1(t)\exp(\alpha y). \end{aligned}$$

The coefficients A_j, B_j, C_j, $j = 1, 2$, are determined by the boundary conditions. For inviscid flow, the normal components of velocity and stress are continuous on interfaces. Continuity of the normal velocity at $y = 0$, $y = -\delta_1$, and $y = \delta_2$ is given by

$$y = 0 : \quad A_1 + B_1 = A_2 + B_2, \tag{A.37}$$

$$y = -\delta_1 : \quad A_1\exp(-\alpha\delta_1) + B_1\exp(\alpha\delta_1) = C_1\exp(-\alpha\delta_1), \tag{A.38}$$

$$y = \delta_2 : \quad A_2\exp(\alpha\delta_2) + B_2\exp(-\alpha\delta_2) = C_2\exp(-\alpha\delta_2). \tag{A.39}$$

Analogous as for the velocity profile (4.1), the continuity condition of normal stresses at the interface $y = 0$ is

$$\hat{p}_1 - \hat{p}_2 = s\alpha^2 f, \tag{A.40}$$

where $p_j(x, y, t) = \hat{p}_j(y, t)\exp(i\alpha x)$, and the interface displacement f satisfies the kinematic condition

$$\dot{f} + i\alpha U_0^* f = i\alpha(A_2 + B_2), \tag{A.41}$$

and

$$\begin{aligned} i\alpha\hat{p}_1 &= -i\rho_1(\dot{A}_1 - \dot{B}_1) + \rho_1\alpha U_0^*(A_1 - B_1) - \rho_1\frac{U_0^* - U_1^*}{\delta_1}(A_1 + B_1), \\ i\alpha\hat{p}_2 &= -i\rho_2(\dot{A}_2 - \dot{B}_2) + \rho_2\alpha U_0^*(A_2 - B_2) - \rho_2\frac{U_2^* - U_0^*}{\delta_2}(A_2 + B_2). \end{aligned}$$

The pressure must be continuous at $y = -\delta_1$, i.e.,

$$\hat{p}_1^+ = \hat{p}_1^-, \tag{A.42}$$

where $\hat{p}_1^+$ and $\hat{p}_2^-$ denote the pressure inside and outside the liquid boundary layer, respectively, and

$$\begin{aligned} i\alpha\hat{p}_1^+ &= -i\rho_1\left(\dot{A}_1\exp(-\alpha\delta_1) - \dot{B}_1\exp(\alpha\delta_1)\right) + \rho_1\alpha U_1^*\left(A_1\exp(-\alpha\delta_1) - B_1\exp(\alpha\delta_1)\right) \\ &\quad -\rho_1\frac{U_0^* - U_1^*}{\delta_1}\left(A_1\exp(-\alpha\delta_1) + B_1\exp(\alpha\delta_1)\right), \\ i\alpha\hat{p}_1^- &= -i\rho_1\dot{C}_1\exp(-\alpha\delta_1) + \rho_1\alpha U_1^* C_1\exp(-\alpha\delta_1). \end{aligned}$$

Similarly, at $y = \delta_2$,

$$\hat{p}_2^+ = \hat{p}_2^-, \tag{A.43}$$

where $\hat{p}_2^+$ and $\hat{p}_2^-$ denote the pressure outside and inside the gas boundary layer, respectively, and

$$\begin{aligned} i\alpha\hat{p}_2^+ &= i\rho_2\dot{C}_2\exp(-\alpha\delta_2) - \rho_2\alpha U_2^* C_2\exp(-\alpha\delta_2), \\ i\alpha\hat{p}_2^- &= -i\rho_2\left(\dot{A}_2\exp(\alpha\delta_2) - \dot{B}_2\exp(-\alpha\delta_2)\right) + \rho_2\alpha U_2^*\left(A_2\exp(\alpha\delta_2) - B_2\exp(-\alpha\delta_2)\right) \\ &\quad -\rho_2\frac{U_2^* - U_0^*}{\delta_2}\left(A_2\exp(\alpha\delta_2) + B_2\exp(-\alpha\delta_2)\right). \end{aligned}$$

Writing the time-dependent variables A_j, B_j, C_j, $j = 1, 2$, and f as $Q(t) = \hat{Q}\exp(-i\omega t)$, equations (A.37)-(A.43) read

$$\begin{aligned}
\hat{A}_1 + \hat{B}_1 - \hat{A}_2 - \hat{B}_2 &= 0,\\
\hat{A}_1\exp(-\alpha\delta_1) + \hat{B}_1\exp(\alpha\delta_1) - \hat{C}_1\exp(-\alpha\delta_1) &= 0,\\
\hat{A}_2\exp(\alpha\delta_2) + \hat{B}_2\exp(-\alpha\delta_2) - \hat{C}_2\exp(-\alpha\delta_2) &= 0,\\
\rho_1(\hat{A}_1 - \hat{B}_1)(\alpha U_0^* - \omega) - \rho_1(\hat{A}_1 + \hat{B}_1)\frac{U_0^* - U_1^*}{\delta_1}&\\
-\rho_2(\hat{A}_2 - \hat{B}_2)(\alpha U_0^* - \omega) + \rho_2(\hat{A}_2 + \hat{B}_2)\frac{U_2^* - U_0^*}{\delta_2} - s\alpha^2\hat{f} &= 0,\\
(\alpha U_0^* - \omega)\hat{f} - \alpha\hat{A}_2 - \alpha\hat{B}_2 &= 0,\\
(\alpha U_1^* - \omega)\left(\hat{A}_1\exp(-\alpha\delta_1) - \hat{B}_1\exp(\alpha\delta_1)\right)&\\
-\frac{U_0^* - U_1^*}{\delta_1}\left(\hat{A}_1\exp(-\alpha\delta_1) + \hat{B}_1\exp(\alpha\delta_1)\right) - (\alpha U_1^* - \omega)\hat{C}_1\exp(-\alpha\delta_1) &= 0,\\
(\alpha U_2^* - \omega)\left(\hat{A}_2\exp(\alpha\delta_2) - \hat{B}_2\exp(-\alpha\delta_2)\right)&\\
-\frac{U_2^* - U_0^*}{\delta_2}\left(\hat{A}_2\exp(\alpha\delta_2) + \hat{B}_2\exp(-\alpha\delta_2)\right) + (\alpha U_2^* - \omega)\hat{C}_2\exp(-\alpha\delta_2) &= 0.
\end{aligned}$$

Defining

$$e_1^+ = \exp(\alpha\delta_1), \quad e_2^+ = \exp(\alpha\delta_2), \quad e_1^- = \exp(-\alpha\delta_1), \quad e_2^- = \exp(-\alpha\delta_2),$$

$$D_1 = \frac{(U_0^* - U_1^*)}{\delta_1}, \quad D_2 = \frac{U_2^* - U_0^*}{\delta_2}, \quad V_j = \alpha U_j^* - \omega, \quad j = 0, 1, 2,$$

the compact notation

$$K\vec{x} = \vec{0} \tag{A.44}$$

is obtained, where $\vec{x} = [\hat{A}_1, \hat{B}_1, \hat{C}_1, \hat{A}_2, \hat{B}_2, \hat{C}_2, \hat{f}]^T$,

$$K = \begin{bmatrix}
1 & 1 & 0 & -1 & -1 & 0 & 0\\
e_1^- & e_1^+ & -e_1^- & 0 & 0 & 0 & 0\\
0 & 0 & 0 & e_2^+ & e_2^- & -e_2^- & 0\\
-\rho_1(V_0 - D_1) & \rho_1(V_0 + D_1) & 0 & \rho_2(V_0 - D_2) & -\rho_2(V_0 + D_2) & 0 & s\alpha^2\\
0 & 0 & 0 & \alpha & \alpha & 0 & -V_0\\
e_1^-(V_1 - D_1) & -e_1^+(V_1 + D_1) & -e_1^- V_1 & 0 & 0 & 0 & 0\\
0 & 0 & 0 & e_2^+(V_2 - D_2) & -e_2^-(V_2 + D_2) & e_2^- V_2 & 0
\end{bmatrix},$$

and $\det(K) = 0$ is the dispersion relation. When the mean velocity $\bar{U} = (U_1^* + U_2^*)/2$ is chosen to be the reference velocity scale, then the asymptotic velocities U_1^* and U_2^* can be written as

$$U_1^* = \bar{U} - \frac{\Delta U}{2}, \quad U_2^* = \bar{U} + \frac{\Delta U}{2},$$

where $\Delta U \equiv U_2^* - U_1^*$, and M is the dimensionless velocity ratio defined by (4.3). Choosing δ_2 as reference length scale, and making the substitutions $U_0^*/\bar{U} \mapsto U_0$, and $\omega/\bar{U} \mapsto \omega$, then the dimensionless dispersion relation is a polynomial of fourth degree in ω and can be written in the form (4.9), where

$$\hat{a} = \hat{e}\left[\left(1 + \frac{1}{r}\right)(\alpha U_0 - \omega) + 1 + M - U_0 + \frac{n}{r}(1 - M - U_0)\right],$$

$$\hat{b} = -\hat{f}\left[\left(1 - \frac{1}{r}\right)(\alpha U_0 - \omega) - (1 + M - U_0) - \frac{n}{r}(1 - M - U_0)\right],$$

$$\hat{c} = \hat{g}\left[\left(1-\frac{1}{r}\right)(\alpha U_0-\omega)+1+M-U_0+\frac{n}{r}(1-M-U_0)\right],$$

$$\hat{d} = -\hat{h}\left[\left(1+\frac{1}{r}\right)(\alpha U_0-\omega)-(1+M-U_0)-\frac{n}{r}(1-M-U_0)\right],$$

$$\hat{e} = \left[2(\alpha(1-M)-\omega)-n(1-M-U_0)\right]\left[2(\alpha(1+M)-\omega)-(1+M-U_0)\right],$$

$$\hat{f} = (1+M-U_0)\left[2(\alpha(1-M)-\omega)-n(1-M-U_0)\right]\exp(-2\alpha),$$

$$\hat{g} = n(1-M-U_0)\left[2(\alpha(1+M)-\omega)-(1+M-U_0)\right]\exp\left(-\frac{2\alpha}{n}\right),$$

$$\hat{h} = n(1-M-U_0)(1+M-U_0)\exp(-2\alpha)\exp\left(-\frac{2\alpha}{n}\right).$$

A.3.3 Derivation of the Absolute Frequency (4.17)

Consider the dispersion relation (A.36) of the piecewise linear velocity profile without liquid boundary layer, given by relations (4.2). — It is simpler to use (A.36) instead of equation (4.5). The difference between both relations is the prefactor $(\alpha(1-M)-\omega)$ only. — To show that the convective/absolute transition value is $M_t = 1$ independent of r, the dispersion relation is considered for $S = 0$. Thus

$$\left(1+\frac{1}{r}\right)(\alpha-\omega)^2+\left(1-\frac{1}{r}\right)(\alpha-\omega)\left(1-e^{-2\alpha}\right)M$$
$$-\left(\left(1+\frac{1}{r}\right)\alpha(\alpha-1)-2\alpha+2-\left[2+\left(1-\frac{1}{r}\right)\alpha\right]e^{-2\alpha}\right)M^2 \;=\; 0. \tag{A.45}$$

Since the dispersion relation takes a simple analytical form, one can directly look for a complex pair (α^0,ω^0) of zero group velocity such that conditions (2.139),

$$\frac{\partial\omega}{\partial\alpha}(\alpha^0)=0, \quad \text{and} \quad \omega^0=\omega(\alpha^0),$$

are fullfilled. Upon considering ω as a function of α, differentiating (A.45) with respect to α and setting

$$\frac{\partial\omega}{\partial\alpha}=0,$$

one obtains

$$2\left(1+\frac{1}{r}\right)(\alpha-\omega)+\left(1-\frac{1}{r}\right)\left[1-(1-2(\alpha-\omega))\,e^{-2\alpha}\right]M$$
$$-\left(\left(1+\frac{1}{r}\right)(2\alpha-1)-2+\left[3+\frac{1}{r}+2\left(1-\frac{1}{r}\right)\alpha\right]e^{-2\alpha}\right)M^2 \;=\; 0.$$

This equation is linear in ω and its solution reads

$$\omega^0 \;=\; \frac{\alpha(r+1)}{r+1+(r-1)e^{-2\alpha}M}+\frac{1}{2}\frac{(r-1)\left[1-(1-2\alpha)e^{-2\alpha}\right]M}{r+1+(r-1)e^{-2\alpha}M}$$
$$-\frac{1}{2}\frac{\left[2\alpha(r+1)-3r-1+(3r+1+2\alpha(r-1))e^{-2\alpha}\right]M^2}{r+1+(r-1)e^{-2\alpha}M}. \tag{A.46}$$

When (A.46) is substituted into dispersion relation (A.45), α^0 is found to be a root of

$$D(\alpha,\omega^0)=0. \tag{A.47}$$

When $M = 1$, equation (A.47) can be written as

$$D(\alpha, \omega^0) = \frac{8r\left[(r+1)\alpha - r + (r+(r-1)\alpha)e^{-2\alpha}\right]e^{-2\alpha}}{\left[r+1+(r-1)e^{-2\alpha}\right]^2} = 0$$

with $\alpha = \alpha_r + i\alpha_i$. Because

$$\lim_{\alpha_r \to \infty} D(\alpha, \omega^0) = 0,$$

$\alpha_r^0 \to \infty$ is the absolute wave number. Applying (A.46) with $M = 1$ in the limit $\alpha_r \to \infty$ yields (4.17) for the absolute frequency ω^0. Thus, the imaginary part of ω^0 is indeed zero for $M = 1$, which therefore is the convective/absolute transition value M_t.

A.3.4 Calculating the Convective/Absolute Transition Velocity Ratio

For the dispersion relation (4.5) of the piecewise linear velocity profile without liquid boundary layer, given by relations (4.2), the velocity ratio M_t of convective/absolute transition can be calculated as follows: Upon considering ω as a function of α, differentiating (4.5) with respect to α and setting

$$\frac{\partial \omega}{\partial \alpha} = 0,$$

one obtains

$$\begin{aligned}
(\alpha(1-M)-\omega)\Bigg[&2\left(1+\frac{1}{r}\right)(\alpha-\omega)+\left(1-\frac{1}{r}\right)\left(1-e^{-2\alpha}+2(\alpha-\omega)e^{-2\alpha}\right)M\\
&-\left(\left(1+\frac{1}{r}\right)(2\alpha-1)-2+\left[3+\frac{1}{r}+2\left(1-\frac{1}{r}\right)\alpha\right]e^{-2\alpha}\right)M^2\Bigg]\\
&+(1-M)\Bigg[\left(1+\frac{1}{r}\right)(\alpha-\omega)^2+\left(1-\frac{1}{r}\right)(\alpha-\omega)\left(1-e^{-2\alpha}\right)M\\
&-\left(\left(1+\frac{1}{r}\right)\alpha(\alpha-1)-2\alpha+2-\left[2+\left(1-\frac{1}{r}\right)\alpha\right]e^{-2\alpha}\right)M^2\Bigg]\\
&+S\alpha^3\left[(2e^{-2\alpha}-1)M-1\right]+3S\alpha^2\left[(1-\alpha-e^{-2\alpha})M-(\alpha-\omega)\right] = 0.
\end{aligned} \tag{A.48}$$

This equation is quadratic in ω and its roots can be written as

$$\omega_0^{(1)} = X + \frac{1}{Y}\sqrt{G}, \qquad \omega_0^{(2)} = X - \frac{1}{Y}\sqrt{G}, \tag{A.49}$$

where

$$Y = -2\left[(r+1)(3-M)+2(r-1)e^{-2\alpha}M\right],$$

$$\begin{aligned}
X = \frac{1}{Y}\Big[&2\left((r+1)(\alpha-1)+(r+1+2(r-1)\alpha)e^{-2\alpha}\right)M^2\\
&+\left(4\alpha(r+1)-2(r-1)\left[1+(2\alpha-1)e^{-2\alpha}\right]\right)M+3\alpha(S\alpha r-2(r+1))\Big],
\end{aligned}$$

$$G = \hat{A}M^4 + \hat{B}M^3 + \hat{C}M^2 + \hat{D}M + \hat{E},$$

$$\begin{aligned}
\hat{A} = {}& 12r^2+16r+4+16\alpha[\alpha-1+r(2\alpha+r(\alpha-2)-3)]\\
&+4[4r^2(3\alpha-2)+4\alpha-2(r+1)+(5r^2-2r+1)e^{-2\alpha}]e^{-2\alpha},
\end{aligned}$$

$$\begin{aligned}
\hat{B} = {}& -24r^2-32r-8-32\alpha[\alpha-1+r(2\alpha+r(\alpha-2)-3)]\\
&+8[4r^2(1-\alpha)-4\alpha+2(r+1)-(r-1)^2e^{-2\alpha}]e^{-2\alpha},
\end{aligned}$$

$$\begin{aligned}\hat{C} = \; & 28r^2 + 16r + 4 + 16\alpha[\alpha - 1 + r(2\alpha + r(\alpha - 2) - 3)] \\ & -4[4r^2(\alpha + 2) - 4\alpha + 2(r + 1) - (r - 1)^2 e^{-2\alpha}]e^{-2\alpha} \\ & +4S\alpha^2 \left[2r(2\alpha(4r - 3) - (r - 1)(3 - (3 - 2\alpha)e^{-2\alpha}))e^{-2\alpha} - \alpha r(r + 1)\right],\end{aligned}$$

$$\hat{D} = 8rS\alpha^2 \left[7(r + 1)\alpha - 3(2r + 1) - (2\alpha(r + 2) - 3(2r + 1))e^{-2\alpha}\right],$$

$$\hat{E} = 3rS\alpha^3 \left[4(r + 1) + 3rS\alpha\right].$$

The solutions of both relations (4.5) and (A.48) are obtained numerically for suitable initial values using Mathematica's *FindRoot* procedure, that is a variant of the secant method. When $\omega_0^{(j)}$, $j = 1, 2$, are substituted into the dispersion relation (4.5), α^0 is found to be a root of

$$D(\alpha, \omega_0^{(1)}) = 0 \quad \text{or} \quad D(\alpha, \omega_0^{(2)}) = 0. \tag{A.50}$$

Upon numerically solving (A.50) for complex α^0, and substituting the result into (A.49), one readily obtains the locus of the complex absolute frequency ω^0. By performing the described procedure for various values of M, the value M_t of convective/absolute transition is obtained when the corresponding absolute frequency satisfies $\omega_i^0 = 0$.

A.3.5 Derivation of the Absolute Frequency (4.20)

Consider the piecewise linear velocity profile including a liquid boundary layer, given by relations (4.7). The dispersion relation $D(\alpha, \omega) = 0$, given by (4.9), is investigated for both $S = 0$, and $U_0 = 0$. Upon considering ω as a function of α, differentiating $D(\alpha, \omega) = 0$ with respect to α, and setting

$$\frac{\partial \omega}{\partial \alpha} = 0,$$

the result including a lot of terms may be briefly written as

$$\frac{\partial}{\partial \alpha} D(\alpha, \omega) = 0.$$

Let $\alpha = \alpha_r + i\alpha_i$. In the limit $\alpha_r \to \infty$, after some manipulations the above equation reduces to give

$$4(1 - M)(1 + M)\left[-\left(1 + \frac{1}{r}\right)\omega + 1 + M + \frac{n}{r}(1 - M)\right] = 0,$$

whose solution ω^0 determines the absolute frequency (4.20). The proof is finished by showing that $\alpha_r \to \infty$ is indeed the absolute wave number. This is verified by showing that

$$\lim_{\alpha_r \to \infty} D(\alpha, \omega^0) = 0$$

for the dispersion relation (4.9) with $S = 0$, $U_0 = 0$, and the absolute frequency ω^0 given by equation (4.20).

A.4 The Viscous Two-Phase Mixing Layer Problem

A.4.1 Temporal Eigenvalue Problem

Introducing boundaries at finite distances $y = -L_1$ and $y = L_2$ away from the interface, the modified formulation of the Orr-Sommerfeld problem (2.58)-(2.66) is implemented as follows: Since, for the temporal spectrum, the governing equations are solved for complex frequencies ω given a real streamwise wave number α, the expressions involving ω are grouped together on the

right-hand side of each equation. Then, the equations for the lower liquid layer ($-L_1 \leq y \leq 0$) read

$$\xi_1(y) - \left(\frac{\partial^2}{\partial y^2} - \alpha^2\right)\phi_1(y) = 0, \tag{A.51}$$

$$\left[i\alpha U_1 - \frac{r}{m}\frac{1}{R}\left(\frac{\partial^2}{\partial y^2} - \alpha^2\right)\right]\xi_1(y) - i\alpha U_1''\phi_1(y) = i\omega\xi_1(y), \tag{A.52}$$

where $' \equiv \partial/\partial y$. For the upper gas layer ($0 \leq y \leq L_2$) one has

$$\xi_2(y) - \left(\frac{\partial^2}{\partial y^2} - \alpha^2\right)\phi_2(y) = 0, \tag{A.53}$$

$$\left[i\alpha U_2 - \frac{1}{R}\left(\frac{\partial^2}{\partial y^2} - \alpha^2\right)\right]\xi_2(y) - i\alpha U_2''\phi_2(y) = i\omega\xi_2(y). \tag{A.54}$$

At the outer boundaries the following conditions are imposed:

$$\phi_1 = \phi_1' = 0 \quad \text{at} \quad -L_1, \tag{A.55}$$

$$\phi_2 = \phi_2' = 0 \quad \text{at} \quad L_2. \tag{A.56}$$

Using the substitutions (A.51) and (A.53), the interface conditions read

$$\phi_1 - \phi_2 = 0, \tag{A.57}$$

$$\phi_1' - \phi_2' - \alpha[U_2' - U_1']f = 0, \tag{A.58}$$

$$\xi_1 + 2\alpha^2\phi_1 - m\left[\xi_2 + 2\alpha^2\phi_2\right] = 0, \tag{A.59}$$

and

$$\begin{aligned}\frac{1}{imR}(\xi_1' - 2\alpha^2\phi_1') - \frac{1}{iR}(\xi_2' - 2\alpha^2\phi_2') + \frac{1}{r}[\alpha U_1'\phi_1 - \alpha U_0\phi_1'] \\ -\alpha U_2'\phi_2 + \alpha U_0\phi_2' - \alpha^2[F + \alpha^2 S]f \;=\; \frac{\omega}{r}\left(r\phi_2' - \phi_1'\right).\end{aligned} \tag{A.60}$$

where $U_0 \equiv U_1(0) = U_2(0)$, $U_1''(0) = U_2''(0) = 0$, and

$$f = \frac{\phi_1(0)}{\omega - \alpha U_0}. \tag{A.61}$$

For using the Chebyshev collocation method, the basic velocity profile is given at the Gauß-Lobatto points y_l given by (3.16). In addition, the intervals $[-L_1, 0]$ for ϕ_1, ξ_1 and $[0, L_2]$ for ϕ_2, ξ_2 are transformed to $[-1, 1]$, on which the Chebyshev polynomials T_n are defined, by means of the mappings (3.35) and (3.36). Then, the outer boundaries are located at $\tilde{y} = -1$, and the interface conditions are imposed at $\tilde{y} = 1$. Expanding ϕ_k and ξ_k in Chebyshev polynomials,

$$\phi_k(\tilde{y}) = \sum_{j=0}^{N} a_j^{(k)} T_j(\tilde{y}), \qquad \xi_k(\tilde{y}) = \sum_{j=0}^{N} b_j^{(k)} T_j(\tilde{y}), \qquad k = 1, 2, \tag{A.62}$$

the above equations constitute a generalized eigenvalue problem of the form

$$\begin{bmatrix} A^1 & 0 & 0 \\ 0 & A^2 & 0 \\ \star & \star & \star \end{bmatrix} \begin{bmatrix} \vec{x}_1 \\ \vec{x}_2 \\ f \end{bmatrix} = \omega \begin{bmatrix} B^1 & 0 & 0 \\ 0 & B^2 & 0 \\ \star & \star & \star \end{bmatrix} \begin{bmatrix} \vec{x}_1 \\ \vec{x}_2 \\ f \end{bmatrix}. \tag{A.63}$$

Here $\vec{x}_k = [\vec{a}_k, \vec{b}_k]^T$, $k = 1, 2$, and the vectors $\vec{a}_1 = [a_0^{(1)}, \ldots, a_N^{(1)}]^T$, $\vec{b}_1 = [b_0^{(1)}, \ldots, b_N^{(1)}]^T$, $\vec{a}_2 = [a_0^{(2)}, \ldots, a_N^{(2)}]^T$ and $\vec{b}_2 = [b_0^{(2)}, \ldots, b_N^{(2)}]^T$ contain the Chebyshev coefficients of ϕ_1, ξ_1, ϕ_2 and ξ_2, respectively. The matrix blocks A^1, A^2, and B^1, B^2 with

$$A^k = \begin{bmatrix} A_{11}^k & A_{12}^k \\ A_{21}^k & A_{22}^k \end{bmatrix}, \qquad B^k = \begin{bmatrix} 0 & 0 \\ 0 & B_{22}^k \end{bmatrix}, \qquad k = 1, 2,$$

are given by the Orr-Sommerfeld equations for both fluids, and are coupled by the interface conditions. The matrix blocks A_{ij}^k and B_{ij}^k, $i, j, k = 1, 2$, are of size $(N-1) \times (N+1)$, and the boundary conditions are denoted by $\star$.

A.4.2 Spatial Eigenvalue Problem

To write the Orr-Sommerfeld equations in terms of a linear eigenvalue problem with complex eigenvalues α one has to further expand equations (A.51)-(A.54) to avoid quadratic terms in α. Therfore the equation in both layers is rewritten as outlined in Section 3.4.2. This finally gives eight equations linear in α. For the lower liquid layer ($-L_1 \leq y \leq 0$) one gets

$$\tilde{\phi}_1(y) = \alpha\phi_1(y), \tag{A.64}$$

$$\tilde{\xi}_1(y) = \alpha\xi_1(y), \tag{A.65}$$

$$\phi_1''(y) - \xi_1(y) = \alpha\tilde{\phi}_1(y), \tag{A.66}$$

$$\left(\frac{\partial^2}{\partial y^2} + i\omega\frac{m}{r}R\right)\xi_1(y) + i\frac{m}{r}RU_1''\tilde{\phi}_1(y) - i\frac{m}{r}RU_1\tilde{\xi}_1(y) = \alpha\tilde{\xi}_1(y). \tag{A.67}$$

The equivalent equations for the upper gas layer ($0 \leq y \leq L_2$) are

$$\tilde{\phi}_2(y) = \alpha\phi_2(y), \tag{A.68}$$

$$\tilde{\xi}_2(y) = \alpha\xi_2(y), \tag{A.69}$$

$$\phi_2''(y) - \xi_2(y) = \alpha\tilde{\phi}_2(y), \tag{A.70}$$

$$\left(\frac{\partial^2}{\partial y^2} + i\omega R\right)\xi_2(y) + iRU_2''\tilde{\phi}_2(y) - iRU_2\tilde{\xi}_2(y) = \alpha\tilde{\xi}_2(y). \tag{A.71}$$

At the outer boundaries one imposes the conditions (A.55) and (A.56). The interface conditions are implemented using the new variables $\tilde{\phi}_1$, $\tilde{\xi}_1$, $\tilde{\phi}_2$ and $\tilde{\xi}_2$. They read

$$\phi_1 - \phi_2 = 0, \tag{A.72}$$

$$\omega\phi_1' - \omega\phi_2' = \alpha\left[U_0(\phi_1' - \phi_2') - U_1'\phi_1 + U_2'\phi_2\right], \tag{A.73}$$

$$\xi_1 - m\xi_2 = \alpha\left[2m\tilde{\phi}_2 - 2\tilde{\phi}_1\right], \tag{A.74}$$

$$\begin{aligned} &\frac{1}{imR}\left(\xi_1' - m\xi_2'\right) + \frac{\omega}{r}\left(\phi_1' - r\phi_2'\right) \\ &= \alpha\left[\frac{2}{imR}\left(\tilde{\phi}_1' - m\tilde{\phi}_2'\right) - \frac{1}{r}\left[U_1'\phi_1 - rU_2'\phi_2 - U_0(\phi_1' - r\phi_2')\right] + \vartheta_1 + \vartheta_2 - \vartheta_3\right], \end{aligned} \tag{A.75}$$

where

$$\vartheta_1 = \frac{F\tilde{\phi}_1}{\omega - \alpha U_0}, \qquad \vartheta_2 = \frac{S\tilde{\phi}_1''}{\omega - \alpha U_0}, \qquad \vartheta_3 = \frac{S\tilde{\xi}_1}{\omega - \alpha U_0}. \tag{A.76}$$

For the Chebyshev collocation method the basic velocity profile again is given at the Gauß-Lobatto points, and the transformations (3.35) and (3.36) are used to map the intervals $[-L_1, 0]$

for ϕ_1, ξ_1, $\tilde{\phi}_1$, $\tilde{\xi}_1$ and $[0, L_2]$ for ϕ_2, ξ_2, $\tilde{\phi}_2$, $\tilde{\xi}_2$ onto $[-1, 1]$, where Chebyshev polynomials T_n are defined. Then, the outer boundaries are again located at $\tilde{y} = -1$, and the interface conditions are imposed at $\tilde{y} = 1$. The Chebyshev ansatz for the spatial setting takes the form

$$\phi_k = \sum_{j=0}^{N} a_j^{(k)} T_j, \quad \xi_k = \sum_{j=0}^{N} b_j^{(k)} T_j, \quad \tilde{\phi}_k = \sum_{j=0}^{N} c_j^{(k)} T_j, \quad \tilde{\xi}_k = \sum_{j=0}^{N} d_j^{(k)} T_j, \qquad k = 1, 2. \tag{A.77}$$

Then, the above equations and boundary conditions constitute a generalized eigenvalue problem of the form

$$\begin{bmatrix} A^1 & 0 & 0 \\ 0 & A^2 & 0 \\ \star & \star & \star \end{bmatrix} \begin{bmatrix} \vec{x}_1 \\ \vec{x}_2 \\ \vec{\vartheta} \end{bmatrix} = \alpha \begin{bmatrix} B^1 & 0 & 0 \\ 0 & B^2 & 0 \\ \star & \star & \star \end{bmatrix} \begin{bmatrix} \vec{x}_1 \\ \vec{x}_2 \\ \vec{\vartheta} \end{bmatrix}. \tag{A.78}$$

Here $\vec{x}_k = [\vec{a}_k, \vec{b}_k, \vec{c}_k, \vec{d}_k]^T$, $k = 1, 2$, $\vec{\vartheta} = [\vartheta_1, \vartheta_2, \vartheta_3]$ and the vectors $\vec{a}_k = [a_0^{(k)}, \ldots, a_N^{(k)}]^T$, $\vec{b}_k = [b_0^{(k)}, \ldots, b_N^{(k)}]^T$, $\vec{c}_k = [c_0^{(k)}, \ldots, c_N^{(k)}]^T$ and $\vec{d}_k = [d_0^{(k)}, \ldots, d_N^{(k)}]^T$, $k = 1, 2$, contain the Chebyshev coefficients of ϕ_k, ξ_k, $\tilde{\phi}_k$, $\tilde{\xi}_k$, $k = 1, 2$. The boundary conditions are denoted by $\star$. The matrix blocks A^k and B^k, $k = 1, 2$, with

$$A^k = \begin{bmatrix} 0 & 0 & A_{13}^k & 0 \\ 0 & 0 & 0 & A_{24}^k \\ A_{31}^k & A_{32}^k & 0 & 0 \\ 0 & A_{42}^k & A_{43}^k & A_{44}^k \end{bmatrix}, \qquad B^k = \begin{bmatrix} B_{11}^k & 0 & 0 & 0 \\ 0 & B_{22}^k & 0 & 0 \\ 0 & 0 & B_{33}^k & 0 \\ 0 & 0 & 0 & B_{44}^k \end{bmatrix}, \qquad k = 1, 2,$$

are given by the Orr-Sommerfeld equations for both fluids. As in the temporal case they are coupled by the interface conditions.

Note, that in the eigenvalue problem there is no restriction to real values of the frequencies ω, and generalized spatial branches with $\omega_i \neq 0$ are computed in order to investigate the transition from convective to absolute instability.

Bibliography

[1] Balsa T.F., "On the spatial instability of piecewise linear free shear layers", J. Fluid Mech. 174, 553-563 (1987)

[2] Bayvel L., Orzechowski Z., "Liquid Atomization" (Taylor & Francis, 1993)

[3] Ben Rayana F., "Étude des instabilités interfaciales liquide-gaz en atomization assistée et tailles de gouttes", PhD thesis, Institut National Polytechnique de Grenoble (2007)

[4] Bers, A., "Space-Time Evolution of Plasma Instabilities – Absolute and Convective" in "Handbook of Plasma Physics" edited by Rosenbluth M.N., Sagdeev R.Z. (North-Holland Publication, 1983)

[5] Boeck T., "Coherent structures, instabilities, and turbulence in interfacial and magneto-hydrodynamic flows", Habilitation, Institut für Thermo- und Fluiddynamik, TU Ilmenau (2010)

[6] Boeck T., Zaleski S., "Viscous versus inviscid instability of two-phase mixing layers with continuous velocity profile", Phys. Fluids 17, 032106 (2005)

[7] Boomkamp P.A.M., Miesen R.H.M., "Classification of Instabilities in Parallel Two-Phase Flow", Int. J. Multiphase Flow 22, 67-88 (1997)

[8] Brevdo L., "Spatially Amplifying Waves in Plane Poiseuille Flow", Z. angew. Math. Mech. 72, 163-174 (1992)

[9] Bridges T.J., Morris P.J., "Differential Eigenvalue Problems in Which the Parameter Appears Nonlinearly", J. Comput. Phys. 55, 437-460 (1984)

[10] Briggs R.J., "Electron-Stream Interaction with Plasmas" (Massachusetts Institute of Technology Press, 1964)

[11] Canuto C., Hussaini Y., Quarteroni A., Zang T.A., "Spectral Methods in Fluid Dynamics" (Springer-Verlag, New York, 1988)

[12] Craik A.D.D., "Wave interactions and fluid flows" (Cambridge University Press, 1985)

[13] Criminale W.O., Jackson T.L., Joslin R.D., "Theory and Computation of Hydrodynamic Stability" (Cambridge University Press, 2003)

[14] Danabasoglu G., Biringen S., "A Chebyshev Matrix Method for Spatial Modes of the Orr-Sommerfeld Equation", NASA Contractor Report 4247 (1989)

[15] Deissler R.J., "The convective nature of instability in plane Poiseuille flow", Phys. Fluids 30, 2303-2305 (1987)

[16] Dongarra J.J., Straughan B., Walker D.W. "Chebyshev tau-QZ algorithm methods for calculating spectra of hydrodynamic stability problems", Appl. Numer. Math. 22, 399-434 (1996)

[17] Drazin P.G., "Introduction to Hydrodynamic Stability" (Cambridge University Press, 2002)

[18] Drazin P.G., Reid W.H., "Hydrodynamic Stability" (Cambridge University Press, 1981)

[19] Eggers J., "Nonlinear dynamics and breakup of free-surface flows", Rev. Mod. Phys. 69, 865-929 (1997)

[20] Gaster M., "A note on the relation between temporally-increasing and spatially-increasing disturbances in hydrodynamic stability", J. Fluid Mech. 14, 222-224 (1962)

[21] Golub G.H., Van Loan C.F., "Matrix Computations" (Johns Hopkins University Press, 1996)

[22] Gumerman R.J., Homsy G.M., "Convective Instabilities in Concurrent Two Phase Flow: Part I. Linear Stability", AIChE J. 20, 981-988 (1974)

[23] Hauke G., Dopazo C., Lozano A., Barreras F., Hernandez A.H., "Linear Stability Analysis of a Viscous Liquid Sheet in a High-Speed Viscous Gas", Flow, Turb. and Combust. 67, 235-265 (2001)

[24] Healey J.J., "Enhancing the absolute instability of a boundary layer by adding a far-away plate", J. Fluid Mech. 579, 29-61 (2007)

[25] Healey J.J., "Destabilizing effects of confinement on homogeneous mixing layers", J. Fluid Mech. 623, 241-271 (2009)

[26] Hinch E.J., "A note on the mechanism of the instability at the interface between two shearing fluids", J. Fluid Mech. 144, 463-465 (1984)

[27] Hooper A.P., Boyd W.G.C., "Shear-flow instability at the interface between two viscous fluids", J. Fluid Mech. 128, 507-528 (1983)

[28] Hopfinger E.J., "atomization dun Jet Liquide par un Jet de Gaz Coaxial: Un Bilan des Connaissances Acquises", in "Combustion dans les moteurs fuses, - Actes du Colloque de Synthse du Groupe de Recherche CNES/CNRS/ONERA/SNECMA", 26-28, Juin Toulouse, Cpadus-Editions pp. 34-47 (2001)

[29] Huerre P., Monkewitz P.A., "Absolute and convective instabilities in free shear layers", J. Fluid Mech. 159, 151-168 (1985)

[30] Huerre P., Monkewitz P.A., "Local and Global Instabilities in Spatially Developing Flows", Annu. Rev. Fluid Mech. 22, 473-537 (1990)

[31] Huerre P., Rossi M., "Hydrodynamic instabilities in open flows" in "Hydrodynamics and Nonlinear Instabilities" edited by Godrèche C., Manneville P. (Cambridge University Press, 1998)

[32] Juniper M.P., "The full impulse response of two-dimensional jet/wake flows and implications for confinement", J. Fluid Mech. 590, 163-185 (2007)

[33] Juniper M.P., Candel S.M., "The stability of ducted compound flows and consequences for the geometry of coaxial injectors", J. Fluid Mech. 482, 257-269 (2003)

[34] Koochesfahani M.M., Frieler C.E., "Instability of Nonuniform Density Free Shear Layers with a Wake Profile", AIAA Pap. No. 87-0047 (1987)

[35] Kupfer K., Bers A., Ram A.K. "The cusp map in the complex-frequency plane for absolute instabilities", Phys. Fluids 30, 3075-3082 (1987)

[36] Lasheras J.C., Hopfinger E.J., "Liquid Jet Instability and Atomization in a Coaxial Gas Stream", Annu. Rev. Fluid Mech. 32, 275-308 (2000)

[37] Lefebvre A.H., "Atomization and Sprays" (Hemisphere Publishing Corporation, 1989)

[38] Lock R.C., "The velocity distribution in the laminar boundary layer between parallel streams", Q. J. Mech. Appl, Math. 4, 42-63 (1951)

[39] Marmottant P., Villermaux E., "On spray formation", J. Fluid Mech. 498, 73-111 (2004)

[40] Maslowe S.A., Kelly R.E., "Inviscid instability of an unbounded heterogeneous shear layer", J. Fluid Mech. 48, 405-415 (1971)

[41] Matas J.P., Marty S., Cartellier A., "Experimental and analytical study of the shear instability of a gas-liquid mixing layer", Phys. Fluids 23, 094112 (2011)

[42] Michalke A., "On the inviscid instability of the hyperbolic-tangent velocity profile", J. Fluid Mech. 19, 543-556 (1964)

[43] Michalke A., "On spatially growing disturbances in an inviscid shear layer", J. Fluid Mech. 23, 521-544 (1965)

[44] Monkewitz P.A., Huerre P., "Influence of the velocity ratio on the spatial instability of mixing layers", Phys. Fluids 25, 1137-1143 (1982)

[45] Orszag S.A., "Accurate solution of the Orr-Sommerfeld stability equation", J. Fluid Mech. 50, 689-703 (1971)

[46] Otto T., Rossi M., Boeck T., "Viscous instability of a sheared liquid-gas interface: dependence on fluid properties and basic velocity profile", *submitted to Phys. Fluids*

[47] Plateau J., "Statique Experimentale et Theoretique des Liquides Soumis aux Seules Forces Moleculaires" (Gauthier Villars, Paris), Vol. II, 1873

[48] Rayleigh F.R.S., "On the Instability of Jets", Proc. London Math. Soc. 10, 4-13 (1879)

[49] Raynal L., "Instabilité et entrainement a l'interface d'un couche de mélange liquide-gaz", PhD thesis, Université Joseph Fourier, Grenoble (1997)

[50] Rees S.J., Juniper M.P., "The effect of surface tension on the stability of unconfined and confined planar jets and wakes", J. Fluid Mech. 633, 71-97 (2009)

[51] Renardy Y., "Weakly nonlinear behaviour of periodic disturbances in two-layer Couette-Poiseuille flow", Phys. Fluids A1, 1666-1676 (1989)

[52] Schmid P.J., Henningson D.S., "Stability and Transition in Shear Flows" (Springer-Verlag, New York, 2001)

[53] Smits J.S., "A Physical Introduction To Fluid Mechanics" (John Wiley & Sons, Inc., 2000)

[54] South M.J., Hooper A.P., "Linear growth in two-fluid plane Poiseuille flow", J. Fluid Mech. 381, 121-139 (1999)

[55] Squire H.B., "On the Stability for Three-Dimensional Disturbances of Viscous Fluid Flow between Parallel Walls", Proc. Roy. Soc. London, A142, 621-628 (1933)

[56] Villermaux E., "Mixing and Spray Formation in Coaxial Jets", Journal of Propulsion and Power 14, 807-817 (1998)

[57] Woodley B.M., Peake N., "Global linear stability analysis of thin airfoil wakes", J. Fluid Mech. 339, 239-260 (1997)

[58] Wozniak G., "Zerstäubungstechnik" (Springer-Verlag Berlin Heidelberg, 2003)

[59] Yecko, P., "Disturbance growth in two-fluid channel flow: The role of capillarity", Int. J. Multiphase Flow 34, 272-282 (2008)

[60] Yecko P., Zaleski S., "Transient growth in two phase mixing layers", J. Fluid Mech. 528, 43-52 (2005)

[61] Yecko P., Zaleski S., Fullana J.M., "Viscous modes in two-phase mixing layers", Phys. Fluids 14(12), 4115-4122 (2002)

[62] Yiantsios S.G., Higgins B.G., "Linear stability of plane Poiseuille flow of two superposed fluids", Phys. Fluids 31, 3225-3238 (1988)

[63] Yih C.S., "Instability due to viscosity stratification", J. Fluid Mech. 27, 337-352 (1967)

[64] Yu M.H., Monkewitz P.A., "The effect of nonuniform density on the absolute instability of two-dimensional inertial jets and wakes", Phys. Fluids A 2, 1175-1181 (1990)